Doctoral theses at NTNU, 2023:326

Marcin Ireneusz Duda

# Geomechanics and Rock Physics of Anisotropic Overburden Shales

Doctoral thesis

**NTNU**
Norwegian University of Science and Technology
Thesis for the Degree of
Philosophiae Doctor
Faculty of Engineering
Department of Geoscience and Petroleum

NTNU
Norwegian University of
Science and Technology

Marcin Ireneusz Duda

# Geomechanics and Rock Physics of Anisotropic Overburden Shales

Thesis for the Degree of Philosophiae Doctor

Trondheim, October 2023

Norwegian University of Science and Technology
Faculty of Engineering
Department of Geoscience and Petroleum

NTNU
Norwegian University of
Science and Technology

**NTNU**
Norwegian University of Science and Technology

Thesis for the Degree of Philosophiae Doctor

Faculty of Engineering
Department of Geoscience and Petroleum



ISBN 978-82-326-7352-0 (printed ver.)
ISBN 978-82-326-7351-3 (electronic ver.)
ISSN 1503-8181 (printed ver.)
ISSN 2703-8084 (online ver.)

Doctoral theses at NTNU, 2023:326

Printed by NTNU Grafisk senter

# Abstract

Shales, with their diverse composition and complex properties, present an interesting research subject and a challenging material to work with. As they constitute a significant portion of the overburden in most currently operational subsurface storage sites and reservoirs, their complicated nature poses significant engineering challenges related to subsurface stability and monitoring. This forces geoscientists and geoengineers, including those who are just starting their scientific journey and aspire to work in the field, to delve deeper into the processes taking place inside them.

The low permeability of shales significantly restricts fluid movement within them, making them ideal candidates for cap rock. However, when subjected to ongoing deformation, fluid cannot enter or exit the pores instantly, causing the rock to respond to changes in external stress with alterations in pore pressure. This response further modifies the effective stress in shales, potentially pushing the rock closer to failure or increasing the risk of borehole and casing-related issues. The first part of this thesis primarily examines the undrained pore pressure response.

Through an in-depth introduction and an article, the author and co-authors describe developement and testing of an anisotropic poroelastic model for the undrained pore pressure response in transversely isotropic shales and rocks with lower symmetry classes. Utilizing experimentally determined poroelastic pore pressure coefficients and geomechanical modeling results, the model is applied to predict induced pore pressure changes in the Valhall reservoir's overburden. This study reveals potentially significant pore pressure changes above the reservoir's top surface, indirect evidence of links between the undrained pore pressure response to known casing failures, and formulates a simplified pore pressure modeling workflow for transversely isotropic overburden shales. The second article assesses the impact of the undrained pore pressure response on total stresses at shear failure for various rocks, sample orientations, and stress loading scenarios. The findings highlight the importance of considering the undrained pore pressure response in shale stability and integrity analysis. The final article in this part of the thesis examines the influence of shale plastification, expected near fault zones, on pore pressure response, revealing a gradual transition in magnitude and direction of response with accumulating plastic strains and presents a simple model accounting for plasticity-induced changes in pore pressure parameters.

Another ramification of shales' dominance in typical overburden is that seismic signals traversing toward a reservoir spend a considerable length of time passing through these deposits. Consequently, alterations in shales' acoustic properties could account for a significant portion of observed time-lapse seismic effects utilized in monitoring injection sites or depleting reservoirs. The second part of this thesis revolves around rock physics models that connect observed changes in P- and S-wave acoustic velocities to shale deformation, enabling the connection of time-lapse effects to subsurface geomechanical processes.

The first paper in this part of the thesis establishes and tests a nonlinear third-order elastic strain-dependent dynamic stiffness model for shales, demonstrating a strong fit across various stress loading scenarios and propagation directions. The second paper introduces a modified inversion scheme for estimating third-order elastic coefficients from low-frequency laboratory data, addressing differences in strain sensitivity between high- and low-frequency seismic signals. This paper highlights potential errors when inverting time-lapse seismic data using ultrasonic frequency laboratory calibrations and documents low-frequency strain-sensitivity factors determined from core plugs in experimental conditions consistent with field observations. The final paper expands the initial model to include non-equal horizontal strains and examines the impact of experimental errors, suggesting that shear components of the strain tensor may significantly influence time-shift and time-strains recorded in overburden shales.

These conclusions and observations are prefaced by a concise introduction to undrained pore pressure changes, nonlinear third-order elastic dynamic stiffness models, shale properties, and associated experimental challenges. The thesis concludes with a summary of findings and recommendations for future work.

# Preface

As I neared the finish line of writing this thesis, I found myself frequently reminiscing about how it all began. According to my hopelessly incomplete and biased recollections, I was simply eager to spend a few years immersed in research, regardless of the topic, as long as it was related to something rock physics-ish. My brain craved stimulation, I yearned to do something interesting, and I was ready to finally focus on a single topic for an extended period, rather than hopping from subject to subject (or exam to exam) as I had done during my previous studies. A PhD just seemed like the natural choice.

In my early conversations with Rune, my dear supervisor who I also dare to call a friend, he mentioned Skempton and his pore pressure parameters. It may be a bit anticlimactic, but at that time I was certain I definitely had heard the name before, but could not recall much else. The topic seemed to lean a bit more towards geomechanics than geophysics for my liking, but it was still about shales which I had always found fascinating (especially their capability to cause a really wide range of problems). I also strongly believed in my ability to force myself to get interested in what I was doing, and so I embarked on this journey in January 2018. Well, it worked, I sincerely think it was actually a great choice.

However, the scope of the thesis quickly expanded towards my field of origin, geophysics. Once again, it was Rune who handed me a paper on third-order elasticity, casually remarking that it was "interesting". Apparently, I didn't need much persuasion. I started reading, became interested, and dove into the problem. Fast-forward a few years, and here I am, writing a preface to a thesis that has clearly bifurcated into two independent directions: undrained pore pressure response to changing stresses and non-linear seismic velocity models. As I did not manage to plant a cherry on top of the cake of this thesis by directly connecting the two main directions of my research, this thesis is formally organized into these two parts. I will not feel in any way offended if you decide to read just one (or none - that is also fine, as the chances that I have read your thesis are terribly slim). Given the substantial amount of paper I have managed to fill with my attempts at doing science during my slightly longer than usual PhD project, I decided to keep the introduction and summary of this thesis rather brief. I simply did not want to bore anyone more than necessary to understand the context and significance of my work.

The variety of my work is reflected not only in the range of topics I have attempted to cover, but also in the tasks I have undertaken - from conducting laboratory experiments and processing data to numerical modelling and theoretical work. I sincerely did not see that coming, but I embraced most of the unexpected turns on this journey. And it has actually been quite a ride - I can confidently say it was anything but boring.

When I first considered pursuing a PhD around April 2017, I never thought it

would take this long. I also never expected that it would make me interact and befriend a group of amazingly diverse and interesting people, both inside NTNU and SINTEF, and outside them. Apparently, my imagination was limited, as I also never envisioned that during my PhD, the world would be grappling with a pandemic and a full-scale war would erupt just outside my home country of Poland.

I also never anticipated how deeply the latter would affect me. The degree of unfairness and scale of human tragedy it brought literally made my interest in finishing this thesis fade away. The final stage of my work was more closely aligned with the law of conservation of momentum than with Newton's second law of motion. Despite Rune's attempts to apply some external force to accelerate the process, it seemed as though terminal velocity had been reached. Interestingly, its maximum value appeared to be inversely proportional to the growing respect and admiration I was developing for the brave people of Ukraine, who were showing unbreakable determination to defend their freedom despite of the terrible cost of human lives.

Anyway, it seems it is finally over.

Marcin Duda
Trondheim, 17 June 2023

# Acknowledgements

**Institutions**

I would like to express my gratitude to the Department of Geoscience and Petroleum at the Norwegian University of Science and Technology (NTNU) in Trondheim, Norway, for providing the opportunity to pursue my doctoral studies. I appreciate all the administrative and formal assistance I have received over the past few years.

This work was financed by the NCCS Centre, under the Norwegian research program, *Centres for Environment-friendly Energy Research* (FME) (257579/E20). I want to extend my sincere appreciation to the administrators of the NCCS Centre, whose daily care, responsiveness, and consideration were simply outstanding.

After January 1st, 2022, this research received additional financial support from the PETROMAKS 2 program through the research project, *"Improved Prediction of Stress and Pore-pressure Changes in the Overburden for Infill Drilling"* (Grant No. 294369) carried out at SINTEF. I am deeply grateful for this invaluable assistance, without which the completion of this PhD would have taken even longer.

I would also like to express my gratitude to the leadership of the Formation Physics group at SINTEF. They generously allowed me to use their infrastructure throughout my research, and in a turn of events that I am still processing, they decided to offer me a job once my PhD funding ended. Whether this decision was for good or bad reasons, I leave to the reader's discretion.

**People**

My research was conducted under the supervision of Professor Rune Martin Holt at NTNU (and later also SINTEF AS) and Andreas Kurt Marcel Bauer from NTNU and SINTEF AS (and subsequently, AkerBP). I am deeply grateful for their faith and trust they placed in me, allowing me to shape the direction of my research with complete independence.

I would like to extend my heartfelt thanks to Rune, the one and only Head of the National Association of Sarcasm and Torn Menisci, for all our "2-minute-long" discussions, both scientific and otherwise. His steadfast refusal to answer a "yes" or "no" question with a simple "yes" or "no" when it came to our often shared research topics coupled with his numerous hints about potentially interesting research avenues led to a variety of fascinating scientific journeys, some short and others long.

I would also like to thank Andreas for his uncanny ability to find 30-minute slots in his tragically overloaded schedule. His and Tron Golder Kristiansen's help in unraveling the tortuous paths of geomechanical data they provided me with and their generous encouragement to "do whatever I only want" with these data were invaluable.

I would like to thank for the substantial help received from Suzanne McEnroe, who headed the Geophysics research group during the tail end of my thesis work and helped me to work on it for "a bit" longer than expected. Additionally, from the Geophysics group, I must extend heartfelt thanks to Andrew James Carter, whose expertise in literature, admirable decency, and unyielding willingness to help are unparalleled.

Next, I would like to express my gratitude to Dawid Szewczyk, Eyvind Frode Sønstebø, Mohammad Hossain Bhuiyan, Nicolaine Agofack and Sigurd Bakheim (listed in purely alphabetical order) for their invaluable assistance in the lab. Without their help at countless instances, I would have been as lost as a goose in a hail storm.

In this regard, I would like to extend special thanks to Anna Magdalena Stroisz for her unwavering support during particularly challenging moments and her consistent readiness to offer help whenever she perceived it was needed. Our discussions were a wild ride, diving into the realms of science, but also society, politics, and life itself. We definitely did not agree on everything (like, seriously, not even close), but we kept initiating these conversations and kept them friendly - we deserve a Polish self-high-five!

Last but certainly not least, among the lab-rats, I would like to express my profound gratitude to our Grand Maestro, the leader of the Formation Physics laboratory, Jørn Fredrik Stenebråten. The depth and breadth of knowledge and skill he has accumulated is truly awe-inspiring. I deeply appreciate every instance when,

instead of handing me a screwdriver with a "good luck" or pointing me in the general direction of the manual, he chose to share his expertise with me in a more direct manner.

Maintaining my focus at SINTEF, I would like to extend my gratitude to Andreas Nicolas Berntsen, Arne Marius Raaen, Idar Larsen, Kamila Maria Gaweł, Lars Erik Walle, Pierre Rolf Cerasi, Xiyang Xie, and all others who lent their support to my journey, both prior to and following my integration into the Formation Physics group.

I owe a particular note of appreciation to Audun Bakk for his unwavering determination, keen intellect, and pursuit of perfection. Our collaborative efforts on our co-authored papers often involved rigorous internal revisions that could be challenging and even somewhat frustrating at times, while our discussions and deliberations were invariably intense and sometimes draining (sorry, I could not help it). Nevertheless, I firmly believe that without such strong stimuli and constant challenges, a significant portion of the work contained within this thesis would never have come to fruition.

Furthermore, I must express my profound gratitude to Serhii Lozovyi, whose patience truly went above and beyond, even in the face of my frequent proclamations of "let's do it a different way", "seriously, I can improve it", "I'll try once more," and "this time it will be better, I promise" which he experienced over a span of few years. I am grateful not only for his initiatives and sense of responsibility pertaining to our scientific cooperation but also in other more important areas.

Switching gears back to NTNU, I want to express my sincere gratitude to all my fellow PhD students: Ammar Ghanim, Filipe Borges, Hong Yan, Kim Mews, Marco Antonio D'o-wait-for-it-leire, Michalis Varkas, Stian Rørheim (a distinguished member of NASTM), and Veronica Alejandra Torres Caceres. Thank you for the shared lunches, hikes, skiing trips, parties (memorable or not so memorable), and for the constant understanding and support I could almost always count on (certainly more than one might expect!). Without you all, this journey just would not have been the same.

In particular, I must extend a special thank you to Maksym Lozovyi, with whom I shared an office and my most concealed thoughts and unpopular opinions. I sincerely doubt I could have found anyone else in Trondheim who would understand me better, in both the highs and lows of this journey and my life in general. My warmest thoughts and best wishes go to you and Sasha, now and always!

Then, as always, I want to express my heartfelt gratitude to my family. My parents, unparalleled in their ability to motivate and ignite curiosity in their very unorthodox ways, have been my steadfast pillars of support. Their unwavering backing enabled me to embark on my journey to Norway in the first place, and for that, I will be forever grateful. I also want to extend my thanks to my aunt Monika, whose understanding and selflessness are remarkable. In critical moments,

she never hesitates to do the right thing, and for that, she has my deepest admiration. My grandmothers, Małgorzata and Barbara, deserve a special mention for their humor, uncanny ability to bring a smile to my face and unlimited support, regardless of the circumstances. To Magda, I am grateful for the countless hours we have spent on the phone over the past few years, providing both a comforting voice and a listening ear.

Finally, I would like to express my deepest appreciation to Joanna. It is a challenge to find the right words to describe her role - a blend of support, motivation, guidance, the provider of not-always-asked-for-but-always-needed reality checks, and a driving force that pushed me to keep going when I thought I just really could not. Her approach was relentless, no holds barred, and no prisoners taken. Words fall short to express the depth of my gratitude and how much I wish it had not taken this long, so I propose we finally take those long-overdue proper holidays.

# Contents

# List of Figures

# List of Tables

# Contributions

## Draft A

The issue of modeling the undrained pore pressure response in large-scale geomodels was initially raised by Rune M. Holt, while the matter of fully-rotational undrained media was first brought up by Marcin I. Duda. The experimental work was performed by Jørn F. Stenebråten and Marcin I. Duda. The theoretical work was performed by Marcin I. Duda and Audun Bakk. Additional theoretical support was provided by Arne M. Raaen and Rune M. Holt. The numerical work was done by Marcin I. Duda, Arne M. Raaen and Hong Yan. The writing was undertaken by Marcin I. Duda with significant contributions from Audun Bakk. The revision was performed by Audun Bakk, Arne M. Raaen, Rune M. Holt, and Marcin I. Duda.

## Paper B

The issue of modeling the undrained pore pressure response in large-scale geomodels was initially raised by Rune M. Holt, while the matter of fully-rotational undrained media was first brought up by Marcin I. Duda. The experimental work was performed by Jørn F. Stenebråten and Marcin I. Duda. The theoretical and numerical work was performed by Marcin I. Duda and Audun Bakk. Additional theoretical support was provided by Rune M. Holt. The writing was undertaken by Marcin I. Duda with notable contributions from Audun Bakk and Rune M. Holt. The revision was performed by Audun Bakk, Rune M. Holt, Jørn F. Stenebråten and Marcin I. Duda.

## Paper C

The problem that inspired this work was first raised by Marcin I. Duda. The experimental work was performed by Jørn F. Stenebråten, Anna M. Stroisz and Marcin I. Duda,. The numerical work was performed by Marcin I. Duda with theoretical support from Rune M. Holt. The writing was undertaken by Marcin I. Duda and revision was performed by Rune M. Holt, Marcin I. Duda, Jørn F. Stenebråten and Anna M. Stroisz.

## Paper D

The problem that inspired this work was first raised by Marcin I. Duda. The experimental work was performed by Marcin I. Duda, Jørn F. Stenebråten and Anna M. Stroisz. The analytical work was performed by Marcin I. Duda with theoretical support from Rune M. Holt. The writing was undertaken by Marcin I. Duda and revision was performed by Rune M. Holt and Marcin I. Duda, Jørn F.

Stenebråten and Anna M. Stroisz.

## Paper E

The problem that inspired this work was first raised by Rune M. Holt. The theoretical and numerical work was performed by Marcin I. Duda and Audun Bakk. Theoretical support was provided by Rune M. Holt. The writing was undertaken by Marcin I. Duda and revision was performed by Audun Bakk and Rune M. Holt and Marcin I. Duda.

## Paper F

The problem of frequency-dependent stress- and strain-sensitivities of acoustic wave velocities was first raised by Serhii Lozovyi and Andreas K. M. Bauer. The experimental work was performed by Serhii Lozovyi and Andreas K. M. Bauer. Data pre-processing was performed by Serhii Lozovyi and Marcin I. Duda. The numerical work was performed by Marcin I. Duda. The analysis of the results was performed by Serhii Lozovyi and Marcin I. Duda. Theoretical support was provided by Andreas K. M. Bauer and Rune M. Holt. The writing was undertaken by Serhii Lozovyi, Marcin I. Duda and Rune M. Holt. The revision was performed by Serhii Lozovyi, Marcin I. Duda, Rune M. Holt and Andreas K. M. Bauer.

## Paper G

The idea of extending the non-linear elastic stiffness model to accommodate the complete strain tensor and addapt it to VTI symmetry was first brought up by Audun Bakk. The experimental work was performed by Jørn F. Stenebråten. Data pre-processing was performed by Audun Bakk. The theoretical work was performed by Audun Bakk and Marcin Duda. Numerical work and was performed by Xiyang Xie, Hong Yan and Marcin Duda. Theoretical support was provided by Colin MacBeth and Rune M. Holt. The writing was undertaken by Audun Bakk. The revision was performed by Audun Bakk, Marcin I. Duda, Rune M. Holt, Colin MacBeth, Xiyand Xie and Hong Yan.

# Introduction and summary

## 1.1 Background

Deep beneath our feet lies an unseen world of geological activity, driven by both natural processes and human intervention. Among the focal points of these underground movements are subterranean storage sites and reservoirs, where the upward journey of pressurized pore fluids is halted by an impermeable barrier known as cap rock (Magoon and Dow 1994). The never-ending adjustments within the subsurface, aiming to achieve or recover a delicate balance of forces, shape our planet, powering both natural phenomena and human technologies. This is a high-stakes subterranean game, where even the smallest changes can result in significant impact.

One such change is the injection or extraction of fluids from a reservoir. Much like a subtle shift in an architectural masterpiece, this can lead to the expansion or compaction of the disturbed structure, causing a reshuffle of stresses and deformation that reverberate far beyond their point of origin. These changes can initiate the stretching or shortening of the overburden, and in some cases, such deformation even reaches the surface in the form of subsidence or uplift. Regardless of the case, a complex dance within the stress field is initiated, occurring both within the reservoir rocks and in the surrounding formations (Geertsma 1973). A simplified example of this choreography, specifically, the depletion-induced stress field changes, is shown in Fig. 1.1 (Fisher et al. 2014).

Let's take a closer look at these stress changes. As shown in Figure 1.1, the impact of these changes extends beyond the deposits immediately surrounding the reservoir. For example, as a reservoir depletes, stress shielding by the overburden rock, or "arching", results in a decrease in vertical stress above the reservoir and an increase in vertical and shear stresses around its edges (conversely, during injection, the effect on the surroundings is expected to be the opposite). These processes can indeed be quantified. By employing analytical or numerical geomechanical models, we can monitor the evolution of stresses and strains, and predict further alterations occurring in the reservoir's surroundings. In this thesis, we will delve into the nuances of how these modelled stresses and strains can be harnessed to simulate changes of pore pressure and velocity of seismic waves in overburden shales.

Before we delve into the details, it is vital to understand why these processes matter. Let's start with the changes in pore pressure. Imagine this: the stress and deformation changes induced by fluid injection into or extraction from the reservoir directly influence the load-bearing matrix and pores of the overburden

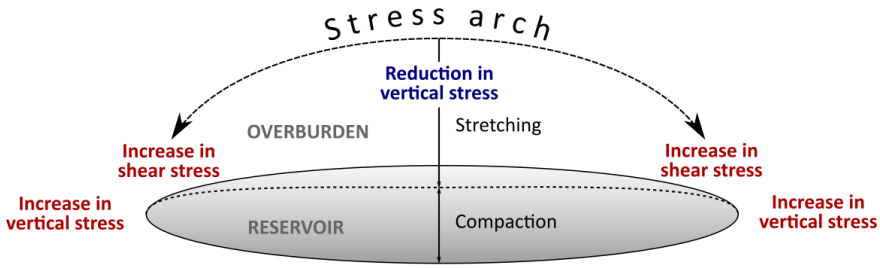


**Figure 1.1:** Depletion-induced stress changes around reservoir (modified after Fisher et al. 2014).

shales, impacting the trapped pore fluid. Now, because these rocks have low permeability, instant fluid flow is restricted, leading to what we call 'undrained conditions'. Here, instead of the fluid migrating, its pressure changes in response to the stress changes.

These undrained pore pressure changes may play a significant role as they affect the effective stress, defined as the difference between total stress and pore pressure, governing rock deformation. In some scenarios, these instant changes in pore pressure can lead to the rock masses' failure, as illustrated in Fig. 1.2.

Eventually, pore pressure does equilibrate, but it is a slow dance. Even across short distances of mere meters, equilibration could significantly outlast the anticipated time-frame of subsurface operations or the lifespan of a typical reservoir. Therefore, accurately understanding and forecasting undrained pore pressure changes near injection zones and producing reservoirs is not merely an academic exercise but an important step towards risk mitigation, addressing issues related to cap rock integrity, fault reactivation, drilling problems, and casing failure. Therefore, within the pages of this thesis, the author will do his best to persuade you, dear reader, to approach this matter with attention it deserves.

But just as you think you have grasped the narrative of this ballet, the plot thickens. The next step is to account for changes to the overburden rock structure caused by stress and strain alterations resulting from reservoir injection or depletion. We are talking about the realignment of grain contacts, the creation of new cracks, or the closure of existing ones (Adams and Williamson 1923). These modifications can significantly change the acoustic properties of extensive rock volumes, leading to fluctuations in the velocity of seismic wave propagation. Consequently, they can affect seismic wave two-way travel time in the overburden (potentially

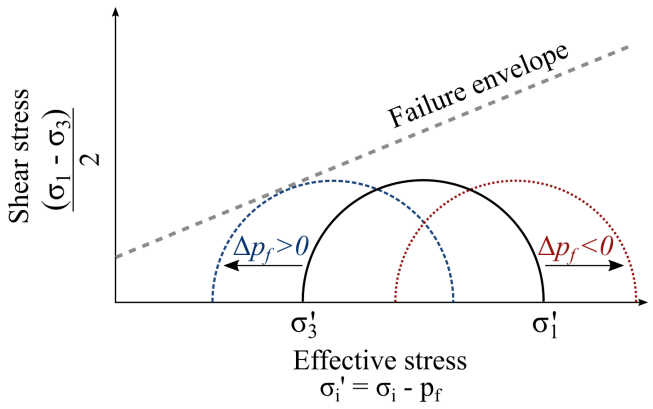


**Figure 1.2:** Pore pressure-driven shear failure or stabilization - impact of the undrained pore pressure changes on Mohr circle.

even outdoing the travel time shifts stemming from changes in reservoir rock properties, Holt and Stenebråten 2013), or result in shear wave splitting. This offers us an invaluable monitoring tool for injection zones and producing reservoirs (Barkved and Kristiansen 2005; Hatchell and Bourne 2005; Kenter et al. 2004; MacBeth et al. 2018; Røste et al. 2006), as illustrated in the modelling example in Fig. 1.3.

The significance of regular and reliable monitoring surveys has been thrust into the spotlight like never before. Take the case of $CO_2$ storage sites, for instance. Here, dependable monitoring acts like the keen eyes of a vigilant sentinel. It tracks the evolution of $CO_2$ plumes, scrutinizes the injection locations, assesses injection efficiency, and maps plume migration in the context of neighboring high-risk areas and subsurface reservoirs—be they groundwater, geothermal, or hydrocarbon. Moreover, it aids in the critical task of detecting potential leakages (Davis et al. 2019).

Shifting our lens to hydrocarbon reservoirs, frequent and reliable monitoring is just as indispensable. It is geo-scientists and -engineers locate inflated or depleted reservoir sections and identify the sometimes elusive sealing faults (Fjær et al. 2021). It is clear then that monitoring is not just about collecting data — it is about recreating the dynamic history of the subsurface world, guiding our actions, and informing our decisions.

Although far from being unique processes taking place in overburden shales, both the undrained pore pressure response and velocity changes may have a significant impact on the safety and economic feasibility of subsurface operations - particularly for low-margin ventures such as $CO_2$ storage. That is why there is a growing push

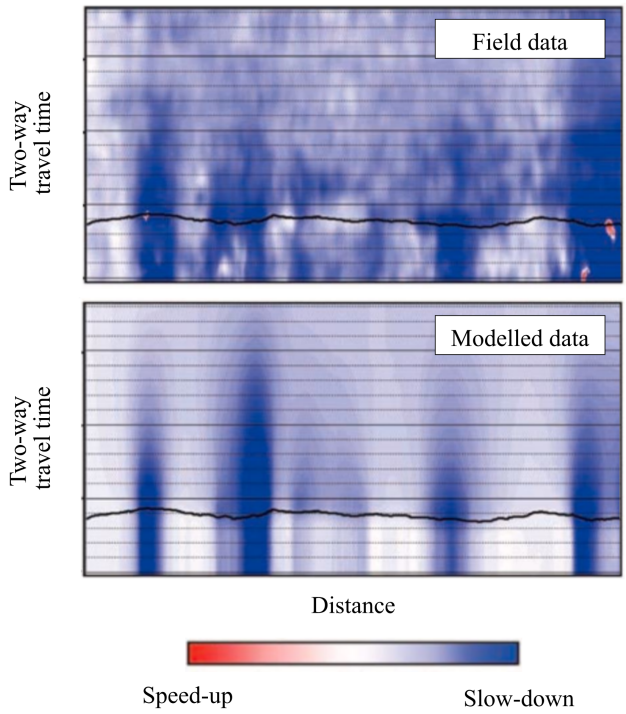


**Figure 1.3:** Comparison of time-shifts in field and modelled data set (modified after Hatchell and Bourne 2005).

to understand, describe, and model these processes, accounting for the distinct behavior of shale rocks.

However, as we delve deeper, it becomes apparent that the widely used conventional methods have their limitations. Consider, for instance, the Janbu et al. (1988) model, a much-favored tool for modeling the subsurface stress evolution in response to injection or depletion of a disc-shaped reservoir. Its isotropic nature and assumption of no contrast between the reservoir and its surroundings result in a forecast that predicts stress changes following constant mean stress constraint above the reservoir. When these results are combined with the often-used Skempton's equations for undrained pore pressure response (Skempton 1954), the modeled pressure changes in isotropic overburden equate to zero in response to such stress variations. However, in reality, the complex geometries and anisotropic nature of rocks indicate that this is a considerable oversimplification. Even if the rock's anisotropy is somehow accounted for by modifying the values of Skempton's parameters, the impact of changes to the entire stress tensor remains unaddressed. Similarly, the R-factor (Hatchell and Bourne 2005; Røste et al. 2006), often employed to model seismic changes, also oversimplifies the situation. By correlating

velocity changes solely to a unique parameter, the vertical strain, it neglects to consider valuable information about the anisotropy of the material and non-vertical stress changes and deformations.

Understanding these limitations pushes subsurface scientists toward a more comprehensive approach. The somehow interconnected nature of these processes dictates that they be studied together for a complete evaluation of storage sites or reservoirs. In this context, the rapidly growing field of quantitative interpretation of time-lapse seismic data opens up exciting possibilities. By utilizing observed time-shifts, we aim to invert for stress and strain changes. These refined estimates can then bolster the accuracy of results obtained through geomechanical modeling. As a result, these enhanced models can be used to estimate the undrained pore pressure response, setting the stage for more accurate predictions of effective stress, improved evaluations of cap rock integrity, and better forecasts of future drilling conditions. Thus, the ambition of this thesis is to traverse both ends of this workflow by exploring models for seismic velocity and pore pressure responses taking into consideration anisotropy of the considered material and three-dimensional character of stress changes and strains.

## 1.2 Brief theoretical and practical overview

To ensure a balanced and engaging discussion, it is vital for us to start with a concise overview of pore pressure changes and velocity models. Subsequently, the introduction will delve into a short description of our main object of interest, shales, and the practical consequences that arise from their characteristics.

### 1.2.1 Undrained pore pressure response

To provide a clear and comprehensive introduction to the undrained pore pressure response, let's take a step back from anisotropic shales and begin with a very selective presentation of the fundamental equations describing isotropic linearly elastic homogeneous solid materials (for a much more complete description, refer to Fjær et al. 2021, and references therein). In such materials, the stress ($\sigma$)-strain ($\varepsilon$) relationship along the principal directions $x$, $y$, and $z$ can be described using the so-called Lamé parameters, $\lambda$ and $G$ (shear modulus):

$$\begin{aligned}
\sigma_x &= (\lambda + 2G)\,\varepsilon_x + \lambda\varepsilon_y + \lambda\varepsilon_z,\\
\sigma_y &= \lambda\varepsilon_x + (\lambda + 2G)\,\varepsilon_y + \lambda\varepsilon_z,\\
\sigma_z &= \lambda\varepsilon_x + \lambda\varepsilon_y + (\lambda + 2G)\,\varepsilon_z,\\
\tau_{yz} &= 2G\Gamma_{yz},\\
\tau_{xz} &= 2G\Gamma_{xz},\\
\tau_{xy} &= 2G\Gamma_{xy}.
\end{aligned} \tag{1.1}$$

Here, the parameters $\tau_{ij}$ and $\Gamma_{ij}$ describe shear stresses and shear strains, respectively. Equation 1.1 can be written in a more compact form using volumetric strain $\varepsilon_{vol} = \varepsilon_x + \varepsilon_y + \varepsilon_z$, Kronecker symbol $\delta_{ij}$ and tensor notation as

$$\sigma_{ij} = \lambda\varepsilon_{vol}\delta_{ij} + 2G\varepsilon_{ij}, \tag{1.2}$$

It is also worth noting that in such isotropic materials, the principal axes of stress and strain always coincide, significantly simplifying the analysis of their behaviour.

The next step involves extending our simplified analysis to encompass porous materials. In the case of these media, the rock's behavior is not solely dependent on the properties of the solid constituents, but also on the non-solid portions of its volume, such as pores and pore fluids. A theory known as Biot's poroelasticity (e.g., Biot 1955; Biot 1941; Biot 1956; Biot 1962) addresses both the static and dynamic behavior of rocks. However, in this part of the introduction, we will concentrate on the static behavior of porous materials using the so-called "Gassmann" approach (Berryman and Res 1995).

To describe a porous medium saturated with a fluid, more parameters are required. Following Biot's theory, equations 1.1 can be rewritten as

$$\begin{aligned}
\sigma_x &= \lambda_u\varepsilon_{vol} + 2\lambda\varepsilon_x - C\zeta\\
\sigma_y &= \lambda_u\varepsilon_{vol} + 2\lambda\varepsilon_y - C\zeta\\
\sigma_z &= \lambda_u\varepsilon_{vol} + 2\lambda\varepsilon_z - C\zeta\\
\tau_{yz} &= 2G\Gamma_{yz},\\
\tau_{xz} &= 2G\Gamma_{xz},\\
\tau_{xy} &= 2G\Gamma_{xy},\\
p_f &= C\varepsilon_{vol} - M\zeta.
\end{aligned} \tag{1.3}$$

Here, $\lambda_u$ and $G$ are parameters of a porous material and the additional parameters are pore pressure $p_f$ (new stress parameter), increment of fluid content $\zeta$ (new strain parameter), and two Biot's moduli of two-phase medium, $M$ and $C$ (not described in detail in this thesis).

Alternatively, equation 1.3 can be written as

$$\sigma_{ij} = \lambda_u \varepsilon_{vol} \delta_{ij} + 2G\varepsilon_{ij} - C\zeta\delta_{ij}. \tag{1.4}$$

In the case of porous material fully saturated with fluid, fluid volume $V_f$ equals to pore volume $V_p$. In such case, if the changes of fluid volume $V_f$ do not equal changes in pore volume $V_p$, the fluid is either expelled or absorbed, and the increment of fluid content $\zeta$ can be expressed as

$$\zeta = \frac{\Delta V_f - \Delta V_p}{V}, \tag{1.5}$$

where $V$ is the total volume of the medium.

Changes in fluid volume $V_f$ can be related to changes in pore pressure $p_f$ through fluid bulk modulus $K_f$,

$$\Delta p_f = -K_f \frac{\Delta V_f}{V_f}. \tag{1.6}$$

By introducing porosity $\phi$ (the fraction of void space relative to the total volume of the medium, such that $V_p = V_f = \phi V$), relative change of volume of the pore space $\Delta V_p/V_p$, change of pore pressure $\Delta p_f$ and bulk modulus of the fluid $K_f$, we can define increment of fluid content $\zeta$ as

$$\zeta = -\phi \left( \frac{\Delta V_p}{V_p} + \frac{\Delta p_f}{K_f} \right). \tag{1.7}$$

The same quantity can be expressed in terms of volumetric strains, i.e., total volumetric strain $\varepsilon_{vol} = \Delta V/V$, volumetric strain of the solid $\varepsilon_{vol,s} = \Delta V_s/V_s$ and volumetric strain of the fluid $\varepsilon_{vol,f}$=$\Delta V_f/V_f$, giving

$$\zeta = \left[\varepsilon_{vol} - (1-\phi)\,\varepsilon_{vol,s}\right] - \phi\varepsilon_{vol,f} \tag{1.8}$$

The undrained conditions are achieved when no fluid movement into or out of the medium takes place, $\zeta = 0$, and therefore according to equation 1.7 any relative change in pore volume $V_p$ must be compensated by pore pressure change $\Delta p_f$. We assume such conditions to apply to shales, in which any fluid movement on time-scale of years or even decades is very limited due to their extremely low permeability.

The magnitude of the undrained pore pressure response to change in mean stress $\bar{\sigma} = (\sigma_x + \sigma_y + \sigma_z)/3$ in an isotropic linearly elastic medium can be expressed

using pore pressure from equations 1.3 and undrained bulk modulus $K_u = \lambda_u + 2/3G$ as

$$\Delta p_f = \frac{C}{K_u}\Delta\bar{\sigma} \tag{1.9}$$

The ratio between $C$ and $K_u$ is referred to as Skempton's $B_S$ (Skempton 1954), and it can also be expressed using porosity $\phi$, bulk moduli of the framework of the medium $K_{fr}$, of the solid $K_s$ and of the fluid $K_f$,

$$B_S = \frac{C}{K_u} = \frac{\Delta p_f}{\Delta\bar{\sigma}} = \frac{\frac{1}{K_{fr}} - \frac{1}{K_s}}{\frac{1}{K_{fr}} - \frac{1}{K_s} + \phi\left(\frac{1}{K_f} - \frac{1}{K_s}\right)}. \tag{1.10}$$

After defining $C$ and $K_u$,

$$C = \frac{K_f\left(1 - \frac{K_{fr}}{K_s}\right)}{\phi + \frac{K_f}{K_s}\left(1 - \phi - \frac{K_{fr}}{K_s}\right)}, \tag{1.11}$$

$$K_u = K_{fr} + \frac{K_f\left(1 - \frac{K_{fr}}{K_s}\right)^2}{\phi + \frac{K_f}{K_s}\left(1 - \phi - \frac{K_{fr}}{K_s}\right)}, \tag{1.12}$$

it can be deduced that Skempton's $B_S \leq 1$.

Skempton (1954) described the undrained pore pressure response in triaxial conditions, i.e. $\sigma_z \neq \sigma_x = \sigma_y$, using two pore pressure parameters, $B_S$ and $A_S$. Skempton's parameter $A_S$ was used to describe the pore pressure response to change in $\sigma_z$ - $\sigma_x$, giving

$$\Delta p_f = B\left[\Delta\sigma_x + A\left(\Delta\sigma_z - \Delta\sigma_x\right)\right] \tag{1.13}$$

In isotropic elastic medium, change in $\sigma_z$ - $\sigma_x$ does not produce any pore pressure change, leaving $A_S = 1/3$. Therefore, in Skempton (1954) the parameter $A_S$ was used as a measure of inelasticity of the material. As this thesis focuses on the undrained pore pressure response in anisotropic shales, the parameter analogous to $A_S$ will express mostly the degree of anisotropy of the studied medium.

### 1.2.2 Non-linear seismic velocity models

Pore fluid substitution, temperature variations, and changes in stresses and strains are the primary factors affecting the acoustic properties of rocks. While the first two factors fall outside the scope of this thesis and will not be described, the latter is the main focus of a significant part of the presented work and also affects the internal structure, density, and volume of rocks.

The most important mechanisms responsible for stress-dependent rock stiffness include changes in porosity, alterations in grain contacts, and the closure or generation of cracks (Adams and Williamson 1923). The latter two factors frequently serve as the foundation for formulating rock models with porosity changes incorporated as an extra parameter, further enhancing their accuracy and applicability. Grain contact-based models focus on scaling the impact of individual contact zone changes on the overall rock volume. Conversely, crack closure analysis underpins the inclusion approach, which treats the rock volume as a solid medium containing inclusions or voids that influence its elastic properties. For a comprehensive understanding of these classes of models, the author highly recommends reading the relevant chapters in Mavko et al. (2020) and Fjær et al. (2021). These sources provide detailed descriptions and offer a complete overview of the models' development and applications. Also, the author of this thesis made an attempt to briefly summarize and compare such models in his Master's thesis (Duda 2017) - an attempt that the author few years later finds delightfully clumsy.

Alternatively, stress- and strain-dependent stiffness changes can be addressed using the non-linear theory of elasticity, which employs the the full elastic tensor of a strained medium (e.g., Sinha and Kostek 1996; Sinha and Plona 2001; Thurston 1974; Winkler and Liu 1996). In this approach, specific elements of the rock structure, such as porosity, average number of contacts between grains, and fracture densities, are not represented by individual parameters. Instead,a third-order elastic tensor is used to describe the relationship between the strain tensor and the second-order stiffness tensor. This method provides a more generalized perspective on strain-dependent stiffness changes without referring to specific rock structure components - although such components are in theory based on underlying physics, they are challenging to determine and may not accurately represent the actual average values in the rocks.

The non-linearly elastic models are based on the elastic strain energy function $W$, describing potential energy accumulated by a strained body which can be released during unloading. Taylor series expansion of $W$ yields

$$W = W^{\circ} + \sigma_{ij}e_{ij} + \frac{1}{2}c_{ijkl}e_{ij}e_{kl} + \frac{1}{6}c_{ijklmn}e_{ij}e_{kl}e_{mn} + O\left(e_{ij}^4\right), \tag{1.14}$$

where $\sigma_{ij}$ represents stresses, $e_{ij}$ strains, $c_{ijkl}$ second-order elastic (stiffness) coefficients, $c_{ijklmn}$ third-order elastic coefficients, and indices range from 1 to 3. In this

setting, the stiffness of a stressed and/or strained medium $c_{ijkl}$ can be expressed as the sum of the initial stiffness $c^{\circ}_{ijkl}$ and the impact of applied stresses and strains appearing in the strain-energy function, with the use of repeated indices summation convention and Kronecker's delta $\delta_{jl}$,

$$c_{ijkl} = c^{\circ}_{ijkl} + c_{ijklmn}\Delta e_{mn} + \Delta\sigma_{ik}\delta_{jl} + c^{\circ}_{ijpk}\Delta e_{lp} + c^{\circ}_{ipkl}\Delta e_{jp}. \tag{1.15}$$

Among the terms in equation 1.15, the largest impact on the change of $c_{ijkl}$ is expected from the term containing the third-order elastic coefficients $c_{ijklmn}$ due to the significant difference in typical magnitudes of the terms ($\sigma_{ij} \ll c_{ijkl} \ll c_{ijklmn}$) (Johnson and Rasolofosaon 1996; Prioul et al. 2004). This simplifies equation 1.15 to

$$c_{ijkl} = c^{\circ}_{ijkl} + c_{ijklmn}\Delta e_{mn} = c^{\circ}_{ijkl} + \Delta c_{ijkl}. \tag{1.16}$$

According to equation 1.16, stiffness of the material depends on strain and its changes are reversible if the deformation causing it is removed. In the case of static stiffness, this would result in a non-linear stress-strain curve with no hysteresis and no permanent deformation after unloading. In the case of dynamic stiffness, reversible changes of acoustic velocities are expected. Therefore, assuming all strains to be elastic, these models can be applied to extract information on subsurface deformations from time-lapse seismic data showing changes in wave propagation velocities.

It is worth noting that in equation 1.16, the effective stiffness of a strained medium depends on all components of the strain tensor. Additionally, this equation does not restrict the third-order elastic tensor elements to appear in expressions for only one stiffness tensor term, which makes non-linear elastic systems potentially quite complex and difficult to solve.

### 1.2.3 Shales

Shales are a diverse group of sedimentary rocks consisting mainly of clay minerals such as kaolinite, illite, smectite, and chlorite (Milliken and Day-Stirrat 2013; Passey et al. 2010) that originate from the weathering and alteration of various minerals in volcanic and metamorphic rocks. They are formed by the accumulation and compaction of mud and silt particles. The small size, abundance and variety of clay minerals in shales results in pore spaces consisting of small, poorly connected pores, and hence limited permeability that hinders fluid flow and pressure diffusion. The small dimensions of the pores result in large surface areas at which negatively charged clay minerals attract positive ions from the pore fluid and structurally bound water particles, making the study of clay mineral properties particularly challenging. Clay minerals usually appear in the form of small plates that are

intrinsically anisotropic, meaning that they have different properties in different directions. These plates tend to stack together forming horizontal laminas and layers (Sayers 1994), and the degree of their alignment depends on depositional conditions, clay content and thermal maturity (Kanitpanyacharoen et al. 2012; Revil et al. 2002; Wenk et al. 2009). This contributes to the anisotropic nature of shales, which is evident in their mechanical and acoustic properties, as well as in their already limited permeability. Additionally, the laminar structure of shales promotes creation of elongated pores aligned with the clay grains (Daigle and Dugan 2011; Leu et al. 2016; Loucks et al. 2012) and of planes of weakness making the rock more susceptible to splitting along them (Jaeger 1960). Shales also contain organic matter and other fine-grained materials. The presence of harder minerals such as quartz, feldspar, mica, calcite, or pyrite can impact not only its strength and stability, but also shape the effective chemical activity of the rock and govern its behaviour during diagenesis.

The complex mineral composition of shales gives origin to various physical and chemical processes that are often strongly interconnected and affect the mechanical and chemical properties of the rocks, its permeablity, integrity and compaction characteristics. As shales are gaining importance in the geo-industry due to the role they play as overburden and sealing rocks for subsurface storage sites and reservoirs, they have gained the attention of both industry and academia and are increasingly more often studied. To the delight of geo-scientists and the dismay of geo-engineers, the complexity of shales creates certain challenges unique for this type of rocks that should be addressed before experimental testing or subsurface operations in the overburden shale can take place.

### 1.2.4 Experimental challenges

Shales, with their very small pore sizes and significant clay content, are characterized by extremely low permeabilities, slow consolidation rates, high capillary suction values and strong capillary forces, making them a painfully challenging subject to study experimentally. All challenges presented in this chapter are reflected in the technical solutions and experimental protocols described in various parts of this thesis.

Challenges arise already during core retrieval and preservation. As core is being drilled and retrieved, it experiences rapid unloading of the in-situ stresses. This can lead to tensile failure, especially in harder shales where pore compressibility lower than fluid compressibility, and therefore the unloading is mostly experienced by the rock frame with pre-existing weakness planes. In softer rocks, where pore compressibility higher than fluid compressibility, the problem of damage during retrieval still remains. Due to the very low permeability, typically ranging from 10-100 $nD$ (Ewy et al. 2003; Yang et al. 2009), even though the stresses are released and the rock expands, fluid entry into the core is limited, causing a decrease in pressure of the unloading fluid and, in some cases, negative pore pressures. In

the case of abundant bubble nuclei, this can result in cavitation, which increases fluid compressibility and furthers rock stress release, potentially ending with the development of microfractures (see Khaledi et al. 2021 and references therein). Alternatively, if the gas release is limited, this tension can help to keep the rock together (Ewy et al. 2001; Ewy 2014; Schmitt et al. 1994), but from now on the environment around the rock has to be carefully controlled to avoid damaging the core. Low relative humidity can lead to a loss of water saturation, rock shrinkage, and ultimately the development of desiccation cracks. Conversely, due to their strong capillary suction (Ewy 2018), exposure to a high relative humidity environment can cause the shale to start absorbing water, swelling, and ultimately splitting along bedding planes. To avoid damage, the sample can be stored in a non-aqueous fluid such as oil, which should also be used to wet the core during cutting and drilling plugs from it (Berre 2011; Ewy and Stankovic 2010; Horsrud et al. 1998; Steiger and Leung 1991).

Although the small pore sizes of shales cause high values of air entry pressure, most shales retrieved from the subsurface are not fully saturated and therefore cannot be directly used in tests aiming to determine pore pressure parameters. Therefore, a shale sample has to re-saturated prior to the experiment. There are several ways to achieve that. The method employed in the Formation Physics laboratory was to actively saturate the sample with brine by flowing it around the sample through the experimental system before the main body of the test. To limit the uncontrollable swelling, the sample has to be pre-stressed before exposure to the brine (which also allows to achieve positive pore pressure inside the sample). Then, stressed can be adjusted during fluid exposure to ensure that the sample does not change volume (Berre 2011; Favero 2017). However, to avoid differences in hydraulic pressure between the fluid inside and outside the sample caused by chemico-osmotic force, brine with matching water activity to the pore filling fluid must be used (Chenevert and Amanullah 2001; Gasc-Barbier and Tessier 2007; Péron et al. 2009; Wild et al. 2015). For that purpose, a sample of the pore fluid must be extracted and analyzed. Due to the positive charge on the clay minerals' surface attracting cations, the extracted fluid may not have the same ionic content as the fluid populating the pores, posing yet another challenge.

In the case of more permeable rocks, re-saturation can be achieved by introducing pressurized fluid to one end of the sample and receiving it through the other end. In the case of shales, due to their low permeability, the flow through the entire length of the sample is assumed to be impossible within a reasonable time. Limited contact between the fluid front introduced through the pore fluid line can also cause serious issues with fluid pressure build-ups and accurate pore pressure measurements during testing. To increase the contact surface between the brine and the rock, a permeable metal mesh can be introduced between the sample and the sleeve isolating the sample from the confining fluid.

Still, the low pressure equilibration rate of shales makes experimental studies time-consuming, requiring hours of equilibration time after slow stress loading or unloading to maintain the internal balance of the sample. Moreover, shales exhibit

creeping behavior under constant stress, which can bias experimental data if waiting time between stress changes is too long. To limit equilibration time and test length, reducing the dimensions of the samples is a potential solution. However, obtaining accurate and reliable measurements of pore pressure requires the dead volume of fluid trapped in the experimental apparatus to be relatively small in comparison to the cumulative pore space volume. This requirement necessitates the use of low volume pressure sensors and small diameter piping, which are susceptible to clogging from loose material or salt precipitating from brine. In addition, the use of small rock samples and low volume hydraulic system elements makes the experimental setup highly sensitive to changes in temperature. Therefore, maintaining a constant temperature level in both the setup and its surroundings is crucial and can be achieved through strict temperature control measures applied to the entire room hosting the experimental apparatus.

The anisotropic nature of shales presents additional challenges for experimental equipment and protocols. To fully characterize the mechanical properties of shales in both perpendicular and parallel directions to their bedding, multiple tests may be necessary on samples of different orientations. Such tests would require setups capable of multi-directional loading and equipped with a large number of sensors to cover multiple directions of sample deformation and sound wave propagation. This can significantly increase the time and cost of the experiments. In addition to the angle-dependent properties, shales have a relatively soft framework and quickly accumulate micro-fractures, causing them to exhibit signs of non-elastic deformation. This further complicates the extraction and description of their elastic properties using conventional models applied to other sub-surface rocks.

## 1.3 From objectives to outcomes

The main objective of this study was to offer a comprehensive understanding of shales, which would facilitate the quantification of induced pore pressure alterations in the overburden situated above a subsurface storage site. As outlined in the preceding section, this necessitated a dual-focus approach, encompassing experimental, theoretical, and numerical investigations of the undrained pore pressure response in shales, as well as the development of acoustic velocity models specifically designed for these rocks. The ultimate, yet unachieved, goal of this project was to merge the two research directions and devise a unified quantitative overburden assessment workflow, incorporating both geomechanical modeling and 4D seismic results.

In order to achieve this broadly-defined goal, the following scope of work was described in the original PhD project proposal:

1. Refining optimal experimental procedure for shale testing providing maximum information on rock properties and their variability,

2. Understanding the relation between Skempton's parameters and other shale properties, including anisotropic parameters and plastic effects,

3. Evaluating the influence of in-situ stresses, stress change amplitude and direction, and near-failure state on undrained pore pressure response in shales,

4. Implementing laboratory results in existing geomechanical modelling software and developing customized modelling algorithm incorporating undrained pore pressure response for refining existing $CO_2$ storage site/hydrocarbon reservoir models,

5. Reviewing field data in search for possible undrained response-related effects suggested by the developed model, with special emphasis on the effects not predicted by the conventional models.

Over the past few years, our team, consisting of the humble author of this thesis, supervisors, and co-authors, has successfully achieved and transformed the initial research objectives into several publishable studies:

**DRAFT A: Undrained pore pressure response in anisotropic poroelastic media**

We examined the theoretical poroelastic framework of the undrained pore pressure response in media of various symmetry classes. This lead us to to establishment of a workflow allowing for modelling of the undrained pore pressure response in poroelastic media, regardless of their orientation with respect to principal stresses. We derived angle-dependent poroelastic pore pressure coefficients for transversely isotropic and orthorhombic media, analogous to Skempton's $A$ and $B$, which consider all three principal stresses. We investigated the impact of wrongly assumed symmetry class of the medium (i.e., oversimplification of the system) on the estimated induced pore pressure change. We also suggested a method for extracting poroelastic parameters of orthorhombic media using data from standard triaxial tests.

**PAPER B: Anisotropic poroelastic modelling of depletion-induced pore pressure changes in Valhall overburden**

We used the workflow presented in Draft A and combined results of undrained experiments on shales retrieved from the Lista formation directly above the Valhall reservoir with results of geomechanical modelling of stress changes previously carried out by the field operator. We estimated undrained pore pressure response and effective stresses in the reservoir's overburden and compared pore pressure changes obtained with isotropic and transversely isotropic pore pressure parameters to assess potential errors from neglecting shale anisotropy. We proposed a simplified pore pressure modeling scheme utilizing the anisotropic properties of typical overburden shales and compared pore pressure change distribution with known casing failure locations in Valhall's overburden.

**PAPER C: Impact of undrained pore pressure response on expected failure stress in anisotropic shales**

We studied the potential connection between undrained pore pressure response in shales and risks of fault reactivation, drilling issues, and distant microseismicity, often overlooked in geomechanical modeling workflows. Our research examined how including pore pressure response impacts stress changes needed to cause shear failure in various shales. We tested the impact of the undrained pore pressure response on the injection or production operation safety assessments by using experimental results to modeled stress increases at failure for different stress loading scenarios and medium orientations, considering both isotropic and anisotropic pore pressure parameters.

**PAPER D: Effects of plastic deformation on poroelastic pore pressure coefficients in Pierre II shale**

We investigated the relationship between poroelastic pore pressure coefficients estimated within an elastic region and the progressing plastification of a transversely isotropic medium. We repeatedly loaded and unloaded shale samples drilled at various angles to the rock's bedding in a series of undrained experiments. We computed poroelastic pore pressure parameters for each loading-unloading cycle, examining the connection between pore pressure parameters and plastic strains. We then compared the experimental pore pressure parameters to those predicted by poroelasticity theory for a transversely isotropic medium.

The objectives related to the time-lapse seismic data quantitative analysis were not delineated in the original research goals statement. Due to a combination of suggestions given by Rune M. Holt, the main supervisor of this PhD project, and author's interests, the non-linearly elastic strain-dependent stiffness models became the focal point of this part of the thesis. The very first objective was to adjust an existing constitutive model to describe changes of acoustic properties of anisotropic shales. Then, the author of this thesis participated in investigations on differences in strain-sensitivity of acoustic velocities at ultrasonic and seismic frequencies and on angular effects emerging from such models. These studies were documented with the following publications:

**PAPER E: Third-order elastic tensor of shales determined through ultrasonic velocity measurements**

We investigated and adjusted constitutive model proposed by Fuck and Tsvankin employing a third-order elastic tensor to describe the non-linear strain sensitivity of anisotropic stiffnesses. Our analysis involved the use of historical laboratory measurements of strains and ultrasonic P- and S-wave velocity obtained in multiple directions relative to the axis of symmetry of transversely isotropic shales. We inverted for all the coefficients of the third-order elastic tensor and used the resultant tensor to model changes in ultrasonic velocities in response to various loading scenarios. We investigated the im-

pact of the selection of the input experimental data used to estimate the third-order coefficients on the accuracy of model predictions to determine loading scenarios giving optimal input for the inversion of the third-order elastic tensor.

**PAPER F: Stress path dependency of time-lapse seismic effects in shales: experimental comparison at seismic and ultrasonic frequencies**

We examined ultrasonic and low-frequency acoustic data from two distinct overburden shales to determine their strain sensitivities coefficients. Due to high relative errors in direct measurements of low-frequency P-wave modulus, we modified the inversion scheme from Paper E to extract the low-frequency third-order elastic tensor using dynamic measurements of Young modulus and Poisson ratio. We then estimated changes in dynamic stiffness and corresponding acoustic velocity changes along the symmetry axes of the transversely isotropic shales using both high- and low-frequency coefficients. By comparing high-frequency and low-frequency vertical velocity changes, we assessed potential discrepancies between laboratory and field measurements on the same rocks. We also evaluated the stress path dependence of velocity changes in both frequency ranges and the ability of field 4D seismic data to provide measurable effects for quantifying stress changes in the subsurface by comparing high-frequency and low-frequency vertical R-factors, a widely used time-lapse seismic attribute.

**PAPER G: Third-order elasticity of transversely isotropic field shales**

We adapted the third-order elastic model of dynamic stiffness, based on Fuck and Tsvankin and detailed in Paper E, to account for unequal strains on a plane perpendicular to the shale's symmetry axis. We determined the third-order coefficients for two overburden shales and analyzed the potential impact of experimental errors on the coefficient values. We model velocity changes for a wide range of acoustic wave propagation angles and loading scenarios. We combined the third-order elastic model with strains from geomechanical modeling of a simplified field scenario involving a depleting penny-shaped reservoir. This allowed us to assess the expected effective dynamic stiffness changes in overburden shales, estimate the impact of shear strain on velocity changes, and compare the results given by isotropic and transversely isotropic velocity models.

Several minor studies, or studies where the contribution of the author of this thesis was limited, are also listed in the appendix section.

## 1.4 Summary, recommendations and comments

This thesis provides a comprehensive overview of the research I conducted during the course of my ("slightly" extended) PhD project, which spanned from January 2018 to June 2023. It represents the key findings and conclusions that emerged from my work. It also summarizes quite well the methodology of working with shales in experimental conditions and approaches to combining the experimental, theoretical and numerical methods to obtain potentially important information on the state of the subsurface. It is important to mention, however, that although this thesis serves as a thorough review of the project, it does not encompass all the results obtained - some of the results (mostly experimental) were omitted due to the time constraints, shifting priorities of the project and my lack of experience in strategic planning of publishing-related efforts.

As I have already mentioned in the introduction, the main contributions to the field of geosciences presented in this thesis can be bifurcated into two primary groups: the undrained pore pressure response and the characterization of velocity changes in shales. Although I did not manage to fully explore the connection between these two topics, my dear colleagues and co-authors have initiated such efforts, which are summarized in Yan et al. (2023).

### 1.4.1 Undrained pore pressure response

Personally, I view the formulation and practical application of an expression for undrained pore pressure changes, grounded in anisotropic poroelasticity theory, as the pinnacle of my work. This model acknowledges the anisotropic nature of shales, takes into account all stress tensor elements, and addresses the misalignment between the stress tensor and medium frame. In doing so, it effectively overcomes surprisingly many of the shortcomings of previous models. Utilizing this model alongside the results of geomechanical modeling of the Valhall overburden, my esteemed colleagues and I were able to estimate the potential magnitude and extent of the undrained pore pressure changes. This enabled us to visualize their far-from-negligible impact on the integrity and stability of overburden shales. Moreover, it offered valuable insights into the potential relationship between pore pressure changes and documented cases of casing failures.

The practical implications of this discovery are substantial. Enhanced understanding and estimation of undrained pore pressure changes allow us to assess and predict the impacts of reservoir operations on the subsurface environment with greater accuracy. This knowledge can promote safer and more efficient reservoir management and drilling operations, significantly reducing risks associated with fluid injection and reservoir depletion. Consequently, stakeholders in the geo-industry and regulatory bodies could leverage these insights to formulate more informed policies and practices, thereby bolstering safety and operational efficiency.

The other contributions and findings related to undrained pore pressure in overburden shales, not necessarily less important, though perhaps lower in my subjective ranking of favorites are:

1. The creation of a method for approximating the undrained pore pressure response in anisotropic overburden shales, utilizing estimated vertical stress changes and a single medium parameter describing its properties along the symmetry axis, supported by increasingly numerous and consistent experimental observations.

2. The development of a straightforward method to account for plastification of shales near fault zones within the undrained pore pressure response modeling workflow.

3. The identification of potential consequences arising from disregarding undrained pore pressure changes during shale stability and integrity assessments, leading to overestimation of acceptable stress changes.

4. The uncovering of the prominent role of cohesion and angle of internal friction in rock failure, compared to undrained pore pressure parameters.

5. The emphasis on the importance of using simplified modeling of undrained pore pressure response in cases with limited information on rock pore pressure parameters, as a safer approach for subsurface operations than neglecting such effects.

6. The observation of consistent alterations in the character of undrained pore pressure changes in response to accumulated plastic deformation in shales, occasionally resulting in changes in the sign of the pore pressure response to stress changes (and mesmerizing experimental observations, such as Fig. 5.5).

These additional contributions permit a more nuanced and precise modeling of pore pressure changes in complex materials, specifically anisotropic shales, enhancing the prediction and management of a variety of operational risks. The developed methodologies to address plastification near fault zones further expand our capability to anticipate and respond to different subsurface scenarios. The emphasis on the key roles of widely-used factors such as cohesion and the internal friction angle in rock failure, as well as the use of simplified modeling in data-limited situations, provides straightforward yet effective tools for the advancement of safety protocols within industry practices.

Regarding future work in this area, my recommendations are:

1. An expanded analysis of the relationship between shale plastification and undrained pore pressure response.

   (a) The use of yet-to-be-published data collected during this PhD project, which fortuitously aligns with previously published conclusions, to establish the correlation between elastic and plastic volumetric strain and the resultant induced pressure changes.

   (b) The integration of purely elastic and non-elastic terms into Skempton-like expressions for undrained pore pressure changes and/or the incorporation of already existing anisotropic elastoplastic models.

2. The execution of laboratory studies on:

   (a) Natural and/or artificially created orthorhombic and monoclinic media to test and validate the theoretical framework and experimental workflows proposed in this thesis.

   (b) The impact of temperature changes on pore pressure in anisotropic shales.

3. Continued investigation of evidence indicating the impact of undrained pore pressure response on overburden and borehole casing integrity, ultimately leading to either the incorporation of induced pressure modeling into industry geo-modeling workflows or the refutation of its importance.

4. Exploration of the potential effect of undrained pore pressure alterations on the reactivation of hydraulically non-connected faults.

### 1.4.2 Non-linear seismic velocity model

In my view, the most significant contribution of the papers included in this thesis to the field of rock physics and geophysics is the development of a method to estimate third-order elastic coefficients using experimental data collected at seismic frequencies. This methodology bridges the divide between experimental and field observations concerning velocity strain- and stress-sensitivity factors. Notably, the R-factors extracted from our low-frequency experimental data align well with field observations reported in existing literature, an alignment not mirrored by their ultrasonic counterparts. This discovery suggests a potential resolution to a long-standing discrepancy, indicating that reliable estimation of stress and strain changes from 4D seismic data might indeed be achievable. Additionally, given the heightened sensitivity of low-frequency seismic properties, these findings suggest that changes in the subsurface have a more substantial impact on the dynamic properties of shales at the most field-relevant seismic frequencies than previously assumed. This greater impact means that such changes may be more readily observable in 4D seismic data, thereby enhancing the potential for more accurate subsurface monitoring and prediction using these techniques.

Apart from that, the advancements and insights pertaining to strain-dependent velocity changes in overburden shales include:

1. The formulation of a strain-dependent velocity model for transversely isotropic shales based on anisotropic third-order elasticity (and to large degree on previous work of other researchers) and capable of predicting velocity changes of P- and S-waves in various loading scenarios and for any propagation angles.

2. The observation that velocity fitting quality is dependent on the extent and choice of sub-set of experimental data used for inversion and identification of the constant mean stress and hydrostatic stress cycles (i.e. the most different tested stress paths) to be the best option.

3. The revelation of significant advantages of using anisotropic velocity models to describe the behaviour of overburden shales and of considerable pitfalls of their isotropic counterparts.

4. The highlighting of the potential for pre-stack time-lapse data analysis for detecting altered stresses and strains and provision of indication of significant impact of shear strains on acoustic signal velocities.

5. The emphasis on the importance of interdisciplinary collaboration between geophysics, geomechanics, and rock physics professions for better interpretation of time-lapse seismic data and understanding subsurface alterations.

These findings give additional tools and indicate interesting direction to researchers and practitioners interested in refining the method and applying it to field data.

My recommendation for further work in this topic would be:

1. Refinement of the method used to estimate low-frequency third-order elastic coefficients.

   (a) Improvement of experimental methods used to directly estimate vertical dynamic stiffness, thus improving the overall accuracy of the estimated stiffness matrix coefficients and allowing for much simpler third-order elastic coefficients estimation process.

   (b) Re-evaluation of the numerical methods with the purpose of elimination of any unnecessary balancing factors to create a more straightforward method.

2. Performing further low-frequency experimental studies with strict control of consolidation and pore pressure stabilization periods:

   (a) to improve the accuracy of results and provide more data sets for more complete analysis of the low-frequency strain and stress sensitivity ranges.

   (b) to explore the correlations between the high- and the low-frequency third-order elastic coefficients.

3. Comparison of the results of forward modelling of time-shifts and time-strains with field data to validate the experimental findings and improve the quantitative interpretation of the time-lapse seismic.

4. Performing experimental studies on the impact of shear strains on acoustic velocities in shales.

5. Increasing the density of strain measurement points on sample surfaces to provide a more comprehensive third-order elastic coefficients inversion input (by e.g., employment of optical fibres).

In the end, a personal note: despite the persistent feeling that not all objectives set during various stages of my PhD project were fully achieved, I must admit that after writing it all down, the output appears rather satisfactory. Let's this serve as a reminder that progress is not always immediately noticeable on the day-to-day basis.

## References

Adams, L. H. and E. D. Williamson (1923). 'On the compressibility of minerals and rocks at high pressures'. In: *Journal of the Franklin Institute* 195.4, pp. 475–529. ISSN: 0016-0032. DOI: https://doi.org/10.1016/S0016-0032(23)90314-5. URL: https://www.sciencedirect.com/science/article/pii/S0016003223903145.

Barkved, O. I. and T. Kristiansen (2005). 'Seismic time-lapse effects and stress changes: Examples from a compacting reservoir'. In: *The Leading Edge* 24.12, pp. 1244–1248. DOI: 10.1190/1.2149636. eprint: https://doi.org/10.1190/1.2149636. URL: https://doi.org/10.1190/1.2149636.

Berre, T. (2011). 'Triaxial testing of soft rocks'. In: *Geotechnical Testing Journal* 34.1.

Berryman, J. and J. Res (May 1995). 'Effective Stress for Transport Properties of Inhomogeneous Porous Rock'. In: *Journal of Geophysical Research* 97. DOI: 10.1029/92JB01593.

Biot, M. A. (1955). 'Theory of Elasticity and Consolidation for a Porous Anisotropic Solid'. In: *Journal of Applied Physics* 26.2, pp. 182–185. DOI: 10.1063/1.1721956.

Biot, M. A. (1941). 'General Theory of Three-Dimensional Consolidation'. In: *Journal of Applied Physics* 12.2, pp. 155–164. DOI: 10.1063/1.1712886. URL: https://aip.scitation.org/doi/abs/10.1063/1.1712886.

Biot, M. A. (1956). 'General solutions of the equations of elasticity and consolidation for a porous material'. In: *Journal of Applied Mechanics* 78, pp. 91–96. URL: https://hal.science/hal-01368662.

Biot, M. A. (1962). 'Mechanics of Deformation and Acoustic Propagation in Porous Media'. In: *Journal of Applied Physics* 33.4, pp. 1482–1498. DOI: 10.1063/1.1728759. URL: https://aip.scitation.org/doi/abs/10.1063/1.1728759.

Chenevert, M. and M. Amanullah (Sept. 2001). 'Shale Preservation and Testing Techniques for Borehole-Stability Studies'. In: *SPE Drilling&Completion - SPE DRILL COMPLETION* 16, pp. 146–149. DOI: 10.2118/73191-PA.

Daigle, H. and B. Dugan (2011). 'Permeability anisotropy and fabric development: A mechanistic explanation'. In: *Water Resources Research* 47.12. DOI: https://doi.org/10.1029/2011WR011110. eprint: https://agupubs.onlinelibrary.wiley.com/doi/pdf/10.1029/2011WR011110. URL: https://agupubs.onlinelibrary.wiley.com/doi/abs/10.1029/2011WR011110.

Davis, T. L., M. Landrø and M. Wilson (2019). *Geophysics and Geosequestration*. Cambridge University Press. DOI: 10.1017/9781316480724.

Duda, M. (2017). *Stress sensitivity of velocities in anisotropic rocks - Rock models comparison and true-triaxial apparatus description*.

Ewy, R., E. Daniels and R. Stankovich (July 2001). 'Behavior of a reactive shale from 12000 feet depth'. In: U.S. Rock Mechanics/Geomechanics Symposium.

Ewy, R., R. Stankovich and C. Bovberg (2003). 'Mechanical behavior of som clays and shales from 200 m to 3800 m depth'. In: *inproceedings of the 12th*

*PanAmerican Conference on Soil Mechanics and Geotechnical Engineering and the 39th US Rock Mechanics Symposium*.

Ewy, R. T. and R. J. Stankovic (Apr. 2010). 'Shale Swelling, Osmosis, and Acoustic Changes Measured Under Simulated Downhole Condition'. In: *SPE Drilling&Completion* 25.02, pp. 177–186. ISSN: 1064-6671. DOI: 10.2118/78160-PA. eprint: https://onepetro.org/DC/article-pdf/25/02/177/2090353/spe-78160-pa.pdf. URL: https://doi.org/10.2118/78160-PA.

Ewy, R. (Oct. 2014). 'Shale swelling/shrinkage and water content change due to imposed suction and due to direct brine contact'. In: *Acta Geotechnica* 9, pp. 869–886. DOI: 10.1007/s11440-013-0297-5.

Ewy, R. (2018). 'Practical approaches for addressing shale testing challenges associated with permeability, capillarity and brine interactions'. In: *Geomechanics for Energy and the Environment* 14. DOI: 10.1016/j.gete.2018.01.001.

Favero, V. (2017). 'Multiphysical behaviour of shales from Northern Switzerland'. PhD dissertation. Lausanne, EPFL.

Fisher, Q., S. Skochkov, S. Al-Hinai and C. Grattoni (2014). *Potential impact of faluts on CO2 injection into saline aquifers & geomechanical concerns of CO2 injection into depleted oil reservoirs*. https://slideplayer.com/slide/785836/. Accessed: 2023–03-11.

Fjær, E., R. Holt, P. Horsrud and A. M. Raaen (2021). *Petroleum Related Rock Mechanics. 3rd edition*. ISBN: 9780128221952.

Gasc-Barbier, M. and D. Tessier (2007). 'Structural Modifications of a Hard Deep Clayey Rock due to Hygro-Mechanical Solicitations'. In: *International Journal of Geomechanics* 7.3, pp. 227–235. DOI: 10.1061/(ASCE)1532-3641(2007)7:3(227).

Geertsma, J. (1973). 'A Basic Theory Of Subsidence Due To Reservoir Compaction; The Homogeneous Case'. In: *Verhandelingen Kon. Ned. Geol. Mijnbouwk. Gen* 28, pp. 43–62.

Hatchell, P. and S. Bourne (2005). 'Rocks under strain: Strain-induced time-lapse time shifts are observed for depleting reservoirs'. In: *The Leading Edge* 24.12, pp. 1222–1225. DOI: 10.1190/1.2149624. URL: https://library.seg.org/doi/abs/10.1190/1.2149624.

Holt, R. M. and J. F. Stenebråten (2013). 'Controlled laboratory experiments to assess the geomechanical influence of subsurface injection and depletion processes on 4D seismic responses'. In: *Geophysical Prospecting* 61.s1, pp. 476–488. ISSN: 0016-8025. DOI: https://doi.org/10.1111/1365-2478.12040. URL: https://onlinelibrary.wiley.com/doi/abs/10.1111/1365-2478.12040.

Horsrud, P., E. F. SØnstebØ and R. BØe (1998). 'Mechanical and petrophysical properties of North Sea shales'. In: *International Journal of Rock Mechanics and Mining Sciences* 35.8, pp. 1009–1020. ISSN: 1365-1609. DOI: https://doi.org/10.1016/S0148-9062(98)00162-4. URL: https://www.sciencedirect.com/science/article/pii/S0148906298001624.

Jaeger, J. C. (Jan. 1960). 'Shear failure of anisotropic rocks'. In: *Geological Magazine* 97.1, pp. 65–72. ISSN: 0016-7568.

Janbu, N., R. Roque, H. Lango and T. Tjetla (1988). 'Cyclic load testing of contractant clays from Gullfaks C'. In: *International Conference on Behaviour of Offshore Structures*.

Johnson, P. and P. Rasolofosaon (1996). 'Nonlinear elasticity and stress-induced anistropy in rock'. In: *Journal of Geophysical Research* 101, pp. 3113–3124. DOI: 10.1029/95JB02880.

Kanitpanyacharoen, W., F. Kets, H.-R. Wenk and R. Wirth (June 2012). 'Mineral Preferred Orientation and Microstructure in the Posidonia Shale in Relation to Different Degrees of Thermal Maturity'. In: *Clays and Clay Minerals* 60. DOI: 10.1346/CCMN.2012.0600308.

Kenter, C., A. Van den Beukel, A. Hatchell, P. Maron, K. Molenaar, M. Molenaar and J. Stammeijer (June 2004). 'Geomechanics And 4D: Evaluation Of Reservoir Characteristics From Timeshifts In The Overburden'. In: vol. All Days. North America Rock Mechanics Symposium. ARMA-04-627. eprint: https://onepetro.org/ARMANARMS/inproceedings-pdf/ARMA04/All-ARMA04/ARMA-04-627/1855018/arma-04-627.pdf.

Khaledi, K., P. Hamdi, L. Winhausen, J. Mohammadreza, D. Jaeggi and F. Amann (2021). 'Unloading induced absolute negative pore pressures in a low permeable clay shale'. In: *Engineering Geology* 295, p. 106451. ISSN: 0013-7952. DOI: https://doi.org/10.1016/j.enggeo.2021.106451. URL: https://www.sciencedirect.com/science/article/pii/S0013795221004622.

Leu, L., A. Georgiadis, M. Blunt, A. Busch, P. Bertier, K. Schweinar, M. Liebi, A. Menzel and H. Ott (Nov. 2016). 'Multiscale Description of Shale Pore Systems by Scanning SAXS and WAXS Microscopy'. In: *Energy & Fuels* 30. DOI: 10.1021/acs.energyfuels.6b02256.

Loucks, R., R. Reed, S. Ruppel and U. Hammes (June 2012). 'Spectrum of pore types and networks in mudrocks and a descriptive classification for matrix related pores'. In: *AAPG Bulletin* 96, pp. 1071–1098. DOI: 10.1306/08171111061.

MacBeth, C., A. Kudarova and P. Hatchell (2018). 'Review Paper: A semi-empirical model of strain sensitivity for 4D seismic interpretation'. In: *Geophysical Prospecting* 66.7, pp. 1327–1348. DOI: https://doi.org/10.1111/1365-2478.12648. eprint: https://onlinelibrary.wiley.com/doi/pdf/10.1111/1365-2478.12648. URL: https://onlinelibrary.wiley.com/doi/abs/10.1111/1365-2478.12648.

Magoon, L. B. and W. G. Dow (1994). *The Petroleum System—From Source to Trap*. American Association of Petroleum Geologists. DOI: 10.1306/m60585.

Mavko, G., T. Mukerji and J. Dvorkin (2020). *The Rock Physics Handbook: Tools for Seismic Analysis of Porous Media*. 3rd ed. Cambridge University Press. DOI: 10.1017/CBO9780511626753.

Milliken, K. L. and R. J. Day-Stirrat (Jan. 2013). 'Cementation in Mudrocks: Brief Review with Examples from Cratonic Basin Mudrocks'. In: *Critical Assessment of Shale Resource Plays*. American Association of Petroleum Geologists. ISBN: 9781629812694. DOI: 10.1306/13401729H55252. URL: https://doi.org/10.1306/13401729H55252.

Passey, Q. R., K. M. Bohacs, W. L. Esch, R. Klimentidis and S. Sinha (June 2010). 'From Oil-Prone Source Rock to Gas-Producing Shale Reservoir – Geologic and Petrophysical Characterization of Unconventional Shale-Gas Reservoirs'. In: vol. All Days. SPE International Oil and Gas Conference and Exhibition in China. SPE-131350-MS. DOI: 10.2118/131350-MS. eprint: https://onepetro.org/SPEIOGCEC/inproceedings-pdf/10IOGCEC/All-10IOGCEC/SPE-131350-MS/1742125/spe-131350-ms.pdf. URL: https://doi.org/10.2118/131350-MS.

Péron, H., L. Laloui, T. Hueckel and L. Hu (Sept. 2009). 'Desiccation Cracking of Soils'. In: *Revue européenne de génie civil* 13. DOI: 10.1080/19648189.2009.9693159.

Prioul, R., A. Bakulin and V. Bakulin (2004). 'Nonlinear rock physics model for estimation of 3D subsurface stress in anisotropic formations: Theory and laboratory verification'. In: *Geophysics* 69, pp. 415–425. DOI: 10.1190/1.1707061.

Revil, A., D. Grauls and O. Brévart (2002). 'Mechanical compaction of sand/clay mixtures'. In: *Journal of Geophysical Research: Solid Earth* 107.B11, ECV 11-1-ECV 11–15. DOI: https://doi.org/10.1029/2001JB000318. eprint: https://agupubs.onlinelibrary.wiley.com/doi/pdf/10.1029/2001JB000318. URL: https://agupubs.onlinelibrary.wiley.com/doi/abs/10.1029/2001JB000318.

Røste, T., A. Stovas and M. Landrø (2006). 'Estimation of layer thickness and velocity changes using 4D prestack seismic data'. In: *GEOPHYSICS* 71.6, S219–S234. DOI: 10.1190/1.2335657. URL: https://library.seg.org/doi/abs/10.1190/1.2335657.

Sayers, C. (1994). 'The Elastic Anisotropy of Shales'. In: *Journal of Geophysical Research* 99, pp. 767–774. DOI: 10.1029/93JB02579.

Schmitt, L., T. Forsans and F. Santarelli (1994). 'Shale testing and capillary phenomena'. In: *International Journal of Rock Mechanics and Mining Sciences&Geomechanics Abstracts* 31.5, pp. 411–427. ISSN: 0148-9062. DOI: https://doi.org/10.1016/0148-9062(94)90145-7. URL: https://www.sciencedirect.com/science/article/pii/0148906294901457.

Sinha, B. K. and S. Kostek (1996). 'Stress-induced azimuthal anisotropy in borehole flexural waves'. In: *GEOPHYSICS* 61.6, pp. 1899–1907. DOI: 10.1190/1.1444105. URL: https://library.seg.org/doi/abs/10.1190/1.1444105.

Sinha, B. K. and T. J. Plona (2001). 'Wave propagation in rocks with elastic-plastic deformations'. In: *GEOPHYSICS* 66.3, pp. 772–785. DOI: 10.1190/1.1444967.

Skempton, A. W. (1954). 'The Pore-Pressure Coefficients A and B'. In: *Géotechnique* 4.4, pp. 143–147. DOI: 10.1680/geot.1954.4.4.143. URL: https://www.icevirtuallibrary.com/doi/abs/10.1680/geot.1954.4.4.143.

Steiger, R. P. and P. K. Leung (July 1991). 'Consolidated Undrained Triaxial Test Procedure For Shales'. In: vol. All Days. U.S. Rock Mechanics/Geomechanics Symposium. ARMA-91-637. eprint: https://onepetro.org/ARMAUSRMS/inproceedings-pdf/ARMA91/All-ARMA91/ARMA-91-637/1997620/arma-91-637.pdf.

Thurston, R. N. (Jan. 1974). 'Waves in solids'. In: 4, pp. 109–308. (Visited on 10/07/2021).

Wenk, H.-R., M. Voltolini, M. Mazurek, L. R. Van Loon and A. Vinsot (Jan. 2009). 'Preferred Orientations and Anisotropy in Shales: Callovo-Oxfordian Shale (France) and Opalinus Clay (Switzerland)'. In: *Clays and Clay Minerals* 56. DOI: 10.1346/CCMN.2008.0560301.

Wild, K. M., L. P. Wymann, S. Zimmer, R. Thoeny and F. Amann (Mar. 2015). 'Water Retention Characteristics and State-Dependent Mechanical and Petro-Physical Properties of a Clay Shale'. In: *Rock Mechanics and Rock Engineering* 48.2, pp. 427–439. DOI: 10.1007/s00603-014-0565-1.

Winkler, K. W. and X. Liu (1996). 'Measurements of third-order elastic constants in rocks'. In: *The Journal of the Acoustical Society of America* 100.3, pp. 1392–1398. DOI: 10.1121/1.415986. URL: https://asa.scitation.org/doi/abs/10.1121/1.415986.

Yan, H., A. Bakk, R. M. Holt and S. Lozovyi (2023). 'Overburden 4D seismic: Influence of stress and pore pressure changes accounting for elastic contrast between a reservoir and its anisotropic surrounding rocks'. In: *GEOPHYSICS* In Press.

Yang, R.-J., P.-C. Yu, C.-C. Chen and F.-S. Yen (2009). 'Growth Thermodynamics of Nanoscaled $\alpha$-Alumina Crystallites'. In: *Crystal Growth & Design* 9.4, pp. 1692–1697. DOI: 10.1021/cg800351d. eprint: https://doi.org/10.1021/cg800351d. URL: https://doi.org/10.1021/cg800351d.

# Part I

# Undrained pore pressure response

This paper is intended for publication and is therefore not included.

# DRAFT A: Undrained pore pressure response in anisotropic poroelastic media

Marcin Ireneusz Duda[1,2], Audun Bakk [2], Arne Marius Raaen[2], Hong Yan[1], Rune Martin Holt[1,2]

[1] Norwegian University of Science and Technology, 7031 Trondheim, Norway
[2] Sintef Petroleum, 7031 Trondheim, Norway

Intended for future publication

## Abstract

In this paper, the framework for the undrained pore pressure response estimation in anisotropic media with respect to the directions of the principal stress changes is reviewed. Anisotropic poroelasticity theory is used to derive parameters governing the angle-dependent undrained pore pressure response in monoclinic, orthorhombic, transversely isotropic, and isotropic media. A comprehensive guide to stress tensor rotations based on Euler angles is provided, along with discussions on pore pressure response calculations in different symmetry classes in true-triaxial stress conditions. The impact of laboratory equipment on the symmetry class and the pore pressure coefficients estimation is considered. A routine to extract poroelastic parameters of an orthorhombic medium from laboratory experiments in the triaxial and true-triaxial conditions is suggested. Through the use of finite element modelling and Amadei's anisotropic solution of stress state around boreholes, we model the stress field evolution due to injection in a disc-shaped reservoir. This model is then used to compare the pore pressure responses given by different symmetry classes.

## Nota bene

The purpose of this chapter in my thesis was to lay the foundation for a publication describing the undrained pore pressure response and the modeling workflow for a three-dimensional medium under a three-dimensional stress state with any relative orientation of the two. Originally, this publication was planned to be released before PAPER B: Anisotropic poroelastic modelling of depletion-induced pore pressure changes in Valhall overburden. It turns out that the call of Valhall was too strong to resist, and we decided to prioritize "Anisotropic proelastic modeling..." as soon as we received the latest geomechanical modelling results from that field.

# PAPER B: Anisotropic poroelastic modelling of depletion-induced pore pressure changes in Valhall overburden

Marcin Ireneusz Duda[1,2], Audun Bakk [2], Rune Martin Holt[1,2], Jørn Fredrik Stenebråten[2]

[1] Norwegian University of Science and Technology, 7031 Trondheim, Norway
[2] Sintef Petroleum, 7031 Trondheim, Norway

Published in Rock Mechanics and Rock Engineering on 18 January 2023

## Abstract

Stress and pore pressure changes due to depletion of or injection into a reservoir are key elements in stability analysis of overburden shales. However, the undrained pore pressure response in shales is often neglected but needs to be considered because of their low permeability. Due to the anisotropic nature of shales, the orientation of both rock and stresses should be considered. To account for misalignment of the medium and the stress tensor, we used anisotropic poroelasticity theory to derive an angle-dependent expression for the pore pressure changes in transversely isotropic media under true-triaxial stress conditions. We experimentally estimated poroelastic pore pressure parameters of a shale from the Lista formation at the Valhall field. We combined the experimental results with finite element modelling to estimate the pore pressure development in the Valhall overburden over a period of nearly 40 years. The results indicate non-negligible pore pressure changes several hundred meters above the reservoir, as well as significant differences between pore pressure and effective stress estimates obtained using isotropic and anisotropic pore pressure parameters. We formulate a simple model approximating the undrained pore pressure response in low permeable overburden. Our results suggest that in the proximity of the reservoir the amplitude of the undrained pore pressure changes may be comparable to effective stresses. Combined with the findings of joint analysis of locations of casing deformation and total and effective stresses, the results suggest that pore pressure modelling may become an important element of casing collapse and caprock failure risk analysis and mitigation.

## 3.1 Introduction

In a typical geological storage or petroleum system, fluids in the reservoir are prevented from migrating towards the surface by low permeability cap rocks, such as shales (e.g., Magoon and Dow 1994). Low permeability of sealing formations hinders upward fluid movement, and therefore limits direct diffusive pore pressure equilibration. Pressurization or depletion of a reservoir changes the pore pressure, and hence the effective stresses in the reservoir itself, and the reservoir deformation consequently changes the stresses in its surroundings (e.g., Geertsma 1973; Gennaro et al. 2008; Hall et al. 2002; Herwanger and Koutsabeloulis 2011; Kenter et al. 2004). This may result in pore pressure changes in the reservoir's low -permeability surroundings caused by their undrained response to the stress changes. Undrained pore pressure responses have been studied and quantified using empirical parameters for several decades (e.g., Henkel and Wade 1966; Henkel 1960; Janbu et al. 1988; Skempton 1954). They are also consistent with fundamental poroelasticity theory (e.g., Biot 1941; Detournay and Cheng 1993; Fjær et al. 2021).

In this paper we will focus on pore pressure changes in overburden shales. This broad class of sediments is usually characterized by permeabilities in the $nD$ range (e.g. Best and Katsube 1995; Goral et al. 2020; Howard 1991; Katsube 2000; Schlömer and Krooss 1997) and commonly exhibits transversely isotropic behavior (i.e., physical properties symmetric about an axis normal to a plane of isotropy), both in terms of their seismic (e.g., Banik 1984; Brocher and Christensen 1990; Johnston and Christensen 1995; Levin 1979; White et al. 1983) and poroelastic static properties (e.g., Duda et al. 2021; Holt et al. 2018a; Holt et al. 2018b; Soldal et al. 2021). Although increasingly studied under laboratory conditions, the impact of the poroelastic anisotropy of shales on reservoir-scale geomechanical modelling remains largely unknown. It may prove to be an important factor for modelling the safety of CO2 storage and hydrocarbon production in circumstances where stresses are commonly found to approach the upper crust's strength limits (Townend and Zoback 2000) and even small effective stress changes may activate faults (Ellsworth 2013; McGarr et al. 2002; Nicholson and Wesson 1990).

The aim of this study is to show the importance of the anisotropic undrained pore pressure response in modelling the development of effective stress, caused by reservoir depletion or pressurization, in low permeability rocks, and to offer a method to approximate the undrained pore pressure response in anisotropic low permeability overburden using limited number of input parameters. To achieve that aim, we model pore pressure changes in the overburden of the Valhall field located in the Norwegian sector of the North Sea. First, we use anisotropic poroelasticity theory (Cheng 1997; Thompson and Willis 1991) to establish a link between changes in a fully three-dimensional stress state, anisotropic pore pressure parameters, and the angular relationship between the principal directions of their corresponding tensors. Then we analyze results of laboratory experiments that provide a set of poroelastic pore pressure parameters of an overburden shale cored from the Lista

formation directly above a hydrocarbon reservoir at the Valhall field. Next, we use the Valhall reservoir and overburden geometry, and corresponding finite-element stress modelling results provided by the field operator (AkerBP), to approximate the pore pressure and the effective stress changes in the proximity of the reservoir over a period of nearly 40 years (1982-2020). Finally, we compare predictions made using anisotropic and isotropic pore pressure coefficients with approximated results obtained solely with a single poroelastic pore pressure parameter (describing pore pressure response to changing stress along symmetry axis of the medium) and vertical stress change.

## 3.2 Theory

Skempton (1954) derived Equation (3.1) to describe the pore pressure changes in soils tested in undrained conditions,

$$\Delta p_f = B_S \left[\Delta\sigma_{RAD} + A_S \left(\Delta\sigma_{AX} - \Delta\sigma_{RAD}\right)\right], \tag{3.1}$$

where $p_f$ is pore pressure, $B_S$ and $A_S$ are Skempton's pore pressure parameters, and $\sigma_{AX}$ and $\sigma_{RAD}$ are axial and radial (in relation to the geometry of a cylindrical sample and its orientation in an experimental setup) stresses. Skempton (1954) assumed that deviations of $A_S$ from 1/3 (the value given by isotropic linear elasticity) are caused by deviations from a strictly elastic material deformation. Cheng (1997) demonstrated that Skempton's parameters can also be derived from anisotropic poroelasticity. Holt et al. (2017) applied this approach for vertically transversely isotropic (VTI) shales and proved experimentally that the value of $A_S$ depends on the angle $\theta$ between the direction of axial stress applied to a sample and the symmetry axis of a transversely isotropic medium. Here, the pore pressure parameters $B_S$ and $A_S$ are expressed in terms of poroelastic constants, $B_{11}$ and $B_{33}$ (defined in the Section 3.9), describing the properties of the medium within the symmetry plane and along the symmetry axis , respectively:

$$B_S = \frac{2B_{11} + B_{33}}{3}, \tag{3.2}$$

$$A_S = \frac{B_{11}\sin^2\theta + B_{33}\cos^2\theta}{3B_S}. \tag{3.3}$$

In our work we use the poroelastic pore pressure parameters from the tensor $\boldsymbol{B}$ and the stress change tensor $\Delta\boldsymbol{\sigma}$, Equation (3.4) and Equation (3.5), to describe the impact of all three principal stress changes on the undrained pore pressure response in transversely isotropic shales. The tensors of transversely isotropic poroelastic pore pressure parameters and stress changes along their respective principal directions are

$$\boldsymbol{B} = \begin{bmatrix} B_{11} & 0 & 0 \\ 0 & B_{11} & 0 \\ 0 & 0 & B_{33} \end{bmatrix}, \tag{3.4}$$

$$\Delta\boldsymbol{\sigma} = \begin{bmatrix} \Delta\sigma_{11} & 0 & 0 \\ 0 & \Delta\sigma_{22} & 0 \\ 0 & 0 & \Delta\sigma_{33} \end{bmatrix}. \tag{3.5}$$

The above stress change tensor is defined as a difference between the final and the initial principal stress tensors,

$$\Delta\boldsymbol{\sigma} = \boldsymbol{\sigma}^{final} - \boldsymbol{\sigma}^{initial}. \tag{3.6}$$

The relationship between the two tensors is given by Cheng (1997):

$$\Delta p_f = \frac{1}{3} B_{ij} \Delta\sigma_{ij}. \tag{3.7}$$

Equation (3.7) assumes that the tensors $\boldsymbol{B}$ and $\boldsymbol{\sigma}$ share the same axes. However, in the reality these tensors may be misaligned, and require rotation to align them. During modeling, we therefore estimate the orientation of the material's principal directions (coinciding with the principal directions of the poroelastic tensor $\boldsymbol{B}$) from the geometry of the layering and compare it with the orientation of the principal stresses. For that purpose, we assume that the symmetry axis of the medium (rock) at a given location is normal to the interface defined in the geomechanical model. Principal stresses, their magnitude and directions, are estimated by computing eigenvectors and eigenvalues of an arbitrarily oriented stress tensor. In most available software packages (including Python's NumPy library that we used) eigenvalues are then arranged along the diagonal of the tensor in ascending order according to their values, i.e., $\sigma_{33}^S$ and $\vec{S}_3$ describe the largest of the principal stresses.

We describe the spatial orientation of the principal directions of the two tensors by defining their frames in the coordinates of an external geo-reference system XYZ (easting, northing and depth) composed of unit vectors: $M$ for medium properties and $S$ for stresses (Figure 3.1),

$$M = \left\{\vec{M}_1, \vec{M}_2, \vec{M}_3\right\} = \left\{[m_{11}, m_{12}, m_{13}], [m_{21}, m_{22}, m_{23}], [m_{31}, m_{32}, m_{33}]\right\}, \tag{3.8}$$

$$S = \left\{\vec{S}_1, \vec{S}_2, \vec{S}_3\right\} = \left\{[s_{11}, s_{12}, s_{13}], [s_{21}, s_{22}, s_{23}], [s_{31}, s_{32}, s_{33}]\right\}. \tag{3.9}$$

In the case of a vertically transversely isotropic medium, the orientation of vectors $M_1$ and $M_2$ is arbitrary and serves only to define their shared isotropic plane. If the symmetry class of the medium was to be modified, e.g. to orthorhombic or monoclinic due to creation of cracks, all symmetry axes would need to be defined more thoroughly.

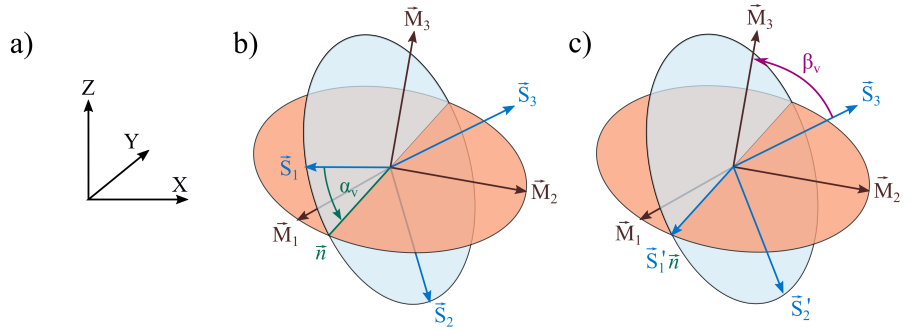


**Figure 3.1:** Orientation of the medium (frame $M$) and the principal stress tensor (frame $S$), relative to the geo-reference system (XYZ). The rotation angles $\alpha$ (rotation around $\vec{S}_3$) and $\beta$ (around $\vec{n}$) are needed to move the stress tensor frame $S$ to the orientation of the medium, $M$. Planes $\vec{S}_1 - \vec{S}_2$ and $\vec{M}_1 - \vec{M}_2$ are marked for better visualization of the vector orientations.

The next step is to rotate the stress tensor frame $S$ to the orientation of the medium frame $M$ using Euler passive rotations according to the right-hand convention. First, we rotate the stress tensor frame around vector $\vec{S}_3$ by angle $\alpha$ (Figure 3.1b), so that vector $\vec{S}_1$ coincides with the so-called lines of nodes $n$ given by equation (10),

$$\vec{n} = \vec{S}_3 \times \vec{M}_3. \tag{3.10}$$

Then, we rotate the stress frame around $n$ by angle $\beta$ (Figure 3.1c). The rotation angles are given by a dot-product of the pair of vectors they relate which yield

$$\alpha_V = \cos^{-1}\left(\frac{\vec{S}_1 \cdot \vec{n}}{|\vec{n}|},\right), \tag{3.11}$$

$$\beta_V = \cos^{-1}\left(\vec{S}_3 \cdot \vec{M}_3\right). \tag{3.12}$$

The rotation angles are confined to -180° < $\alpha$ < 180° and 0 < $\beta$ < 180°. If the initial stress tensor has a frame aligned with the external coordinate system (i.e., $s_{ij} = \delta_{ij}^{Kronecker}$), the expressions for the rotation angles simplify to

$$\alpha_V = \cos^{-1}\left(\frac{m_{32}}{\sqrt{1-m_{33}^2}}\right), \tag{3.13}$$

$$\beta_V = \cos^{-1}\left(m_{33}\right). \tag{3.14}$$

This step can yield angles representing rotations around the actual rotation axes, as well as around their negative vectors (e.g., $\vec{S}_3$ and -$\vec{S}_3$). This may be verified by the cross-product of the rotated and objective vectors (e.g. $\vec{S}_1$ rotated by $\alpha$ to $\vec{n}$) scaled by product of their magnitudes, and eventually corrected by multiplying the rotation angle by -1, as shown for angle $\alpha_V$ in Equation (3.15).

$$\alpha = \begin{cases} \alpha_V & \text{if} \quad \frac{\vec{S}_1 \times \vec{n}}{\left|\vec{S}_1\right||\vec{n}|\sin\alpha_V} = \vec{S}_3, \\ -\alpha_V & \text{if} \quad \frac{\vec{S}_1 \times \vec{n}}{\left|\vec{S}_1\right||\vec{n}|\sin\alpha_V} = -\vec{S}_3. \end{cases} \tag{3.15}$$

To avoid problems related to the number precision limitations, we correct the rotations angles according to the sign of the Equation (3.15), rather than its exact value — assuming $\vec{S}_3$ = [0,0,1], as in Equation (3.13) and Equation (3.14), the conditions become

$$\alpha = \begin{cases} \alpha_V & \text{if} \quad \frac{m_{31}}{\sin\alpha_V} > 0, \\ -\alpha_V & \text{if} \quad \frac{m_{31}}{\sin\alpha_V} < 0. \end{cases} \tag{3.16}$$

Mathematically, the frame rotations are expressed by rotation matrices

$$\boldsymbol{R}_3\left(\alpha\right) = \begin{bmatrix} \cos\alpha & -\sin\alpha & 0 \\ \sin\alpha & \cos\alpha & 0 \\ 0 & 0 & 1 \end{bmatrix}, \tag{3.17}$$

$$\boldsymbol{R}_1\left(\beta\right) = \begin{bmatrix} 1 & 0 & 0 \\ 0 & \cos\beta & -\sin\beta \\ 0 & \sin\beta & \cos\beta \end{bmatrix}. \tag{3.18}$$

For this type of rotation, the cumulative intrinsic ("moving body") rotation matrix is

$$\boldsymbol{R}\left(\alpha,\beta\right)=\boldsymbol{R}_1(\beta)^T\boldsymbol{R}_3(\alpha)^T=\begin{bmatrix}\cos\alpha & \sin\alpha & 0\\ -\sin\alpha\cos\beta & \cos\alpha\cos\beta & \sin\beta\\ \sin\alpha\sin\beta & -\cos\alpha\sin\beta & \cos\beta\end{bmatrix}. \tag{3.19}$$

Then, we are ready to rotate the principal stress tensor ($\boldsymbol{\sigma}^S$) into the medium frame ($\boldsymbol{\sigma}^M$),

$$\boldsymbol{\sigma}^M=\boldsymbol{R}\left(\alpha,\beta\right)\boldsymbol{\sigma}^S\boldsymbol{R}(\alpha,\beta)^T. \tag{3.20}$$

Now we rotate stress tensors representing the stress state before and after the change in stress (caused by fluid injection or drainage operation) was introduced. The angles $\alpha$ and $\beta$ need to be estimated separately for the two stress tensors to account for potential stress state rotation.

Such changes of the principal stress directions in the reservoir and its overburden may be caused by depletion- or injection-related arching effects R.(e.g., Fjær et al. 2021; Geertsma 1973; Rudnicki 1999; Segall and Fitzgerald 1998). This is of relevance for soft, strongly compacting reservoirs (such as Ekofisk or Valhall) having quite non-uniform spatial patterns Tron Golder and Bertold 2010. Principal stress rotation can be also caused by stress concentrations and re-alignment in proximity of faults and fractures during hydrocarbon production R.(e.g., Han et al. 2015; Zoback 2007), response to high-rate injections R.(e.g., Martínez-Garzón et al. 2013; Martínez-Garzón et al. 2014; Schoenball et al. 2014; Ziegler et al. 2017) or large earthquakes R.(e.g., Bohnhoff et al. 2006; Hardebeck and Hauksson 2001; Ickrath et al. 2015)

An alternative approach would be to use geo-referenced stress tensor (stresses measured along the external $X$, $Y$ and $Z$ directions) instead of principal stress tensor as the starting points of the rotation procedure. In this case, the initial stress tensors have nine non-zero elements. On the other hand, the orientation of the tensor frames is identical, and hence only one set of rotation angles is needed to rotate both the initial and the final stress tensors.

Finally, we can insert the expression for stresses obtained in Equation (3.20) into Equation (3.7),

$$\Delta p_f=\frac{1}{3}B_{ij}\left(\sigma_{ij}^{M,final}-\sigma_{ij}^{M,initial}\right). \tag{3.21}$$

For a transversely isotropic elastic medium with the stress tensor initially aligned with its constant principal stress directions (i.e., not changing during loading or unloading, as in typical laboratory conditions), Equation (3.21) takes the form

$$\begin{aligned}\Delta p_f = \frac{1}{3}\big(&\Delta\sigma_{11}^S\left[2B_{11}^M + B_{33}^M\right] \\ &+ \left[\Delta\sigma_{33}^S - \Delta\sigma_{11}^S\right]\left[B_{11}^M\sin^2\beta + B_{33}^M\cos^2\beta\right] \\ &+ \left[\Delta\sigma_{22}^S - \Delta\sigma_{11}^S\right]\left[B_{11}^M\sin^2\alpha + B_{33}^M\cos^2\alpha + \left\{B_{11}^M - B_{33}^M\right\}\cos^2\alpha\cos^2\beta\right]\big)\end{aligned} \tag{3.22}$$

Alternatively, Equation (3.22) can be expressed in terms of Skempton-like parameters

$$\Delta p_f = \bar{B}\left(\Delta\sigma_{11}^S + A_{3-1}\left[\Delta\sigma_{33}^S - \Delta\sigma_{11}^S\right] + A_{2-1}\left[\Delta\sigma_{22}^S - \Delta\sigma_{11}^S\right]\right), \tag{3.23}$$

where $\bar{B}$, $A_{3-1}$ and $A_{2-1}$ are defined as

$$\bar{B} = \frac{2B_{11}^M + B_{33}^M}{3}, \tag{3.24}$$

$$A_{3-1} = \frac{B_{11}^M\sin^2\beta + B_{33}^M\cos^2\beta}{3\bar{B}}, \tag{3.25}$$

$$A_{2-1} = \frac{B_{11}^M\sin^2\alpha + B_{33}^M\cos^2\alpha + \left(B_{11}^M - B_{33}^M\right)\cos^2\alpha\cos^2\beta}{3\bar{B}}. \tag{3.26}$$

Here, parameter $A_{3-1}$ is equivalent to $A_S$ from Equation (3.3), whereas parameter $A_{2-1}$ is an expansion to Skempton (1954), capturing the impact of the third principal stress (when elasticity is assumed). These Skempton-like parameters allow us to maintain the clarity of the original Equation (3.1) and may serve as a useful tool to describe the impact of the shear stress changes on the undrained pore pressure response. The impact of $\Delta\sigma_{33}^S - \Delta\sigma_{11}^S$, controlled by parameter $A_{3-1}$, depends only on $\beta$, i.e., the angle between the direction of the principal stress $\sigma_{33}^S$ ($\vec{S}_3$) and the symmetry axis of the medium ($\vec{M}_3$). The angle-dependence of the impact of $\Delta\sigma_{22}^S - \Delta\sigma_{11}^S$ on the undrained pore pressure response, scaled by $A_{2-1}$, is more nuanced and depends on both $\alpha$ and $\beta$.

Once the pore pressure parameters have been estimated from experimental data, the undrained pore pressure response obtained with Equation (3.22) can be compared with results given by Equation (3.11) under assumption of linear isotropy of the medium, i.e., with $A = 1/3$. Proper identification of the symmetry class of the medium and determination of the pore pressure parameters can have a large impact on the estimation of the Terzaghi effective stresses $\sigma'_{ii}$ (commonly used in the context of rock failure),

$$\sigma'_{ii} = \sigma_{ii} - p_f. \tag{3.27}$$

Here, pore pressure shifts the stress state described using a Mohr circle without changing its radius. In the case of stress changes different from hydrostatic ($\Delta\sigma_{11}^M = \Delta\sigma_{22}^M = \Delta\sigma_{33}^M$), the undrained pore pressure response in anisotropic media can be significantly different from that predicted using the isotropic Skempton's parameter. Consequently, the distance between the Mohr circle and a potential failure envelope can be smaller than anticipated, as shown schematically in Figure 3.2 (Duda et al. 2022, for more details see). This can strongly affect stability assessment of media of interest and in a field scenario can potentially lead to increased problems during drilling and with the integrity of existing wells, or to fault reactivation. Alternatively, an overestimation of $\Delta p_f$ may give a narrower acceptable mud weight window, and therefore rule out some reasonable well-planning scenarios.

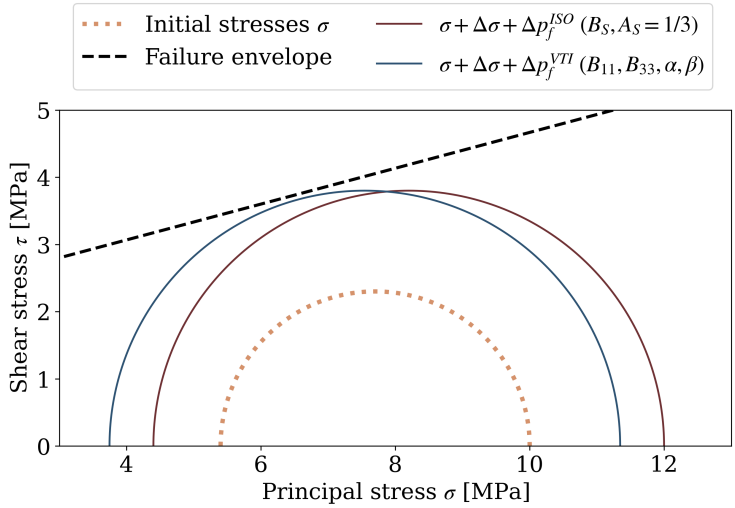


**Figure 3.2:** Mohr circle predicted by the anisotropic (blue) and the isotropic (brown) pore pressure parameters for Lista overburden shale loaded with 2 MPa in the direction along the symmetry axis and unloaded by 1 MPa along the symmetry plane direction. The applied stress path (constant mean stress) is consistent with predictions given for the overburden by Geertsma (1973).

## 3.3 Experiments

The material used in this study originates from a borehole drilled at the Valhall oilfield. The reddish-brown shale was cored at measured depths of 2890-2900 m

in the Lista formation, several meters above the chalk reservoir itself (for more details on the stratigraphy of the field see e.g., Kristiansen 2004).

Initially, the core was stored in the original core liner, with oil-base drilling mud , and then cut into 1 m sections and placed into a cylinder filled with base-oil and sealed with end caps. Once it arrived to our laboratory, the drilling fluid was wiped off and the core was stored in Marcol-82 (chemically inert purified mixture of liquid saturated hydrocarbons) in a closed container to avoid any changes to its water content (Ewy 2015; Ewy 2018; Giger et al. 2018; Wild et al. 2017). The chemical composition of the pore fluid was determined to avoid artifacts associated with osmotic effects during experiments (Mazurek et al. 2015). A cylindrical sample of 38.1 mm in diameter and 50 mm in length was placed inside an oedometer and compressed axially while collecting the effluent in syringes from the end pistons. Axial stress exerted on the sample was held at 10 MPa for five days and at 15 MPa for another ten days – this allowed us to collect approximately 1.5 ml of the pore fluid which was sent to the Institute of Geological Sciences at the University of Bern, Switzerland for ion chromatography and inductively coupled plasma-optical emission spectrometry analysis to quantify its ionic content. The results of these analyses served as a basis for the preparation of a brine compatible with the pore fluid in its physical and chemical properties, which we used as an analogue fluid in the pore pressure lines in our main experiment.

The porosity of the rock was determined to be 31%. To estimate this value we selected a sample of the core neighboring the location of the plug used in the triaxial test, weighted it and estimated its volume (using Archimedes principle). Then, the sample was heated to 105°C for 15 days. Finally, the sample was weighed again and its porosity was estimated from the weight loss (associated with water content loss) under assumption of full water saturation prior to heating. Assuming a homogenous porosity distribution in the section of the core we had chosen for testing, the cylindrical sample of 25.5 mm in diameter and 51.6 mm in length used in the triaxial test contained approximately 8.1 ml of pore fluid. The sample was drilled perpendicularly to the bedding, i.e., the lamination-related symmetry axis of the medium ($M_3$) was parallel to the geometrical long axis of the sample. During coring and end-grinding the sample was kept oil wet with Marcol-82, which was used as a circulation and cooling fluid, to avoid any changes to the pore fluid content. The sample was installed inside a viton sleeve with radial drains to allow drainage at the sides of the plug, and hence to increase the consolidation rate and in consequence shorten the duration of the experiment.

The test was conducted using a triaxial apparatus consisting of a load frame and pressure vessel (for more details, see Bakk et al. 2020). In the pressure vessel the sample was exposed to an isotropic external pressure exerted by fluid, and an axial differential stress was applied with an axial actuator. The pore pressure was controlled using a hydraulic servo-controlled pressure intensifier and pore fluid lines were connected to both end-pistons. The pore pressure measurements were taken outside the pressure cell near the in- and out-lets of the pore fluid lines. The estimated dead volume of the pore fluid system was significantly lower than the

estimated pore volume (0.7 and. 8.1 ml, respectively), which gives us confidence in the measured values of pore pressure change. Axial strain was measured with a set of three evenly azimuthally distributed linear variable differential transformers (LVDTs). Radial strain was measured in two orthogonal directions using strain-gauged extensometers (cantilevers) in contact with the sample at its mid-height through metal pins penetrating the sleeve. The reported values of strains are the averages of the values given by the set of sensors measuring deformation in corresponding directions. Temperature was measured inside the pressure cell during the entire experiment to check for temperature variations that would impact the observed pore pressure changes.

After instrumentation and after the sample was installed in the pressure vessel, a nominal confining pressure of 2 MPa was established. The analog brine was introduced and about 60 ml was passed along the sample through the side drains while confining pressure was automatically adjusted by the control system to maintain the isochoric boundary condition. Then, the back pressure in the pore pressure line was increased to 2 MPa and approximately 30 ml of the analog brine was flowed along the sample to ensure removal of any trapped air. During this saturation stage (24 hours), the confining pressure increased to 29.2 MPa while pore pressure was kept at 2 MPa. After approx. 4 days the estimated in-situ stress and pore pressure were established (total stresses of 49.8 MPa in radial and 54.4 MPa in axial directions, and a pore pressure of 44.4 MPa). The sample was left for 6 days to consolidate. This resulted in a swelling of -7 millistrain radially and -8 millistrain axially. The estimates of initial in-situ conditions were provided by the operating company.

During this initial stage of the experiment, we determined the allowable axial strain rate from the consolidation coefficient (Head and Epps 2011). Once the system stabilized at the initial in-situ stress and pore pressure levels, four low-amplitude axial stress (1 MPa) and one confining pressure (3 MPa) undrained unloading-reloading cycles were carried out to ensure proper positioning and alignment of the sample inside the cell and to investigate possible stress-dependence of the amplitude of the pore pressure response.

The main undrained part of the experiment consisted of four further unloading-reloading cycles (Figure 3.3).

Unloading the sample starting from the maximum stress level experienced in the experiment allowed us to keep shear stresses low and to avoid effects such as microfracture closure, hence limiting the extent of non-elastic and non-linear deformation which could occur during virgin loading. The moduli measured during such an unloading-reloading cycle are also closer to the elastic moduli than in the case of a loading-unloading cycle. The amplitude of the axial stress changes (in the experimental context, $\Delta\sigma_{AX}$ equivalent to $\Delta\sigma^S_{33}$) was 3 MPa and the radial stress ($\Delta\sigma_{RAD}$ equivalent to $\Delta\sigma^S_{11}$) followed specific stress paths,

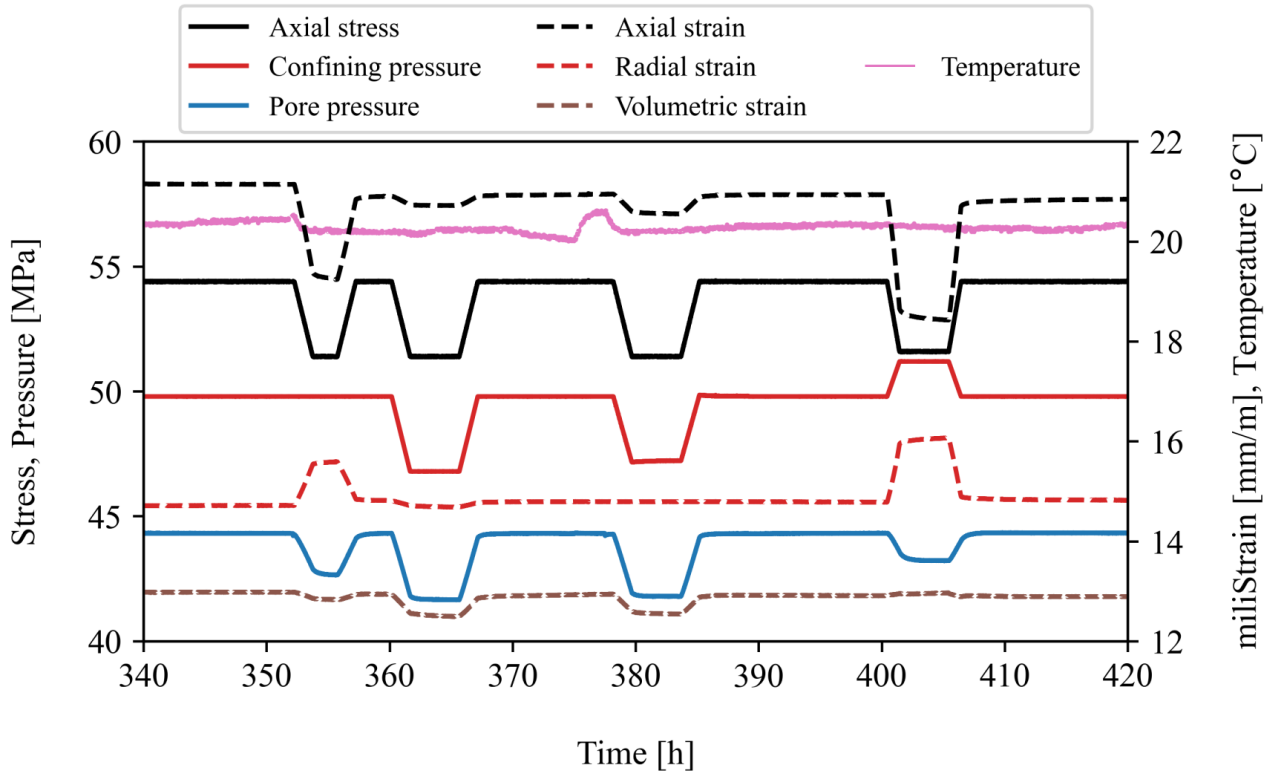


**Figure 3.3:** Main undrained part of the multistage stress loading-unloading experiment carried out on a cylindrical plug of the Valhall overburden shale drilled perpendicularly to bedding ($\beta = 0$, see Figure 3.1)

$$\kappa = \frac{\Delta\sigma_{11}^S}{\Delta\sigma_{33}^S}, \tag{3.28}$$

starting with so-called a "triaxial" cycle ($\kappa = 0$, time interval approx. 352-358 h), followed by an "isotropic" cycle ($\kappa = 1$, 360 – 368 h), a "K0" stress path cycle ($\kappa = 0.87$, adjusted to yield no radial strain, 378-386 h) and a "constant mean stress" ($\kappa = -0.5$, 400-408 h) stress path. The last cycle had a slightly lower amplitude axial stress change to keep it above the confining pressure (the exact measured stress and pore pressure values are given in Table 1 in the Section 3.9) – in the case of the confining pressure higher than the axial stress, the confining fluid would be able to push the axial piston away from the upper surface of the sample. After every undrained cycle the valve connecting the pore fluid intensifier and the pore fluid system inside of the cell was opened, and the pore pressure was brought back to its initial in-situ value, and the sample re-consolidated. Further analysis of the data was carried out using the stress and pore pressure measurements taken directly before the initiation of the unloading and 1000s after its completion (to let the pore pressure equilibrate).

As the sample was drilled perpendicularly to the bedding ($\beta = 0$) and radial stress is always isotropic (i.e., $\sigma_{11}^S = \sigma_{22}^S$ and $\Delta\sigma_{11}^S = \Delta\sigma_{22}^S$), Equation (3.22) simplifies to

$$\Delta p_f = \frac{1}{3}\left(2\Delta\sigma_{11}^S B_{11}^M + \Delta\sigma_{33}^S B_{33}^M\right), \tag{3.29}$$

or alternatively

$$\frac{\Delta p_f}{\Delta\sigma_{33}^S} = \frac{1}{3}\left(2\kappa B_{11}^M + B_{33}^M\right). \tag{3.30}$$

The use of four different stress paths allowed us to verify the expected linearity of the experimental results in the $\Delta p_f/\Delta\sigma_{33}$ - $\kappa$ space Figure 3.4 and strengthen our trust in the obtained poroelastic pore pressure parameters values.

To estimate the values of the anisotropic pore pressure coefficients $B_{11}$ and $B_{33}$ we solved a set of four linear Equation (3.29), one for each of the unloading stages, numerically. This yielded $B_{11} = 0.53$ and $B_{33} = 1.51$, or alternatively $B_S = 0.86$ and $A_S(\alpha = 0) = 0.59$ from Equation (3.2) and Equation (3.3). The experimental results yield the poroelastic coefficient $B_{33}$ almost three times larger than $B_{11}$ - such a high degree of anisotropy indicates large contrast in rock compliance to loading applied along and perpendicular to the symmetry axis. It also signals the dominant role of $B_{33}$ in the pore pressure response in horizontally or near-horizontally layered Lista shale.

For the purposes of our overburden response modelling, we simply assume that these experimentally estimated properties are representative for the entire volume

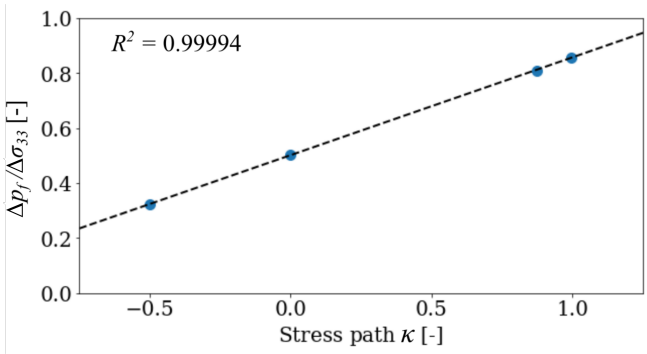


**Figure 3.4:** Change in pore pressure normalized by axial stress change vs. stress path parameter for the Valhall overburden shale sample drilled perpendicularly to the bedding ($\beta = 0$, see Figure 3.1)

of the Valhall overburden.

We used $B_{11}$ and $B_{33}$ together with Equation (3.25) and Equation (3.26) to visualize the angle dependence of coefficients $A_{3-1}$ (Figure 3.5, left) and $A_{2-1}$ (Figure 3.5, right) which control the impact of shear stresses on the pore pressure response. The values of both parameters vary between 0.21 ($B_{11}/3\bar{B}$) and 0.59 ($B_{33}/3\bar{B}$), deviating significantly from 1/3 (their values predicted by isotropic linear elasticity). This confirms previous observations made on shales by Holt et al. (2018b), Holt et al. (2018a) and Soldal et al. (2021).

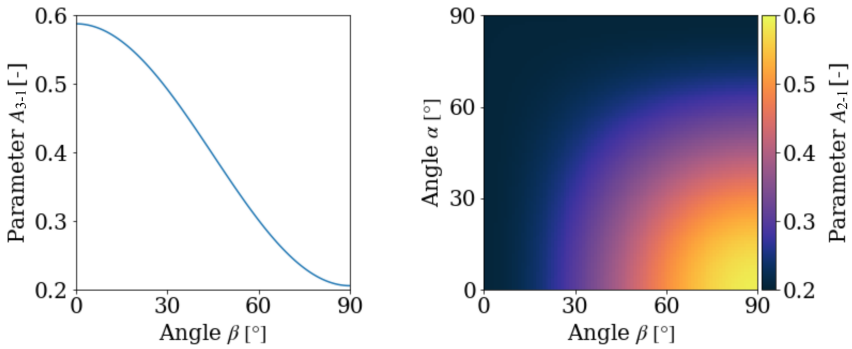


**Figure 3.5:** Angle-dependency of parameters $A_{3-1}(\beta)$ and $A_{2-1}(\alpha, \beta)$ which describe the impact of shear stresses on the undrained pore pressure response in the Valhall overburden shale (for angles definition see Figure 3.1)

## 3.4 Modeling

We combine our estimated poroelastic pore pressure parameters for the Lista shale with Valhall field geometry and stress state evolution modelling results provided by the field operator, AkerBP, to model the undrained pore pressure response to reservoir depletion. The decrease in reservoir pore pressure is non-uniform, and locally reaches as much as 28 MPa (Kristiansen 2020). In the layer of model nodes directly above the reservoir (the bottom part of the Lista formation, on average 8.9 m above the first layer of nodes in the reservoir) the average stress paths $\kappa$, Equation (3.28), computed for all points with $\Delta\sigma_{33}^{M} > 0.1$ MPa were 0.38 and 0.39 for $\sigma_{11}^{M}$ and $\sigma_{22}^{M}$, respectively, with standard deviations of 1.11 and 1.13. This variety of estimated stress paths suggests a wide range of possible stress-induced pore pressure changes, as previously shown in Figure 3.4 (where the sampled stress paths had the average of 0.34 and the standard deviation of 0.72).

The geomechanical model of the reservoir overburden consists of 50 layers. Each layer above the reservoir consists of nodes for which the vertical projection forms a 50 x 50 m regular grid (outside the central part of the model the lateral distance between neighboring points increases). The vertical distance between the layers is variable (although it remains comparable to the lateral distance between nodes) and is adjusted so that the model layers resemble the geological 3D structure of the layers and features in the subsurface. The model accounts for the anisotropy of mechanical properties in the overburden by assigning different horizontal and vertical undrained elastic parameters (in total: two Young's moduli, two Poisson's ratios and a single shear modulus) in the layers above the reservoir. The values of the elastic moduli in the overburden were estimated by the field operator with the use of correlations relating measurements of in-situ sonic velocity measurements with static stiffnesses determined through laboratory testing (Kristiansen 1998). In the newer iterations of geomechanical modelling, the properties of both the reservoir and the overburden were updated to provide maximum fit of the modelling results to compaction and subsidence history combined with the information on the volumes produced from the reservoir. We base our analysis on a recent geomechanical model which has not been yet described in the literature.

We assume that the orientation of the symmetry axis of the medium ($M_3$) at every model node coincides with the vector normal to the corresponding model layer at given point. Hence, the normal can be estimated for each of the nodes by comparing its position with the location of two out of four of its nearest neighbors from the same layer (Figure 3.6a-d), chosen such that the three considered points form a right angle. The normal vector is determined for the point in the vertex of the angle as the dot-product of the vectors forming the angle. With this method we obtain four normal vectors at each point (one for each of valid neighbor pairs) – their averaged coordinates are used to describe a representative normal vector for the surface (Figure 3.6e).

Statistical comparison between the four estimated normal-vector variants showed

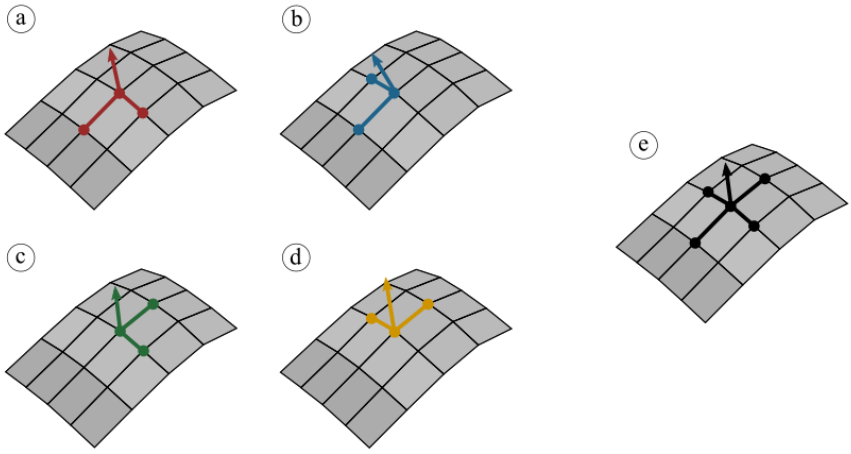


**Figure 3.6:** Estimation of the surface normal at given point by comparing its position with the location of its two nearest neighbors – the dot-product of the vectors forming the right angle gives the parameters of the normal vector. For each point of the model four variants (a-d) are estimated and then averaged (e).

no significant differences, and hence their average should be a good representation of the local orientation of the medium. As the stresses we rotate are initially oriented along the directions of the external coordinate system, the orientation of the rock symmetry axis is sufficient to estimate the angles $\alpha$ and $\beta$ using Equation (3.13) and Equation (3.14).

Rotation angles between the external (or geo-reference) coordinates system $XYZ$ (i.e., $S$ = ([1,0,0], [0,1,0], [0,0,1])) and the orientation of the medium estimated for the surface corresponding to the top of the Tor formation (reservoir rocks) are shown in Figure 3.7. As the initial stress tensor does not represent principal stresses (i.e., it contains non-diagonal stress tensor elements) and the principal stress directions change due to the depletion, Equation (3.22) and Equation (3.23) take a more complex form. Hence, the rotation angles do not give full insight into the impact of the particular principal stresses on the undrained pore pressure response. Referring to their definitions shown in Figure 3.1, the angles displayed in Figure 3.7a tell us about the rotation of the stress frame around the vertical axis. The rotation by the angle $\alpha$ moves $\vec{S}_1$ (which represents direction of $\sigma^S_{11}$) into the assumed material symmetry plane. It therefore depends mostly on the local dipping direction. The use of a cyclic color scale is necessary as rotations of 180 or -180 degrees give the same result. The rotation angles shown in Figure 3.7b are more intuitive, as $\beta$ is the angle between the vertical axis, $Z$ (or $\vec{S}_3$), and the symmetry axis of the material $\vec{M}_3$.Thus, near-zero angles indicate a nearly-

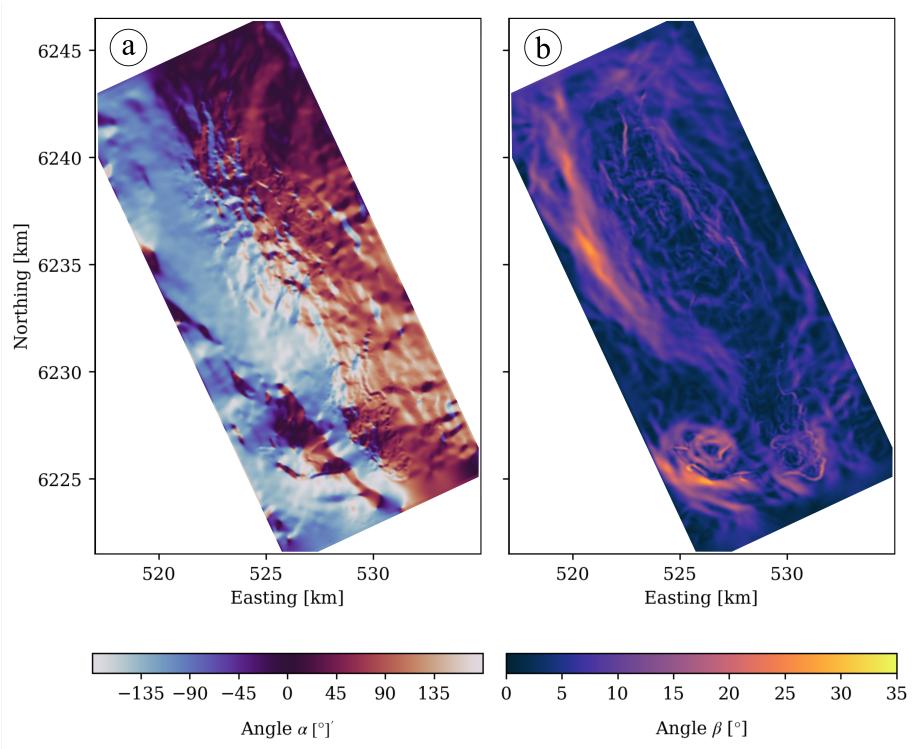


**Figure 3.7:** Top view of the distribution of the rotation angles $\alpha$ (a) and $\beta$ (b) on the upper surface of the Tor formation (for angles definition see Figure 3.1). The easting direction corresponds to $X$ direction and the northing direction to $Y$ direction in Figure 3.1a.

flat surface, whereas large angles mark steep slopes or faults intersecting model surfaces and creating local discontinuities.

We model the undrained pore pressure response to the stress state changes that took place between 1982 (start of the hydrocarbon production in Valhall) and 2020. Using stress tensors aligned with the external frame $XYZ$ allows us to account for the stress rotations caused by the reservoir depletion without having to estimate rotation angles separately for the two stress states.

The pore pressure changes were first estimated with the use of the anisotropic poroelastic tensor $\boldsymbol{B}$, Equation (3.4), representing the vertically transversely isotropic shale. They were later re-estimated using the same input stress changes, but with the effective isotropic Skempton's parameter $B_S = 0.86$ and $A_S = 1/3$ (Equation (3.2) and Equation (3.3)). Estimation of pore pressure changes based on stresses from the geomechanical model computed with anisotropic elastic moduli and the isotropic pore pressure parameters is meant to quantify the consequences

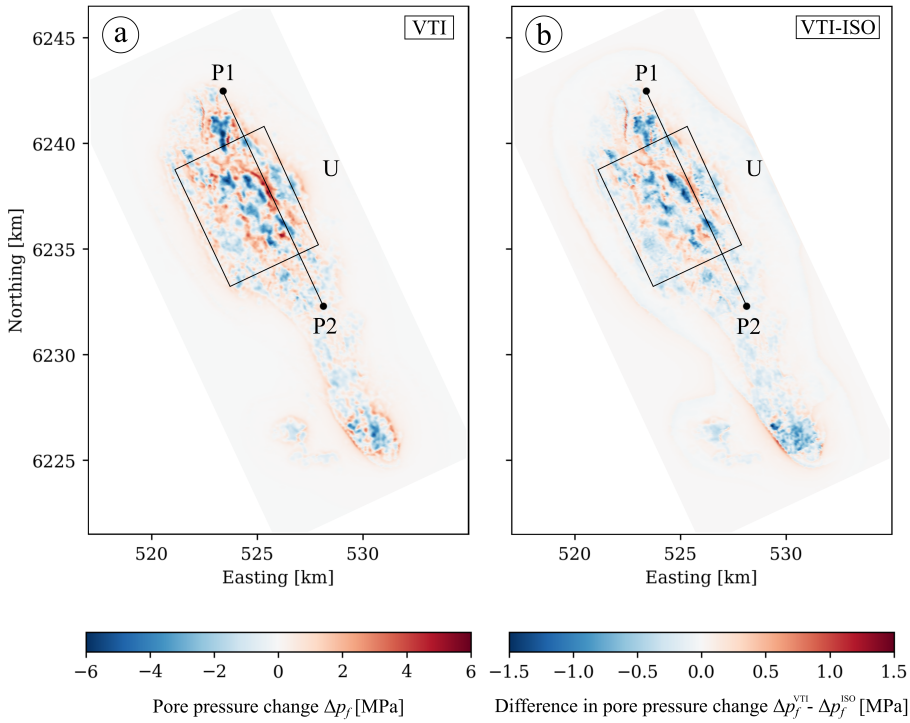


**Figure 3.8:** Top view of undrained pore pressure response predicted using transversely isotropic poroelastic tensor $\boldsymbol{B}$ in the layer directly above the reservoir (a), and the difference between pore-pressure predictions made using the anisotropic and isotropic tensors $\boldsymbol{B}$ (b). In both cases, stress changes were estimated with the use of transversely isotropic geomechanical model of the overburden. P1 and P2 mark the end points of the vertical cross-sections (Figure 3.9). Rectangle U marks the boundaries of a part of the model above the central part of the reservoir chosen for further analysis (Figure 3.10-Figure 3.14). The color scale range was limited in both plots to better visualize the dominating low-magnitude pore pressure changes and differences.

of neglecting the anisotropic character of the undrained pore pressure response. A fully isotropic case (i.e., isotropic geomechanical model and isotropic poroelastic pore pressure parameters) was not considered, because no up-to-date isotropic geomechanical model of the Valhall field was available.

The distribution of $\Delta p_f$ given by the anisotropic tensor in the layer directly above the reservoir (corresponding to the Lista formation) is shown in Figure 3.8a. The undrained pore pressure changes show a rather complex pattern above the central part of the reservoir (zone U, 522-528 km easting and 6234-6240 km northing) with amplitudes within this layer reaching -7.2 MPa in the negative and 6.2 MPa in the positive direction. For comparison, the minimum principal stress change ranged from -8.3 and 4.8 MPa, the intermediate from -6.0 to 6.0 MPa and the maximum

from -8.6 to 9.7 MPa in the same area.

The difference between the anisotropic and the isotropic pore pressure estimates is shown in Figure 3.8b. Above the central part of the reservoir (zone U), the maximum difference between the two solutions within this model layer is 2.0 MPa. As indicated by the similarity of the features in both plots in this figure, the directions of the pore pressure changes given by the anisotropic and isotropic solutions agree for most of the points on the surface. The undrained pore pressure response given by the anisotropic tensor has generally higher amplitudes, regardless of the polarity of the pore pressure changes.

To investigate the vertical extent of the undrained pore pressure response we interpolated the modelled pore pressure changes in individual layers of nodes onto the P1-P2 cross-section marked in Figure 3.8. This cross-section (Figure 3.9), passing through a zone of large pore pressure increase, shows that the pattern of pore pressure changes observed in the layer of nodes directly above the reservoir (Figure 3.8) does not change significantly with the distance from the reservoir. The magnitude of the undrained response given by the anisotropic poroelastic tensor decreases gradually with distance from the reservoir but remains larger than 1 MPa up to 340 m above its top surface (this maximum vertical extent of at least 1 MPa change is observed at $X = 5230$ m). The isotropic prediction gives a maximum vertical extent of at least 1 MPa pore pressure change of only 210 m above the reservoir.

The difference between the anisotropic and the isotropic predictions (Figure 3.9b) follows the same pattern of distribution as in the layer shown in Figure 3.8, mimicking the features observed in Figure 3.9a. The largest absolute differences are observed closest to the reservoir, where the stress changes were largest. To study the differences in more detail, we computed the relative difference profile for a vertical column at $X = 5230$ m, where the vertical extent of significant pore pressure changes (>1 MPa) was the largest. The relative difference between the two solutions initially increases vertically upwards, reaching its maximum of 48% at a depth of 2210 m, roughly 270 m above the reservoir. The relative difference remains above 40% for the next 360 m of the column. Despite these large percentage changes, the inclusion of the poroelastic anisotropy should not have much impact on pore pressure predictions in the part of the overburden further away the reservoir, as the corresponding absolute magnitude of the undrained pore pressure change given by both of the two predictions is small. In the case of isotropic geomechanical model of the overburden and isotropic poroelastic pore pressure parameters, the expected differences in predicted undrained pore pressure responses are significantly larger (Holt et al. 2022).

Next, we use Equation (3.27) to investigate the impact of the undrained pore pressure changes on the horizontal effective stress $\sigma'_{XX}$ in the zone U in the layer directly above the reservoir, as shown in Figure 3.10. Both normal horizontal stresses changes, $\Delta\sigma_{XX}$ oriented along easting direction and $\Delta\sigma_{YY}$ oriented along northing direction, have similar spatial distributions and amplitudes, and hence we

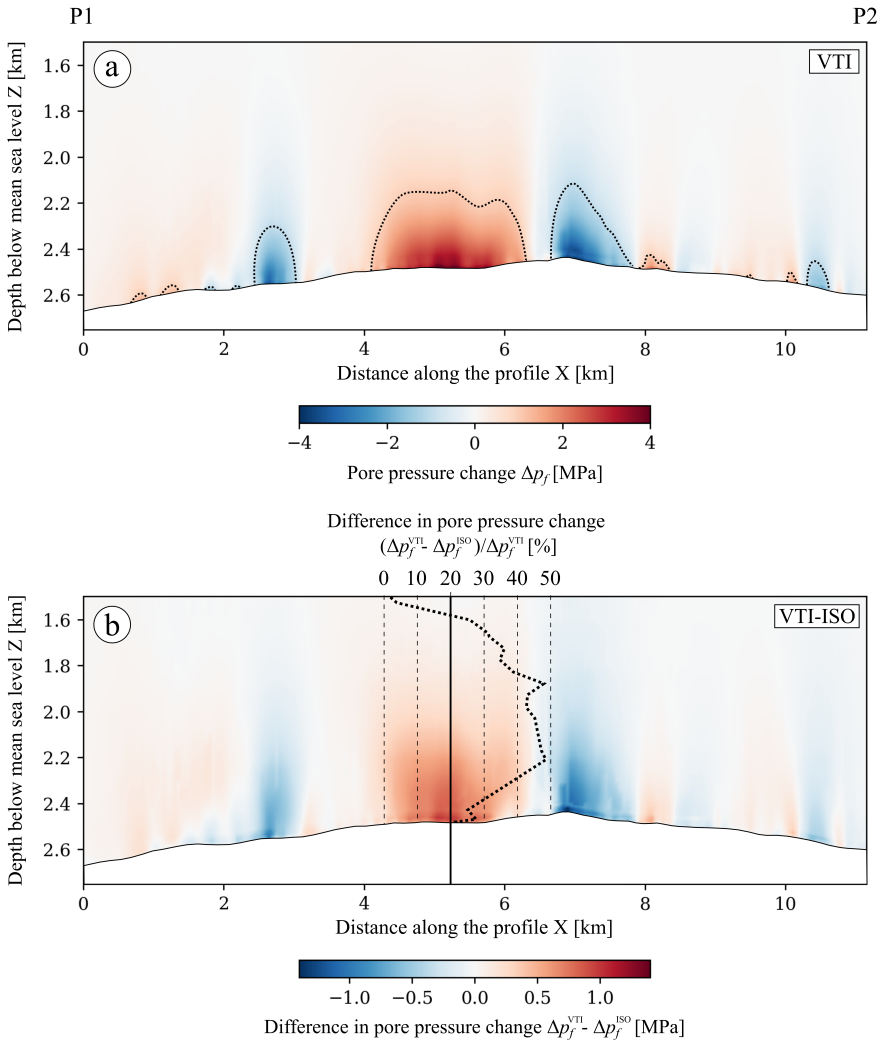


**Figure 3.9:** Cross-section between points P1 and P2 (Figure 3.8) through the modelled undrained pore pressure response predicted using the transversely isotropic poroelastic tensor $\boldsymbol{B}$ (a) and the difference between solutions given by the anisotropic tensor $\boldsymbol{B}$ and the isotropic parameter $B_S$ (b). Dotted lines in (a) delineate areas where the absolute values of the pore pressure changes predicted using the anisotropic tensor $\boldsymbol{B}$ are larger than 1 MPa. The dotted line in (b) illustrates the percentage difference between the two solutions computed along a vertical profile at $X = 5230$ m (thick solid line).

show only one of the two modelled stress change maps. The distribution pattern of total horizontal stress changes (Figure 3.10a) qualitatively reflects the distribution of the undrained pore pressure changes shown in Figure 3.8a. However, in some areas of the analyzed zone U the amplitude of the undrained pore pressure response is larger than the amplitude of the normal horizontal stress changes, causing a change of sign of the effective stress change. Hence, the distribution of the modelled effective stress changes does not resemble the distribution of changes of the two components of effective stress (total stress and pore pressure), both in terms of changes direction and magnitude.

This non-uniformity is expressed by displacement or disappearance of the features dominating the total horizontal stress change in the effective stress change map (Figure 3.10b), e.g., strong reduction of absolute value in the local minimum F1, change of sign in the eastern part of the total stress increase ridge F3 or change of sign and significant increase in change magnitude at F2. The extrema of the changes shift from – 5.76 and 6.50 MPa in the total horizontal stress $\sigma_{XX}$ to –2.75 and 5.26 MPa in the effective horizontal stress $\sigma'_{XX}$. In the case of the horizontal stress oriented along the northing direction, $\sigma_{YY}$, the extreme values change from -5.31 and 5.33 MPa to -2.15 and 4.02 MPa. The effective stresses estimated with the use of the isotropic poroelastic pore pressure parameters yield similar distribution of effective stress changes but with significantly lower amplitudes; these changes are between – 2.04 MPa and 3.31 MPa for $\Delta\sigma'^{ISO}_{XX}$ and between -1.50 MPa and 2.27 MPa for $\Delta\sigma'^{ISO}_{XX}$.

To further explore the impact from the symmetry class of the pore pressure parameters on the geomechanical modelling results, we estimated the minimum effective principal stress (oriented predominantly horizontally, used to determine Mohr's circles, as in Figure 3.2) using both isotropic and transversely isotropic poroelastic pore pressure parameters (Figure 3.11). Both isotropic and VTI symmetries generally yield similar patterns in minimum effective principal stress distribution (as expected from our analyses of Figure 3.8 and Figure 3.9). The average value of the predicted minimum effective principal stresses within zone U is 4.08 MPa for the anisotropic and 4.01 MPa for the isotropic solutions. Their standard deviations over zone U are 0.65 and 0.50 MPa, respectively. This is reflected by the more abrupt stress changes seen in Figure 3.11a. Moreover, changes in the amplitude relationships between some adjacent extrema are observed. One such change is seen when comparing two low effective stress valleys located between F4 and F5. There, the effective stress in the western minimum decreases and the amplitude of the eastern minimum increases when moving from the anisotropic to the isotropic pore pressure response.

The comparison of the total and the effective vertical stress changes does not reveal such significant differences between the two stress distributions and amplitudes as in the case of the horizontal stresses. To extend our analysis to the entire examined volume, we show the comparison of total stress changes and pore pressure changes in the corresponding nodes of the model in Figure 3.12. The distributions of the clouds of points (over 113 000 points each) were approximated with the use

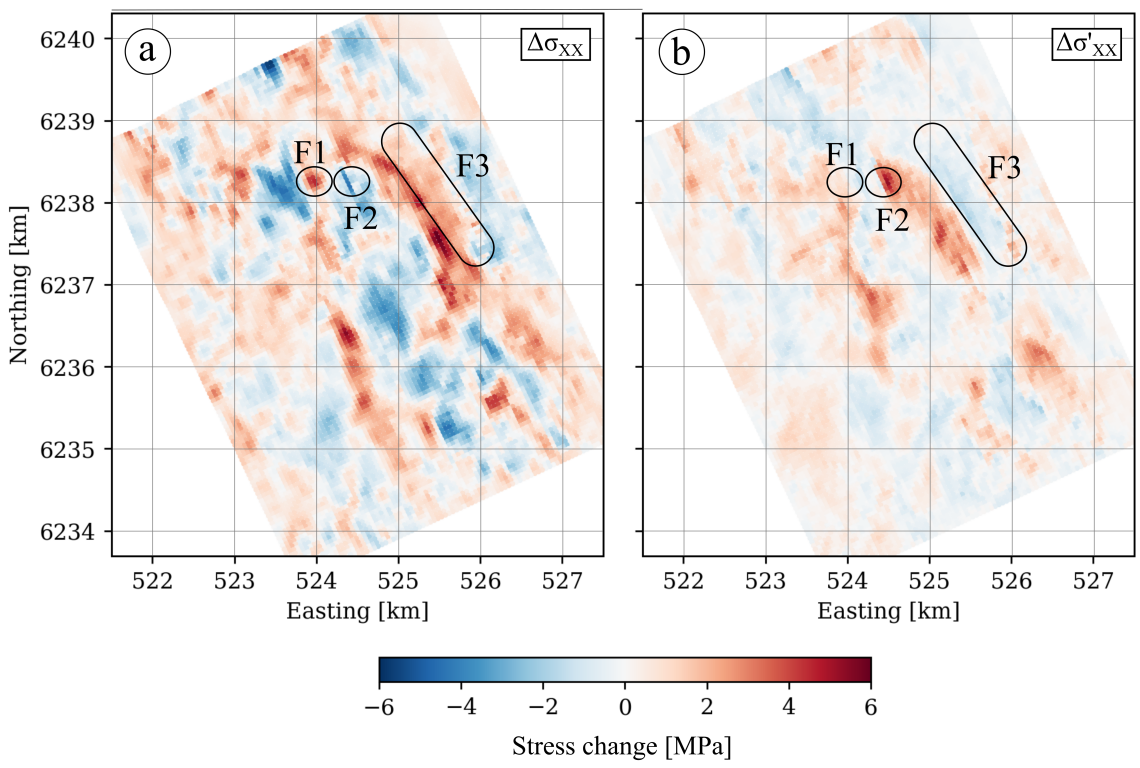


**Figure 3.10:** Map of the horizontal (parallel to easting direction) stress change distribution within zone U. The maps display total (a) and effective (b) stress changes between years 1982 and 2020 in the layer directly above the reservoir. The horizontal effective stress was computed using pore pressure changes given by using the transversely isotropic poroelastic tensor (VTI). The color scale range was limited to better visualize the effective stress changes (b) of relatively lower amplitudes in comparison to the total stress changes (a). The polygons F1, F2, and F3 indicate examples of zones with significant differences between maps (a) and (b).

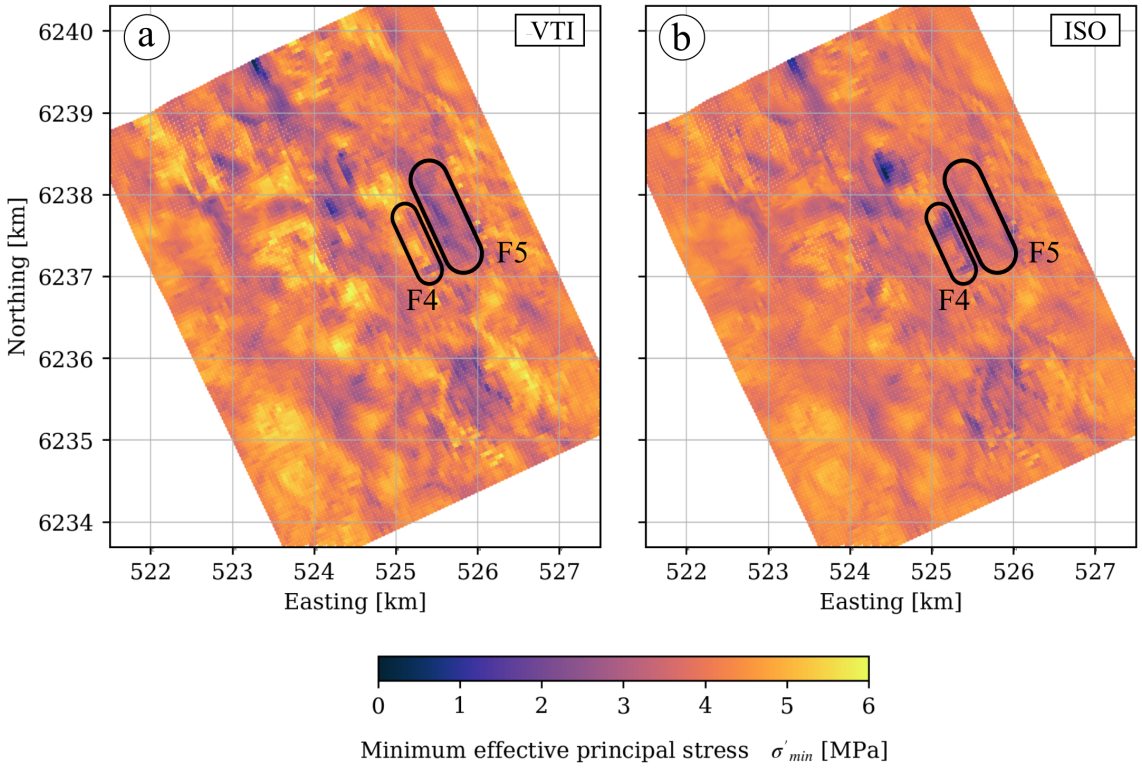


**Figure 3.11:** Map of the minimum effective principal stress distribution within zone U. The maps display stresses in year 2020 in the layer directly above the reservoir computed using pore pressure values from year 1982 updated with changes given by using the transversely isotropic poroelastic tensor $\boldsymbol{B}$ (a) and the corresponding isotropic tensor (b). The polygons F4 and F5 indicate examples of zones with significant differences between maps (a) and (b).

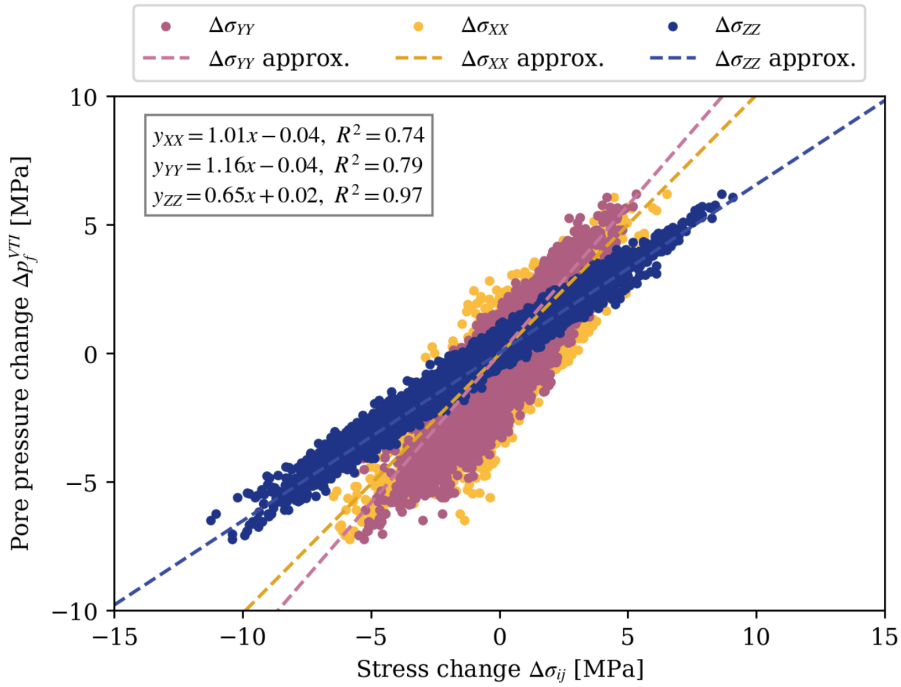


**Figure 3.12:** Comparison of the normal stress changes (defined along the geographical easting direction) and the undrained pore pressure response (estimated with the use of transversely isotropic VTI poroelastic parameters) in corresponding nodes of the model. The box contains equations for the linear trend lines and their linear regression coefficients $R^2$.

of linear trend lines and the quality of the fits was assessed with the regression parameter $R^2$ (i.e., coefficient of determination, here describing the proportion of the variance of $\Delta p_f$ explained by the variance of corresponding $\Delta\sigma_{ij}$).

In all three cases, the intercept of the linear trend lines is very small (as expected from Equation (3.23)), and therefore can be treated as negligible. In the case of the vertical total stress changes, the slope of the $\Delta\sigma_{ij}$ - $\Delta p_f$ trend line is 0.65 – the inverse of this value is 1.53, approximately equal to $B_{33}$ (= 1.51). No such relationships are observed for horizontal stress changes and the other pore pressure parameters. At the same time, the parameter $R^2$ for the trend line relating the total vertical stress changes with the values of the undrained pore pressure response is 0.97, suggesting clear linear correlation between the two variables. In the cases of the horizontal stress changes $\Delta\sigma_{XX}$ and $\Delta\sigma_{YY}$, the value of the parameter $R^2$ is 0.74 and 0.79, respectively. In the case of the pore pressure changes estimated with the use of the isotropic poroelastic pore pressure parameters, the parameter $R^2$ is between 0.85 and 0.90 for all three considered normal stress changes. No

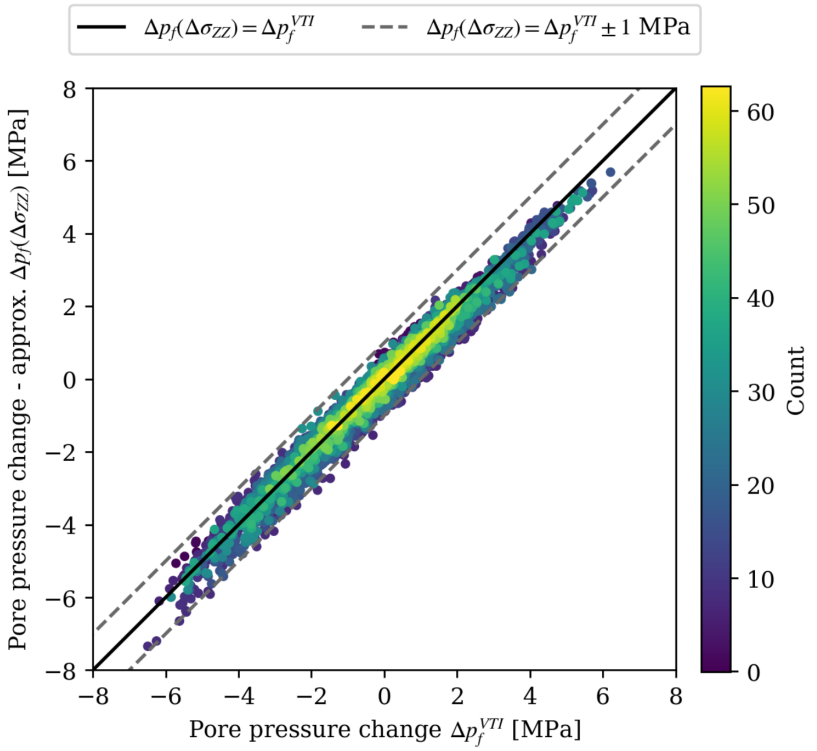


**Figure 3.13:** Comparison of the undrained pore pressure response estimated with the use of transversely isotropic (VTI) poroelastic parameters with the undrained pore pressure response approximated with equation (31) in the zone U in the layer directly above the reservoir. The dimension of bins used to count the points was 0.1 by 0.1 MPa. Dashed lines contour area within which the difference between the modelled and the approximated values of the undrained pore pressure changes is smaller than 1 MPa.

direct relationships between the estimated value of the slope parameter and the values of the pore pressure parameters is observed in the isotropic case.

Encouraged by the high value of the $R^2$ factor for $\Delta\sigma_{ZZ}$ we approximated and showed (Figure 3.13) the undrained pore pressure changes with the total vertical stress changes and its corresponding slope value,

$$\Delta p_f = \frac{1}{B_{33}}\Delta\sigma_{ZZ} \approx 0.66\Delta\sigma_{ZZ}. \tag{3.31}$$

We compared these predictions with the response computed with the use of the anisotropic poroelastic pore pressure parameters (Equation (3.22)) in the entire model and in the zone U in the layer directly above the reservoir where the pore

pressure changes are expected to be largest. We supplemented the scatter plot with the number of points falling within a bin of 0.1 by 0.1 MPa expressed by the color of the individual points, which revealed high density of points directly on and in the direct proximity of the $\Delta p_f(\Delta\sigma_{ZZ}) = \Delta p_f^{VTI}$ line.

To assess the quality of the pore pressure change approximation quantitatively, we computed the difference between the two models, i.e. $\Delta p_f^{VTI}$ - $\Delta p_f(\Delta\sigma_{ZZ})$. Standard deviations of prediction differences in the entire model and in the zone U in the layer directly above the reservoir are 0.11 and 0.25 MPa, respectively. This means that approximately 68.2 % of the pore pressure change differences have magnitudes lower than these values. Standard deviations of prediction differences between isotropic and anisotropic pore pressure estimates, i.e. $\Delta p_f^{VTI}$ - $\Delta p_f^{ISO}$, in the same data volumes are 0.14 and 0.33 MPa, respectively.

To complement the analysis of the effective stresses, we projected the reported casing deformation locations onto the maps of pore pressure changes (Figure 3.14a) and total vertical stress (Figure 3.14b) in the zone U. We consider projecting to be a valid mean to visualize the locations of the casing deformation incidents, as both the undrained pore pressure response and stress change distributions are not varying much vertically within the relevant interval (as shown for the pore pressure response in Figure 3.9). Moreover, we cross-plot the horizontal and vertical effective stress changes at known casing deformation locations, and to add some context and to present general data trends we supplement them with estimated values of these parameters in the entire zone U (Figure 3.14c). To explore the relationship between the location, the stress and pressure changes and casing deformation depths, the casing collapse points were colored according to their vertical distance to the top of the reservoir. Combined analysis of the predicted pore pressure changes (Figure 3.14a) and the total vertical stress (Figure 3.14b) distributions indicates that a substantial number of the reported casing deformations were located in places characterized with rapid lateral changes of both parameters.

The first analyzed cluster of points is situated directly above the central part of the reservoir (points 8, 9, 10, 12 and 19). Although located relatively close to each other, these casing deformation points are not grouped together in the effective stress changes cross-plot (Fig. 14c) – they are distributed roughly along a line connecting points 10 and 19 in the order resembling their geographical distribution. This alignment is not reproduced in corresponding cross-plots obtained with isotropic pore pressure parameters, nor obtained with total stresses changes.

Points in the next group, located above the north-eastern flank of the reservoir (2, 15, 17, 20 and 21) follow transition lines between zones of positive and negative pore pressure changes (which reflect well changes in the total vertical stress changes, as discussed before). This group is not aligned in the effective stress cross-plot; however, these points seem to be on average located further away from the reservoir (average height above the reservoir surface of 280 m) than the rest of the analyzed points (99 m). Points grouped above the south-western flank of the reservoir (1, 3, 5, 7 and 11) form a rather loose cluster with positive values of the

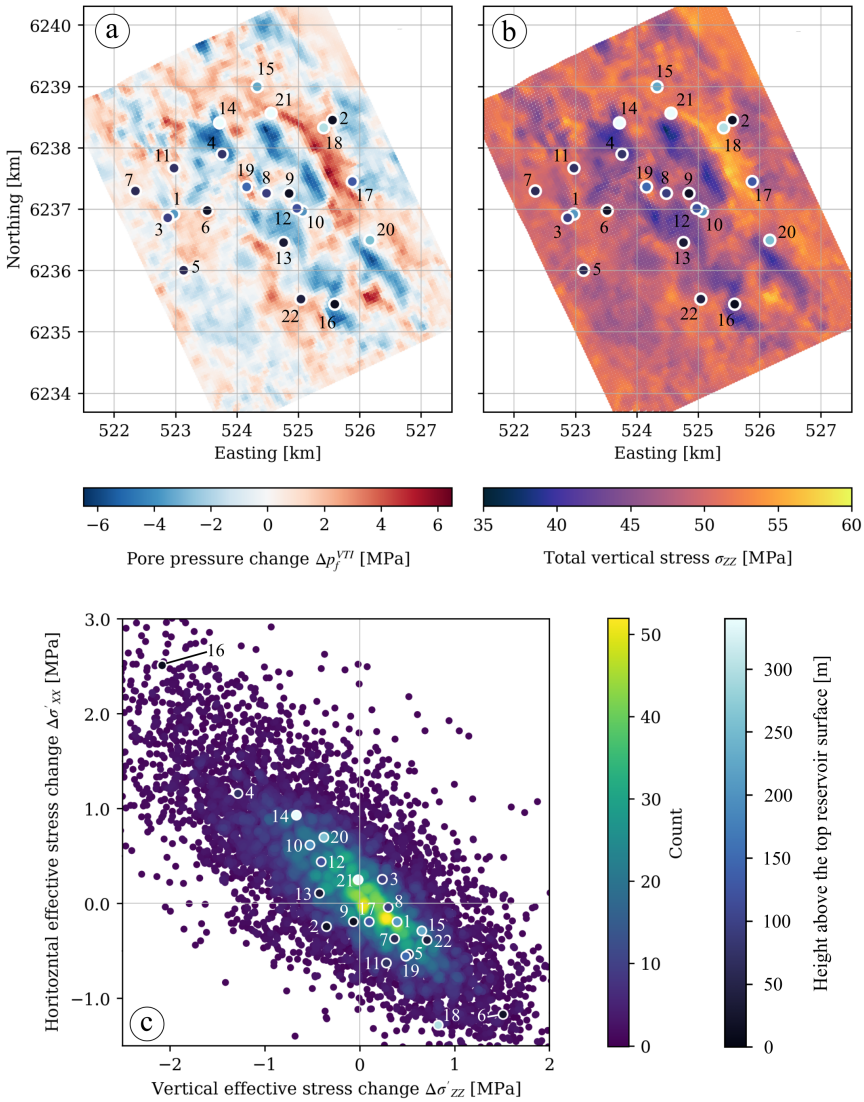


**Figure 3.14:** Map of the undrained pore pressure response computed with the use of anisotropic poroelastic parameters (a) and total vertical stress distribution within zone U in year 2020 (b), supplemented with cross-plot of horizontal and vertical effective stress changes in the same area in the layer directly above the reservoir (c). Both the maps and the cross-plot were overlaid with points marking the location of vertical projections (a, b) and the values of corresponding parameters at the location (c) of known casing deformations. The filling color of the casing failure points (a, b and c) indicates the height above the top reservoir surface at which casing deformation was registered and it was clipped to 340 m, although point 21 is located 753 m above the reservoir surface. The size of bins used to count the points in (c) was 0.1 by 0.1 MPa.

vertical and negative values of horizontal effective stress changes (except for point 3). Points 6 and 18, although spatially belonging to the clusters above the flanks of the reservoir, are characterized with higher predicted magnitude of vertical effective stress and pore pressure changes, as well as with larger decreases in the horizontal effective stress.

Points 4, 14 and 16 located above the edges of the central part of the dome along the NNW-SSE reservoir axis, while characterized with relatively large drops in pore pressure and low values of total vertical stress, form a group with anomalously high values of horizontal effective stress increment and vertical effective stress decrease in the effective stress cross-plot. Points 13 and 22, although located roughly along the same axis, do not show such extreme effective stress changes.

## 3.5 Discussion

The results of the undrained experiment we carried out on the Lista overburden shale (Figure 3.3) indicate a very consistent behavior of the rock within its elastic deformation range in assumed in-situ stress and pore pressure conditions and yielded $B_{11} = 0.53$ and $B_{33} = 1.51$, or alternatively $B_S = 0.86$ and $A_S = A_{3-1}(\beta = 0) = 0.59$.

Experimental results reported by Holt et al. (2018b), Holt et al. (2018a), Duda et al. (2021) and Soldal et al. (2021) confirm the anisotropic angle-dependent character of the undrained pore pressure response and the transverse isotropy of various shales. Encouraged by these results, we took a next step towards better description of the anisotropic pore pressure changes and extended Equation (3.1)-Equation (3.3), which are limited to isotropic horizontal stress changes, to obtain Equation (3.22) which includes the entire stress tensor needed in a field modelling scenario. We also defined an additional Skempton-like pore pressure parameter $A_{2-1}$, Equation (3.26), capturing the impact of the intermediate principal stress. In our test we measured $A_{2-1}(\alpha = 0, \beta = 0) = 0.21$ (Figure 3.5), which confirmed the observations in the aforementioned literature indicating that for shales the pore pressure parameters expressing the influence of shear stress changes within the elastic deformation range generally differ significantly from 1/3, the value expected under the assumption of linear elastic isotropy of the material (Skempton 1954).

An apparent limitation of our experimental study arises from using a triaxial apparatus with isotropic horizontal stresses and horizontal stress changes, contrary to a true-triaxial setup where the effect of changing the principal stresses individually may be investigated. Application of anisotropic horizontal stresses may have revealed lower symmetries of the medium. However, from the point of view of the anisotropic poroelasticity (Cheng 1997; Thompson and Willis 1991), a single undrained triaxial experiment suffices to fully describe pore pressure changes in a transversely isotropic material characterized by a single symmetry plane and a

symmetry axis oriented along $\sigma_{AX}$. Moreover, in the case of both historical and current stresses modelled in the Valhall overburden, the horizontal stresses are statistically nearly identical (analysis of all model nodes in the overburden yields mean value of the ratio between $\sigma_{XX}$ and $\sigma_{YY}$ of 1.0 and standard deviations of $\sigma_{XX}$ and $\sigma_{YY}$ of 0.010 and 0.009, respectively), as reported by e.g. Kristiansen (1998). Hence, the modelled settings are expected to be equivalent to the experimental conditions. Intermediate stress estimates are usually burdened with large uncertainties, as the determination of the maximum horizontal stress under field conditions still remains a challenge (e.g., Fjær et al. 2021; Zoback 2007), and therefore the potentially small differences between the horizontal true-triaxial in-situ stresses, even if achieved, would still be uncertain and probably of smaller importance.

Secondly, the somewhat subjective duration of the assumed post-unloading stabilization period (1000 s) can be also questioned. Although apparently random, it was an observation-based compromise between giving the system enough time for pressure equilibration (the gradient of the pore pressure changes decreases significantly within this interval) and not allowing the time-delayed deformation (e.g. creep) of the shale to impact the measurement results. A nearly perfectly linear behavior is observed in the $\Delta p_f/\Delta\sigma_{33}$ - $\kappa$ plot (Figure 3.4), as predicted from anisotropic poroelasticity in Equation (3.30). Supported by a negligible onset of permanent deformation after each of the unloading-reloading cycles (Figure 3.3), it indicates excellent measurement precision and an only marginal impact of changes in the values of the poroelastic pore pressure parameters due to non-elastic effects (Duda et al. 2021) on the pore pressure changes within the chosen stress range and stabilization interval.

The assumption about the large-scale undrained behavior of the overburden shales can be addressed through classical consolidation theory. As outlined by Biot (1941), if the integrity of the cap rock is not compromised, the sealing ability should maintain the undrained pore pressure response on a time-scale given by consolidation. One can estimate the time to reach pore pressure equilibrium with the surroundings given by diffusive behavior using a simplified description presented by Fjær et al. (2021):

$$t_D \approx \frac{l_D^2}{C_D}. \tag{3.32}$$

where $l_D$ is a characteristic diffusion length and $C_D$ is a diffusion coefficient controlled primarily by permeability, but also by porosity, and rock and pore fluid stiffnesses. In Valhall, the reservoir prior to production was highly over-pressurized (Pattillo et al. 1998) and the overburden pore pressure remains abnormally high for around 2000 m above the reservoir (Fjær et al. 2021). The geological age of the reservoir is around 20 million years (Kristiansen and Sandberg 2018), which means that in-situ effective $C_D$ of the overburden must have been 0.2 m2/year or lower. If we assume that this estimate of the diffusion coefficient is representative

for the direct overburden of the reservoir now, the approximate time to equilibrate the pore pressure 10 m above the reservoir given by Equation (3.32) is 500 years. The diffusion coefficient based on laboratory data is about 10 times larger (permeability was estimated to be of around 5 nanoDarcy), which reduces the consolidation time to approximately 40 years. However, if we further assume that this value of diffusion coefficient is representative for the first 100 m of the cap rock above the reservoir, the equilibration at that distance would be 4000 years. All these estimates are uncertain, but since the stress altered volume stretches hundreds of meters above the reservoir, the assumption of undrained overburden response in the course of reservoir lifetime appears realistic. Fluid flow between the reservoir and the cap rock may still occur along faults or fractures activated or opened in the result of changes in reservoir pore pressure (depletion or injection), but in low-permeability formations it would be spatially limited to these features and their proximity.

In the numerical part of our study, we combined the pore pressure parameters given by the laboratory experiments with the results of finite element stress modelling of the Valhall field and estimated the undrained pore pressure response in the entire overburden. The resultant pore pressure changes directly above the central part of the reservoir (Figure 3.8a, zone U) were of several MPa in magnitude, reaching absolute amplitudes as high as 7.2 MPa. The modelled pore pressure development remained significant for several hundred meters above the reservoir top surface, exceeding 1 MPa as far as 340 m above the chalk reservoir-overburden shale interface (Figure 3.9). Moreover, the impact of the undrained pore pressure response on the effective stress values is far from negligible — in Figure 3.10 we show that effective horizontal stress changes differ from total horizontal stress changes not only in magnitude, but also in the direction of changes and their distribution. Considering the large rock volume experiencing substantial pore pressure alteration , the commonly near-failure stress conditions in the upper crust (Townend and Zoback 2000), and the unquestionable presence of pre-existing faults and fractures in the subsurface around the reservoir, we conclude that the undrained pore pressure response should be accounted for in the assessment of the stability of the reservoir's surroundings, during production and injection operations. In our opinion, the magnitude and range of the modelled undrained pore pressure changes and their resultant impact on the effective stresses (directly in shales and also indirectly in layers around them) make them a good candidate to explain some of the instabilities and microseismic events reported at considerable distances from injection locations (e.g., Rutqvist 2012; Vasco et al. 2018; Verdon et al. 2011; Williams-Stroud et al. 2020) and references therein), as well as events recorded at depths of 2300-2350 m, i.e. above the reservoir, during a short passive monitoring campaign at Valhall in 1998 (Dyer et al. 1999; Kristiansen et al. 2000; Zoback and Zinke 2002). Until now, these have been explained mainly as caused either by fluid migration through systems of discontinuities and cracks or by injection-induced stress transfer.

To explore the consequences of disregarding the anisotropic character of the pore

pressure changes, we compared the modelling results we obtained with anisotropic parameters and with their isotropic counterparts, estimated only from the isotropic unloading-loading undrained experimental cycle (i.e., $\kappa = 1$, yielding $B_S = 0.86$ and $A_S = 1/3$). The comparisons, shown in Figure 3.8b and Figure 3.9b, indicate that for the two solutions the general large-scale trends are somehow similar and that the anisotropic pore pressure response tends to have higher absolute amplitudes. In consequence, the undrained pore pressure changes predicted with the anisotropic pore pressure parameters not only have larger relative impact on the value of effective stresses, but also may potentially exert non-negligible influence on the subsurface at distances larger than initially expected. The differences between the isotropic and anisotropic solutions transferred to the effective stress analysis (Figure 3.11) are also expressed in terms of the larger standard deviation (quantifying the deviance of the observed values given by a model from their global mean value.) of the effective stresses changes given by the anisotropic solution. In the case of the minimum principal stress changes $\Delta\sigma'_{min}$ in the zone U, standard deviation increases from 0.50 MPa for the isotropic approach to 0.65 MPa when the anisotropic character of shales is accounted for. These standard deviations describe large populations of points, however our interest lies predominantly in the points characterized with the largest pressure changes, where differences between the isotropic and anisotropic results are significantly larger. Changes in amplitude between neighboring local extrema of effective stress are also observed when going from isotropic to anisotropic estimates. This indicates that the zones with the lowest effective stresses in anisotropic overburden (i.e., potentially closest to caprock failure or to fault reactivation) may not be identified if poroelastic anisotropy is not accounted for.

In the direct proximity of the reservoir, effective stresses are relatively low (in the zone U the average predicted minimum effective principal stress is just above 4 MPa, Figure 3.11) and quantitatively comparable with effective stress changes (Figure 3.10b). This emphasizes that even small differences in the undrained pore pressure response prediction, let alone differences in the predicted direction of pore pressure change, may have significant implications for overburden stability and integrity assessment (as shown in Figure 3.2) and drilling operations design (due to a narrowing mud window). The consequences of the anisotropic undrained pore pressure changes for the borehole wall stability were recently theoretically explored by Raaen et al. (2019) and successfully identified in field observations by Asaka and Holt (2021).

Higher amplitude of the pore pressure changes predicted with the anisotropic pore pressure parameters suggests a relatively large impact of $B_{33}$, the parameter capturing the properties of the medium along its symmetry axis, which is significantly higher than the isotropic parameter $B_S$. Moreover, statistical analysis of principal stress directions in zone U in the areas with pore pressure increase shows that the maximum principal stress in these nodes is predominantly vertical, even after depletion. In the modelling results corresponding to year 2020, the vertical component of the direction unit vector of the maximum principal stress ($s_{i3}$) is larger

than 0.95 in 91 % of such points. This is true only for 58% of points in the areas with negative pore pressure changes, indicating a less vertical orientation of the maximum principal stress in these zones. It also signals the impact of stress field orientation and the poroelastic anisotropy of shales on the direction and magnitude of the undrained pore pressure response.

This makes it impossible to simply correct the pore pressure changes obtained with the isotropic pore pressure parameters to make them fit the anisotropic predictions. For example, the use of a scalar scaling factor (i.e., multiplication of Skempton's $B_S$ or of the isotropic pore pressure change predictions by a constant) could locally adjust the amplitude but would not affect the distribution of zones with pore pressure increase or decrease, as this operation takes no account for the causes of differences in behavior between the isotropic and anisotropic media in non-hydrostatic stress conditions.

On the other hand, the observed correlation between the vertical stress changes and the undrained pore pressure changes estimated with the use of the anisotropic poroelastic pore pressure parameters (shown in Figure 3.12) emerges from both geometry and properties of the modelled medium and the amplitude and direction of the on-going stress changes. First, as already mentioned before, the deviation of the bedding normal from the vertical direction is small in a substantial part of the model. Second, the value of the poroelastic parameter $B_{33}$ expressing the impact of the stress changes along the direction normal to the bedding (along symmetry axis) in Lista shale is significantly larger than the value of $B_{11}$ expressing the impact of the stress changes along the bedding (in symmetry plane). It is worth noting that the ratio of these two parameters is mostly a function of elastic stiffness anisotropy, as described more in detail in Section 3.8. Finally, the total vertical stress changes are generally larger in comparison to horizontal stress changes.

This combination of factors allows us to approximate the distribution of the undrained pore pressure changes in transversely isotropic shales with the use of the total vertical stress changes $\Delta\sigma_{ZZ}$ and parameter $B_{33}$ only. While requiring less input information than the isotropic undrained pore pressure response model, this approximation yields pore pressure changes closer to the most physically accurate transversely anisotropic model. Moreover, it does not require information on the geometry of the model and hence is significantly less complicated and time-consuming than modelling of the undrained pore pressure changes with the use of the poroelastic $\boldsymbol{B}$ and stress $\boldsymbol{\sigma}$ tensors and rotation angles $\alpha$ and $\beta$. This may have practical implications not only for geomechanical modelling, but also for experimental practices, as these results indicate that in the case of time-limited undrained tests carried out on overburden shales it may be beneficial to substitute a rather standard hydrostatic cycle (the so-called "Skempton test") with an undrained uniaxial stress cycle providing information on $B_{33}$. However, we consider measuring directly both Skempton's $B_S$ (in an hydrostatic cycle) and $B_{33}$ (in an uniaxial cycle) to be the best option, as it makes it possible to estimate the entire poroelastic tensor $\boldsymbol{B}$ (Equation (3.2)).

Nevertheless, one should have in mind that although apparently successful above the central part of Valhall reservoir, this approximation may produce larger errors for reservoirs with less dominant vertical stress changes and more complex geometries. For other overburden shales, less pronounced dominance of the poroelastic parameters $B_{33}$ over its in-plane counterpart $B_{11}$ may also play a role in decreasing the quality of approximation. However, the comparison of Lista shale with other overburden shales described by Holt et al. (2017), Holt et al. (2018b), Holt et al. (2018a), Lozovyi and Bauer (2018), Soldal et al. (2021) and Duda et al. (2022) suggests that Lista's poroelastic parameters lie within a range typical for relatively soft caprock shales (in terms of static moduli and strength). In the case of Lista shale, parameter $B_{11} = 0.53$, parameter $B_{33} = 1.51$ and the ratio between them $B_{11}/B_{33} = 0.35$. In the case of the other five considered shales, the mean values of the poroelastic pore pressure parameters are: $B_{11} = 0.52$, $B_{33} = 1.37$, $B_{11}/B_{33} = 0.38$, and their corresponding standard deviations are 0.10, 0.18 and 0.09, respectively.

The main uncertainties in our approach result from the assumption that the properties of the Lista shale are representative for the entire overburden of the reservoir. Although the values of the pore pressure parameters seem to be close to the values experimentally measured in other North Sea overburden shales, the modelling results do not include any effects that would be caused by the natural variation of these parameters and the potential presence of inter-bedded permeable formations exhibiting drained behavior. Nor at this stage do we consider the impact of plastic deformation (reported by Duda et al. 2021). In this modeling scenario, we register stress changes larger than the 3 MPa that we applied in the laboratory. We might therefore expect a larger influence of non-elastic effects on the pore pressure evolution than we observed experimentally. We also neglect the influence of the gas cloud, which is apparent in the seismic data, above the Valhall reservoir (e.g., Lewis et al. 2003; Whaley 2009), which could significantly affect the mechanical properties of the overburden and its poroelastic pore pressure parameters sensitive to fluid properties, i.e. $\bar{B}$ (parameters $A_{3-1}$ and $A_{2-1}$ are measures of anisotropy of the medium and do not depend on fluid properties, as can be concluded from Equation (3.24)-Equation (3.26), Section 3.8 and Cheng (1997)). However, including these factors in the analysis would require very detailed information on the overburden rocks such as local relative saturations and deformation modes (elastic or plastic), that is not available for our case, nor in most other field cases.

To extend our analysis to the impact of the stress and pore pressure changes on casing integrity in boreholes located above and around a depleting reservoir, we need to define the most probable scenarios responsible for casing deformations. In the first scenario, casing collapses due to large pressure contrast between the inside of the casing and pore pressure in the surrounding formation. Although this scenario fits best into our analysis (as we focus on pore pressure changes in the overburden), such situations are expected to be extremely rare. Other scenarios assume that casing shear deformation is the result of slip on bedding planes, lithological interfaces or fault planes (Bruno 2002; Dusseault et al. 2001; Ewy 2021),

which in shales would not necessarily cause seismic events. Displacement along such surfaces may take place when shear stress along the slip surface increases or effective stress normal to the slip plane drops (or the combination of the two).

The distribution of the shear stresses in the reservoir overburden is difficult to predict accurately due to strong influence of local discontinuities and heterogeneities. However, it can be approximated using maps of vertical total stress, where the zones characterized with rapid lateral variability caused by reservoir compaction are expected to have the largest shear stress values. Modelling results presented in Figure 3.14b indicate that most of the 22 registered cases of casing deformation were located in the zones with large lateral gradients of total vertical stresses where bending and flexing of casing become probable (Ewy 2021). To facilitate the shear slip along the plane, the effective stress normal to the slip surface should be low. In the case of slipping on bedding planes or lithological interface, this normal stress can be approximated by vertical effective stress (under assumption of nearly-horizontal orientation of these surfaces). In the case of slipping on fault surface, the normal effective stress depends strongly on the orientation of the fault plane, but generally it can be approximated with horizontal effective stresses. In both cases, an increase of pore pressure would push the subsurface closer towards shear slip (Figure 3.2). This becomes particularly important if pore pressure changes are of amplitude similar or larger than total stress changes. This is observed in Valhall overburden for the undrained pore pressure response predicted with the anisotropic pore pressure parameters, which in general yielded larger amplitudes of pore pressure changes than their isotropic counterparts (Figure 3.12). This observation suggests that some of the casing deformations incidences assumed to be facilitated by the presence of permeable fractures, could be explained by pore pressure change caused by stress state alteration in low permeability shales.

We used the undrained pore pressure response estimated with the use of anisotropic poroelastic pore pressure parameters to evaluate changes in the effective stresses (Figure 3.14c) with the intent to identify casing deformation mechanisms promoted by such changes at known casing deformation locations. In the light of the previous paragraph, we may point two pairs of registered casing deformations at which locations the modelled effective stresses changes could facilitate shear slip. In the case of points 4 and 16, relatively large decrease of the vertical effective stress could create conditions favorable for the slip along bedding planes or geological interfaces. The second pair consists of points 6 and 18, located on the opposite end of the effective stress cross-plot shown in Figure 3.14c. These two points are characterized with relatively large increase of the vertical and relatively large decrease of the horizontal effective stress, which combined promote shear slip along near vertically oriented fault or fractures. It is worth noting that if no pore pressure changes are assumed, both total stresses gain in value at the casing deformation locations. Nevertheless, without more detailed observations from the inside of the analyzed boreholes and information on the location and orientation of discontinuities, we can only indicate promoted mechanisms, but not determine them unequivocally.

An additional observation which may indicate that the predictions of stresses and

resultant pore pressure changes recreate actual trends in the overburden is the correlation between spatial distribution of the points located above the central part of the reservoir (8, 9, 10, 12 and 19) and their distribution in the effective stress cross-plot (Figure 3.14c). This correlation between the plots indicates gradual transition from one stress change regime to another along NNW-SSE reservoir axis.

## 3.6 Conclusions

Estimation of effective stresses is imperative for assessing the stability of reservoir overburdens and the integrity of boreholes, as even small perturbations in the near-failure or stress-concentration regions may lead to fault activation or rock failure. One of the key factors influencing the effective stress is pore pressure, which in low-permeability media, such as shales, changes in an undrained response to modification of the stress state. This undrained pore pressure response seems to be neglected in many studies, probably guided by an intuition that there will be negligible pore pressure response associated with fluid flow in the low-permeability shale over the lifetime of a reservoir. In this paper, we propose an expression for the undrained pore pressure change which takes into account the impact of the anisotropic properties of a medium, all stress tensor elements, and the misalignment of the stress tensor frame with the frame of the medium. Although overcoming most of the shortcomings of commonly used stress-based expressions, it does not include the impact of plastic deformation on the undrained pore pressure response.

A triaxial loading apparatus allowed us to estimate the anisotropic poroelastic pore pressure parameters of an overburden shale extracted from the Lista formation directly above the chalk reservoir in the Valhall field. The experimental results indicate that the values of the pore pressure parameters in Lista shale are generally far from those expected in an isotropic medium, supporting the expected anisotropic (transversely isotropic) nature of this material.

We combined our estimates of the pore pressure parameters with the geometry of the subsurface and the results of finite element stress field evolution modelling in the Valhall reservoir overburden to compare the undrained pore pressure responses given by the anisotropic and isotropic pore pressure parameters. The undrained pore pressure response given by the anisotropic tensor has generally higher absolute amplitudes, with the largest discrepancies observed in the areas with the largest pore pressure changes. The comparison reveals differences, not only in the magnitude but also in the spatial distribution of the pore pressure and effective stress changes in both horizontal and vertical directions, highlighting the importance of accounting for poroelastic anisotropy in overburden shale behavior modelling.

Experimental observations and correlations observed in the modelled data allowed

us to formulate a method to accurately approximate the undrained pore pressure response in anisotropic overburden shales using merely estimated vertical stress changes and a single parameter describing rock poroelastic properties along its symmetry axis.

Finally, the joint analysis of the locations of known casing deformation incidents and modelled total and effective stresses indicates correlation between casing failures and areas with rapid lateral changes of total vertical stress. At the analyzed casing deformation locations, the predicted undrained pore pressure changes have magnitudes comparable to the total stress changes. Moreover, we observed correlation between the spatial distribution of such casing failures and their locations in the modelled effective stress cross-plots which may indicate that we recreated an actual transition between stress change regimes. This makes us believe that the undrained pore response modelling could become a useful tool for casing collapse risk analysis and mitigation.

## 3.7 Acknowledgements

First of all, we would like to thank AkerBP for access to their data and for their support, with special thanks to Tron Golder Kristiansen and Andreas Bauer. Our sincere thanks go to Andrew Carter for all the corrections, suggestions, comments, and insightful questions. We would also like to thank both Reviewers for their exceptional effort to help us improve this paper. This publication has been produced with support from the NCCS Centre, performed under the Norwegian research program *Centres for Environment-friendly Energy Research* (FME). The authors acknowledge the following partners for their contributions in the project: Aker Solutions, ANSALDO Energia, CoorsTek Membrane Sciences, Electromagnetic Geoservices (EMGS), Equinor, Gassco, KROHNE, Larvik Shipping, Lundin, Norcem, Norwegian Oil and Gas, Quad Geometrics, TOTAL, Vår Energi, and the Research Council of Norway (257579/E20). We would also like to thank the Research Council of Norway through the PETROMAKS 2 programme (Grant 294369), AkerBP, Equinor, Shell, and Vår Energi in the project *Improved prediction of stress and pore-pressure changes in the overburden for infill drilling.*

## 3.8 Appendix A

Using the framework given by Cheng (1997), the poroelastic pore pressure parameters can be defined as:

$$B_{11} = \frac{3M \cdot (C_{33}\alpha_{11} - C_{13}\alpha_{33})}{2C_{33}\,(C_{11} - C_{66}) - 2C_{13}^2}, \tag{3.33}$$

$$B_{33} = \frac{3M\,(2\,[C_{11} - C_{66}]\,\alpha_{33} - 2C_{13}\alpha_{11})}{2C_{33}\,(C_{11} - C_{66}) - 2{C_{13}}^2}. \tag{3.34}$$

Where $\alpha_{11}$ and $\alpha_{33}$ are anisotropic Biot's parameters, different from the effective stress parameter assumed to be equal 1 in Equation (3.27) (as we consider effective stresses mostly in the failure-related context, we assumed that this parameter is very close to 1, as indicated by empirical evidence in the literature). The stiffness parameters $C_{ij}$ can be expressed with Young's moduli and Poisson's ratios (Bower 2009):

$$
\begin{aligned}
C_{33} &= E_V(1-\nu_{HH}^2)\Lambda, \\
C_{11} &= E_H(1-\nu_{HV}\nu_{VH})\Lambda, \\
C_{66} &= E_H/2(1+\nu_{HH}), \\
C_{13} &= E_H\nu_{VH}(1+\nu_{HH})\Lambda, \\
\Lambda &= \left(1-\nu_{HH}^2-2\nu_{HV}\nu_{VH}-2\nu_{HV}\nu_{VH}\nu_{HH}\right)^{-1}.
\end{aligned}
\tag{3.35}
$$

The ratio between the two poroelastic parameters is

$$
\frac{B_{33}}{B_{11}} = \frac{2C_{13}\alpha_{11} - 2\left(C_{11}-C_{66}\right)\alpha_{33}}{C_{13}\alpha_{33} - C_{33}\alpha_{11}}. \tag{3.36}
$$

Using the correlations between the stiffness parameters estimated by Sayers and Boer (2018) and Asaka et al. (2021), we can assume that the values of $C_{13}$ and $C_{66}$ are small in comparison to $C_{11}$ and $C_{33}$. Hence, the latter two stiffness parameters dominate the final values of $B_{11}$ and $B_{33}$, and of the ratio between them.

## 3.9 Appendix B

| Stress paths | Axial stress [MPa] | Radial stress [MPa] | Pore pressure [MPa] |
|---|---|---|---|
| Triaxial | -2.98 | 0 | -1.50 |
| Isotropic | -3.01 | 3.00 | -2.58 |
| $K_0$ | -3.00 | -2.61 | -2.43 |
| Constant mean stress | -2.81 | 1.40 | -0.91 |

**Table 3.1:** Stress and pore pressure changes during the undrained unloading stages of the triaxial experiment carried out on Lista overburden shale from Valhall field shown in Figure 3.3

# References


Asaka, M., R. Holt and A. Bakk (2021). 'Rock Physics Model of Shale: Predictive Aspect'. In: *Journal of Geophysical Research: Solid Earth* 126.9. ISSN: 2169-9313. DOI: https://doi.org/10.1029/2021JB021993. URL: https://agupubs.onlinelibrary.wiley.com/doi/abs/10.1029/2021JB021993.

Asaka, M. and R. Holt (2021). 'Anisotropic Wellbore Stability Analysis: Impact on Failure Prediction'. In: *Rock Mechanics and Rock Engineering* 54, pp. 1–23. DOI: 10.1007/s00603-020-02283-0.

Bakk, A., R. M. Holt, A. Bauer, B. Dupuy and A. Romdhane (2020). 'Offset dependence of overburden time-shifts from ultrasonic data'. In: *Geophysical Prospecting* 68.6, pp. 1847–1863. ISSN: 0016-8025. DOI: https://doi.org/10.1111/1365-2478.12963. URL: https://onlinelibrary.wiley.com/doi/abs/10.1111/1365-2478.12963.

Banik, N. C. (1984). 'Velocity anisotropy of shales and depth estimation in the North Sea basin'. In: *GEOPHYSICS* 49.9, pp. 1411–1419. DOI: 10.1190/1.1441770. URL: https://library.seg.org/doi/abs/10.1190/1.1441770.

Best, M. E. and T. J. Katsube (1995). 'Shale permeability and its significance in hydrocarbon exploration'. In: *The Leading Edge* 14.3, pp. 165–170. DOI: 10.1190/1.1437104. URL: https://library.seg.org/doi/abs/10.1190/1.1437104.

Biot, M. A. (1941). 'General Theory of Three-Dimensional Consolidation'. In: *Journal of Applied Physics* 12.2, pp. 155–164. DOI: 10.1063/1.1712886. URL: https://aip.scitation.org/doi/abs/10.1063/1.1712886.

Bohnhoff, M., H. Grosser and G. Dresen (2006). 'Strain partitioning and stress rotation at the North Anatolian fault zone from aftershock focal mechanisms of the 1999 Izmit Mw= 7.4 earthquake'. In: *Geophysical Journal International* 166.1, pp. 373–385. ISSN: 0956-540X. DOI: https://doi.org/10.1111/j.1365-246X.2006.03027.x. URL: https://onlinelibrary.wiley.com/doi/abs/10.1111/j.1365-246X.2006.03027.x.

Bower, A. (2009). *Applied Mechanics of Solids*. CRC Press. ISBN: 9781439802489. URL: https://books.google.no/books?id=1_sCzMNZMEsC.

Brocher, T. M. and N. I. Christensen (1990). 'Seismic anisotropy due to preferred mineral orientation observed in shallow crustal rocks in southern Alaska'. In: *Geology* 18.8, pp. 737–740. ISSN: 0091-7613. DOI: 10.1130/0091-7613(1990)018⟨0737:Sadtpm⟩2.3.Co;2. URL: https://doi.org/10.1130/0091-7613(1990)018%3C0737:SADTPM%3E2.3.CO;2.

Bruno, M. S. (2002). 'Geomechanical and Decision Analyses for Mitigating Compaction - Related Casing Damage'. In: *SPE Drilling & Completion* 17.03, pp. 179–188. ISSN: 1064-6671. DOI: 10.2118/79519-pa. URL: https://doi.org/10.2118/79519-PA.

Cheng, A. H. D. (1997). 'Material coefficients of anisotropic poroelasticity'. In: *International Journal of Rock Mechanics and Mining Sciences* 34.2, pp. 199–205. ISSN: 1365-1609. DOI: https://doi.org/10.1016/S0148-9062(96)

00055-1. URL: http://www.sciencedirect.com/science/article/pii/S0148906296000551.

Detournay, E. and A. H. D. Cheng (1993). 'Fundamentals of Poroelasticity'. In: *Analysis and Design Methods*. Ed. by C. Fairhurst. Oxford: Pergamon, pp. 113–171. ISBN: 978-0-08-040615-2. DOI: https://doi.org/10.1016/B978-0-08-040615-2.50011-3. URL: https://www.sciencedirect.com/science/article/pii/B9780080406152500113.

Duda, M., R. Holt, J. F. Stenebråten and A. M. Stroisz (2022). 'Impact of Undrained Pore Pressure Response on Expected Failure Stress in Anisotropic Shales'. In: *56th U.S. Rock Mechanics/Geomechanics Symposium*. Vol. All Days. ARMA-2022-0672. DOI: 10.56952/arma-2022-0672. URL: https://doi.org/10.56952/ARMA-2022-0672.

Duda, M., R. Holt, J. F. Stenebråten and A. Stroisz (2021). *Effects of plastic deformation on Skempton's poroelastic parameters*. Conference Paper.

Dusseault, M. B., M. S. Bruno and J. Barrera (2001). 'Casing Shear: Causes, Cases, Cures'. In: *SPE International Oil and Gas Conference and Exhibition in China*. Vol. All Days. SPE-48864-MS. DOI: 10.2118/48864-ms. URL: https://doi.org/10.2118/48864-MS.

Dyer, B. C., R. H. Jones, J. F. Cowles, O. Barkved and P. G. Folstad (1999). 'Microseismic survey of a North Sea reservoir'. In: *World Oil* 220.3. Cited By :48 Export Date: 15 November 2021, pp. 74–78.

Ellsworth, W. L. (2013). 'Injection-Induced Earthquakes'. In: *Science* 341.6142, p. 1225942. DOI: doi:10.1126/science.1225942. URL: https://www.science.org/doi/abs/10.1126/science.1225942.

Ewy, R. (2015). 'Shale/claystone response to air and liquid exposure, and implications for handling, sampling and testing'. In: *International Journal of Rock Mechanics and Mining Sciences* 80, pp. 388–401. DOI: 10.1016/j.ijrmms.2015.10.009.

Ewy, R. (2018). 'Practical approaches for addressing shale testing challenges associated with permeability, capillarity and brine interactions'. In: *Geomechanics for Energy and the Environment* 14. DOI: 10.1016/j.gete.2018.01.001.

Ewy, R. T. (2021). 'Well Shear Associated with Conventional and Unconventional Operations: Diagnosis and Mechanisms'. In: *SPE Drilling & Completion* 36.02, pp. 427–444. ISSN: 1064-6671. DOI: 10.2118/205007-pa. URL: https://doi.org/10.2118/205007-PA.

Fjær, E., R. Holt, P. Horsrud and A. M. Raaen (2021). *Petroleum Related Rock Mechanics. 3rd edition*. ISBN: 9780128221952.

Geertsma, J. (1973). 'A Basic Theory Of Subsidence Due To Reservoir Compaction; The Homogeneous Case'. In: *Verhandelingen Kon. Ned. Geol. Mijnbouwk. Gen* 28, pp. 43–62.

Gennaro, S. de, A. Onaisi, A. Grandi, L. ben brahim and V. Neillo (2008). '4D reservoir geomechanics: A case study from the HP/HT reservoirs of the Elgin and Franklin fields'. In: *First Break* 26. DOI: 10.3997/1365-2397.2008019.

Giger, S. B., R. T. Ewy, V. Favero, R. Stankovic and L. M. Keller (2018). 'Consolidated - undrained triaxial testing of Opalinus Clay: Results and method

validation'. In: *Geomechanics for Energy and the Environment* 14, pp. 16–28. ISSN: 2352-3808. DOI: https://doi.org/10.1016/j.gete.2018.01.003.

Goral, J., P. Panja, M. Deo, M. Andrew, S. Linden, J.-O. Schwarz and A. Wiegmann (2020). 'Confinement Effect on Porosity and Permeability of Shales'. In: *Scientific Reports* 10. DOI: 10.1038/s41598-019-56885-y.

Hall, S. A., C. MacBeth, O. I. Barkved and P. Wild (2002). 'Time-lapse seismic monitoring of compaction and subsidence at Valhall through cross-matching and interpreted warping of 3D streamer and OBC data'. In: *SEG Technical Program Expanded Abstracts 2002*, pp. 1696–1699. DOI: 10.1190/1.1817004. URL: https://library.seg.org/doi/abs/10.1190/1.1817004.

Han, J., R. Hurt and A. Sookprasong (2015). 'Stress Field Change Due to Reservoir Depletion and Its Impact on Refrac Treatment Design and SRV in Unconventional Reservoirs'. In: *SPE/AAPG/SEG Unconventional Resources Technology Conference*. Vol. All Days. URTEC-2144941-MS. DOI: 10.15530/urtec-2015-2144941. URL: https://doi.org/10.15530/URTEC-2015-2144941.

Hardebeck, J. L. and E. Hauksson (2001). 'Crustal stress field in southern California and its implications for fault mechanics'. In: *Journal of Geophysical Research: Solid Earth* 106.B10, pp. 21859–21882. ISSN: 0148-0227. DOI: https://doi.org/10.1029/2001JB000292. URL: https://agupubs.onlinelibrary.wiley.com/doi/abs/10.1029/2001JB000292.

Head, K. and R. Epps (2011). *Manual of Soil Laboratory Testing*. 3rd. Vol. II. Whittles Publishing.

Henkel, D. J. and N. H. Wade (1966). 'Plane strain tests on a saturated remolded clay'. In: *Journal of Soil Mechanics & Foundations* 92, pp. 67–80.

Henkel, D. (1960). *The shear strength of saturated remoulded clays*. Conference Paper.

Herwanger, J. and N. Koutsabeloulis (2011). *Seismic Geomechanics: How to Build and Calibrate Geomechanical Models using 3D and 4D Seismic Data*. ISBN: 978-90-73834-10-1.

Holt, R., A. Bakk, M. Duda and H. Yan (2022). 'Effects of Anisotropic Poroelasticity on Stress and Pore Pressure Changes Around Subsurface Reservoirs and Storage Sites'. In: *56th U.S. Rock Mechanics/Geomechanics Symposium*. ARMA-2022-0694. DOI: 10.56952/arma-2022-0694.

Holt, R., A. Bakk, J. F. Stenebråten, A. Bauer and E. Fjær (2018a). *Skempton's A — A Key to Man-Induced Subsurface Pore Pressure Changes*. Conference Paper.

Holt, R., A. Bauer and A. Bakk (2017). 'Overburden pore pressure changes and their influence on 4D seismic'. In: *SEG International Exposition and 87th Annual Meeting*.

Holt, R. M., A. Bakk and A. Bauer (2018b). 'Anisotropic poroelasticity: Does it apply to shale?' In: *SEG Technical Program Expanded Abstracts 2018*, pp. 3512–3516. DOI: 10.1190/segam2018-2994785.1. URL: https://library.seg.org/doi/abs/10.1190/segam2018-2994785.1.

Howard, J. J. (1991). 'Porosimetry Measurement of Shale Fabric and Its Relationship to Illite/Smectite Diagenesis'. In: *Clays and Clay Minerals* 39.4,

pp. 355–361. ISSN: 1552-8367. DOI: 10.1346/CCMN.1991.0390403. URL: https://doi.org/10.1346/CCMN.1991.0390403.

Ickrath, M., M. Bohnhoff, G. Dresen, P. Martínez-Garzón, F. Bulut, G. Kwiatek and O. Germer (2015). 'Detailed analysis of spatiotemporal variations of the stress field orientation along the Izmit-Düzce rupture in NW Turkey from inversion of first-motion polarity data'. In: *Geophysical Journal International* 202, pp. 2120–2132. DOI: 10.1093/gji/ggv273.

Janbu, N., R. Roque, H. Lango and T. Tjetla (1988). 'Cyclic load testing of contractant clays from Gullfaks C'. In: *International Conference on Behaviour of Offshore Structures*.

Johnston, J. E. and N. I. Christensen (1995). 'Seismic anisotropy of shales'. In: *Journal of Geophysical Research: Solid Earth* 100.B4, pp. 5991–6003. ISSN: 0148-0227. DOI: https://doi.org/10.1029/95JB00031. URL: https://agupubs.onlinelibrary.wiley.com/doi/abs/10.1029/95JB00031.

Katsube, T. (2000). 'Shale Permeability and Pore-Structure Evolution Characteristics'. In: 2000.

Kenter, C., A. Van den Beukel, A. Hatchell, P. Maron, K. Molenaar, M. Molenaar and J. Stammeijer (June 2004). 'Geomechanics And 4D: Evaluation Of Reservoir Characteristics From Timeshifts In The Overburden'. In: vol. All Days. North America Rock Mechanics Symposium. ARMA-04-627. eprint: https://onepetro.org/ARMANARMS/inproceedings-pdf/ARMA04/All-ARMA04/ARMA-04-627/1855018/arma-04-627.pdf.

Kristiansen, T. G. and F. Sandberg (2018). *The reservoir*. Web Page. URL: https://valhall.industriminne.no/en/the-reservoir.

Kristiansen, T. (2004). 'Drilling Wellbore Stability in the Compacting and Subsiding Valhall Field'. In: *SPE Drilling & Completion* 22. DOI: 10.2118/87221-MS.

Kristiansen, T. G. (1998). 'Geomechanical characterization of the overburden above the compacting chalk reservoir at Valhall'. In: *SPE/ISRM Rock Mechanics in Petroleum Engineering*. OnePetro.

Kristiansen, T. G. (2020). 'Well Design Changes Extend Well Life in Subsiding Overburden at Valhall From 7 to 24 Years'. In: *SPE Norway Subsurface Conference*. Vol. Day 1 Mon, November 02, 2020. D011S001R001. DOI: 10.2118/200749-ms. URL: https://doi.org/10.2118/200749-MS.

Kristiansen, T. G., O. Barkved and P. Pattillo (2000). 'Use of Passive Seismic Monitoring in Well and Casing Design in the Compacting and Subsiding Valhall Field, North Sea'. In: *SPE European Petroleum Conference*. Vol. All Days. SPE-65134-MS. DOI: 10.2118/65134-ms. URL: https://doi.org/10.2118/65134-MS.

Levin, F. K. (1979). 'Seismic velocities in transversely isotropic media'. In: *GEOPHYSICS* 44.5, pp. 918–936. DOI: 10.1190/1.1440985. URL: https://library.seg.org/doi/abs/10.1190/1.1440985.

Lewis, S. M., O. Barkved and R. Kjelstadli (2003). *Planning waterflood wells in a gas cloud: Optimizing the use of a 4C ocean bottom survey and setting the scene for a life of field seismic implementation in the Valhall Field, Norwegian North Sea*. Conference Paper. DOI: 10.1190/1.1817602. URL: https://library.seg.org/doi/abs/10.1190/1.1817602.

Lozovyi, S. and A. Bauer (2018). 'Static and dynamic stiffness measurements with Opalinus Clay'. In: *Geophysical Prospecting* 67. DOI: 10.1111/1365-2478.12720.

Magoon, L. B. and W. G. Dow (1994). *The Petroleum System—From Source to Trap*. American Association of Petroleum Geologists. DOI: 10.1306/m60585.

Martínez-Garzón, P., M. Bohnhoff, G. Kwiatek and G. Dresen (2013). 'Stress tensor changes related to fluid injection at The Geysers geothermal field, California'. In: *Geophysical Research Letters* 40.11, pp. 2596–2601. ISSN: 0094-8276. DOI: https://doi.org/10.1002/grl.50438. URL: https://agupubs.onlinelibrary.wiley.com/doi/abs/10.1002/grl.50438.

Martínez-Garzón, P., G. Kwiatek, H. Sone, M. Bohnhoff, G. Dresen and C. Hartline (2014). 'Spatiotemporal changes, faulting regimes, and source parameters of induced seismicity: A case study from The Geysers geothermal field'. In: *Journal of Geophysical Research: Solid Earth* 119.11, pp. 8378–8396. ISSN: 2169-9313. DOI: https://doi.org/10.1002/2014JB011385. URL: https://agupubs.onlinelibrary.wiley.com/doi/abs/10.1002/2014JB011385.

Mazurek, M., T. Oyama, P. Wersin and P. Alt-Epping (2015). 'Pore-water squeezing in indurated shales'. In: *Chemical Geology* 400. DOI: 10.1016/j.chemgeo.2015.02.008.

McGarr, A., D. Simpson, L. Seeber and W. Lee (2002). 'Case histories of induced and triggered seismicity'. In: *International Geophysics Series* 81.A, pp. 647–664. ISSN: 0074-6142.

Nicholson, C. and R. L. Wesson (1990). *Earthquake hazard associated with deep well injection: a report to the U.S. Environmental Protection Agency*. Report 1951. DOI: 10.3133/b1951. URL: http://pubs.er.usgs.gov/publication/b1951.

Pattillo, P., T. Kristiansen, G. Sund and R. Kjelstadli (1998). 'Reservoir Compaction and Seafloor Subsidence at Valhall'. In: *SPE/ISRM Rock Mechanics in Petroleum Engineering*. Vol. All Days. SPE-47274-MS. DOI: 10.2118/47274-ms. URL: https://doi.org/10.2118/47274-MS.

Raaen, A. M., I. Larsen, E. Fjær and R. Holt (2019). 'Pore Pressure Response in Rock: Implications of Tensorial Skempton B in an Anisotropic Formation'. In: *53rd U.S. Rock Mechanics/Geomechanics Symposium*. Vol. All Days. ARMA-2019-1918.

Rudnicki, J. (1999). 'Alteration of regional stress by reservoirs and other inhomogeneities: Stabilizing or destabilizing?' In: *inproceedings of the Ninth International Congress on Rock Mechanics* 3, pp. 1629–1637.

Rutqvist, J. (2012). 'The Geomechanics of CO2 Storage in Deep Sedimentary Formations'. In: *Geotechnical and Geological Engineering* 30.3, pp. 525–551. ISSN: 1573-1529. DOI: 10.1007/s10706-011-9491-0. URL: https://doi.org/10.1007/s10706-011-9491-0.

Sayers, C. M. and L. D. den Boer (2018). 'The Elastic Properties of Clay in Shales'. In: *Journal of Geophysical Research: Solid Earth* 123.7, pp. 5965–5974. ISSN: 2169-9313. DOI: https://doi.org/10.1029/2018JB015600. URL: https://agupubs.onlinelibrary.wiley.com/doi/abs/10.1029/2018JB015600.

Schlömer, S. and B. M. Krooss (1997). 'Experimental characterisation of the hydrocarbon sealing efficiency of cap rocks'. In: *Marine and Petroleum Geology*

14.5, pp. 565–580. ISSN: 0264-8172. DOI: https://doi.org/10.1016/S0264-8172(97)00022-6. URL: https://www.sciencedirect.com/science/article/pii/S0264817297000226.

Schoenball, M., L. Dorbath, E. Gaucher, J. F. Wellmann and T. Kohl (2014). 'Change of stress regime during geothermal reservoir stimulation'. In: *Geophysical Research Letters* 41.4, pp. 1163–1170. ISSN: 0094-8276. DOI: https://doi.org/10.1002/2013GL058514. URL: https://agupubs.onlinelibrary.wiley.com/doi/abs/10.1002/2013GL058514.

Segall, P. and S. D. Fitzgerald (1998). 'A note on induced stress changes in hydrocarbon and geothermal reservoirs'. In: *Tectonophysics* 289.1, pp. 117–128. ISSN: 0040-1951. DOI: https://doi.org/10.1016/S0040-1951(97)00311-9. URL: https://www.sciencedirect.com/science/article/pii/S0040195197003119.

Skempton, A. W. (1954). 'The Pore-Pressure Coefficients A and B'. In: *Géotechnique* 4.4, pp. 143–147. DOI: 10.1680/geot.1954.4.4.143. URL: https://www.icevirtuallibrary.com/doi/abs/10.1680/geot.1954.4.4.143.

Soldal, M., E. Skurtveit and J. C. Choi (2021). 'Poroelastic and Mechanical Anisotropy of the Draupne Caprock'. In: *55th U.S. Rock Mechanics/Geomechanics Symposium*. Vol. All Days. ARMA-2021-1903.

Thompson, M. and J. R. Willis (1991). 'A Reformation of the Equations of Anisotropic Poroelasticity'. In: *Journal of Applied Mechanics* 58.3, pp. 612–616. ISSN: 0021-8936. DOI: 10.1115/1.2897239. URL: https://doi.org/10.1115/1.2897239.

Townend, J. and M. D. Zoback (2000). 'How faulting keeps the crust strong'. In: *Geology* 28.5, pp. 399–402. ISSN: 0091-7613. DOI: 10.1130/0091-7613(2000)28⟨399:Hfktcs⟩2.0.Co;2. URL: https://doi.org/10.1130/0091-7613(2000)28%3C399:HFKTCS%3E2.0.CO;2.

Tron Golder, K. and P. Bertold (2010). 'History Matched Full Field Geomechanics Model of the Valhall Field Including Water Weakening and Re-Pressurisation'. In: *SPE EUROPEC/EAGE Annual Conference and Exhibition*. Vol. All Days. SPE-131505-MS. DOI: 10.2118/131505-ms. URL: https://doi.org/10.2118/131505-MS.

Vasco, D. W., R. C. Bissell, B. Bohloli, T. M. Daley, A. Ferretti, W. Foxall, B. P. Goertz-Allmann, V. Korneev, J. P. Morris, V. Oye, A. Ramirez, A. P. Rinaldi, A. Rucci, J. Rutqvist, J. White and R. Zhang (2018). 'Monitoring and Modeling Caprock Integrity at the In Salah Carbon Dioxide Storage Site, Algeria'. In: *Geological Carbon Storage*, pp. 243–269. DOI: https://doi.org/10.1002/9781119118657.ch12. URL: https://agupubs.onlinelibrary.wiley.com/doi/abs/10.1002/9781119118657.ch12.

Verdon, J. P., J. M. Kendall, D. J. White and D. A. Angus (2011). 'Linking microseismic event observations with geomechanical models to minimise the risks of storing CO2 in geological formations'. In: *Earth and Planetary Science Letters* 305.1, pp. 143–152. ISSN: 0012-821X. DOI: https://doi.org/10.1016/j.epsl.2011.02.048. URL: https://www.sciencedirect.com/science/article/pii/S0012821X11001270.

Whaley, J. (2009). 'The Valhall Story'. In: *GeoExPro* 6.5.

White, J. E., L. Martineau-Nicoletis and C. Monash (1983). 'Measured Anisotropy in Pierre Shale'. In: *Geophysical Prospecting* 31.5, pp. 709–725. ISSN: 1365-2478. DOI: https://doi.org/10.1111/j.1365-2478.1983.tb01081.x. URL: https://www.earthdoc.org/content/journals/10.1111/j.1365-2478.1983.tb01081.x.

Wild, K., M. Barla, G. Turinetti and F. Amann (2017). 'A multi-stage triaxial testing procedure for low permeable geomaterials applied to Opalinus Clay'. In: *Journal of Rock Mechanics and Geotechnical Engineering* 9. DOI: 10.1016/j.jrmge.2017.04.003.

Williams-Stroud, S., R. Bauer, H. Leetaru, V. Oye, F. Stanek, S. Greenberg and N. Langet (2020). 'Analysis of Microseismicity and Reactivated Fault Size to Assess the Potential for Felt Events by CO2 Injection in the Illinois Basin'. In: *Bulletin of the Seismological Society of America* 110.5, pp. 2188–2204. ISSN: 0037-1106. DOI: 10.1785/0120200112. URL: https://doi.org/10.1785/0120200112.

Ziegler, M. O., O. Heidbach, A. Zang, P. Martínez-Garzón and M. Bohnhoff (2017). 'Estimation of the differential stress from the stress rotation angle in low permeable rock'. In: *Geophysical Research Letters* 44.13, pp. 6761–6770. ISSN: 0094-8276. DOI: https://doi.org/10.1002/2017GL073598. URL: https://agupubs.onlinelibrary.wiley.com/doi/abs/10.1002/2017GL073598.

Zoback, M. D. and J. C. Zinke (2002). 'Production-induced Normal Faulting in the Valhall and Ekofisk Oil Fields'. In: *pure and applied geophysics* 159.1, pp. 403–420. ISSN: 1420-9136. DOI: 10.1007/PL00001258. URL: https://doi.org/10.1007/PL00001258.

Zoback, M. D. (2007). *Reservoir Geomechanics*. Cambridge: Cambridge University Press. ISBN: 9780521146197. DOI: DOI:10.1017/CBO9780511586477. URL: https://www.cambridge.org/core/books/reservoir-geomechanics/71717D4521278CE16D1DED0476ACEDBE.

# PAPER C: Impact of undrained pore pressure response on expected failure stress in anisotropic shales

Marcin Ireneusz Duda[1,2], Rune Martin Holt[1,2], Jørn Fredrik Stenebråten[2], Anna Maria Stroisz[2]

[1] Norwegian University of Science and Technology, 7031 Trondheim, Norway
[2] Sintef Petroleum, 7031 Trondheim, Norway

Published in the Proceedings of the 56th US Rock Mechanics/Geomechanics Symposium held in Santa Fe, New Mexico, USA, 26-29 June 2022

## Abstract

The connection between undrained pore pressure response to stress in shales and fault reactivation, drilling problems and microseismicity observed at significant distances from hydrocarbon reservoirs and injection zones has not been thoroughly studied and is usually disregarded in geomechanical modelling workflows. In our study, we examine to what extent the inclusion of the pore pressure response affects the amplitude of total stress changes expected to cause shear failure in several overburden and outcrop shales. We combine poroelastic pore pressure coefficients and Mohr-Coulomb failure envelope parameters estimated through triaxial laboratory experiments to model the total stress increases at failure for a wide range of loading scenarios and medium orientations. We consider both isotropic and anisotropic pore pressure parameters - we explore the differences in modelling outcomes the two sets of parameters yield, as well as the impact of the individual parameters on the expected stresses at failure. We observed that shear failure in shales is expected at significantly lower stresses changes and is plausible in a much wider range of loading paths once the undrained pressure response in considered, and therefore we postulate that it should be taken into account during injection or production operations safety assessment.

## 4.1 Introduction

Injection into or production from a subsurface reservoir have been documented to lead to fault activation, microseismic activity, and borehole stability issues in the reservoir and its surroundings (e.g., Pine et al. 1983; Raleigh et al. 1976; Zoback and Harjes 1997). In some cases, these undesired phenomena occurred in the over- and underburden at significant distances from the reservoir subjected to pore pressure change (e.g., Odonne et al. 1999; Rutqvist et al. 2008; Segall 1989).

This has triggered an ongoing discussion of the causes of these events. Until now, it was primarily associated with pore fluid migration through fractures and fault planes throughout low permeable under- and over-burden, as well as with stress transfer (e.g., Vasco et al. 2018; Verdon et al. 2011; Williams-Stroud et al. 2020; Zhou et al. 2008) caused by injection- or production-induced pore pressure changes in the reservoir (e.g., Geertsma 1973; Morita et al. 1989; Rudnicki 1999).

In porous low permeability rocks, such as shales, these external stress changes may cause an undrained pore pressure response (Henkel 1960; Janbu et al. 1988; Skempton 1954). This mechanism can potentially alter the pore pressure at significant distances from the considered injection or production sites (Duda et al. 2023) on a time scale much shorter than that of the pore pressure changes induced by fluid flow. Consequently, it may lead to non-negligible effective stress changes in the reservoir surrounding within a typical reservoir lifetime. However, the undrained pore pressure response estimation is still rarely included in overburden geomechanical modelling workflows.

In this paper, we ask whether the undrained pore pressure response could be considered as one of the suspects behind fault reactivation incidents, microseismicity, and borehole instabilities observations in the over- and under-burden reported in the literature. We combine the estimates of the pore pressure coefficients with parameters describing Mohr-Coulomb failure envelopes of several shales and use them to study total stresses at shear failure with and without the impact of the undrained pore pressure response. To investigate the influence of anisotropy on the stability of overburden shales, we compare the results given by the isotropic and anisotropic pore pressure parameters for a range of stress change and stress orientation scenarios.

## 4.2 Theory

Our analysis considers a set of modelling scenarios in which anisotropic linearly elastic samples are loaded until shear failure. The loadings follow pre-defined stress paths $\kappa$, i.e. ratios between the horizontal ($\sigma_{11}$) and vertical total principal stress ($\sigma_{33}$) changes:

$$\kappa = \frac{\Delta\sigma_{11}}{\Delta\sigma_{33}}, \tag{4.1}$$

In this paper, the subscripts accompanying stresses indicate only the direction of stress and not relations between magnitudes of particular stresses. In the typical laboratory conditions (i.e., cylindrical sample geometry), the horizontal principal stress is often referred to as "radial" and vertical principal stress as "axial" stress. In the laboratory one can control the stress path, whereas in the field, it is controlled by reservoir geometry, elastic properties and in particular contrast between drained moduli of the reservoir and undrained moduli of the surroundings, and further by non-elastic effects. Analytical modelling limited to the case of no elastic contrast (Geertsma 1973) predicts constant mean stress around the reservoir ($\kappa$ = -1/2) - above the center of the reservoir, the vertical stress will decrease while the horizontal stress will increase as a result of depletion, whereas the opposite scenario occurs near the edges. Numerical geomechanical modeling is required in order to forecast realistic stress paths within the overburden in a more general case. Such simulations show that the stress changes and hence the parameter $\kappa$ in Equation (4.1) may vary significantly from the analytical solution, and also demonstrate significant spatial variability (e.g., Gennaro et al. 2008).

Pore pressure change ($\Delta p_f$) caused by total stress changes in so-called triaxial conditions (uniform radial stresses, hence $\Delta\sigma_{11}$=$\Delta\sigma_{22}$) can be quantitatively described with a set of pore-pressure parameters ($A_S$ and $B_S$) introduced for soils by Skempton (1954) and adapted for anisotropic rocks by Holt et al. (2017),

$$\Delta p_f = B_S \left[\Delta\sigma_{11} + A_S \left(\Delta\sigma_{33} - \Delta\sigma_{11}\right)\right]. \tag{4.2}$$

According to poroelasticity theory, in isotropic media the value of parameter $B_S$ depends on the mechanical properties of the medium and the fluid and $A_S = 1/3$ (as often assumed for practical purposes). In transversely isotropic (TI) shales, the value of parameter $A_S$ depends on the relative orientation of the medium symmetry axis and the directions of principal stresses (Holt et al. 2018; Holt et al. 2017). These two parameters can be expressed with two poroelastic invariants, $B_{11}$ and $B_{33}$, describing the properties of TI medium in the directions parallel and perpendicular to the symmetry plane of the medium, respectively, and angle $\theta$ in triaxial conditions representing the deviation of the axial stress direction from the symmetry axis of the medium,

$$B_S = \frac{B_{33} + 2B_{11}}{3}, \tag{4.3}$$

$$A_S = \frac{B_{11}\sin^2\theta + B_{33}\cos^2\theta}{3B_S}. \tag{4.4}$$

To determine the limits of available stress states, we use the Mohr-Coulomb failure

criterion. The failure envelope (i.e. the maximum shear stress $\tau_{max}$ for given normal stress $\sigma$ value) is defined by cohesion $c$ and angle of internal friction $\phi$,

$$\tau_{max} = c + \sigma \tan \phi. \tag{4.5}$$

Parameters $B_{11}$, $B_{33}$, $c$ and $\phi$ are determined experimentally, separately for each of the considered rocks.

Most shales are defined as quasi-brittle rocks that exhibit an onset of plastic deformation even prior to rock failure (e.g., Parisio et al. 2015). Apart from gradual accumulation of irreversible strain and degradation of elastic properties of the material, one should also expect a decrease in the value of poroelastic parameter $A_S$ (Duda et al. 2021). However, due to the lack of experimental data on plastic deformation in all shales investigated in this study, we limit our analysis to the purely elastic behavior of these rocks.

## 4.3 Experiments and data processing

All in-house measurements of the poroelastic parameters, cohesion and angle of internal friction were carried out using a triaxial apparatus. During the tests, axial (vertical) stress was exerted directly onto the top surface of cylindrical samples of diameter of 15 mm and length of approximately 30 mm by a steel piston. Uniform radial (horizontal) stress was applied through a Viton sleeve by confining fluid.

Pore fluid (brine, 3.5% NaCl) was delivered into the sleeve through a hole in the bottom piston. To facilitate the fluid flow and to ensure uniform saturation and quick pressure equilibration between the sample and the rest of the pore fluid system, a metal mesh was placed between the side surface of the sample and the sleeve. The out-let of the pore fluid was located in the upper piston. The dead volume of the pore fluid system was approximately 0.4 ml.

Axial strains were measured using a set of three LVDTs (Linear Variable Differential Transformer) distributed evenly around the sample. Radial strain was measured using two pairs of strain-gaged extensometers installed at the mid-length of the sample in two orthogonal directions. Contact between the extensometers and the samples was provided by metal pins penetrating the sleeve in the sections not covered by the metal mesh.

The poroelastic parameters $B_{33}$ and $B_{11}$ were estimated from multi-stage undrained experiments carried out on samples drilled perpendicularly to their bedding plane (i.e., $\theta = 0$). An experiment performed on a shale from Valhall field overburden (Lista formation) is shown in Figure 4.1. Each of the five tests in this group consisted of several loading-unloading or unloading-reloading cycles following different stress paths $\kappa$ ranging from -0.5 to 2.

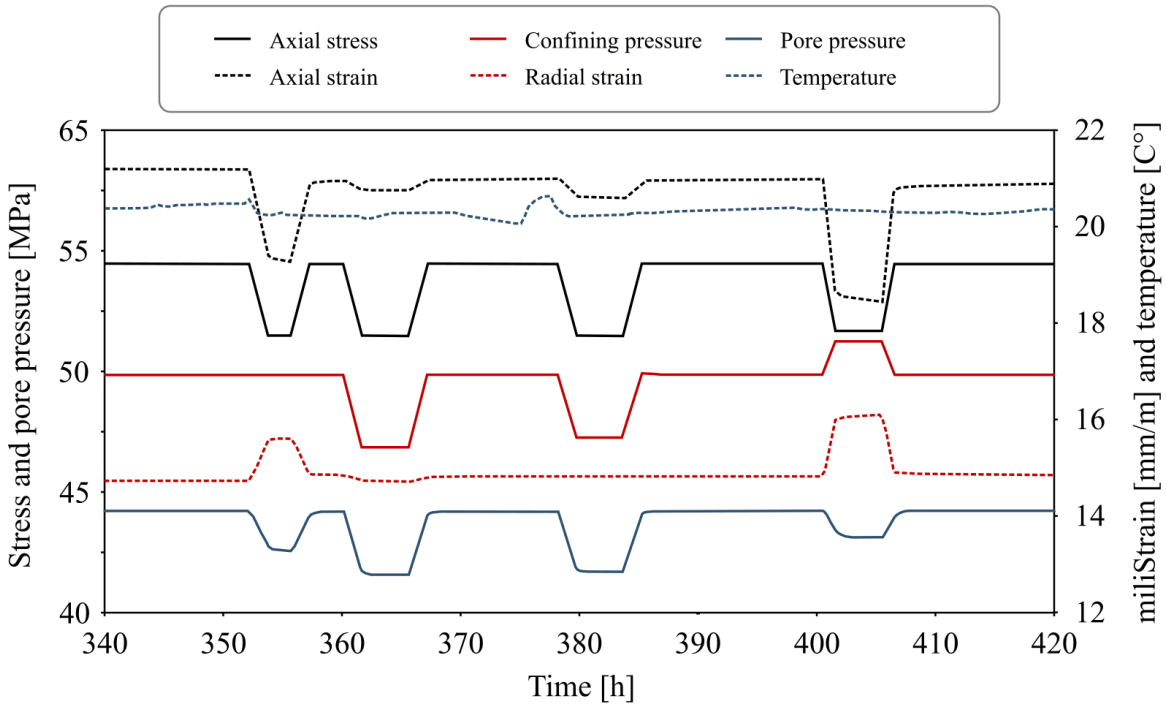


**Figure 4.1:** Multi-stage undrained experiment carried out on a cylindrical sample of Lista overburden shale drilled perpendicularly to bedding ($\theta = 0$).

The value of $B_S$ can be estimated directly from an isotropic cycle ($\kappa = 1$, hence $\Delta\sigma_{11} = \Delta\sigma_{33}$) using Equation (4.2). In combination with an additional pore pressure change measurement taken during a cycle with stress path $\kappa \neq 1$, Equation (4.2) and $B_S$ give the value of $A_S$. In the case of two non-isotropic or three or more different stress cycles, the values of $B_S$ and $A_S$ can be simultaneously estimated numerically from solving a set of Equation (4.2), where each equation corresponds to a single stress cycle.

The values of $B_{33}$ and $B_{11}$ estimated from a test performed on a sample drilled perpendicularly to the bedding, $\theta = 0$, allows us to compute the theoretical value of $A_S$ for any deviation angle. This provides us with a tool to verify the quality of measurements carried out on samples of different orientations, as shown by Holt et al. (2017) and Duda et al. (2021) or for Lista overburden shale in Figure 4.2.

To maintain consistency, for all computational purposes, we use $A_S$ values estimated from measurements performed at $\theta = 0$. This means that the extent of our analysis was limited only by the availability of the data on cohesion and internal friction angles for various orientations of the media.

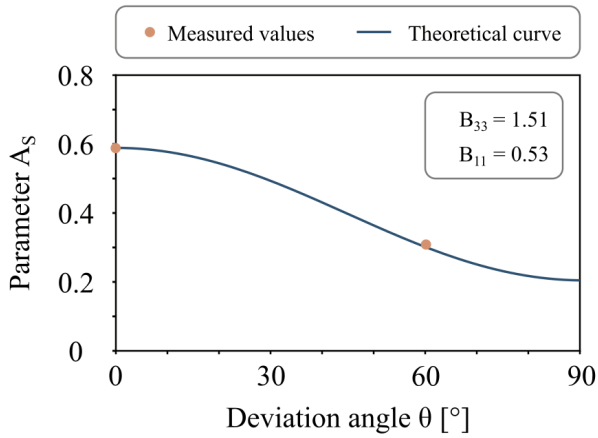


**Figure 4.2:** Comparison of experimentally measured values of $A_S$ in Lista overburden shale with a theoretical curve computed using parameters $B_{33}$ and $B_{11}$ determined through the test carried out on a sample drilled perpendicularly to the bedding ($\theta = 0$).

Cohesion $c$ and angle of internal friction $\phi$ were determined for various orientations ($\theta$) of each shale through a series of undrained uniaxial loading ($\kappa = 0$) experiments. In all the tests, the axial strain was increased with a constant rate adjusted to the consolidation rate of the tested rock (Head and Epps 2011), driving the samples towards and beyond failure. In several uniaxial loading experiments, the main part of the test was preceded by a short loading-unloading cycle (as shown in Figure 4.3 demonstrating an experiment carried out on Pierre II outcrop shale). This cycle

was used to verify the value of the previously determined parameter $A_S$.

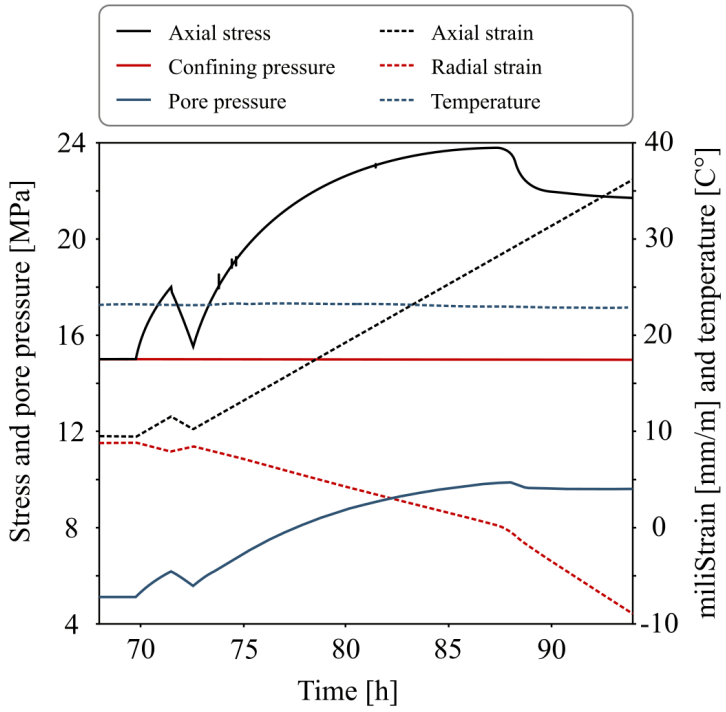


**Figure 4.3:** Uniaxial loading undrained experiment carried out on a cylindrical sample of Pierre II outcrop shale drilled perpendicularly to bedding ($\theta = 0$).

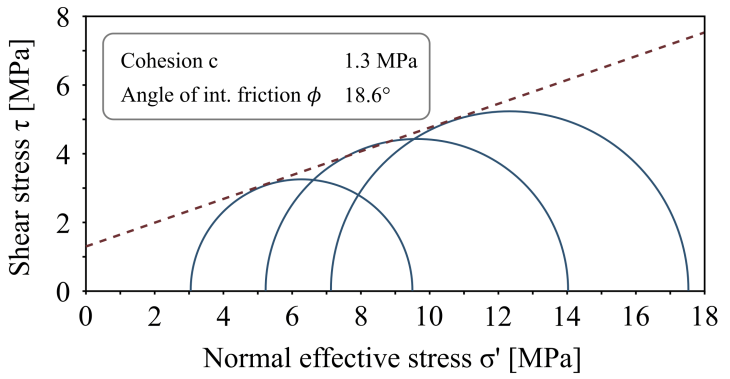


**Figure 4.4:** Failure envelope determined from three Mohr circles drawn for stresses at rock failure registered during three independent tests carried out on Pierre II outcrop shale samples drilled at the deviation angle of $\theta = 60°$.

| Shale | $\theta$ [deg] | $c$ [MPa] | $\phi$ [deg] | $B_S$ | $A_S$ |
|---|---|---|---|---|---|
| Pierre II | 0 | 2.6 | 12.7 | 0.86 | 0.45 |
| | 60 | 1.3 | 18.7 | | 0.32 |
| Lista | 0 | 2.4 | 15.1 | 0.86 | 0.59 |
| | 60 | 1.6 | 12.5 | | 0.31 |
| O1 | 0 | 1.8 | 15.0 | 0.83 | 0.53 |
| | 30 | 0.9 | 19.9 | | 0.46 |
| | 60 | 1.3 | 12.5 | | 0.31 |
| | 90 | 2.2 | 12.8 | | 0.23 |
| O2 | 0 | 2.9 | 30.2 | 0.80 | 0.66 |
| | 60 | 1.9 | 29.0 | | 0.29 |
| O3 | 0 | 4.4 | 20.3 | 0.80 | 0.48 |
| | 60 | 1.3 | 25.2 | | 0.32 |
| Opalinus | 0 | $3.7^{(1)}$ | $22.0^{(1)}$ | $0.89^{(2)}$ | $0.56^{(2)}$ |
| | 90 | $5.4^{(1)}$ | $23.0^{(1)}$ | | $0.22^{(2)}$ |
| Draupne | 0 | $7.8^{(3)}$ | $18.7^{(3)}$ | 0.58 | 0.54 |
| | 90 | $8.4^{(3)}$ | $19.4^{(3)}$ | | 0.23 |

**Table 4.1:** Summary of both types of described experiments supplemented with information retrieved from literature. The symbols in the headers stand for: $\theta$ – deviation of the maximum principal stress direction from the symmetry axis of the medium, $c$ – cohesion, $\theta$ – angle of internal friction, $B_S$ and $A_S$ – Skempton's parameters. Values of $A_S$ for $\theta > 0$ were estimated from measurements done at $\theta = 0$. Numbers in superscripts indicate corresponding source in the literature: $^{(1)}$ Bock (2009), $^{(2)}$ Lozovyi and Bauer (2018), $^{(3)}$ Soldal et al. (2021).

For each of the considered deviation angles $\theta$, we carried out two or three tests characterized by different confining pressure levels maintained during the undrained part of the experiments. We used the stress levels recorded at failure to draw Mohr circles and later numerically determined coefficients of a line tangent to the circle edges, as shown in Figure 4.4 summarizing three tests carried out on Pierre II samples drilled at the deviation angle of $\theta = 60°$. We determine cohesion and angle of internal friction by comparing the coefficients of the tangent line with Equation (4.5).

In total, we tested four overburden shales (Lista, O1, O2, O3, and Draupne) and a single outcrop shale (Pierre II). The summary of all tests is shown in Table 4.1. We supplemented the table with values representative for Opalinus and Draupne shales reported in the literature (references given in the table).

## 4.4 Modelling results

We used the estimated sets of parameters to model effective stresses at failure caused by loading following stress paths $\kappa$ from -0.5 to 1. In all analyzed loading scenarios, we assumed the initial radial stress ($\sigma_{11}$) of 15 MPa, axial stress ($\sigma_{33}$) of 20 MPa and pore pressure ($p_f$) of 10 MPa.

For each of the loading stress paths we modelled three different scenarios:

i. Only stress changes are considered, no undrained pore pressure change is taken into account,

ii. Undrained pore pressure change is modelled using pore pressure parameters of an isotropic medium (i.e. $B_S$ estimated from an isotropic stress cycle and $A_S = 1/3$),

iii. Undrained pore pressure change is modelled using pore pressure parameters of an anisotropic medium (i.e. both $B_S$ and $A_S$ estimated experimentally).

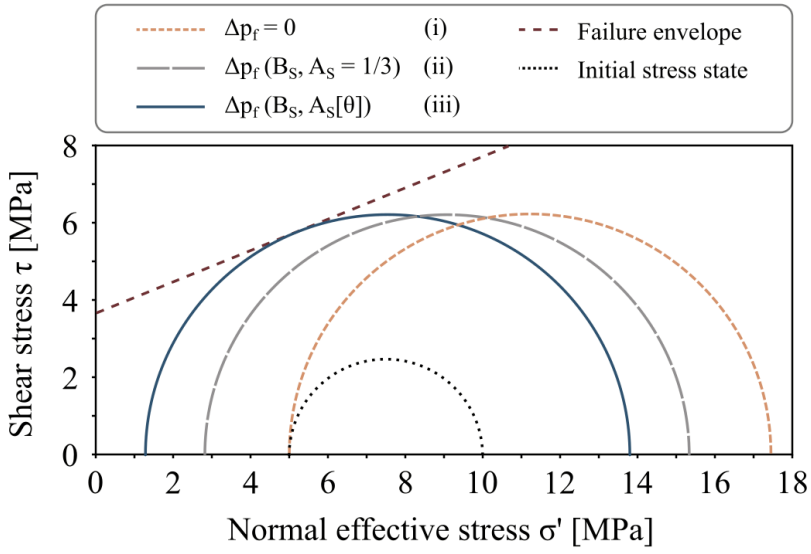


**Figure 4.5:** Modelled uniaxial loading by $\Delta\sigma_{33} = 7.49$ MPa of Opalinus shale sample drilled at $\theta = 0$. The initial stress conditions were: $\sigma_{11} = 15$ MPa, $\sigma_{33} = 20$ MPa and $p_f = 10$ MPa. The three considered scenarios are: (i) no undrained pore pressure changes, (ii) pore pressure changes modelled with isotropic parameters, (iii) pore pressure changes modelled with anisotropic parameters. Total axial stress increase displayed in the plot results in failure in scenario (iii).

A comparison of such scenarios in the case of uniaxial loading ($\kappa = 0$) and effective stresses corresponding to the failure of Opalinus shale sample oriented at $\theta = 0$ is shown in Figure 4.5. For this stress path, any changes of radial (or horizontal) effective stress $\sigma'_{11}$ result exclusively from changes in pore pressure inside the analyzed rock volume. The value of the total axial stress change resulting in contact between Mohr circle and failure envelope was found using the numerical bi-section method (e.g., Mathews and Fink 2004).

In Figure 4.5 the maximum increase of axial stress (i.e. at which shear failure occurs) for the medium modelled using the anisotropic pore pressure parameters (scenario iii) is $\Delta\sigma_{33}^{F} = 7.49$ MPa giving an increase in effective axial stress of 3.76 MPa. The same increase in total axial stress results in a rise in effective axial stress of 5.29 MPa in the medium modelled with the isotropic pore pressure parameters (scenario ii) and translates directly to an increase of 7.49 MPa in effective axial stress in the medium with no pore pressure changes (scenario i).

In the scenarios ii and iii, shear failure would be expected at higher total axial stress values (not shown in Figure 4.5). In the case of Opalinus shale modelled with the isotropic pore pressure parameters (scenario ii), failure would occur at a total axial stress increase of 8.83 MPa. In a medium not experiencing undrained pore pressure changes (scenario i), the total axial stress change at failure would be 11.99 MPa.

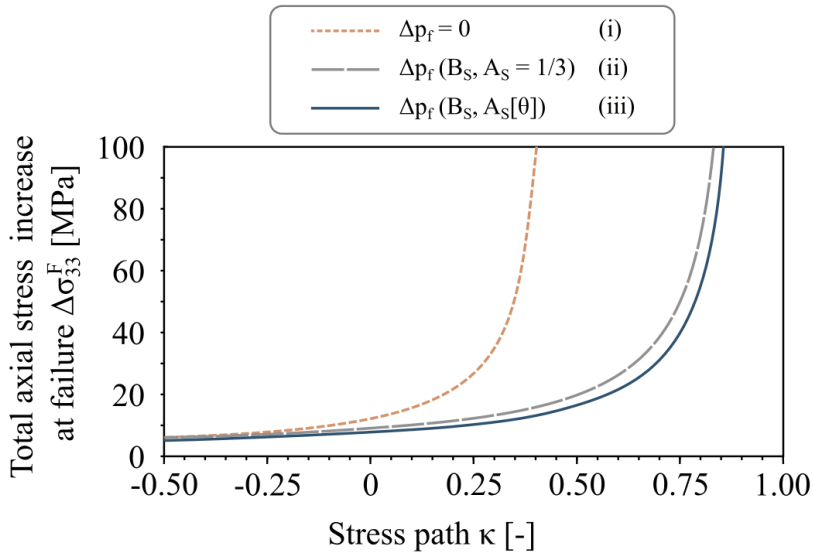


**Figure 4.6:** Total axial stress increase at failure $\Delta\sigma_{33}^{F}$ modelled for a range of stress paths for Opalinus shale sample drilled at $\theta = 0$. The three considered scenarios are: (i) no undrained pore pressure changes, (ii) pore pressure changes modelled with isotropic parameters, (iii) pore pressure changes modelled with anisotropic parameters.

A comparison of total axial stress change values at failure $\Delta\sigma_{33}^{F}$ for Opalinus shale with $\theta = 0$ modelled for all three scenarios within the entire analyzed range of stress paths is shown in Figure 4.6. The differences between the scenario with no pore pressure change and the two accounting for the undrained pore pressure response is minor for loading with stress path coefficient $\kappa$ value below 0. For such loading, differential stress $\sigma_{33}$-$\sigma_{11}$ increases faster than axial stress $\sigma_{33}$, and hence shear failure in general is expected to take place for relatively low axial stress increments. For higher stress path coefficient $\kappa$ values, the difference increases quickly and surpasses 10 MPa already for $\kappa = 0.14$.

Compilation of all modelled curves of total axial stress increase at failure given by the anisotropic pore pressure parameters (scenario iii) is shown in Figure 4.7. In the plots showing modelling results for low (0 and 30°, Figure 4.7A) as well as high (60 and 90°, Figure 4.7B) inclination angles $\theta$, the curves have similar character as observed in Figure 4.6 and can be divided into three main groups. The first group consists of curves corresponding to rocks with low cohesion c and low values for the angle of internal friction $\phi$ (Pierre II, Lista, O1). In this group, total axial stress increase at failure $\Delta\sigma_{33(iii)}^{F}$ remains very low for a wide range of stress path coefficient values only to increase dramatically for $\kappa\approx$ 0.75. In the second group consisting of curves representing rocks with intermediate cohesion c and high internal friction angles $\phi$ (Opalinus, O2, O3) the increase of $\Delta\sigma_{33(iii)}^{F}$ starts earlier and is generally less abrupt for high stress path coefficient $\kappa$ values. The third group is represented by curves corresponding to Draupne shale, characterized by exceptionally high cohesion c and intermediate angle of internal friction $\phi$. The two curves in this group have by far the highest values at $\kappa$ = -0.5, but the change of their trajectory is relatively slow. The order and relative position of curves do not seem to correlate with the values of pore pressure parameters of their corresponding rocks.

To investigate the impact of including the undrained pore pressure response on shale shear failure predictions, we plotted the difference between scenarios (i) and (iii) in Figure 4.8.The trend of an increasing discrepancy between the scenarios (i) and (iii) observed in Figure 4.6 can be seen in all the considered rocks and for all deviation angles $\theta$. This means that shear failure is generally expected at lower total axial stress increments once the influence of the undrained pore pressure response is considered.

All the curves have a similar exponential character. The difference in expected axial stress increments at shear failure between the scenario disregarding and the scenarios considering undrained pore pressure response to stress changes increases with stress path coefficient $\kappa$.

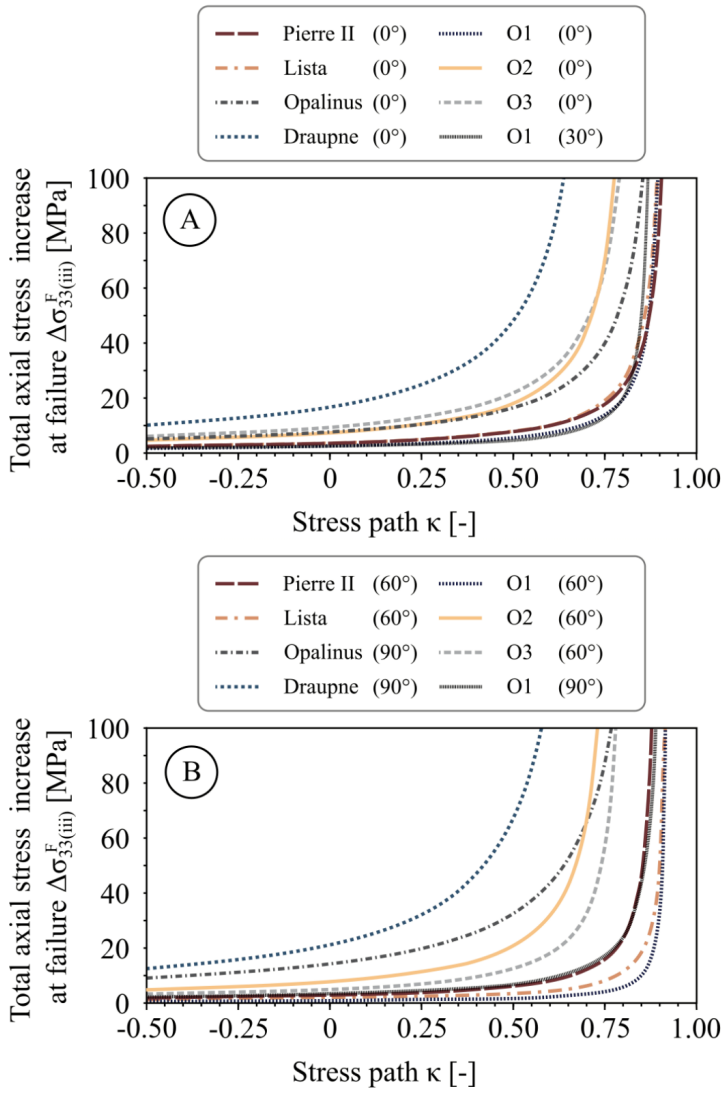


**Figure 4.7:** Total axial stress increase at failure $\Delta\sigma_{33}^{F}$ modelled using anisotropic pore pressure parameters (scenario iii) for a range of stress paths in shale samples drilled at $\theta = 0$, 30° (A, top), 60° and 90° (B, bottom).

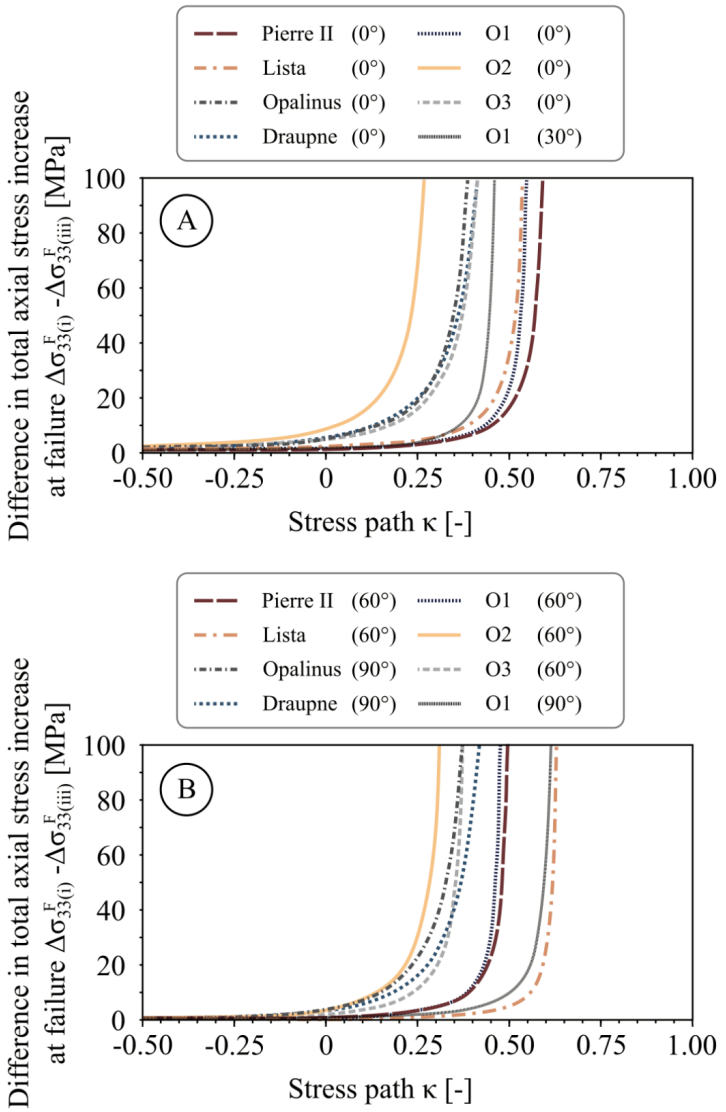


**Figure 4.8:** Difference in total axial stress increase at failure between the scenario of no pore pressure changes (i) and the scenario of pore pressure changes modelled using anisotropic parameters (iii) in shale samples drilled at $\theta = 0$, 30° (A, top), 60° and 90° (B, bottom).

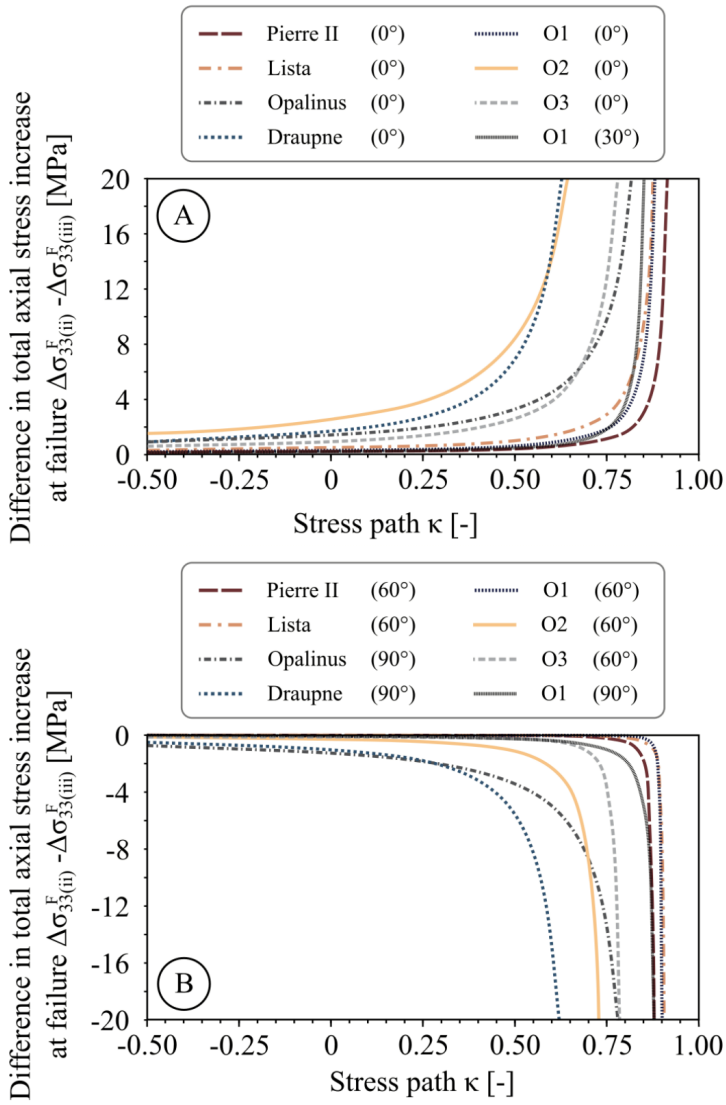


**Figure 4.9:** Difference in total axial stress increase at failure between the scenarios of pore pressure changes modelled using isotropic (ii) and anisotropic pore pressure parameters (iii) in shale samples drilled at $\theta = 0$, 30° (A, top), 60° and 90° (B, bottom). Note that the scale of Y-axis is different than in the previous plots.

The average difference between the two scenarios at $\kappa = 0$ is 3.04 MPa for rocks oriented at $\theta = 0$ and 30° (Figure 4.8A), and 1.61 MPa for rocks oriented at $\theta =$ 60° and 90° (Figure 4.8B). For $\theta = 0$ and 30° the difference $\Delta\sigma^F_{33(i)}$- $\Delta\sigma^F_{33(iii)}$ of 10 MPa is reached between $\kappa = 0.02$ and 0.46, and for higher angles between $\kappa = 0.13$ and 0.56. This increase accelerates significantly for positive stress path coefficient values $\kappa$. The range of stress paths within which the differences between the scenarios escalate is fairly narrow – for rocks oriented at $\theta = 0$ and 30° it increases from 10 to 100 MPa on average within $\Delta\kappa = 0.20$ and for rocks oriented at $\theta =$ 60° and 90° within $\Delta\kappa = 0.14$.

To examine the impact of taking the anisotropy of shales into account, we plotted the difference between the scenarios based on the isotropic (ii) and the anisotropic pore pressure parameters (iii) in Figure 4.9. In this case, the absolute differences between the scenarios are significantly smaller and they start to increase at higher stress path coefficients values, regardless of the inclination angles. The average difference between the two scenarios at $\kappa = 0$ is 0.91 MPa for $\theta = 0$ and 30° (Figure 4.9A), and -0.36 MPa for $\theta = 60°$ and 90° (Figure 4.9B). For $\theta = 0$ and 30° the absolute difference $\Delta\sigma^F_{33(ii)}$- $\Delta\sigma^F_{33(iii)}$ of 10 MPa is reached between $\kappa =$ 0.54 and 0.90, and for $\theta = 60°$ and 90° between $\kappa = 0.58$ and 0.92.

In contrast to the difference between scenarios (i) and (iii), the sign of the difference between scenarios (ii) and (iii) changes with the increase of inclination angle $\theta$. For all analyzed materials, total axial stresses increase at shear failure estimated using the anisotropic pore pressure parameters is larger than the stress increase obtained using the isotropic parameters for $\theta = 0$ and 30°. The opposite is true for $\theta = 60°$ and 90°.

## 4.5 Conclusions

As more instances of microseismicity, borehole instability and fault reactivation taking place at considerable distances from original injection or production zone locations are reported, it is important to understand processes potentially causing these undesirable phenomena. In this paper, we focused on how the inclusion of the undrained pore pressure response to stress changes in the stability assessment process impacts the expected stress levels at shear failure modelled for several reservoir overburden and outcrop shales.

The main conclusion of our study is that once the undrained pore pressure change is taken into account, shear failure in shales is expected for significantly lower stress changes than if we consider only the direct impact of total stress changes on the Mohr circles. Furthermore, shear failure may occur during loading following stress paths for which it seemed highly unlikely if only the direct impact of the stress changes were considered. Both facts imply that injection- and depletion-induced stress and resultant pore pressure changes may play a role in causing instabilities

at larger distances from the induction or production sites than previously assumed (for more details see Duda et al. 2023).

Secondly, our observations indicate that the parameters of the failure envelope (cohesion $c$ and angle of internal friction $\phi$) have a larger impact on the modelled value of total axial stress increase at failure in anisotropic shales than their pore pressure parameters ($A_S$ and $B_S$).

Our study shows that the relation between the total stress changes expected at failure obtained with the isotropic and the anisotropic pore pressure parameters is angle-dependent. Hence, none of the approaches can be assumed to give more conservative (or safer) results if principal directions of stress do not coincide with the principal directions of the medium (symmetry axis and symmetry plane).

We consider the anisotropic pore pressure parameters to improve quantitative description of the behavior of over- and underburden shales. In cases where experimental estimates are lacking, it would still be preferrable to model the undrained pore pressure changes using isotropic parameters. This is significantly more responsible than neglecting the induced pore pressure effect while evaluating safety of injection or production operations.

## 4.6 Acknowledgements

This publication has been produced with support from the NCCS Centre, performed under the Norwegian research program Centres for Environment-friendly Energy Research (FME). The authors acknowledge the following partners for their contributions in the project: Aker Solutions, ANSALDO Energia, CoorsTek Membrane Sciences, Electromagnetic Geoservices (EMGS), Equinor, Gassco, KROHNE, Larvik Shipping, Lundin, Norcem, Norwegian Oil and Gas, Quad Geometrics, TOTAL, Vår Energi, and the Research Council of Norway (257579/E20). We would also like to thank the Research Council of Norway through the PETROMAKS 2 programme (Grant 294369), AkerBP, Equinor, and Shell in the project "Improved prediction of stress and pore-pressure changes in the overburden for infill drilling". This work was also supported by the Research Council of Norway, Aker BP ASA, BP Exploration Operating Company Ltd, ConocoPhillips Skandinavia AS, Equinor Energy AS, Lundin Norway AS, Petrobras and Total E&P Norge AS through the KPN project "Shale Barrier Toolbox: Designing future wells for efficient completion and simpler P&A" (280650/E30) at SINTEF Industry.

# References


Bock, H. (2009). *RA Experiment: Updated Review of the Rock Mechanics Properties of the Opalinus Clay of the Mont Terri URL based on Laboratory and Field Testing*. Report. Q+S Consult.

Duda, M., A. Bakk, R. Holt and J. F. Stenebråten (2023). 'Anisotropic Poroelastic Modelling of Depletion-Induced Pore Pressure Changes in Valhall Overburden'. In: *Rock Mechanics and Rock Engineering*. ISSN: 1434-453X. DOI: 10.1007/s00603-022-03192-0. URL: https://doi.org/10.1007/s00603-022-03192-0.

Duda, M., R. Holt, J. F. Stenebråten and A. Stroisz (2021). *Effects of plastic deformation on Skempton's poroelastic parameters*. Conference Paper.

Geertsma, J. (1973). 'A Basic Theory Of Subsidence Due To Reservoir Compaction; The Homogeneous Case'. In: *Verhandelingen Kon. Ned. Geol. Mijnbouwk. Gen* 28, pp. 43–62.

Gennaro, S. de, A. Onaisi, A. Grandi, L. ben brahim and V. Neillo (2008). '4D reservoir geomechanics: A case study from the HP/HT reservoirs of the Elgin and Franklin fields'. In: *First Break* 26. DOI: 10.3997/1365-2397.2008019.

Head, K. and R. Epps (2011). *Manual of Soil Laboratory Testing*. 3rd. Vol. II. Whittles Publishing.

Henkel, D. (1960). *The shear strength of saturated remoulded clays*. Conference Paper.

Holt, R., A. Bakk, J. F. Stenebråten, A. Bauer and E. Fjær (2018). *Skempton's A — A Key to Man-Induced Subsurface Pore Pressure Changes*. Conference Paper.

Holt, R., A. Bauer and A. Bakk (2017). 'Overburden pore pressure changes and their influence on 4D seismic'. In: *SEG International Exposition and 87th Annual Meeting*.

Janbu, N., R. Roque, H. Lango and T. Tjetla (1988). 'Cyclic load testing of contractant clays from Gullfaks C'. In: *International Conference on Behaviour of Offshore Structures*.

Lozovyi, S. and A. Bauer (2018). 'Static and dynamic stiffness measurements with Opalinus Clay'. In: *Geophysical Prospecting* 67. DOI: 10.1111/1365-2478.12720.

Mathews, J. H. and K. D. Fink (2004). *Numerical methods using MATLAB*. 4th ed. Upper Saddle River, N.J: Pearson Prentice Hall. ISBN: 9780130652485.

Morita, N., D. Whitfill, O. Nygaard and A. Bale (1989). 'A Quick Method To Determine Subsidence, Reservoir Compaction, and In-Situ Stress Induced by Reservoir Depletion'. In: *Journal of Petroleum Technology* 41.01, pp. 71–79. ISSN: 0149-2136. DOI: 10.2118/17150-pa. URL: https://doi.org/10.2118/17150-PA.

Odonne, F., I. Ménard, G. J. Massonnat and J.-P. Rolando (1999). 'Abnormal reverse faulting above a depleting reservoir'. In: *Geology* 27.2, pp. 111–114. ISSN: 0091-7613. DOI: 10.1130/0091-7613(1999)027⟨0111:Arfaad⟩2.3.Co;2. URL: https://doi.org/10.1130/0091-7613(1999)027%3C0111:ARFAAD%3E2.3.CO;2.

Parisio, F., S. Samat and L. Laloui (2015). 'Constitutive analysis of shale: a coupled damage plasticity approach'. In: *International Journal of Solids and Structures* 75-76, pp. 88–98. ISSN: 0020-7683. DOI: https://doi.org/10.1016/j.ijsolstr.2015.08.003. URL: https://www.sciencedirect.com/science/article/pii/S0020768315003509.

Pine, R. J., P. Ledingham and C. M. Merrifield (1983). 'In-situ stress measurement in the Carnmenellis granite—II. Hydrofracture tests at Rosemanowes quarry to depths of 2000 m'. In: *International Journal of Rock Mechanics and Mining Sciences & Geomechanics Abstracts* 20.2, pp. 63–72. ISSN: 0148-9062. DOI: https://doi.org/10.1016/0148-9062(83)90328-5. URL: https://www.sciencedirect.com/science/article/pii/0148906283903285.

Raleigh, C., J. Healy and J. Bredehoeft (1976). 'An Experiment in Earthquake Control at Rangely, Colorado'. In: *Science (New York, N.Y.)* 191, pp. 1230–7. DOI: 10.1126/science.191.4233.1230.

Rudnicki, J. (1999). 'Alteration of regional stress by reservoirs and other inhomogeneities: Stabilizing or destabilizing?' In: *inproceedings of the Ninth International Congress on Rock Mechanics* 3, pp. 1629–1637.

Rutqvist, J., J. T. Birkholzer and C.-F. Tsang (2008). 'Coupled reservoir – geomechanical analysis of the potential for tensile and shear failure associated with CO2 injection in multilayered reservoir–caprock systems'. In: *International Journal of Rock Mechanics and Mining Sciences* 45.2, pp. 132–143. ISSN: 1365-1609. DOI: https://doi.org/10.1016/j.ijrmms.2007.04.006. URL: https://www.sciencedirect.com/science/article/pii/S1365160907000548.

Segall, P. (1989). 'Earthquakes triggered by fluid extraction'. In: *Geology* 17.10, pp. 942–946. ISSN: 0091-7613. DOI: 10.1130/0091-7613(1989)017⟨0942:Etbfe⟩2.3.Co;2. URL: https://doi.org/10.1130/0091-7613(1989)017%3C0942:ETBFE%3E2.3.CO;2.

Skempton, A. W. (1954). 'The Pore-Pressure Coefficients A and B'. In: *Géotechnique* 4.4, pp. 143–147. DOI: 10.1680/geot.1954.4.4.143. URL: https://www.icevirtuallibrary.com/doi/abs/10.1680/geot.1954.4.4.143.

Soldal, M., E. Skurtveit and J. C. Choi (2021). 'Laboratory Evaluation of Mechanical Properties of Draupne Shale Relevant for CO2 Seal Integrity'. In: *Geosciences* 11.6, p. 244. ISSN: 2076-3263. URL: https://www.mdpi.com/2076-3263/11/6/244.

Vasco, D. W., R. C. Bissell, B. Bohloli, T. M. Daley, A. Ferretti, W. Foxall, B. P. Goertz-Allmann, V. Korneev, J. P. Morris, V. Oye, A. Ramirez, A. P. Rinaldi, A. Rucci, J. Rutqvist, J. White and R. Zhang (2018). 'Monitoring and Modeling Caprock Integrity at the In Salah Carbon Dioxide Storage Site, Algeria'. In: *Geological Carbon Storage*, pp. 243–269. DOI: https://doi.org/10.1002/9781119118657.ch12. URL: https://agupubs.onlinelibrary.wiley.com/doi/abs/10.1002/9781119118657.ch12.

Verdon, J. P., J. M. Kendall, D. J. White and D. A. Angus (2011). 'Linking microseismic event observations with geomechanical models to minimise the risks of storing CO2 in geological formations'. In: *Earth and Planetary Science Letters* 305.1, pp. 143–152. ISSN: 0012-821X. DOI: https://doi.org/10.1016/

j.epsl.2011.02.048. URL: https://www.sciencedirect.com/science/article/pii/S0012821X11001270.

Williams-Stroud, S., R. Bauer, H. Leetaru, V. Oye, F. Stanek, S. Greenberg and N. Langet (2020). 'Analysis of Microseismicity and Reactivated Fault Size to Assess the Potential for Felt Events by CO2 Injection in the Illinois Basin'. In: *Bulletin of the Seismological Society of America* 110.5, pp. 2188–2204. ISSN: 0037-1106. DOI: 10.1785/0120200112. URL: https://doi.org/10.1785/0120200112.

Zhou, Q., J. T. Birkholzer, C.-F. Tsang and J. Rutqvist (2008). 'A method for quick assessment of CO2 storage capacity in closed and semi-closed saline formations'. In: *International Journal of Greenhouse Gas Control* 2.4, pp. 626–639. ISSN: 1750-5836. DOI: https://doi.org/10.1016/j.ijggc.2008.02.004. URL: https://www.sciencedirect.com/science/article/pii/S1750583608000091.

Zoback, M. and H.-P. Harjes (1997). 'Injection-induced earthquakes and crustal stress at 9 km depth at the KTB deep drilling site, Germany'. In: *Journal of Geophysical Research* 1021, pp. 18477–18492. DOI: 10.1029/96JB02814.

# PAPER D: Effects of plastic deformation on poroelastic pore pressure coefficients in Pierre II shale.

Marcin Ireneusz Duda[1], Rune Martin Holt[1], Jørn Fredrik Stenebråten[2], Anna Maria Stroisz[2]

[1] Norwegian University of Science and Technology, 7031 Trondheim, Norway
[2] Sintef Petroleum, 7031 Trondheim, Norway

Published in the Proceedings of the 55th US Rock Mechanics/Geomechanics Symposium held in Houston, Texas, USA, 20-23 June 2021 (Modified: Figure 2, consisting of two subfigures, was split into two separate figures)

## Abstract

Skempton's parameters $B_S$ and $A_S$ describe the undrained pore pressure response to stress state changes in porous media. In our study we examined the relationship between two poroelastic coefficients, $B$ and $A$, equivalent to Skempton's parameters within given elastic region and plastification of a transversely isotropic (TI) medium. We used a triaxial apparatus to perform a series of experiments on ten Pierre II shale samples drilled at various angles with respect to rock's bedding and saturated with brine equivalent to their original pore medium. The tests consisted of stress- and strain-driven loading and unloading cycles carried out in undrained conditions, during which stresses, strains, pore fluid pressure and temperature were measured. We determined the poroelastic parameters and estimated axial and radial plastic strains for each of the unloading steps and investigated the relationship between them. We documented a transition of unloading-induced pore pressure change from negative to positive values in the constant mean stress conditions, as well as gradual deviation from purely elastic TI medium symmetry. We found the ratio between elastic and total axial strains to correlate well with $A$ changes and identified it as a potentially useful parameter for modelling of pore pressure response in shales in the direct proximity of faults.

## 5.1 Introduction

Stress-dependent pore pressure response in low-permeable soils and rocks has been researched and successfully quantified for several decades (Henkel and Wade 1966; Henkel 1960; Janbu et al. 1990; Skempton 1954). One of the very first studies, described by Skempton (1954), introduced two parameters capturing the impact of the principal stress changes on the undrained pore pressure response in triaxial conditions (i.e. equal horizontal stresses). Skempton's coefficient $B_S$ describes the effect of the mean stress and coefficient $A_S$ of the deviatoric stress changes, as shown in Equation (5.1):

$$\Delta p_f = B_S(\Delta\sigma_3 + A_S(\Delta\sigma_1 - \Delta\sigma_3)), \tag{5.1}$$

where $p_f$ is the pore pressure, $\sigma_3$ and $\sigma_1$ are the minimum and maximum principal total stresses, respectively.

In the case of a transversely isotropic (TI) medium deformed elastically (e.g., during initial unloading or small unloading-reloading cycles), poroelasticity theory predicts undrained pore pressure response to be given by a similar relationship (Cheng 1997):

$$\Delta p_f = \frac{1}{3}\sum_{ij} B_{ij}\Delta\sigma_{ij}. \tag{5.2}$$

The tensor $B_ij$ in a TI medium has two invariant components, termed parameters $B_1$ and $B_3$. Subscript "3" denotes the direction of the material symmetry axis while subscript 1 denotes a direction within the symmetry plane. For a material with the symmetry axis oriented along $\sigma_{11}$ principal stress direction, Equation (5.1) and Equation (5.2) can be written in the same way, relating poroelastic equivalents of Skempton's original parameters, $B$ and $A$, to the poroelastic invariants as

$$B = \frac{2B_3 + B_1}{3}, \tag{5.3}$$

$$A = \frac{B_1}{B}. \tag{5.4}$$

Notice that this poroelastically derived $A$ is not invariant and hence will vary with angle $\theta$ between maximum principal stress and material symmetry axis:

$$A(\theta) = \frac{B_3 \sin^2\theta + B_1 \cos^2\theta}{3B}. \tag{5.5}$$

Laboratory experiments with shales, that largely obey the behavior predicted by poroelasticity for TI symmetry, demonstrate that such a relationship holds for stress cycling with moderate stress amplitudes - 5 MPa and less, according to Holt et al. (2018b) and Holt et al. (2018a). The poroelastic parameters do not capture the direct effects of plastic deformation on the pore pressure change they describe - they depict only the response to stress changes in the corresponding elastic region.

According to the poroelasticity theory (Biot 1941; Biot 1962), the parameter $A$ of an isotropic linearly elastic medium should be equal to 1/3, which translates to no pore volume changes (i.e. constant $p_f$) from shearing. Even the coefficients experimentally determined by Skempton (1954) were however, generally far from that theoretical value. Skempton (1954) associated $A_S$ value at failure with the composition and the degree of consolidation of tested rocks. Previous studies carried out on both, sandstones (e.g., Lockner and Stanchits 2002) and significantly softer and more anisotropic shales (Holt et al. 2018a; Lozovyi and Bauer 2018), show the influence of confining pressure on Skempton's $B_S$ and deviatoric stress on $A_S$ parameter. Their results suggest that the confining pressure tends to decrease $B_S$ by stiffening the rock, while the impact on $A_S$ during triaxial tests depends on confining pressure in accord with observed dilatant/contracting behavior.

The objective of this study is to investigate how the poroelastic parameters $A$ and $B$ gradually evolve in transversely isotropic shales repeatedly exceeding the elastic limit throughout triaxial experiments. Moreover, we aim to establish a relation between the values of the poroelastic parameters measured during unloading stages and the increasing plastification developed during preceding loading episodes. Instead of linking the poroelastic parameters with stress level currently experienced by rocks, we seek to quantitatively correlate their measured values with accumulation of plastic strains estimated from our experimental data.

Other factors that may affect the poroelastic parameters values measured in shales like saturation, fluid exposure, swelling, system response, fluid dead volume, et cetera, (e.g., Ewy 2015; Ewy 2018; Wild et al. 2017), which were accounted for and controlled during the experimental part of the work we present here, are not described in this paper.

## 5.2 Laboratory experiments

We carried out a series of ten experiments on Pierre II shale – an outcrop rock characterized by porosity of 40.3%, 50% of clay minerals content, 27% of quartz, 15% of feldspars, 6.5% of pyrite and less than 1% of calcite, dolomite and siderite. The cylindrical samples with diameter of 15 mm and length of 30 mm were drilled from a core at various angles with respect to rocks bedding: five samples were drilled perpendicular ($\theta = 0°$), one parallel ($\theta = 90°$) and four at intermediate angles of 30° and 60° to the bedding plane.

The tests were conducted with a triaxial apparatus (Figure 5.1). Axial stress is exerted directly on a sample by steel pistons and the radial stress is applied throughout a viton sleeve by confining oil. The pore fluid is delivered to the inside of the sleeve through a hole in the bottom piston, distributed with a metal mesh placed between the sample and the sleeve, and received by a hole in the upper piston. The dead volume of the pore fluid system is 0.4 ml (dead volume-to-pore volume ratio of approximately 1:5.4) and it allows to directly measure pore pressure changes of order of magnitude of 0.01 MPa Small dimensions of the samples ensured quick pressure equilibration between the inside of the pores and fluid saturating the mesh. During the experiment we measured axial and radial stresses and strains, pore fluid pressure and temperature (to rule out it had a significant impact on the pore pressure measurements). The axial force loadcell, providing input for the axial stress determination, was mounted inside the pressure vessel. Axial strain was measured by three linear variable differential transformers (LVDTs) placed every 120° around the sample. Radial deformation was measured in two orthogonal directions at sample mid-height using strain-gaged extensometers.

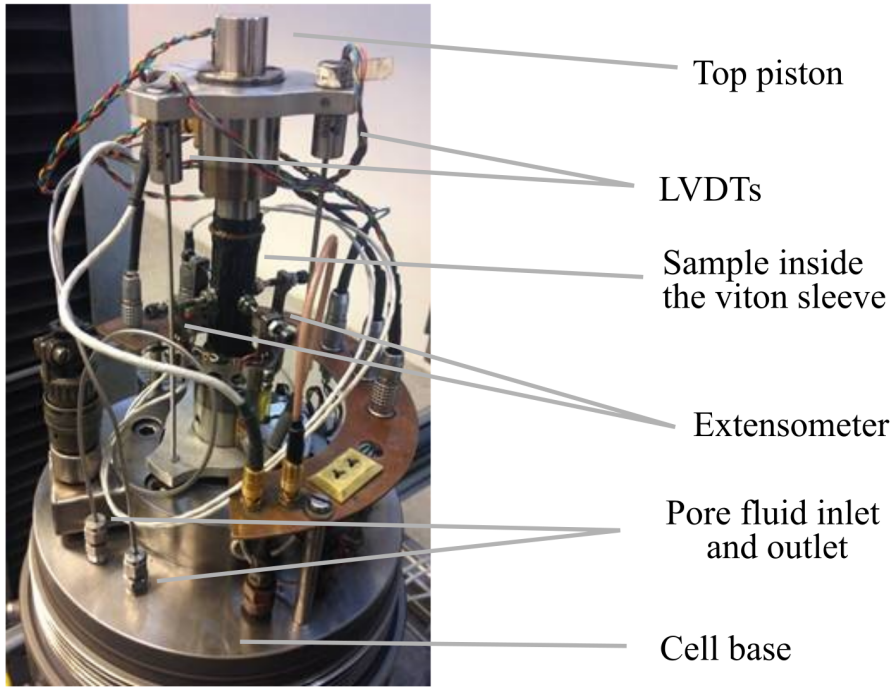


**Figure 5.1:** Inside of the triaxial apparatus used in the experimental part of this study

The extensometers were in contact with the sample through metal plates installed into the sleeve, touching the sample surface in sections not covered with the metal

mesh. To avoid an intrusion of rock fragments into the pore fluid system, we placed brass plates of 0.05 mm thickness between the pistons and the sample.

To fully saturate the samples and to remove air trapped in the pore fluid system, the samples held under hydrostatic stress of 3 MPa were exposed to 50 ml of 3.5% NaCl brine (equivalent to the original pore medium) circulated under pressure of 1 MPa.

The first group of experiments consists of two multistage tests, C1 and C2, carried out on samples drilled perpendicular to the bedding. The samples were first brought to a reference stress state with axial stress ($\sigma_1$) of 13 MPa, confining pressure ($\sigma_3$) of 9 MPa and pore pressure ($p_f$) of 5 MPa. Consolidation of high porosity clay-rich shales is a long process. It significantly affects measurements taken before the full equilibrium of the sample is reached. To minimize its effects, but at the same time keep the length of the experiments within reasonable limits, we tracked the consolidation curve. Once the estimated maximum consolidation-related deformation is nearly reached, we initiated the main part of the test procedure (Head and Epps 2011).

The initial consolidation phase was followed by two undrained stress-driven (controlled with stress-rate and stress amplitude) cycles of different stress paths, i.e. ratios between radial and axial stress changes, $\kappa = \Delta\sigma_3/\Delta\sigma_1$. These two cycles were used to estimate the initial values of parameters $A$ and B. The main criterion of stress paths $\kappa$ selection at this point of the test has been to cause only limited plastic deformation (preferably stress paths close to $\kappa = 1$) and at the same time to yield large pore pressure changes (relatively high $\kappa$, $1/2 < \kappa < 2$, according to the linear relationship between stress path coefficient $\kappa$ and the undrained pore pressure response reported by Holt et al. (2018c). Between the cycles the pore fluid system was re-connected to a pump and pore pressure was brought back to its initial value.

The later, strain-driven (controlled with axial strain-rate and strain amplitude) part of the two experiments consisted of series of loading and partial unloading cycles gradually driving the sample towards failure. As the cycling was performed in undrained conditions, we had insight into the evolution of the poroelastic parameters - the repetition of unloading cycles allowed us to estimate $B$ and $A$ values at different stages of the tests. Optimal strain rates, used in this part of the test, were determined during the initial loading phase with the use of corresponding consolidation curves, separately for each of the samples (Head and Epps 2011).

In the case of test C1 (Figure 5.2), the stress paths $\kappa$ in the initial part of the experiment were 2 and 1 ( $\kappa = 1$ is commonly referred to as "isotropic" stress path, $\kappa$ = -1/2 as "constant mean stress" and $\kappa = 0$ as "triaxial"), with the amplitude of axial stress change ($\Delta\sigma_1$) of 2 MPa. The strain-driven part of the test was carried out under highly damaging constant mean stress conditions (Holt and Stenebråten 2013) – axial stress change amplitude simply resulted from changes in strain and radial stresses were adjusted accordingly to fulfill the requirement

of the constant mean stress value. During the first two strain-driven cycles of test C1, the sample was axially loaded by strains of 3 mm/m (or milistrains) and unloaded by 1 mm/m. In the remaining cycles, loading was limited to 2 mm/m. The sample failed during the test, reaching its maximum axial stress level during the third strain-driven loading cycle.

In the test C2 (Figure 5.3), the stress paths $\kappa$ used in the stress-driven part of the test were 1/2 and 1 with the amplitude of axial stress of 1 MPa. In the strain-driven part a triaxial stress path was used and the sample was repetitively loaded by 1 mm/m and unloaded by 0.5 mm/m. Between the triaxial cycles, the sample was additionally loaded and unloaded by 0.1 mm/m under isotropic stress change conditions (except for the first cycle where the amplitude was 0.25 mm/m). This allowed us to update the value of parameter $B$ for each of the cycles. Test C2 was finalized before the sample failed.

The second group of experiments (S1-S8) consisted of a simpler triaxial strain-driven undrained loading routine interrupted by a single unloading-reloading cycle before and another one after the failure occurred. In the case of experiments S1 and S3, there is no post-failure cycle. The initial hydrostatic stress levels ($\sigma_3^0$) and the angles at which the samples were drilled with respect to the direction normal to their bedding ($\theta$) are shown in Table 1. Initial pore pressure values for tests S1-S8 were between 4.8 and 5.2 MPa. Experiment S5 included an undrained isotropic unloading-reloading segment in the initial part of the tests.

| | | θ | | | |
|---|---|---|---|---|---|
| | | 0° | 30° | 60° | 90° |
| $\sigma_3^0$ | 10 MPa | S1 | S8 | S4 | S7 |
| | 15 MPa | S2 | - | S5* | - |
| | 20 MPa | S3 | - | S6 | - |

**Table 5.1:** Tests matrix. Columns divide test IDs according to the angle ($\theta$) at which the samples corresponding to the tests were drilled. Rows indicate the initial hydrostatic stress ($\sigma_3^0$) at which axial loading began. Asterisk (*) next to the test ID indicates that the test included a $B$ measurement

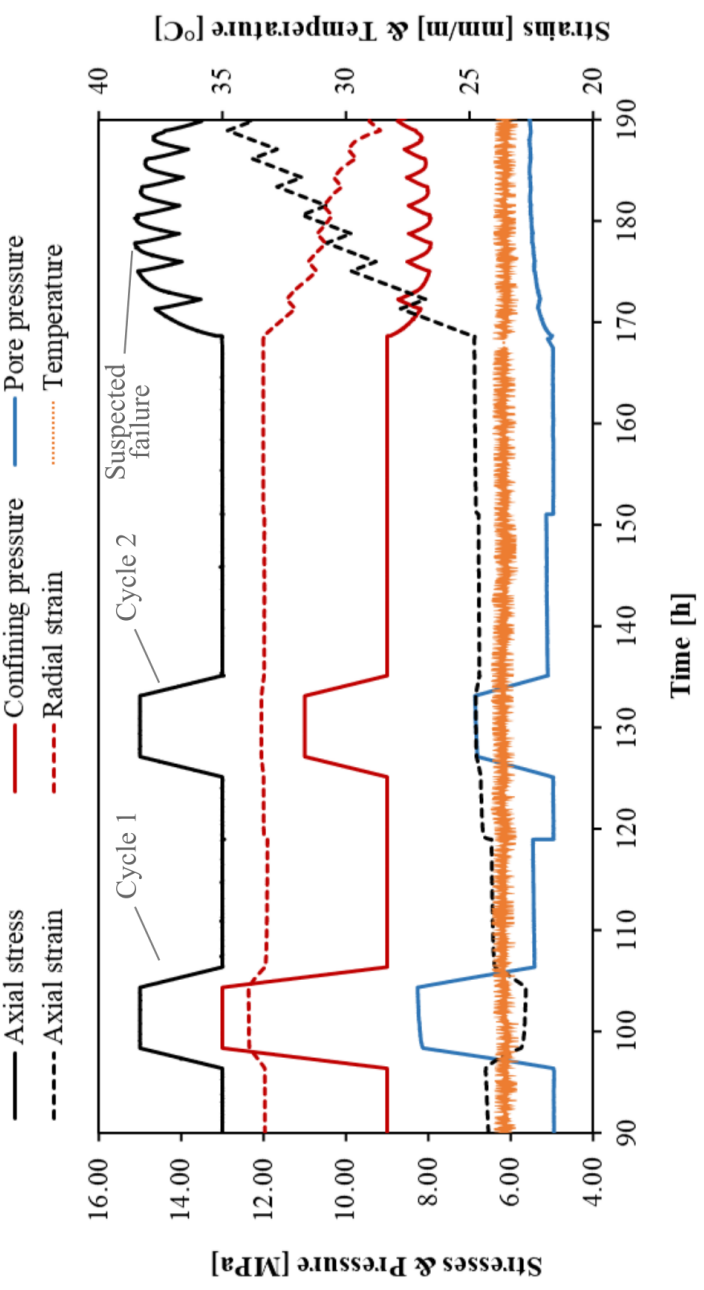


**Figure 5.2:** Results of experiment C1. The first two cycles (97-107h and 126-136h) represent the part of the experiment controlled by stress rate and stress amplitude. The axial loading in the second part of the test (starting at 169h) was controlled by strain rates and strain amplitude, and the radial stress value was given by constant mean stress requirement ($\Delta\sigma_3$ = -0.5 $\Delta\sigma_1$). Axial strain was shifted by 9 mm/m (or milistrains) and radial strains by 31 mm/m for the purpose of clearer visualization of results.

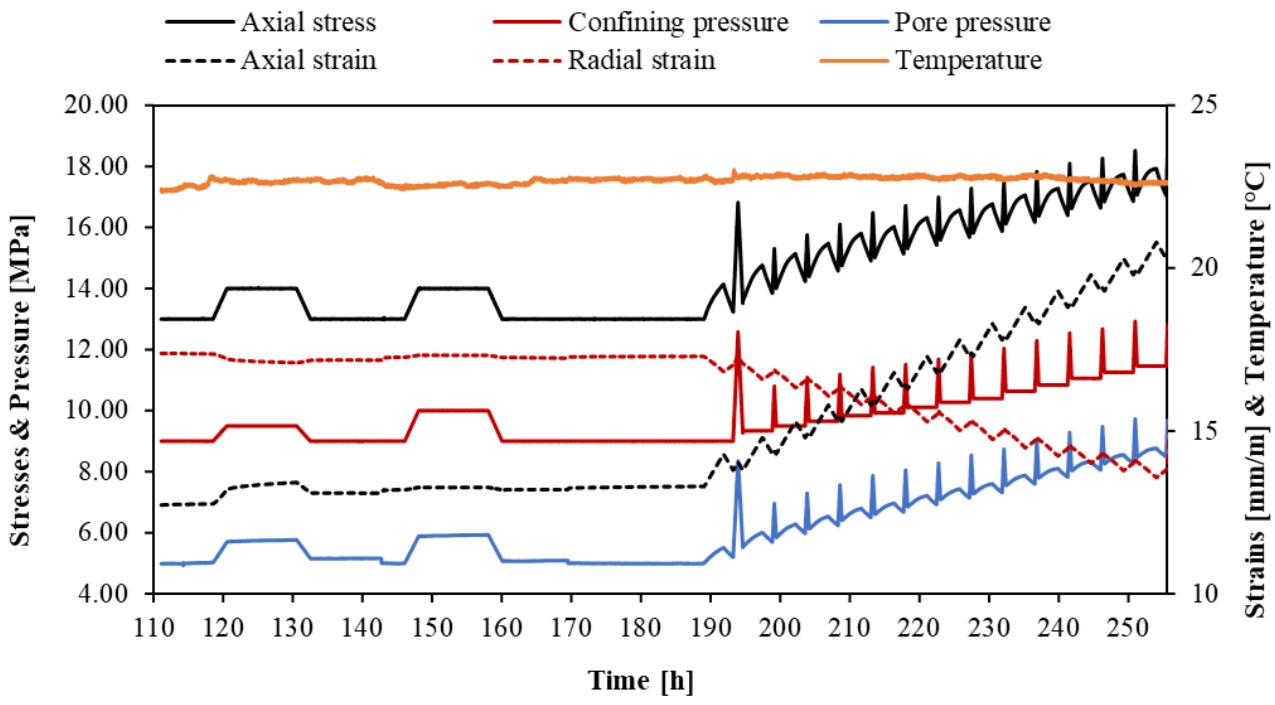


**Figure 5.3:** Results of experiment C2. The first two cycles (118-132h and 146-160h) represent the part of the experiment controlled by stress rate and stress amplitude. The axial loading in the second part of the test (starting at 189h) was controlled by strain rates and strain amplitude, and the radial stress value was given by constant mean stress requirement ($\Delta\sigma_3$ = -0.5 $\Delta\sigma_1$). Axial strain was shifted by 9 mm/m (or milistrains) and radial strains by 10 mm/m for the purpose of clearer visualization of results.

## 5.3 Methods and results

The first objective of our data processing routine was to estimate the values of the poroelastic parameters before large plastic strains were introduced. In tests C1 and C2 coefficients $B$ were obtained directly from the isotropic cycles according to Equation (5.1) – they were determined to be 0.86 and 0.87, respectively. Corresponding $A$ parameters had values of 0.43 and 0.46, respectively. Parameter $B$ in experiment S5 was measured to be 0.84. The next step was to investigate

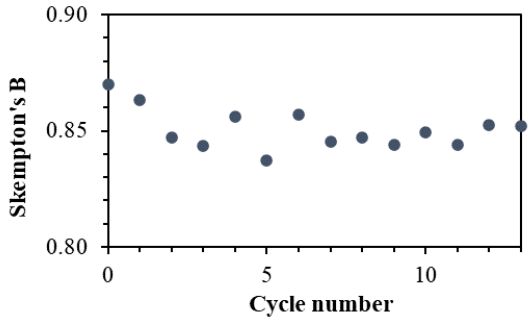


**Figure 5.4:** B measurements (test C2).

the changes in the undrained pore pressure response during the strain-driven sections of the tests. To limit the impact of potential plastic dilatancy on the pore pressure values we analyzed only the measurements taken during unloading, when the samples were assumed to be within their elastic region and no further plastic deformation was expected (Fjær et al. 2012; Fjær et al. 2013).

In test C2 we measured 14 values of $B$ - this parameter did not change regardless of increasing plastification of the sample (Figure 5.4). The difference between B obtained in tests C1 and C2 ($\sigma_3^0$ = 9 MPa), and the one measured in test S5 ($\sigma_3^0$ = 15 MPa) was also small. This apparent lack of change allowed us to assume a constant $B = 0.85$ for the rest of our analysis (the average of all measurements, with standard deviation below 0.01). Having an estimate of B we were able to approximate A value for each of the unloading stages in both groups of the tests.

The results of test C1 proved to be the most demanding to process due to the requirement of maintaining the mean stress constant during the strain-driven loading. The combination of this specific stress path, stress change amplitudes and poroelastic properties of the rock resulted in pore pressure changes of amplitude comparable with the resolution of the pressure sensors (Figure 5.5). To limit the impact of the measurement noise, we approximated the pore pressure measurements in the axial stress-pore pressure space with linear trends and used their slope to estimate $A$. From Equation (5.1), the assumptions of constant mean stress during cycling (i.e., $\Delta\sigma_3$ = -1/2 $\Delta\sigma_1$) and constant $B$ value, we obtained $\Delta p_f (= y)/\Delta\sigma_1 (= x) = 1.275A - 0.425$.

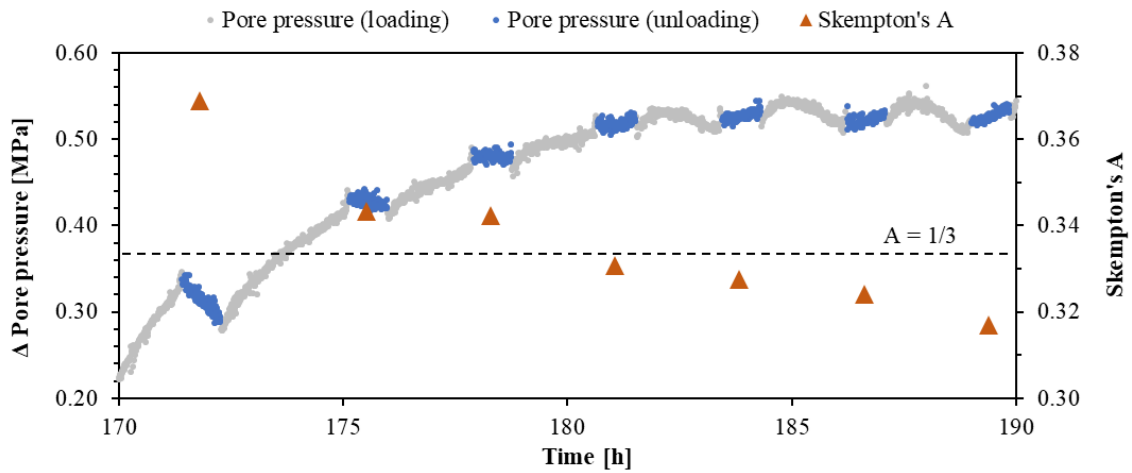


**Figure 5.5:** Pore pressure measurements and $A$ estimates during the strain-driven part of experiment (test C1)

Pore pressure – axial stress slope estimation for unloading steps 1, 4 and 7 of test C1 is shown in Figure 5.6. In experiment C1 we managed to observe a gradual transition from unloading-induced decrease to unloading-induced increase of $p_f$. This translates to a drop of $A$ value, as visualized in Figure 5.5, where a horizontal line at $A = 1/3$ marks the turning point of the undrained pore pressure response. During the strain-driven parts of tests C1 and S1-S8 the stresses followed the triaxial stress path yielding significantly larger $\Delta p_f$. Hence, in these tests we estimated $A$ parameter simply by comparison of the pore pressure and the axial stress readings directly before and after unloading. To quantitatively describe the correlation between the changes in $A$ with the development of plastic deformation in the samples, it was necessary to estimate plastic strains. We performed that by extrapolation of quasi-linear parts of the stress-strain curves during unloading, as shown in Figure 5.7. In most of the tests radial stress was kept constant, so we used axial stress for both axial and radial plastic strains estimation. Plastic volumetric strain was calculated using estimated values of axial and radial plastic strains.

We found the ratio between elastic and total axial strains ($\varepsilon_{ax}^{el}/\varepsilon_{ax}^{tot}$) to be the parameter with the most consistent and the most linear relationship with $A$. This parameter (referred to as parameter $P$ later on) is similar to the most basic definition of "brittleness" (Coates and Parsons 1966; Holt et al. 2011; Mews et al. 2019), but instead of referring to strains at failure, it expresses the ratio between the strains at the beginning of unloading. The relation between poroelastic parameter $A$ and parameter $P$ is shown in Figure 5.8. The figure contains all A values measured during the experimental part of the study. The datapoints were divided into groups according to the angle $\theta$ between the vertical axis of the sample (i.e., direction of the maximum principal stress) and the vector normal to the sample bedding, governing the angular dependence of $A$ given by Equation (5.5). Parameter $A$ values in all angle groups decline with decrease of parameter $P$*.

The largest reduction in an individual sample was observed during test S2 in which A dropped from 0.47 ($P = 0.78$) to 0.30 ($P = 0.28$). In the rest of the tests $A$ decreased by less than 0.1. To be able to compare between angle groups at specific values of $P$ and to extract trends potentially useful in geomechanical modelling, we performed linear regression for the datapoints representing samples with $\theta = 0°$ and 60°.The coefficients of determination $R^2$ of the linear fits were 0.83 and 0.60, respectively. The quality of the fit in the latter group is significantly lower than that in the 0° angle group. However, its slope recreates well the character and amplitude of change for each of the individual tests (S4, S5 and S6). In the 30° and 90° angle groups we determined slope and intercept of lines passing through the only available pairs of data points.

To validate the fits, we compared the values of $A$ estimated with the use of the

*There was an error in the original published text, where the term *increase* was used instead of *decrease*. This was corrected despite concerns from my dear supervisor, Rune, who cautioned (for the records, he was laughing hard while making this comment) that "paying attention to minus or plus signs or factors smaller than ten may be perceived as a sign of weakness."

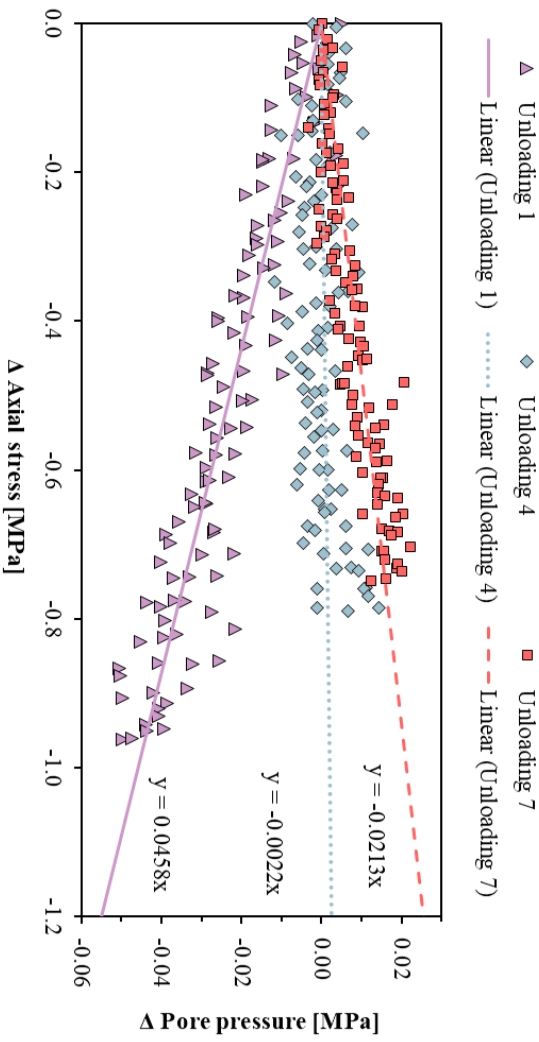


**Figure 5.6:** Linear approximation of pore pressure changes in relation to axial stresses in constant mean stress conditions (test C1).

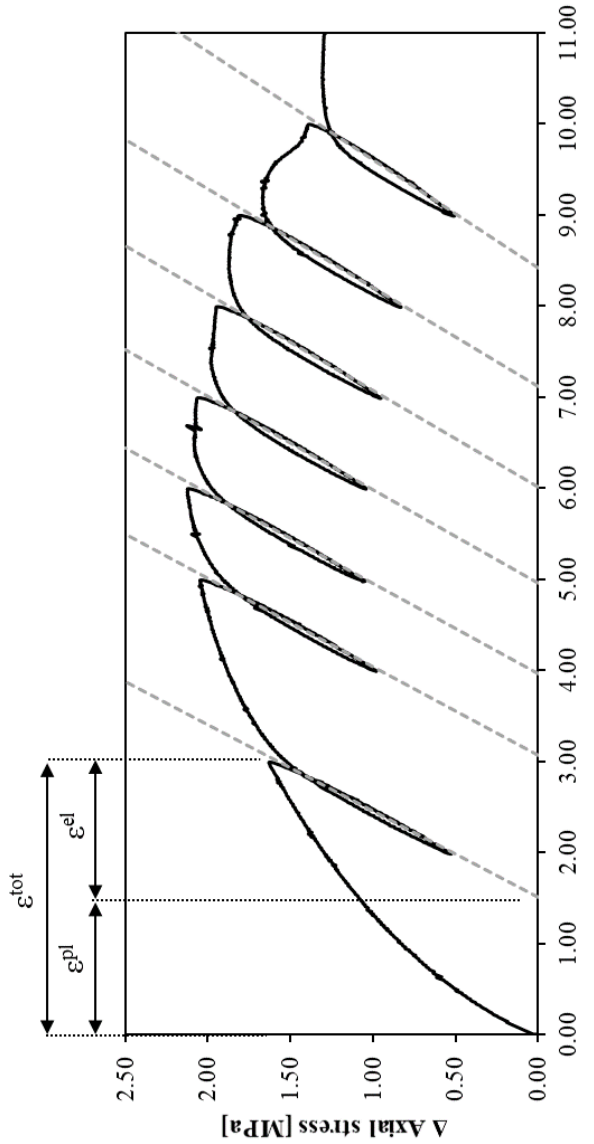


**Figure 5.7:** Axial plastic strain estimation in the strain-driven part of test C1.

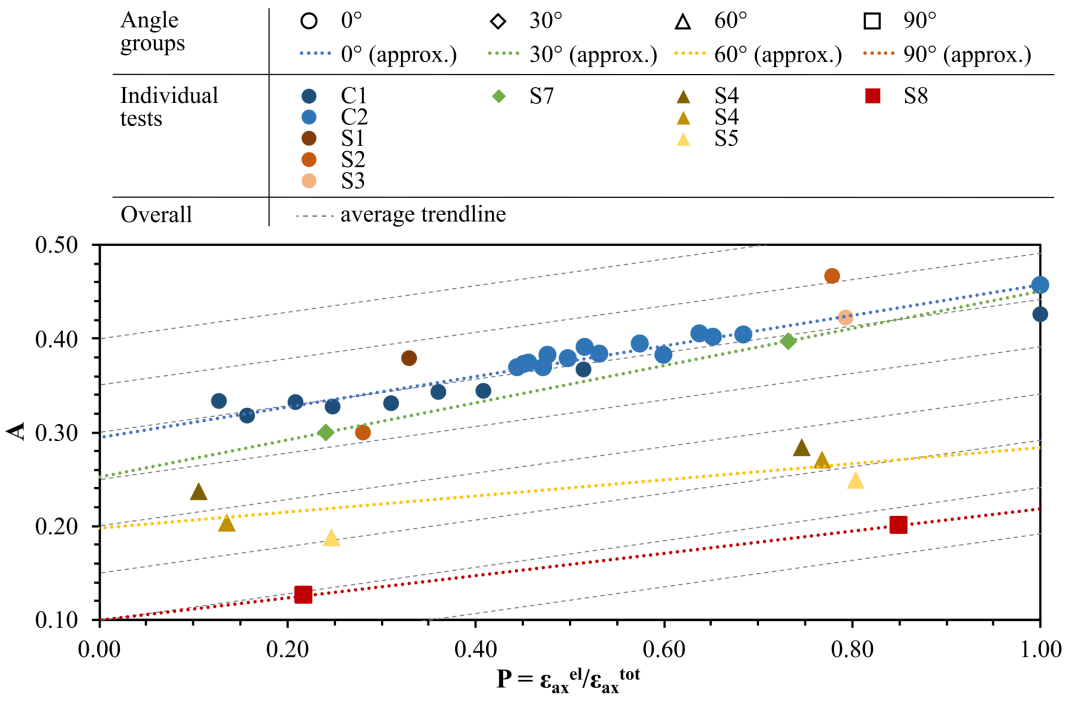


**Figure 5.8:** Evolution of parameter $A$ associated with accumulating plastic deformation. The data points represent the results of all 10 tests grouped according to the angle between the vertical axis of the corresponding sample and the vector normal to the sample lamination. Dotted lines represent linear fit lines (0° and 60°) or extrapolated lines connecting the only available data points (30° and 90°). Dashed lines show the average slope of all the linear approximations.

linear trend lines at $P = 0.1$, 0.5 and 1 against the theoretical curves describing the angular dependency of parameter $A$ (Equation 5.5). The first set of curves was obtained by direct determination of parameters $B_1$ and $B_3$ using $A$ estimates for $\theta = 0$. The second group of curves was obtained by numerical optimization of $B_1$ and $B_3$ to provide the best possible fit to experimental $A$ values at all angles. In both cases, it was assumed that TI symmetry of the samples was maintained (i.e., Equations 5.3 and 5.5 are applicable) and $B = 0.85$. The results, shown in Figure 5.9, indicate a good fit between the experimentally derived $A$ and both theoretical curves at $P = 1$, where $A$ value is not yet affected by plasticity. The curve obtained from measurements on samples with inclination angle $\theta = 0$ approximated at $P = 1$ relatively well predicts $A$ values at higher inclination angles, and hence increases our confidence in the measurements and the linear fit accuracy.

The comparison of the experimentally determined values and both theoretical curves for $P = 0.5$ shows large discrepancies at higher angles. For $P = 0.1$, theoretical curves diverge significantly from corresponding data points, and the curve computed with experimental $A$ values at $\theta = 0$ fails to predict the trend of $A$ change, which remains typical for TI symmetry. This discrepancy indicates that it is no longer possible to directly predict $A$ values at higher inclination angles using $A(\theta = 0)$ once plastic effects become relevant and points to a need to introduce and differentiate between elastic and non-elastic components in Skempton's equations.

To highlight any possible systematic changes of parameter $A$ evolution character with the angle $\theta$, in Figure 5.8 we added background lines with inclination given by the average of slopes of all linear approximations shown in the plot. The evident lack of systematic trend change may indicate an approximately constant rate of $A$ degradation regardless of the inclination angle, however a more extensive experimental study of pore pressure response in samples drilled at non-zero $\theta$ angles is needed to verify this observation. The average trendline represents quite well the general character of $A$ change with accumulation of plastic deformation and may be used as a simplistic tool for geomechanical modelling of the undrained pore pressure response in shales. This can prove to be of great importance for modelling of reservoir overburden shales behavior in the direct proximity of faulting zones, where the largest impact of plastic deformation is expected.

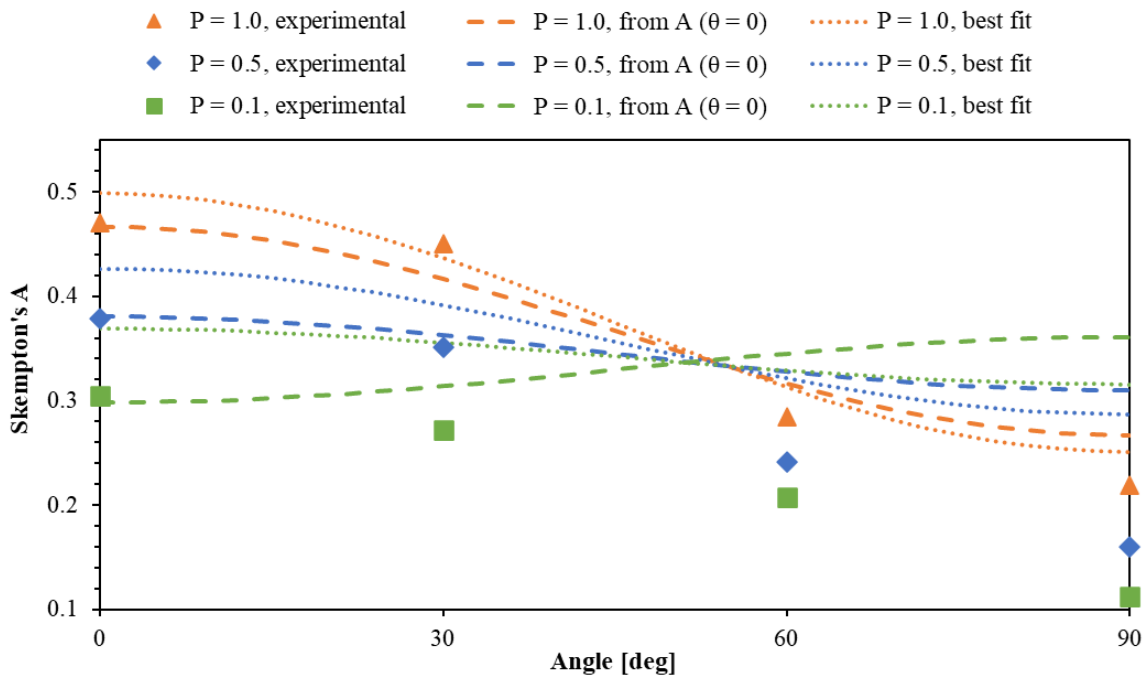


**Figure 5.9:** Comparison of $A$ values extracted from the experimental data and theoretically computed curves. The angle $\theta$ expresses the difference between the symmetry axis of the sample and the direction of the maximum principal stress.

## 5.4 Conclusions

Our experimental study focusing on poroelastic parameters measured during unloading indicates that the parameter $B$ is not significantly affected by plasticity, while $A$ value clearly decreases with accumulation of plastic deformation in shale samples. This stands in contrast with observations of pore pressure coefficients reported by e.g. Muir Wood (1990), which may be related to the fact that the measurements of $A$ and $B$ are taken uniquely during unloading stages, and hence they correspond only to deformation within corresponding elastic regions. We found coefficient $P = \varepsilon_{ax}^{el}/\varepsilon_{ax}^{tot}$ to be a suitable parameter to approximate and potentially model changes of $A$ in shales in the direct proximity of faulting zones.

We documented an extreme case of the undrained pore pressure character change. In test C1 axial unloading in the constant mean stress conditions, initially yielding pore pressure decrease, started producing pressure increase once enough plastic damage accumulated. We observed gradual deviation of experimentally estimated $A$ parameter from theoretical purely elastic predictions for TI symmetry. The experimental results maintain the typical shape of $A$ – inclination angle $\theta$ curve, but measured $A$ are shifted towards lower values. This suggest a need to introduce and differentiate between elastic and non-elastic terms in equations (like Equation (5.1)) for the undrained pore pressure response to stress, which will be the object of future work.

Potential next steps would be to carry out a more systematic study on samples drilled at non-zero angle to the rock bedding to explore in detail the relationship between $A$ degradation trends and increasing inclination angles. Finally, we plan to address the impact of volumetric plastic strain on the undrained pore pressure response in shales during rock loading and the integration of the changing character of the pore pressure response with existing elastoplastic rock models.

## 5.5 Acknowledgements

This publication has been produced with support from the NCCS Centre, performed under the Norwegian research program Centres for Environment-friendly Energy Research (FME). The authors acknowledge the following partners for their contributions in the project: Aker Solutions, ANSALDO Energia, CoorsTek Membrane Sciences, Electromagnetic Geoservices (EMGS), Equinor, Gassco, KROHNE, Larvik Shipping, Lundin, Norcem, Norwegian Oil and Gas, Quad Geometrics, TOTAL, Vår Energi, and the Research Council of Norway (257579/E20). This work was also supported by the Research Council of Norway, Aker BP ASA, BP Exploration Operating Company Ltd, ConocoPhillips Skandinavia AS, Equinor Energy AS, Lundin Norway AS, Petrobras and Total E&P Norge AS through the KPN project “Shale Barrier Toolbox: Designing future wells for efficient com-

pletion and simpler P&A" (280650/E30) at SINTEF Industry.

# References


Biot, M. A. (1941). 'General Theory of Three-Dimensional Consolidation'. In: *Journal of Applied Physics* 12.2, pp. 155–164. DOI: 10.1063/1.1712886. URL: https://aip.scitation.org/doi/abs/10.1063/1.1712886.

Biot, M. A. (1962). 'Mechanics of Deformation and Acoustic Propagation in Porous Media'. In: *Journal of Applied Physics* 33.4, pp. 1482–1498. DOI: 10.1063/1.1728759. URL: https://aip.scitation.org/doi/abs/10.1063/1.1728759.

Cheng, A. H. D. (1997). 'Material coefficients of anisotropic poroelasticity'. In: *International Journal of Rock Mechanics and Mining Sciences* 34.2, pp. 199–205. ISSN: 1365-1609. DOI: https://doi.org/10.1016/S0148-9062(96)00055-1. URL: http://www.sciencedirect.com/science/article/pii/S0148906296000551.

Coates, D. F. and R. C. Parsons (1966). 'Experimental criteria for classification of rock substances'. In: *International Journal of Rock Mechanics and Mining Sciences & Geomechanics Abstracts* 3.3, pp. 181–189. ISSN: 0148-9062. DOI: https://doi.org/10.1016/0148-9062(66)90022-2. URL: https://www.sciencedirect.com/science/article/pii/0148906266900222.

Ewy, R. (2015). 'Shale/claystone response to air and liquid exposure, and implications for handling, sampling and testing'. In: *International Journal of Rock Mechanics and Mining Sciences* 80, pp. 388–401. DOI: 10.1016/j.ijrmms.2015.10.009.

Ewy, R. (2018). 'Practical approaches for addressing shale testing challenges associated with permeability, capillarity and brine interactions'. In: *Geomechanics for Energy and the Environment* 14. DOI: 10.1016/j.gete.2018.01.001.

Fjær, E., R. Holt and A. Stroisz (2012). 'Combining Static And Dynamic Measurements For Evaluation of Elastic Dispersion'. In: *46th U.S. Rock Mechanics/Geomechanics Symposium*. Vol. All Days. ARMA-2012-537.

Fjær, E., A. M. Stroisz and R. M. Holt (2013). 'Elastic Dispersion Derived from a Combination of Static and Dynamic Measurements'. In: *Rock Mechanics and Rock Engineering* 46.3, pp. 611–618. ISSN: 1434-453X. DOI: 10.1007/s00603-013-0385-8. URL: https://doi.org/10.1007/s00603-013-0385-8.

Head, K. and R. Epps (2011). *Manual of Soil Laboratory Testing*. 3rd. Vol. II. Whittles Publishing.

Henkel, D. J. and N. H. Wade (1966). 'Plane strain tests on a saturated remolded clay'. In: *Journal of Soil Mechanics & Foundations* 92, pp. 67–80.

Henkel, D. (1960). *The shear strength of saturated remoulded clays*. Conference Paper.

Holt, R., A. Bakk, J. F. Stenebråten, A. Bauer and E. Fjær (2018a). *Skempton's A — A Key to Man-Induced Subsurface Pore Pressure Changes*. Conference Paper.

Holt, R., E. Fjaer, O. Nes and H. Alassi (2011). 'A Shaly Look At Brittleness'. In: *45th U.S. Rock Mechanics / Geomechanics Symposium*. Vol. All Days. ARMA-11-366.

Holt, R. M., A. Bakk and A. Bauer (2018b). 'Anisotropic poroelasticity: Does it apply to shale?' In: *SEG Technical Program Expanded Abstracts 2018*, pp. 3512–3516. DOI: 10.1190/segam2018-2994785.1. URL: https://library.seg.org/doi/abs/10.1190/segam2018-2994785.1.

Holt, R. M., A. Bauer and A. Bakk (2018c). 'Stress-path-dependent velocities in shales: Impact on 4D seismic interpretation'. In: *GEOPHYSICS* 83.6, MR353–MR367. DOI: 10.1190/geo2017-0652.1. URL: https://library.seg.org/doi/abs/10.1190/geo2017-0652.1.

Holt, R. M. and J. F. Stenebråten (2013). 'Controlled laboratory experiments to assess the geomechanical influence of subsurface injection and depletion processes on 4D seismic responses'. In: *Geophysical Prospecting* 61.s1, pp. 476–488. ISSN: 0016-8025. DOI: https://doi.org/10.1111/1365-2478.12040. URL: https://onlinelibrary.wiley.com/doi/abs/10.1111/1365-2478.12040.

Janbu, N., R. Roque, H. Lango and T. Tjelta (1990). 'Cyclic load testing of contractant clays from Gullfaks C : Proc BOSS'88, Trondheim, June 1988 V1, P32U 341. Publ Trondheim: Tapir, 1988'. In: *International Journal of Rock Mechanics and Mining Sciences & Geomechanics Abstracts* 27.

Lockner, D. and S. Stanchits (2002). 'Undrained poroelastic response of sandstones to deviatoric stress change'. In: *Journal of Geophysical Research* 107. DOI: 10.1029/2001JB001460.

Lozovyi, S. and A. Bauer (2018). 'Static and dynamic stiffness measurements with Opalinus Clay'. In: *Geophysical Prospecting* 67. DOI: 10.1111/1365-2478.12720.

Mews, K. S., M. M. Alhubail and R. G. Barati (2019). 'A Review of Brittleness Index Correlations for Unconventional Tight and Ultra-Tight Reservoirs'. In: *Geosciences* 9.7, p. 319. ISSN: 2076-3263. URL: https://www.mdpi.com/2076-3263/9/7/319.

Muir Wood, D. (1990). *Soil behaviour and critical state soil mechanics*. Cambridge: Cambridge University Press. ISBN: 9780521337823.

Skempton, A. W. (1954). 'The Pore-Pressure Coefficients A and B'. In: *Géotechnique* 4.4, pp. 143–147. DOI: 10.1680/geot.1954.4.4.143. URL: https://www.icevirtuallibrary.com/doi/abs/10.1680/geot.1954.4.4.143.

Wild, K., M. Barla, G. Turinetti and F. Amann (2017). 'A multi-stage triaxial testing procedure for low permeable geomaterials applied to Opalinus Clay'. In: *Journal of Rock Mechanics and Geotechnical Engineering* 9. DOI: 10.1016/j.jrmge.2017.04.003.

# Part II

# Non-linear seismic velocity model

# PAPER E: Third-order elastic tensor of shales determined through ultrasonic velocity measurements

Marcin Ireneusz Duda[1], Audun Bakk[2], Rune Martin Holt[1]

[1] Norwegian University of Science and Technology, 7031 Trondheim, Norway
[2] Sintef Petroleum, 7031 Trondheim, Norway

Published in the Proceedings of the 54th US Rock Mechanics/Geomechanics Symposium held in Golden, Colorado, USA, 28 June-1 July 2020

## Abstract

Static and dynamic behavior of isotropic or anisotropic media, including rocks, are conveniently described with a second-order stiffness matrix using the Voigt notation, which linearly relates stress changes to strains. However, experimental and field observations indicate that the dynamic stiffness of rocks is stress dependent. We investigate a model proposed by Fuck and Tsvankin employing a constitutive third-order elastic tensor to describe the non-linear strain sensitivity of the stiffness. By using laboratory measurements of strains and ultrasonic P- and S-wave velocities in multiple directions, we were able to invert for all the third-order parameters. We used the third-order elastic tensor to model changes in ultrasonic velocities and investigated the impact of different third-order tensor component optimization schemes on the accuracy of the velocity estimates. To our knowledge this is the first fit of dynamic stiffness of a shale to a third order constitutive model that is not restricted to isotropic strain sensitivity.

## 6.1 Introduction

Elastic properties of most of the earth crust rocks are direction-dependent (e.g., Thomsen 1986), which makes anisotropy an important factor for rock stiffness and seismic wave velocity analysis. The static and dynamic properties of an anisotropic medium are usually represented by a second-order elastic (SOE) matrix $C_{ij}$, which linearly relates stress changes with corresponding strains (Fjær et al. 2021).

However, experimental and field data suggest that the dynamic stiffness of rocks is stress-dependent (e.g., Johnson and Rasolofosaon 1996), i.e. the relationship between stress and deformation is non-linear. This behavior can be described in terms of stiffening grain contacts (Bachrach and Avseth 2008; Mindlin 1949; Walton 1987) or with the use of crack-based models (Budiansky and O'Connell 1976; Fjaer 2006; Hudson 1981). Alternatively, we can use higher order constitutive models (e.g., Prioul et al. 2004), which until now have not been systematically investigated for sedimentary rocks.

Our aim was to derive a third-order elastic (TOE) tensor $c_{ijk}$ which we could use to approximate the dynamic behavior of transversely isotropic shales under different stress state development scenarios and verify it using laboratory data collected on shale samples. This approach is based on a fully physical strain-dependent third-order constitutive model for which we assume vertical transverse isotropy (VTI, i.e. the symmetry axis normal to the plane of isotropy) of stiffnesses and the applied stresses, which allowed us to limit the number of model parameters. Contrary to previous studies (Fuck et al. 2009; Johnson and Rasolofosaon 1996; Prioul et al. 2004), we do not assume isotropic strain sensitivity of the velocities, which may seem to be an over-simplification for inherently anisotropic materials like shales. Velocity changes are measured in multiple directions for different stress changes. These data are used to determine the elastic parameters of two different non-linear models and to evaluate their performance.

## 6.2 Theoretical Background

The starting point for our model is the TOE tensor proposed by Fuck and Tsvankin (2009). The relationship between changes in stiffness and changes in strains for a VTI medium, where the anisotropy symmetry axis coincides with the axial loading direction, becomes:

$$C_{ij} = C_{ij}^0 + \Delta C_{ij} = C_{ij}^0 + c_{ijk}\Delta\varepsilon_k, \tag{6.1}$$

where $C_{ij}^0$ is the stiffness measured at the in-situ stress. Due to Voigt's notation $c_{ijk} = c_{ikj} = c_{kij} = c_{jik} = c_{jki} = c_{kji}$. For the general (triclinic) case, the distinct VTI components become:

$$
\begin{aligned}
C_{11} &= C_{11}^0 + c_{111}\Delta\varepsilon_1 + c_{112}\Delta\varepsilon_2 + c_{113}\Delta\varepsilon_3,\\
C_{12} &= C_{12}^0 + c_{112}\Delta\varepsilon_1 + c_{122}\Delta\varepsilon_2 + c_{123}\Delta\varepsilon_3,\\
C_{13} &= C_{13}^0 + c_{113}\Delta\varepsilon_1 + c_{123}\Delta\varepsilon_2 + c_{133}\Delta\varepsilon_3,\\
C_{22} &= C_{22}^0 + c_{122}\Delta\varepsilon_1 + c_{222}\Delta\varepsilon_2 + c_{223}\Delta\varepsilon_3,\\
C_{23} &= C_{23}^0 + c_{123}\Delta\varepsilon_1 + c_{223}\Delta\varepsilon_2 + c_{233}\Delta\varepsilon_3,\\
C_{33} &= C_{33}^0 + c_{133}\Delta\varepsilon_1 + c_{233}\Delta\varepsilon_2 + c_{333}\Delta\varepsilon_3,\\
C_{44} &= C_{44}^0 + c_{144}\Delta\varepsilon_1 + c_{244}\Delta\varepsilon_2 + c_{344}\Delta\varepsilon_3,\\
C_{55} &= C_{55}^0 + c_{155}\Delta\varepsilon_1 + c_{255}\Delta\varepsilon_2 + c_{355}\Delta\varepsilon_3,\\
C_{66} &= C_{66}^0 + c_{166}\Delta\varepsilon_1 + c_{266}\Delta\varepsilon_2 + c_{366}\Delta\varepsilon_3.
\end{aligned}
\tag{6.2}
$$

Transverse isotropic symmetry puts additional constrains on the tensor elements:

$$
\begin{aligned}
c_{112} &= c_{111} - c_{166} - 3c_{266},\\
c_{122} &= c_{111} - 2c_{166} - 2c_{266},\\
c_{222} &= c_{111} + c_{166} - c_{266},\\
c_{223} &= c_{113},\\
c_{123} &= c_{113} - 2c_{366},\\
c_{244} &= c_{155} = c_{144} + 2c_{456},\\
c_{255} &= c_{144},\\
c_{355} &= c_{344}.
\end{aligned}
\tag{6.3}
$$

In consequence, the number of parameters reduces to ten: $c_{111}$, $c_{113}$, $c_{133}$, $c_{144}$, $c_{166}$, $c_{266}$, $c_{333}$, $c_{344}$, $c_{366}$ and $c_{456}$. By assuming that the radial strains are equal ($\Delta\varepsilon_1 = \Delta\varepsilon_2$, due to equal stiffnesses and stress changes in the horizontal plane) we reduce Equation (6.2) and Equation (6.3) to:

$$
\begin{aligned}
C_{11} &= C_{11}^0 + (2c_{111} - c_{166} - 3c_{266})\Delta\varepsilon_1 + c_{113}\Delta\varepsilon_3,\\
C_{13} &= C_{13}^0 + (2c_{113} - 2c_{366})\Delta\varepsilon_1 + c_{133}\Delta\varepsilon_3,\\
C_{33} &= C_{33}^0 + 2c_{133}\Delta\varepsilon_1 + c_{333}\Delta\varepsilon_3,\\
C_{44} &= C_{44}^0 + (2c_{144} + 2c_{456})\Delta\varepsilon_1 + c_{344}\Delta\varepsilon_3,\\
C_{66} &= C_{66}^0 + (c_{166} + c_{266})\Delta\varepsilon_1 + c_{366}\Delta\varepsilon_3.
\end{aligned}
\tag{6.4}
$$

The assumption of isotropic radial strains results in additional constraints for the third-order elastic coefficients. This gives an opportunity to reparametrize the system in order to obtain a unique solution and limit the overall number of coefficients. First, the $c_{144}$ and $c_{456}$ coefficients are unique for $C_{44}$, and therefore can be substituted by:

$$
c_{144}^* = 2c_{144} + 2c_{456}. \tag{6.5}
$$

Furthermore, $c_{111}$ is unique for $C_{11}$, and consequently $c_{166}$ and $c_{266}$ in $C_{66}$ may be

reparametrized, giving:

$$\begin{aligned} c^*_{111} &= 2c_{111} - c_{166} - 3c_{266}, \\ c^*_{166} &= c_{166} + c_{266}. \end{aligned} \tag{6.6}$$

Consequently, the eight unique model parameters are: $c^*_{111}$, $c_{113}$, $c_{133}$, $c^*_{144}$, $c^*_{166}$, $c_{333}$, $c_{344}$ and $c_{366}$. The reparametrized system of Equation (6.4):

$$\begin{aligned} C_{11} &= C^0_{11} + c^*_{111}\Delta\varepsilon_1 + c_{113}\Delta\varepsilon_3, \\ C_{13} &= C^0_{13} + 2(c_{113} - c_{366})\Delta\varepsilon_1 + c_{133}\Delta\varepsilon_3, \\ C_{33} &= C^0_{33} + 2c_{133}\Delta\varepsilon_1 + c_{333}\Delta\varepsilon_3, \\ C_{44} &= C^0_{44} + c^*_{144}\Delta\varepsilon_1 + c_{344}\Delta\varepsilon_3, \\ C_{66} &= C^0_{66} + c^*_{166}\Delta\varepsilon_1 + c_{366}\Delta\varepsilon_3. \end{aligned} \tag{6.7}$$

It is worth noting that all the TOE tensor elements in Equation (6.7), except for $c^*_{144}$ and $c_{344}$, are influencing (directly or indirectly) more than one $C_{ij}$. Therefore, the determination of these TOE coefficients implies a joint inversion of all model elements (except for $C_{44}$).

## 6.3 Experimental data

For the purpose of this study we analyzed a field shale sample cored at 2750 meters true vertical depth in the North-Sea. Clay minerals content in the sample is approximately 75%. It has a porosity of 29% and a density of 2.23 g/cm$^3$.

The experimental dataset, acquired in the SINTEF Formation Physics Laboratory, consists of records of axial and radial stresses and strains, pore pressure, temperature, and ultrasonic P- and S-wave travel times.

The measurements of ultrasonic P-wave travel times were carried out for several propagation angles, i.e. angles between the direction of wave propagation and the symmetry axis of the sample (bedding normal): 0° (axial, $v_{Pz}$), 37°, 47°, 68° and 90° (radial, $v_{Pr}$). The travel-times of the S-waves were measured along the axial and the radial directions ($v_{Sz}$ and $v_{Srr}$).

The data were recorded under different stress paths ($\kappa$), i.e. different ratios between the radial and the axial stress changes [Equation (6.8)], around the expected in-situ stress. Between every undrained loading-unloading cycle, there was a short drainage stage designed to change the pore pressure back to the expected true in-situ pore pressure. Figure 6.1 shows the time-development of the static and dynamic measurements during the experiment.

$$\kappa = \frac{\Delta\sigma_{radial}}{\Delta\sigma_{axial}}. \tag{6.8}$$

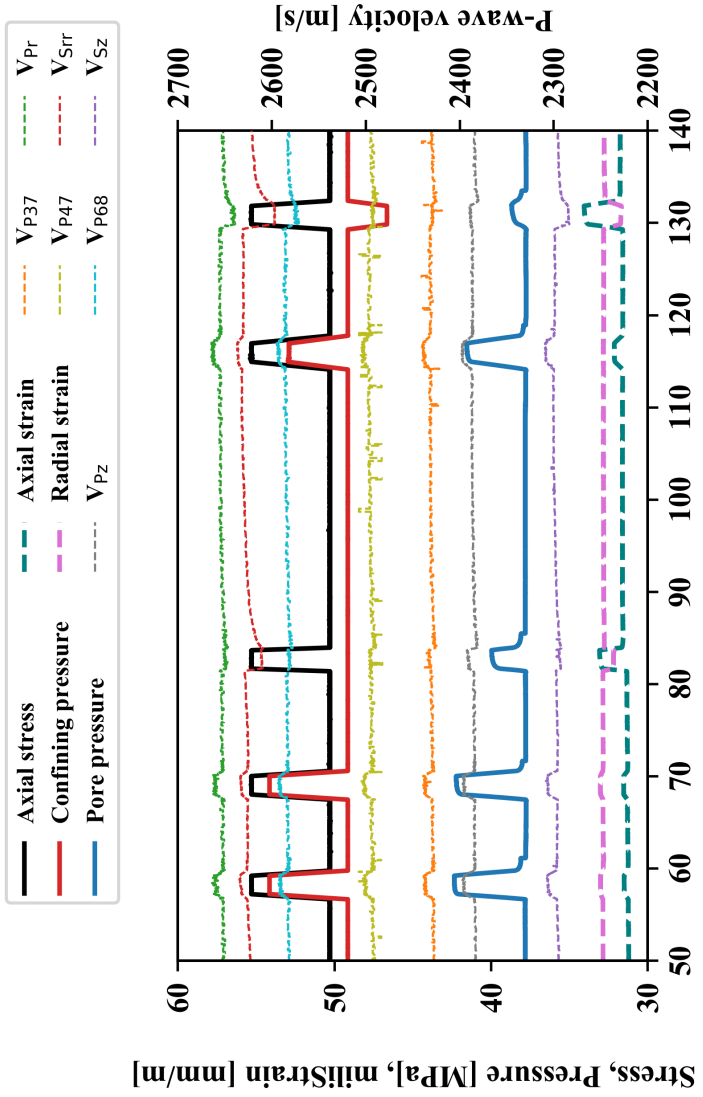


**Figure 6.1:** Laboratory test results (stresses, strains, pore pressure and ultrasonic velocities). The test consisted of two repeated hydrostatic cycles ($\kappa = \Delta\sigma_{radial}/\Delta\sigma_{axial} = 1$, stages 1-4, cf. Table 1), one triaxial cycle ($\kappa = 0$, stages 5 and 6), one K0 cycle (no radial strain, here $\kappa \approx 0.75$, stages 7 and 8) and one constant mean stress (abbreviated as CMS, $\kappa = -0.5$, stages 9 and 10) loading-unloading cycle.

## 6.4 Methodology

In order to determine ultrasonic P- and S-wave velocities within the sample, we need to estimate travel times and combine them with information on sample dimensions given by initial sample length, radius and recorded strains. We use axial and radial velocities measured directly after the initial consolidation phase to estimate dynamic stiffness parameters $C_{11}$, $C_{33}$, $C_{44}$ and $C_{66}$.

$$\begin{aligned} C_{11} &= v_{Pr}^2 \rho, \\ C_{33} &= v_{Pz}^2 \rho, \\ C_{44} &= v_{Sz}^2 \rho, \\ C_{66} &= v_{Sr}^2 \rho, \end{aligned} \tag{6.9}$$

where $\rho$ is bulk density*.

Estimation of $C_{13}$ requires a different approach (Thomsen 1986). Due to the small size of ultrasonic transducers we used in the experiment, we assume the oblique P-wave velocity measurements (at 37°, 47°, and 68°) to represent true group velocities. We have confirmed this assumption by numerical modelling. Consequently, we approximate $C_{13}$ by fitting the estimated group velocities to the measured group velocities by minimization of root-mean-square (RMS) error. The phase velocity $v_P$ at phase angle $\theta$ expressed by the elastic constants in a transversely isotropic medium is given by Thomsen (1986):

$$v_p(\theta) = \left( \frac{1}{2\rho} \left[ C_{33} + C_{44} + (C_{11} - C_{33})\, sin^2\theta + D(\theta) \right] \right)^{\frac{1}{2}}, \tag{6.10}$$

where the $D^2(\theta)$ is defined as:

$$\begin{aligned} D^2(\theta) = &(C_{33} - C_{44})^2 \\ &+ 2\left[2\left(C_{13} + C_{44}\right)^2 - \left(C_{33} - C_{44}\right)\left(C_{11} + C_{33} - 2C_{44}\right)\right] \sin^2\theta \\ &+ \left[\left(C_{11} + C_{33} - 2C_{44}\right)^2 - 4\left(C_{13} + C_{44}\right)^2\right] \sin^4\theta. \end{aligned} \tag{6.11}$$

The corresponding group angle $\phi$ becomes:

$$\phi\left(\theta\right) = tan^{-1}\left( \left[ \tan\theta + \frac{1}{v_p}\frac{dv_p}{d\theta} \right] \left[ 1 - \frac{\tan\theta}{V_p}\frac{dv_p}{d\theta} \right]^{-1} \right), \tag{6.12}$$

and finally, the group velocity $V_P$ is:

$$V_P^2\left(\phi\right) = v_p^2(\theta) + \left( \frac{dv_p}{d\theta} \right). \tag{6.13}$$

*In the original published text, all squares in Equation (6.9) were missing - this has been corrected in this text.

An example of optimization of the fit of $C_{13}$ to the experimental data is provided in Figure 6.2.

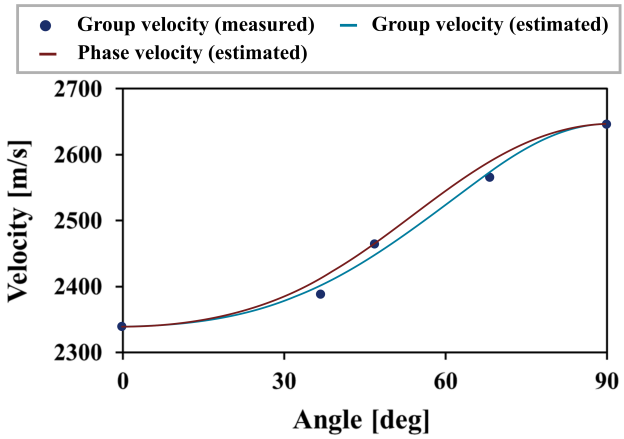


**Figure 6.2:** Example of $C_{13}$ estimation plot and the relationship between group and phase velocity angular dependency. In this case, the estimated $C_{13} = 7.0$ GPa, or alternatively Thomsen's $\delta = 0.12$.

To estimate the TOE tensor elements, for every undrained loading or unloading step we compare the reference stress state, just before the stress change, with the stressed state after the change. In both cases, we average over 20 data points at the end of the consolidation periods. For each of the points we estimate the reference stiffness $C_{ij}^0$ and the final stiffnesses $C_{ij}$ with associated strains $\varepsilon_k$, and express them as stiffness and strain changes corresponding to the given loading or unloading stage. Then, we estimate the eight unique third-order elastic constants by numerically solving Equation (6.4), i.e. optimizing the values of $c_{ijk}$ tensor to minimize the RMS error between the modelled and the experimental $C_{ij}$ matrix.

We can adjust the input to the available data. In order to have a (over-)determined system, we use at least two distinct stress cycles as input for the inversion of the eight unique TOE tensor elements. Generally, some of the expressions from Equation (6.4) can be omitted in the inversion process (due to e.g. lack of input data), but once the expression for $C_{13}$ is not used, the physical relationship between the elastic components of the model is lost. Therefore, even if the model predicts velocity changes with high accuracy, the elements of the TOE tensor should not be interpreted as medium's physical parameters.

## 6.5 Results and discussions

Results of the inversion for the TOE tensor are shown in Table 6.1. First, we inverted for $c_{ijk}$ using data points from all available loading-unloading cycles (column "all $\kappa$"). Then we combined the third-order coefficients with recorded strains to obtain updated SOE matrix $C_{ij}$ elements [Equation (6.7)] and back-calculated velocity changes [Equation (6.9)-Equation (6.13)], shown in Figure 6.3.

Modelling of P- and S-wave velocity changes captured all general trends observed in the experimental data. Modelled radial P-wave velocities are slightly overestimated, whereas the modelled changes of vertical P-waves are generally too conservative (Figure 6.3, plot A), which is reflected in a relatively high RMS error.

| Stress paths $\kappa$[-] | all $\kappa$ | $\kappa = 1$ & $\kappa \approx 0.75$ | $\kappa = 0$ & $\kappa$ = -0.5 | $\kappa = 1$ & $\kappa$ = -0.5 |
|---|---|---|---|---|
| Stage no. | 1,2,5-10 | 1,2,7,8 | 5,6,9,10 | 1,2,9,10 |
| $c_{ijk}$ [GPa] | | | | |
| $c_{113}$ | 130.4 | 146.4 | 165.0 | 114.7 |
| $c_{133}$ | 104.6 | 49.1 | 103.0 | 114.9 |
| $c_{333}$ | 127.4 | 232.4 | 122.1 | 129.1 |
| $c_{344}$ | 31.6 | 34.8 | 46.7 | 28.3 |
| $c_{366}$ | 26.3 | 51.9 | 61.2 | 8.9 |
| $c^*_{111}$ | 388.8 | 291.4 | 468.4 | 360.4 |
| $c^*_{144}$ | 88.6 | 71.7 | 122.8 | 82.7 |
| $c^*_{166}$ | 111.4 | 24.1 | 191.1 | 74.8 |

**Table 6.1:** Summary of inversion for the full TOE tensor. The data have been divided according to input information used for inversion of $c_{ijk}$ tensor (selection of stress paths, Equation (6.8), i.e. loading/unloading stages used to estimate the TOE tensor): "all $\kappa$" – all available stress paths, all cycles except the repeated hydrostatic cycle ($\kappa = 1$, stages 3 and 4, Figure 6.1), used as a reference case for further comparison; "$\kappa = 1$ & $\kappa = 0.75$" – hydrostatic and K0, where $\kappa \approx 0.75$ gives $\Delta\varepsilon_r = 0$ for this shale; "$\kappa = 0$ & $\kappa$ = -0.5" – triaxial and constant mean stress; and "$\kappa = 1$ & $\kappa$ = -0.5" – hydrostatic and constant mean stress

In the case of S-waves (Figure 6.3, plot B), the development of vertical velocity changes is well recreated. However, radial S-wave modelling accuracy varies from one stress path to another – the modelled velocities are the most accurate for the hydrostatic and the K0 stress paths.

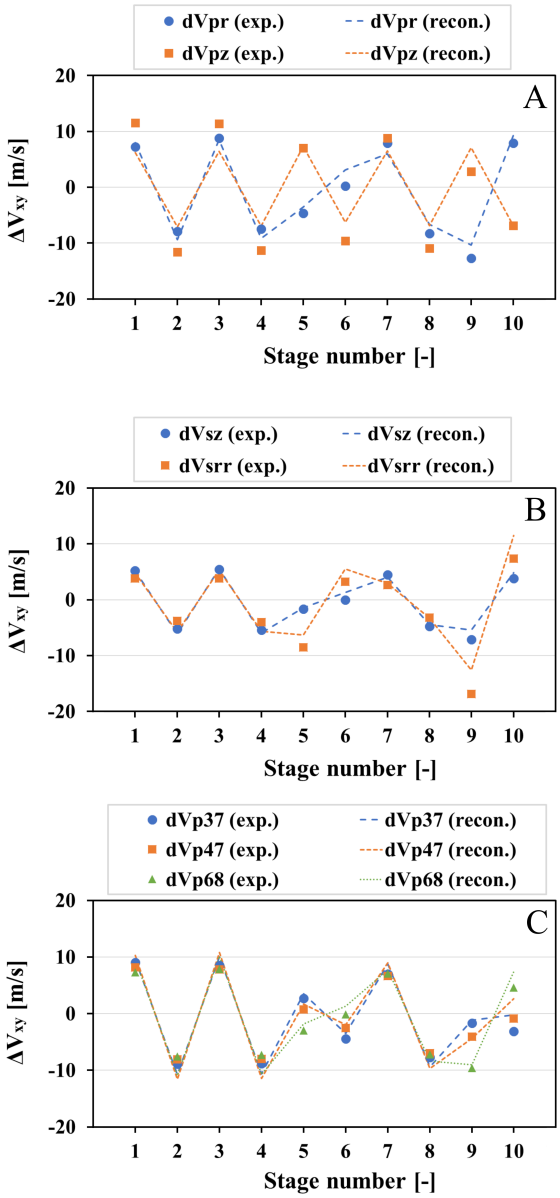


**Figure 6.3:** Comparison of experimentally measured ("exp.") and modelled ("recon.") ultrasonic velocity changes. Predictions of velocity changes were obtained with TOE tensor estimated using data from all stress paths (Table 1, column "all $\kappa$"). Plot A: P-waves, radial (dVpr) and vertical (dVpz).Plot B: S-waves, vertical (dVsz) and radial and horizontally-polarized (dVsrr). Plot C: P-wave, measured at 37° (dVp37), 47° (dVp47) and 68° (dVp68).

The back-calculated (using inverted TOE tensor elements and strains) velocities of the oblique P-waves (Figure 6.3, plot C) fit the experimental data with high accuracy, both in terms of absolute velocity values prediction and velocity change trends reproduction. The modelling results managed to recreate gradual transition of P-wave behavior for the oblique angles (between the vertical and the radial direction) of propagation.

The RMS errors between modeled and measured P-wave velocities are shown in Table 6.2. For the P-waves, the misfit value is consistently low for all analyzed propagation directions except for the vertical $v_{Pz}$. This deficiency may be originating from relative values of the TOE tensor elements and relationships between them (Equation 6.7). In the case of $C_{11}$, i.e. the $v_{Pr}$, the largest third-order tensor element (indicating largest impact of corresponding strain) is $c^*_{111}$, which is not constrained by any other SOE matrix component $C_{ij}$.

| Stress paths $\kappa$[-] | all $\kappa$ | $\kappa = 1$ & $\kappa \approx 0.75$ | $\kappa = 0$ & $\kappa$ = -0.5 | $\kappa = 1$ & $\kappa$ = -0.5 |
|---|---|---|---|---|
| Stage no. | 1,2,5-10 | 1,2,7,8 | 5,6,9,10 | 1,2,9,10 |
| RMS fit error [m/s] | | | | |
| $v_{Pz}$ | 3.79 | 19.48 | 3.90 | 3.55 |
| $v_{P37}$ | 1.23 | 8.50 | 1.28 | 1.21 |
| $v_{P47}$ | 1.37 | 5.51 | 2.03 | 1.36 |
| $v_{P68}$ | 1.59 | 4.37 | 2.61 | 1.42 |
| $v_{Pr}$ | 1.71 | 6.69 | 2.27 | 1.85 |
| $v_{P,all}$ | 1.94 | 8.91 | 2.42 | 1.88 |
| $v_{Sz}$ | 0.83 | 3.36 | 2.04 | 0.90 |
| $v_{Srr}$ | 2.35 | 17.06 | 4.89 | 2.38 |
| $v_{S,all}$ | 1.59 | 10.21 | 3.46 | 1.64 |
| $v_{all}$ | 1.84 | 9.28 | 2.72 | 1.81 |
| RMS fit error [GPa] | | | | |
| $C_{ij,all}$ | 0.0227 | 0.0895 | 0.0277 | 0.0237 |

**Table 6.2:** RMS error between the modelled and measured velocities and stiffness parameters for different TOE tensor variants. The RMS errors are shown separately for all velocities ($v_{Pz}$, $v_{P37}$, $v_{P47}$, $v_{P68}$, $v_{Pr}$, $v_{Sz}$, $v_{Srr}$), averages for given modes ($v_{P,all}$, $v_{S,all}$), the average for all velocities ($v_{all}$) and average for all considered stiffness parameters ($C_{ij,all}$). The data have been divided according to input information used for inversion of $c_{ijk}$ tensor (selection of stress paths, i.e. loading or unloading stages used to estimate the TOE tensor, Figure 6.1)

For $C_{33}$, the unconstrained third-order coefficient $c_{333}$ is smaller than the associated coefficient ($2c_{133}$). The dominating parameter $c_{133}$, constrained by both $C_{13}$ and $C_{33}$, is more affected by the inevitable presence of ultrasonic velocity estimation errors and inaccuracy of $C_{13}$ approximation, which may explain the relatively high error of $C_{33}$, i.e. $v_{Pz}$, estimation.

In the case of the error in the S-wave velocities, the misfit differs significantly between the radial and vertical propagation direction. It may be caused by complete independence of the TOE tensor elements in the expression for $C_{44}$ from the rest of the system of Equation (6.7). This lack of additional constrains yields relatively good fit of modelled vertical S-wave velocity to the experimental values, but at the same time reduces our confidence in how accurately $c^*_{144}$ and $c_{344}$ values represent the actual physical medium parameters. Our next step was to verify if we could obtain satisfactory modelling results using only a part of experimental data as the inversion input. We estimated $c_{ijk}$ values using several sub-sets of stress paths and compared the resultant TOE parameters and velocity estimation errors to the previously described reference case based on the inversion of the entire data set.

The combination of input data from cycles following hydrostatic ($\kappa = 1$) and K0 ($\kappa \approx 0.75$) stress paths yielded the largest discrepancies in TOE tensor element values, with an average difference between corresponding $c_{ijk}$ parameters of 47% (compared to the reference TOE tensor), followed by triaxial ($\kappa = 0$) and constant mean stress (CMS, $\kappa$ = -1/2) stress paths giving the average difference of 43%. The third-order coefficients set closest to the reference case was given by inversion of the data from the hydrostatic and the CMS stress paths ($\kappa = 1$ and -1/2, respectively), and its elements differed from the reference tensor on average by 18%.

However, it is worth noting that this variance is strongly affected by the discrepancy between values of $c_{366}$ – one of the smallest elements of $c_{ijk}$ tensor (i.e. does not have strong influence on stiffness strain-dependency).

Next, we used the $c_{ijk}$ tensors obtained using only a part of experimental data to model velocity changes for all available loading or unloading stages, following the same procedure as in the reference case. The comparison of the different model realizations with the experimental data is shown in Figure 6.4 and Table 6.2.

The large differences between the values of the reference TOE tensor coefficients and the ones estimated from hydrostatic and K0 stress cycles are also reflected in the general fit quality (Figure 6.4, plot A). Velocity changes are in good correspondence only for stress paths that were used in the inversion and are significantly overestimated for the triaxial and the CMS stress cycles. We observed the same type of misfit for S- and oblique P-waves. This observation is not surprising as the inverted stress paths ($\kappa = 1$ and $\kappa \approx 0.75$, respectively) are similar in nature, and differ significantly from the triaxial ($\kappa = 0$) and CMS ($\kappa$ = -0.5) stress paths.

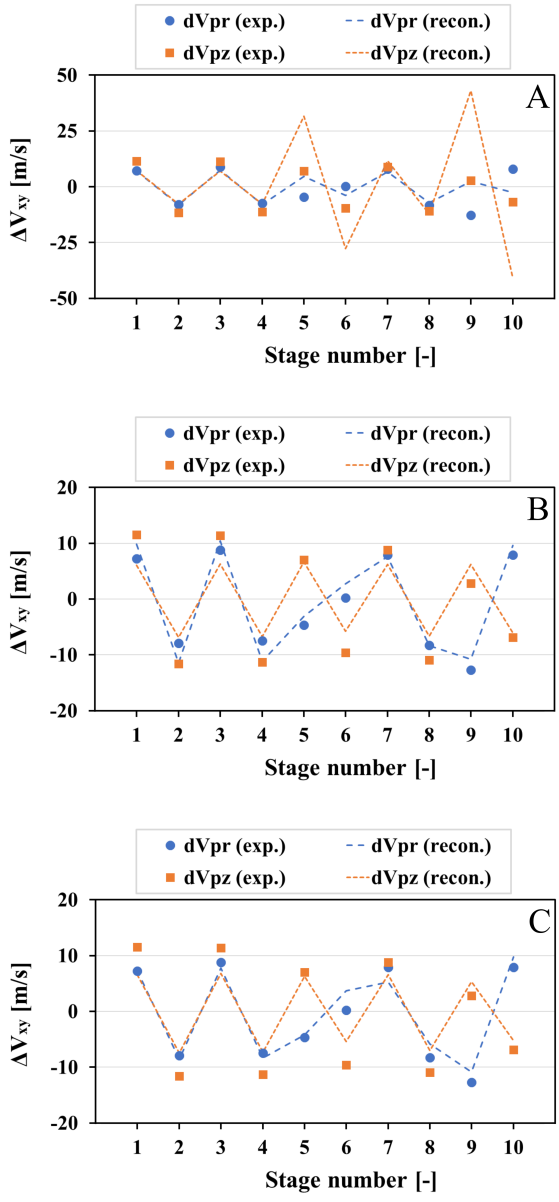


**Figure 6.4:** Comparison of experimentally measured ("exp.") and modelled ("recon.") ultrasonic vertical (dVpz) and radial (dVpr) P-wave velocity changes. Predictions of velocity changes were obtained with TOE tensor estimated using data from combinations of different loading-unloading cycles. Plot A: hydrostatic and K0 stress paths (table 1, column "$\kappa = 1$ & $\kappa = 0.75$"). Plot B: triaxial and CMS stress paths column ("$\kappa = 0$ & $\kappa$ = -0.5"). Plot C: hydrostatic and CMS stress paths ("$\kappa = 1$ & $\kappa$ = -0.5").

In the case of modelling using the TOE tensor determined from the triaxial and the CMS stress cycles, the difference between the corresponding TOE parameters and the reference parameters is not affecting the value of the velocity modelling error to the same extend as in the case in which for the inversion we used only the hydrostatic and K0 stress paths. Although the data provides enough input characterized by relatively large strains to constrain the estimated stiffness changes, the average RMS error suggests that it still does not provide enough well-balanced information to optimize the TOE tensor elements (Figure 6.4, plot B).

The best overall velocity changes model was provided by the TOE tensor obtained from hydrostatic and constant mean stress cycles (Figure 6.4, plot C). On average, the accuracy of velocity modelling in this case is even slightly better than in the reference case. This is possible because $c_{ijk}$ tensor was optimized using stiffnesses, not velocities. The two stress paths, representing the opposite extremes of the tested deformations spectrum, allow to obtain the TOE tensor not so different from the reference TOE parameters. This suggests that a large separation of stress paths ($\kappa$) used as input in the inversion may be suitable for interpolation of the measured deformation range and give better results than extrapolation by using two neighboring stress paths. Therefore, we may argue that in a case when the intermediate stress paths data are not available, using extreme stress paths yields a decent approximation of the actual physical tensor and gives satisfactory estimates of the dynamic stiffness.

Finally, we used our dataset to compare the model we defined in Equation (6.7) with a non-linearly elastic model proposed by Prioul et al. (2004). This model was derived under assumption of implicit isotropy of the TOE tensor, which allowed to limit the number of independent model parameters to three ($c^{iso}_{111}$, $c^{iso}_{112}$ and $c^{iso}_{123}$). If we assume equal radial strains, the model is defined as:

$$
\begin{aligned}
C_{11} &= C^0_{11} + \left(c^{iso}_{111} + c^{iso}_{112}\right)\Delta\varepsilon_1 + c^{iso}_{112}\Delta\varepsilon_3,\\
C_{13} &= C^0_{13} + \left(c^{iso}_{112} + c^{iso}_{123}\right)\Delta\varepsilon_1 + c^{iso}_{112}\Delta\varepsilon_3,\\
C_{33} &= C^0_{33} + 2c_{112}\Delta\varepsilon_1 + c_{111}\Delta\varepsilon_3,\\
C_{44} &= C^0_{44} + \frac{1}{4}\left(c^{iso}_{111} + c^{iso}_{112} - 2c^{iso}_{123}\right)\Delta\varepsilon_1 + \frac{1}{4}\left(c^{iso}_{111} - c^{iso}_{112}\right)\Delta\varepsilon_3,\\
C_{66} &= C^0_{66} + \frac{1}{2}\left(c^{iso}_{111} - c^{iso}_{112}\right)\Delta\varepsilon_1 + \frac{1}{2}\left(c^{iso}_{112} - c^{iso}_{123}\right)\Delta\varepsilon_3.
\end{aligned}
\tag{6.14}
$$

In order to compare the isotropic TOE tensor (Prioul et al. 2004) with the anisotropic reference tensor (Fuck and Tsvankin 2009), we estimated the $c^{iso}_{ijk}$ elements using data from all stress paths as input for the tensor inversion (as in the reference case). Next, we back-calculated velocity changes and estimated modelling error following the same procedure as in the previous examples (see Table 6.3).

| $c_{ijk}^{iso}$ [GPa] | | | |
|---|---|---|---|
| $c_{111}^{iso}$ | $c_{112}^{iso}$ | $c_{123}^{iso}$ | |
| 133.6 | 92.4 | 96.6 | |
| RMS fit error [m/s] | | | |
| $v_{P,all}$ [m/s] | $v_{S,all}$ [m/s] | $v_{all}$ [m/s] | $C_{ij,all}$ [GPa] |
| 4.10 | 5.03 | 4.37 | 0.0366 |

**Table 6.3:** The isotropic third-order elastic tensor $c_{ijk}^{iso}$ (Prioul et al. 2004) estimated using measured strains and stiffnesses from all available stress paths (top) and the corresponding averages of RMS error of velocity modelling: for axial, radial and oblique P-waves ($v_{P,all}$), axial and radial S-waves ($v_{S,all}$), global average for all measured waves ($v_{all}$, bottom) and global average for all considered stiffness coefficients ($C_{ij,all}$). Average RMS errors can be directly compared with values shown in column "all $\kappa$" in Table 6.2.

The comparison of vertical and radial velocities predicted by the two models is shown in Figure 6.5 (plots A and B, respectively). In the case of vertical P-wave ($v_{Pz}$), for which the isotropic TOE tensor gives RMS error of 4.62 m/s, both models achieve similar velocity prediction accuracy. For vertical S-wave ($v_{Sz}$), the isotropic model fails to reproduce the velocities correctly, and for triaxial and CMS stress paths (stages 5, 6, 9 and 10) fails to predict the direction of velocity changes. For radial P- and S-waves, the $c_{ijk}^{iso}$ produces velocity changes roughly following the trends observed in the laboratory data, but significantly less accurate than in the anisotropic reference case. The oblique P-wave velocity estimates obtained with the use of the anisotropic model exhibit similarly better fit to experimental data in comparison to the isotropic model. This difference in modelling accuracy is reflected in the relatively high average RMS error values, as shown in Table 6.3.

## 6.6 Conclusions

With the use of the anisotropic third-order elastic (TOE) tensor for hexagonal symmetry proposed by Fuck and Tsvankin (2009), we derived a strain-dependent velocity model for transversely isotropic shales for the case of horizontally isotropic stress changes and strains.

The model employs a set of eight independent parameters obtained by numerical inversion of laboratory data. Our dataset consists of statically measured axial and radial strains and changes of the five VTI medium stiffness matrix ($C_{ij}$) elements estimated from dynamic measurements of ultrasonic velocities.

The resultant TOE tensor allowed to back-calculate ultrasonic velocity changes directly from strains with high accuracy and to correctly recreate trends observed

in the experimental data.

We confirmed the predictive power of the model by inverting for the TOE parameters using only a limited portion of the laboratory data and using the resultant tensor to successfully recreate experimentally observed velocity changes in the entire dataset. We found that the velocity fitting quality depends strongly on the extent and on the choice of sub-set of the experimental data used for the inversion. We compared three different model realizations based on the TOE tensors obtained by inverting only two out of four available stress paths (ratio of horizontal and vertical stress changes, $\kappa$). The TOE tensor closest to the reference tensor (obtained by inversion of all available loading-unloading cycles) and providing the best ultrasonic velocity fit was obtained by inverting the data taken from stress cycles differing significantly in deformation character (hydrostatic and CMS stress paths, $\kappa = 1$ and $\kappa = -0.5$, respectively). Therefore, we conclude that if no data from the intermediate stress paths are available, the extreme stress paths may be used to approximate the actual physical TOE tensor and the dynamic stiffness.

We compared the velocity change prediction accuracy of the anisotropic model with a simplified non-linearly elastic model assuming implicit isotropy of the third-order elastic tensor (Prioul et al. 2004). The comparison shows that anisotropic strain sensitivity is required to adequately estimate velocity changes in intrinsically anisotropic sedimentary rocks, such as shales.

To further deepen our analysis, more shales need to be examined. This may reveal trends and correlations between the TOE parameters and other petrophysical properties

## 6.7 Acknowledgements

This publication has been produced with support from the NCCS Centre, performed under the Norwegian research program Centres for Environment-friendly Energy Research (FME); and the Knowledge-building Projects for Industry under the Norwegian Research Council: “Shale rock physics: Improved seismic monitoring for increased recovery” and “Improved prediction of stress and pore pressure changes in the overburden for infill drilling”. The authors acknowledge the following partners for their contributions: Aker Solutions, ANSALDO Energia, CoorsTek Membrane Sciences, EMGS, Gassco, KROHNE, Larvik Shipping, Norcem, Norwegian Oil and Gas, Quad Geometrics, Shell, Equinor, TOTAL, and the Research Council of Norway (257579/E20); AkerBP, Engie, INEOS, and Total (234074/E30); and AkerBP, Equinor, and Shell (294369/E30).

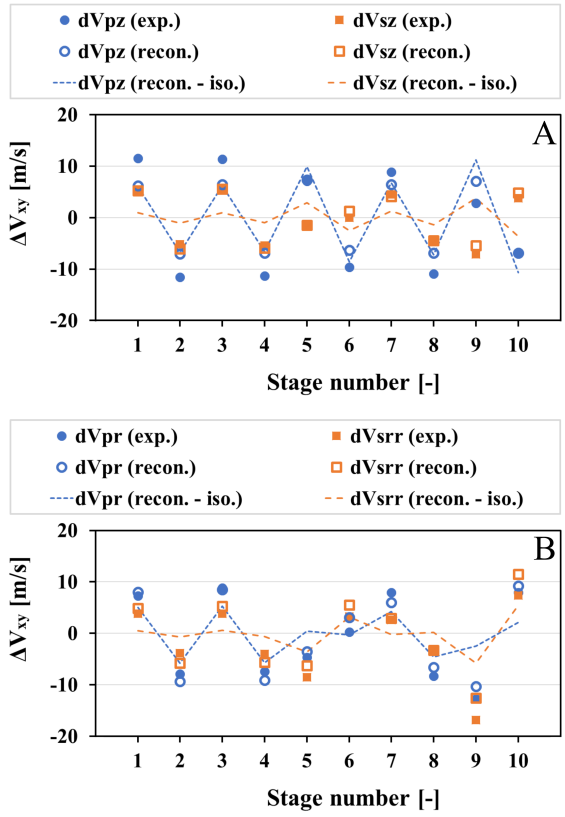


**Figure 6.5:** Comparison of velocity changes modelled with the anisotropic third-order elastic tensor under assumption of transverse isotropy of stiffnesses, stresses and strains ("recon.") and the third-order elastic tensor derived with assumption of its implicit isotropy ("recon. – iso." (Prioul et al. 2004)) with velocity changes estimated directly from laboratory measurements ("exp."). Plot A: vertical P- (dVpz) and S-wave (dVsz). Plot B: radial P- (dVpr) and radial and horizontally polarized S-wave (dVsrr).

# References


Bachrach, R. and P. Avseth (2008). 'Rock physics modeling of unconsolidated sands: Accounting for nonuniform contacts and heterogeneous stress fields in the effective media approximation with applications to hydrocarbon exploration'. In: *Geophysics* 73. DOI: 10.1190/1.2985821.

Budiansky, B. and R. J. O'Connell (1976). 'Elastic moduli of a cracked solid'. In: *International Journal of Solids and Structures* 12.2, pp. 81–97. ISSN: 0020-7683. DOI: https://doi.org/10.1016/0020-7683(76)90044-5. URL: https://www.sciencedirect.com/science/article/pii/0020768376900445.

Fjær, E., R. Holt, P. Horsrud and A. M. Raaen (2021). *Petroleum Related Rock Mechanics. 3rd edition.* ISBN: 9780128221952.

Fjaer, E. (2006). *Modeling the stress dependence of elastic wave velocities in soft rocks.* Conference Paper. URL: https://doi.org/.

Fuck, R. F. and I. Tsvankin (2009). 'Analysis of the symmetry of a stressed medium using nonlinear elasticity'. In: *GEOPHYSICS* 74. DOI: 10.1190/1.3157251.

Fuck, R. F., A. Bakulin and I. Tsvankin (2009). 'Theory of traveltime shifts around compacting reservoirs: 3D solutions for heterogeneous anisotropic media'. In: *GEOPHYSICS* 74.1, pp. D25–D36. DOI: 10.1190/1.3033215. URL: https://library.seg.org/doi/abs/10.1190/1.3033215.

Hudson, J. A. (1981). 'Wave speeds and attenuation of elastic waves in material containing cracks'. In: *Geophysical Journal International* 64.1, pp. 133–150. ISSN: 0956-540X. DOI: 10.1111/j.1365-246X.1981.tb02662.x. URL: https://doi.org/10.1111/j.1365-246X.1981.tb02662.x.

Johnson, P. and P. Rasolofosaon (1996). 'Nonlinear elasticity and stress-induced anistropy in rock'. In: *Journal of Geophysical Research* 101, pp. 3113–3124. DOI: 10.1029/95JB02880.

Mindlin, R. D. (1949). 'Compliance of Elastic Bodies in Contact'. In: *Journal of Applied Mechanics* 16.3, pp. 259–268. ISSN: 0021-8936. DOI: 10.1115/1.4009973. URL: https://doi.org/10.1115/1.4009973.

Prioul, R., A. Bakulin and V. Bakulin (2004). 'Nonlinear rock physics model for estimation of 3D subsurface stress in anisotropic formations: Theory and laboratory verification'. In: *Geophysics* 69, pp. 415–425. DOI: 10.1190/1.1707061.

Thomsen, L. (1986). 'Weak elastic anisotropy'. In: *GEOPHYSICS* 51.10, pp. 1954–1966. DOI: 10.1190/1.1442051. URL: https://library.seg.org/doi/abs/10.1190/1.1442051.

Walton, K. (1987). 'The effective elastic moduli of a random packing of spheres'. In: *Journal of the Mechanics and Physics of Solids* 35.2, pp. 213–226. ISSN: 0022-5096. DOI: https://doi.org/10.1016/0022-5096(87)90036-6. URL: https://www.sciencedirect.com/science/article/pii/0022509687900366.

This paper is submitted for publication and is therefore not included.

# PAPER F: Stress path dependency of time-lapse seismic effects in shales: experimental comparison at seismic and ultrasonic frequencies

Serhii Lozovyi[1], Marcin Ireneusz Duda[1,2], Andreas Kurt Bauer[3], Rune Martin Holt[1,2]

[1] Sintef Petroleum, 7031 Trondheim, Norway
[2] Norwegian University of Science and Technology, 7031 Trondheim, Norway
[3] AkerBP, 7011 Trondheim, Norway

Submitted to Geophysical Journal International in June 2023

## Abstract

Pore pressure changes in the reservoir during hydrocarbon production or $CO_2$ storage operations may result in substantial stress changes in the overburden. Since wave velocities in rocks are stress and strain sensitive, the changes induce time shifts in the overburden that are detectable on 4D seismic surveys. To interpret the time shifts, stress sensitivity of rocks is studied in the laboratory experiments on core plugs. Such measurements are in most cases done at ultrasonic frequencies. However, previous studies indicate that the stress sensitivity of velocities at seismic frequencies could be higher than that at ultrasonic frequencies. Hence, laboratory calibration by ultrasonic data may lead to erroneous prediction of stresses and strains when applied to 4D seismic data. To this end, a series of laboratory experiments was performed to quantify the stress sensitivities of acoustic wave velocities at both seismic and ultrasonic frequencies. Two preserved field shales were tested using a low-frequency apparatus. Different combinations of vertical and horizontal stress changes were applied to the undrained rocks to mimic possible stress variation in the overburden. The results indicate that stress sensitivities and strain sensitivities (R-factor) of P-wave velocities might be several times higher at seismic frequencies than at ultrasonic frequencies. Furthermore, changes in elastic rock properties tend to depend linearly on the stress path at both seismic and ultrasonic frequencies. These findings should be taken into account when inverting time-lapse seismic data for changes in stresses and strains.

# PAPER G: Third-order elasticity of transversely isotropic field shales

Audun Bakk[1], Marcin Ireneusz Duda[1,2], Xiyang Xie [1], Jørn Fredrik Stenebråten[1], Hong Yan[2], Colin MacBeth[3], Rune Martin Holt[1,2]

[1] Sintef Petroleum, 7031 Trondheim, Norway
[2] Norwegian University of Science and Technology, 7031 Trondheim, Norway
[3] Heriot-Watt University, Institute of GeoEnergy Engineering, Edinburgh, EH14 4AS, United Kingdom

Submitted to Geophysical Prospecting in February 2023, currently under revision

## Abstract

The formations above a producing or depleting reservoir can exhibit large mechanical changes posing a risk for significant subsidence and loss of rock integrity. Third-order elastic theory can be used to connect subsurface strain and stress changes to velocity changes and seismic time-shifts. However, commonly used existing models assume an isotropic strain dependence of the dynamic stiffness, which overlooks the anisotropy of shales. This is particularly important considering the abundance of shales in the overburden. To address this, we propose a third-order elastic model with transversely isotropic strain dependence of the dynamic stiffness to better capture the behaviour of shales. The calibrated model satisfactorily predicts changes in P-wave velocity changes determined in laboratory experiments with two overburden field shales, covering a wide range of propagation directions and stress variations. The P-wave velocity change under uniaxial strain along the wave propagation direction exhibits a significant dependency on the propagation angle. Geomechanical modelling was employed to obtain strains, considering a depleting penny-shaped reservoir surrounded by shales. These strains were utilized to calculate the effective dynamic stiffness of the overburden after depletion using the calibrated third-order elastic model. The overburden time-shifts increase with offset angle, peaking at about 45 degrees, suggesting a strong influence from shear strains on the time-shifts. In contrast, an isotropic third-order elastic model, calibrated on the same shales, exhibits a significantly lower sensitivity to shear strains due to smaller values of the shear-dependent third-order coefficients as compared to the anisotropic third-order model. These results emphasize the importance of considering anisotropic strain dependence of the dynamic stiffness when studying shales. Leveraging offset trends in pre-stack time-lapse seismic data, along with geomechanical modelling and an appropriate strain dependent rock physics model, can enhance the quantification of subsurface strains and stresses.

## 8.1 Introduction

Experiments have shown that velocities in rocks depend on both strain and stress (Johnston 1987; Jones and Wang 1981). Most of the rocks in the crust are anisotropic (Crampin et al. 1984; Helbig and Thomsen 2005; Thomsen 1986; Tsvankin 1997). Shales, frequently encountered in the overburden, exhibit inherent anisotropy and significant stress sensitivity, resulting in substantial velocity changes. These velocity changes are dependent on the specific stress path, commonly defined as the ratio between horizontal and vertical stress variations (Bakk et al. 2020b; Bauer et al. 2008; Herwanger and Koutsabeloulis 2011; Holt et al. 2018; Hornby 1998; Jr. 2007; Pervukhina et al. 2008; Sarout and Guéguen 2008). Already the first time-lapse seismic studies at Ekofisk (Hall et al. 2002) and Valhall (Guilbot and Smith 2002) demonstrated a significant strain dependence of velocities in the overburden. Thus, 4D seismic data are not only influenced by the changes in the reservoir itself but also by the induced geomechanical changes in the overburden associated with detectable time-shifts (Gennaro et al. 2008; Guilbot and Smith 2002; Hatchell and Bourne 2005; Hawkins 2008; Herwanger and Horne 2009; Hodgson 2009; Kenter et al. 2004; MacBeth et al. 2018; Roste and Ke 2017). The compaction of the reservoir can have a critical impact on the overburden, influencing sea-floor subsidence (Angus et al. 2015; Barkved et al. 2005), fault integrity (Kristiansen et al. 2005; Zoback and Zinke 2002), and well stability both during drilling (Ditlevsen et al. 2018) and in cased holes (Ewy 2021).

By integrating geomechanical data and rock physics models, 4D seismic data have a significant potential in quantifying strains and stress changes. The Hatchell–Bourne– Røste (HBR) model, which assigns a constant ratio between the fractional vertical P-wave velocity-change and the vertical strain (Hatchell and Bourne 2005; Røste et al. 2006) has been widely used. Even though such simplified empirical models can give insight into dominating trends, more refined models are often needed to understand and predict the behaviour of the rocks in more detail. Anisotropic micromechanical models for the dynamic stiffness, often based on cracks and inclusions, have long been popular due to their ability to link the physics at different length scales (e.g., Hudson 1981; Mavko et al. 1995; Sayers and Kachanov 1995). The effective third-order elastic (TOE) models constitute another significant group (Fuck and Tsvankin 2009; Hughes and Kelly 1953; Prioul et al. 2004; Rasolofosaon 1998; Shapiro 2017; Sinha 1982; Thurston and Brugger 1964; Winkler and Liu 1996). The TOE theory provides a constitutive framework for quantification of the dynamic stiffness changes resulting from strains and stresses exerted on rocks. Sripanich et al. (2021) showed that the isotropic TOE coefficients are connected to adiabatic pressure derivatives of elastic moduli. The TOE model proposed by Prioul et al. (2004), that assumes isotropic symmetry of the third-order tensor, which has been calibrated to ultrasonic data obtained from different lithologies (Prioul and Lebrat 2004). This model has also ben utilized to predict seismic response (Asaka 2023; Fuck et al. 2009; Herwanger and Koutsabeloulis 2011; MacBeth et al. 2018). Duda et al. (2020) and Bakk et al.

(2020a) studied a calibrated anisotropic TOE model limited by the assumption of isotropic horizontal strains. As far as we know, a TI symmetric TOE tensor has not been proposed in general form until now. Furthermore, the utilization of a calibrated anisotropic TOE tensor, accounting for the complete strain tensor has not been proposed or employed in the study of sedimentary rocks before our research. Anisotropic TOE models are important because of the general anisotropic behaviour of sedimentary rocks, particularly in overburden shales. Such models can give insight into time-shift's dependence on offset and azimuth, and thereby improve quantification of strains and stresses. It is therefore important to quantify the extent of third-order anisotropy in rocks and compare between predictions obtained from anisotropic TOE models and isotropic TOE models, which is addressed in this study. Such velocity models may be beneficial for the quality and interpretation of both pre-stack and post-stack time-lapse data.

In this work we propose an anisotropic TOE tensor with transversely isotropic (TI) symmetry. The elastic coefficients of this model and the corresponding isotropic TOE model are determined from ultrasonic experimental data from three different field shales. The fit of the TOE models to the experimental data is discussed in terms of velocity changes as a function of angle and stress path. To discuss implications relevant for 4D seismic data processing, a finite-element geomechanical modelling case is studied with a depleting reservoir embedded in shales populated by the properties of the tested shales. The resulting strains from the modelling are used along with the TOE models to demonstrate potential differences of angular time-shift trends with respect to the shale stiffness and the symmetry of the TOE tensor.

The novelty of the present work is:

1. development of an anisotropic TOE tensor with TI symmetry that accommodates the complete strain tensor;

2. calibration of the TOE tensor to laboratory data from different overburden field shales;

3. discussion of angular time-shift trends for a geomechanical modelling case with both TI and isotropic symmetries of the TOE tensor.

## 8.2 Third-order elastic model

In the subsequent section, the anisotropic TOE stiffness tensor with TI symmetry is developed. The third-order elastic theory provides a basis for prediction of the strain-dependence of velocities, also called acousto-elasticity. The expansion of the elastic strain energy of a medium to the third-order around a reference state of zero strain takes the common form (Barker et al. 1974; Brugger 1964; Fuck

and Tsvankin 2009; Lubarda 1997; Rasolofosaon 1998; Shapiro 2017; Sinha 1982; Wang and Schmitt 2021):

$$W = \frac{1}{2}C_{ijkl}\varepsilon_{ij}\varepsilon_{kl} + C_{ijklmn}\varepsilon_{ij}\varepsilon_{kl}\varepsilon_{mn}. \tag{8.1}$$

$C_{ijkl}$ and $C_{ijklmn}$ are coefficients of the second-order elastic stiffness (SOE) and the third-order elastic stiffness (TOE) tensors, respectively, $\varepsilon_{ij}$ are the Green-Lagrangian strain components, and $i$, $j$, $k$, $l$, $m$ and $n$ are dummy indices where the summation over repeated indices in each term is implied. The strains in the experiments and simulations herein are of order of $10^{-3}$ or less, i.e., $|\varepsilon_{ij}| \gg \varepsilon_{ij}^2$. Thus, we will ignore the nonlinear terms in the strain. Strain is defined positive for compaction. The TOE theory was initially applied to crystals where the unstrained configuration may serve as an appropriate reference state (Barker et al. 1974, p.216). Given our focus on field shales, the reference configuration is more naturally defined as the in-situ stress and pore pressure, which applies to both laboratory experiments and seismic surveys. The reference state and the strained state are hereinafter called the baseline state and the monitor state, respectively.

For convenience, we adopt Voigt notation, also called abbreviated notation or engineering notation. The tensor components $\varepsilon_{ij}$ of the strain are expressed as vector components $e_i$ in Voigt notation:

$$[\varepsilon_{11}, \varepsilon_{22}, \varepsilon_{33}, 2\varepsilon_{23}, 2\varepsilon_{12}, 2\varepsilon_{12}]^T \equiv [e_1, e_2, e_3, e_4, e_5, e_6]^T, \tag{8.2}$$

where superscript T stands for transpose. In Voigt notation, the strain energy to the third-order becomes (Brugger 1964):

$$W = \frac{1}{2}\sum_i C_{ii}e_i^2 + \sum_{i<j} C_{ij}e_ie_j + \frac{1}{6}\sum_i C_{iii}e_i^3 + \frac{1}{2}\sum_{i\neq j} C_{iij}e_i^2e_j + \sum_{i<j<k} C_{ijk}e_ie_je_k, \tag{8.3}$$

where the substripts run from 1 to 3. The SOE and TOE tensors have permuation symmetrye, i.e., $C_{ij} = C_{ji}$ and $C_{ijk} = C_{jik} = C_{kij} = C_{ikj} = C_{jki} = C_{kji}$.

Stiffness tensor of a strained body (or "monitor") is generally asymmetric, which is a fundamental difference from an unstrained anisotropic body with symmetric stiffness (Barker et al. 1974, p.227). However, the asymmetry of the monitor stiffness is relatively small since the stress change, as observed here, is much smaller than both second- and third-order stiffnesses (Barker et al. 1974; Fuck and Tsvankin 2009; Fuck et al. 2009; Prioul et al. 2004; Rasolofosaon 1998) and is neglected in the following analysis. Consequently, the monitor (m) stiffness for small amplitude waves becomes (Fuck and Tsvankin 2009; Prioul et al. 2004; Shapiro 2017)

$$C_{ij}^{m} = C_{ij} + C_{ijk}e_k, \tag{8.4}$$

where $C_{ij}$ are the second-order (linear) coefficients in the baseline state that can be represented by 6×6 matrix. In Voigt notation, the TOE tensor can be represented by a 6×6×6 matrix or a six-component vector composed of 6×6 matrices. The principle of invariance of the strain energy with respect to identity transformations implies the maximum number of 21 independent SOE coefficients and 56 independent TOE coefficients (Brugger 1965; Fumi 1951; Fumi 1952; Hearmon 1953).

In this work we study shales with assumed TI symmetry. The hexagonal SOE tensor, which also possesses TI symmetry, has five independent coefficients: $C_{11}$, $C_{13}$, $C_{33}$, $C_{44}$, and $C_{66}$. The constraint of the last non-vanishing SOE coefficient is (e.g., Fjær et al. 2021, p.60)

$$C_{12} = C_{11} - 2C_{66}. \tag{8.5}$$

However, the hexagonal TOE tensor does not possess the required TI symmetry in general, as pointed out by Fuck and Tsvankin (2009), except for the case in which stress change has a rotational symmetry around a six-fold hexagonal symmetry axis. To constrain the TI TOE tensor, a TI medium with a symmetry axis along $x_3$ is considered (Figure 8.1). The axis orientation and notation ($x_i$) refer to the coordinate system of the material symmetry. Hearmon (1953) noted that the constraints for the isotropic TOE coefficients were obtained by combining the highest symmetries in the cubic and hexagonal systems. We a similar reasoning for the TI system, where isotropy is required in the $[x_1, x_2]$ plane, and we hypothesize that TI symmetry is obtained by combining the maximum symmetries in the tetragonal and hexagonal systems. This effectively adds a four-fold symmetry axis along $x_3$ in the hexagonal system. Thus, one new constraint emerges as compared to the hexagonal TOE tensor, $C_{166} = C_{266}$. The number of independent third-order coefficients in the TI system is thus nine: $C_{111}$, $C_{113}$, $C_{133}$, $C_{144}$, $C_{166}$, $C_{333}$, $C_{344}$, $C_{366}$ and $C_{456}$. The constraints in the hexagonal system (Fumi 1952) are then further constrained in the TI system to

$$\begin{aligned}
C_{113} &= C_{122} = C_{111} - 4C_{166},\\
C_{123} &= C_{113} - 2C_{366},\\
C_{222} &= C_{111},\\
C_{223} &= C_{113},\\
C_{233} &= C_{133},\\
C_{244} &= C_{155} = C_{144} + 2C_{456},\\
C_{255} &= C_{144},\\
C_{355} &= C_{344}.
\end{aligned} \tag{8.6}$$

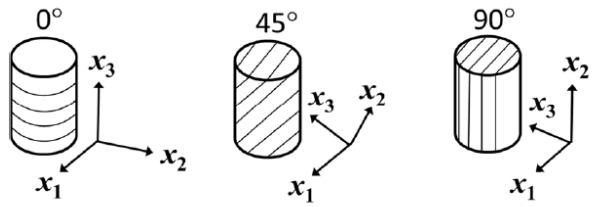


**Figure 8.1:** Schematic illustration of the different samples oriented at 0°, 45°, and 90° relative to the TI symmetry axis ($x_3$) . The isotropic (bedding) plane is in the $[x_1, x_2]$ plane.

To verify our hypothesis, the strain energy of the system must be invariant to all transformations corresponding with the symmetry (Birch 1947; Hearmon 1953). Because the TI system builds on the hexagonal symmetry, for which the constraints are known (Fumi 1952), it remains to verify invariance of the strain energy regarding any rotation around $x_3$. The strain energy $W$ for this system is obtained by combining Equation (8.3) with the constraints from equation (6), yielding

$$\begin{aligned} 2W =& C_{11}\left(e_1+e_2\right)^2 + 2C_{13}\left(e_1+e_2\right)e_3 + C_{33}e_3^2 + C_{44}\left(e_4^2+e_5^2\right) + C_{66}\left(e_6^2-4e_1e_2\right) \\ &+ \frac{1}{3}C_{111}\left(e_1+e_2\right)^3 + C_{113}\left(e_1+e_2\right)^2 e_3 + C_{133}\left(e_1+e_2\right)e_3^2 \\ &+ C_{144}\left(e_1+e_2\right)\left(e_4^2+e_5^2\right) + C_{166}\left(e_1+e_2\right)\left(e_6^2-4e_1e_2\right) \\ &+ \frac{1}{3}C_{333}e_3^3 + C_{344}\left(e_4^2+e_5^2\right)e_3 + C_{366}\left(e_6^2-4e_1e_2\right)e_3 \\ &+ 2C_{456}\left(e_1e_5^2+e_2e_4^2+e_4e_5e_6\right). \end{aligned} \tag{8.7}$$

Consider a clockwise rotation of a strain tensor $\boldsymbol{\varepsilon}$ by an arbitrary angle $\theta$ around $x_3$. The transformed strain tensor $\boldsymbol{\varepsilon}$ is obtained by (Fjær et al. 2021, p.687)

$$\begin{bmatrix} \bar{\varepsilon}_{11} & \bar{\varepsilon}_{12} & \bar{\varepsilon}_{13} \\ \bar{\varepsilon}_{12} & \bar{\varepsilon}_{22} & \bar{\varepsilon}_{23} \\ \bar{\varepsilon}_{13} & \bar{\varepsilon}_{23} & \bar{\varepsilon}_{33} \end{bmatrix} = \begin{bmatrix} \cos\theta & \sin\theta & 0 \\ -\sin\theta & \cos\theta & 0 \\ 0 & 0 & 1 \end{bmatrix} \begin{bmatrix} \varepsilon_{11} & \varepsilon_{12} & \varepsilon_{13} \\ \varepsilon_{12} & \varepsilon_{22} & \varepsilon_{23} \\ \varepsilon_{13} & \varepsilon_{23} & \varepsilon_{33} \end{bmatrix} \begin{bmatrix} \cos\theta & -\sin\theta & 0 \\ \sin\theta & \cos\theta & 0 \\ 0 & 0 & 1 \end{bmatrix}, \tag{8.8}$$

that in Voigt notation becomes

$$\begin{bmatrix} \bar{e}_1 \\ \bar{e}_2 \\ \overline{e_3} \\ \overline{e_4} \\ \bar{e}_5 \\ \bar{e}_6 \end{bmatrix} = \begin{bmatrix} e_1\cos^2\theta + e_2\sin^2\theta + e_6\cos\theta\sin\theta \\ e_1\sin^2\theta + e_2\cos^2\theta - e_6\cos\theta\sin\theta \\ e_3 \\ \frac{1}{2}\left(e_4\cos\theta - e_5\sin\theta\right) \\ \frac{1}{2}\left(e_4\sin\theta + e_5\cos\theta\right) \\ (e_2 - e_1)\cos\theta\sin\theta + \frac{1}{2}e_6\left(\cos^2\theta - \sin^2\theta\right) \end{bmatrix}. \tag{8.9}$$

The strain energy in Equation (8.7) can be recast to

$$\begin{aligned} 2W = &\left(C_{11} + \frac{1}{3}C_{111}I_1\right)I_1^2 + \left(C_{33} + \frac{1}{3}C_{333}I_3\right)I_3^2 \\ &+ \left(2C_{13} + C_{113}I_1 + C_{133}I_3\right)I_1I_3 + \left(C_{44} + C_{144}I_1 + C_{344}I_3\right)I_2 \\ &+ \left(C_{66} + C_{166}I_1 + C_{366}I_3\right)I_4 + 2C_{456}I_5. \end{aligned} \tag{8.10}$$

where

$$\begin{aligned} &I_1 \equiv \bar{e}_1 + \bar{e}_2 = e_1 + e_2, \\ &I_2 \equiv \bar{e}_4^2 + \bar{e}_5^2 = e_4^2 + e_5^2, \\ &I_3 \equiv \bar{e}_3 = e_3, \\ &I_4 \equiv \bar{e}_6^2 - 4\bar{e}_1\bar{e}_2 = e_6^2 - 4e_1e_2, \\ &I_5 \equiv \bar{e}_1\bar{e}_5^2 + \bar{e}_2\bar{e}_4^2 + \bar{e}_4\bar{e}_5\bar{e}_6 = e_1e_5^2 + e_2e_4^2 + e_4e_5e_6. \end{aligned} \tag{8.11}$$

All five combinations of strain in equation Equation (8.11) are verified as invariants of the transformation in equation Equation (8.8) by substituting $e$ with $\bar{e}$ from equation Equation (8.9), which show that $I_i(\bar{e}) = I_i(e)$ for all $i = \{1,2,3,4,5\}$. These strain invariants should not be mistaken for the ordinary strain invariants that are applicable to arbitrary transformations of the strain tensor (e.g., Fjær et al. 2021, p.19). Importantly, this implies that the strain energy is invariant as well, i.e., $W(\bar{e}) = W(e)$. Thus, the imposition of any rotation around $x_3$ on the strain energy will simply lead to an identity and there can be no further reduction in the number of independent coefficients. This proves that the proposed TOE tensor with nine independent coefficients along with the constraints in Equation (8.6) has the required TI symmetry. This confirms our hypothesis that constraining the hexagonal system with a four-fold symmetry axis is consistent with a TI TOE tensor. Hence, the 21 distinct monitor stiffness coefficients with TI symmetry of both the SOE and TOE tensors are:

$$
\begin{aligned}
C^{\mathrm{m}}_{11} &= C_{11} + C_{111}e_1 + (C_{111} - 4C_{166})\, e_2 + C_{113}e_3,\\
C^{\mathrm{m}}_{12} &= C_{11} - 2C_{66} + (C_{111} - 4C_{166})\,(e_1 + e_2) + (C_{113} - 2C_{366})\, e_3,\\
C^{\mathrm{m}}_{13} &= C_{13} + C_{113}e_1 + (C_{113} - 2C_{366})\, e_2 + C_{133}e_3,\\
C^{\mathrm{m}}_{14} &= C_{144}e_4,\\
C^{\mathrm{m}}_{15} &= (C_{144} + 2C_{456})\, e_5,\\
C^{\mathrm{m}}_{16} &= C_{166}e_6,\\
C^{\mathrm{m}}_{22} &= C_{11} + (C_{111} - 4C_{166})\, e_1 + C_{111}e_2 + C_{113}e_3,\\
C^{\mathrm{m}}_{23} &= C_{13} + (C_{113} - 2C_{366})\, e_1 + C_{113}e_2 + C_{133}e_3,\\
C^{\mathrm{m}}_{24} &= (C_{144} + 2C_{456})\, e_4,\\
C^{\mathrm{m}}_{25} &= C_{144}e_5,\\
C^{\mathrm{m}}_{26} &= C_{166}e_6,\\
C^{\mathrm{m}}_{33} &= C_{33} + C_{133}\,(e_1 + e_2) + C_{333}e_3,\\
C^{\mathrm{m}}_{34} &= C_{344}e_4,\\
C^{\mathrm{m}}_{35} &= C_{344}e_5,\\
C^{\mathrm{m}}_{36} &= C_{366}e_6,\\
C^{\mathrm{m}}_{44} &= C_{44} + C_{144}e_1 + (C_{144} + 2C_{456})\, e_2 + C_{344}e_3,\\
C^{\mathrm{m}}_{45} &= C_{456}e_6,\\
C^{\mathrm{m}}_{46} &= C_{456}e_5,\\
C^{\mathrm{m}}_{55} &= C_{44} + (C_{144} + 2C_{456})\, e_1 + C_{14}e_2 + C_{344}e_3,\\
C^{\mathrm{m}}_{56} &= C_{456}e_4,\\
C^{\mathrm{m}}_{66} &= C_{66} + C_{166}\,(e_1 + e_2) + C_{366}e_3.
\end{aligned}
\tag{8.12}
$$

The model given by Equation (8.12) can be used with a strain tensor with the directional indices referring to the principal coordinate system of the baseline (TI) symmetry of the rock, which is fulfilled in the laboratory tests (Section 8.3.5) as well as in the considered geomechanical modelling case (Section 8.3.6). Note that the TI TOE tensor does not generally imply TI symmetry of the monitor SOE stiffness in Equation (8.4), because the symmetry of the strained medium depends on the direction of the principal strains, as pointed out by Fuck and Tsvankin (2009) as well as the symmetry of the strain. It is also worth mentioning that the model in equation Equation (8.12) can accommodate any symmetry of the baseline stiffness $C_{ij}$, although assuming equal symmetry for both second- and third-order tensors is a natural choice in most cases.

The corresponding isotropic TOE model has three independent isotropic TOE coefficients $C^{iso}_{111}$, $C^{iso}_{113}$ and $C^{iso}_{144}$, along with the constraints (Fuck and Tsvankin 2009; Hearmon 1953):

$$
\begin{aligned}
C^{\text{iso}}_{133} &= C^{\text{iso}}_{113}, \\
C^{\text{iso}}_{333} &= C^{\text{iso}}_{111}, \\
C^{\text{iso}}_{166} &= C^{\text{iso}}_{344} = \frac{1}{4}\left(C^{\text{iso}}_{111} - C^{\text{iso}}_{113}\right), \\
C^{\text{iso}}_{366} &= C^{\text{iso}}_{144}, \\
C^{\text{iso}}_{456} &= \frac{1}{8}\left(C^{\text{iso}}_{111} - C^{\text{iso}}_{113}\right) - \frac{1}{2}C^{\text{iso}}_{144}.
\end{aligned}
\tag{8.13}
$$

Note the constraints of Hearmon (1953) need to be transposed because we apply Voigt notation implying $C_{ijklmn} = C_{IJK}$ (Brugger 1964; Fuck and Tsvankin 2009). The monitor stiffness for the isotropic TOE is obtained by replacing the $C_{ijk}$ on the right hand side of Equation (8.12) with the $C^{iso}_{ijk}$ in Equation (8.13). By accommodating for shear strains, this isotropic TOE model is thus generalizing the model proposed by Prioul et al. (2004).

## 8.3 Method

### 8.3.1 Materials, experimental setup, and establishment of in-situ conditions

Standard guidelines of geomechanical tests are utilized in the experiments (Dudley et al. 2016). Samples made of aluminium and Polyetheretherketone (PEEK) were used for the static and dynamic calibration of the setup. Laboratory experiments were conducted on three different field shales: M shale, D shale, and B shale. After coring at the rig, the shale cores were protected using the "seal peel" method before being stored, which involves wrapping the cores in plastic film, covering them with aluminium foil, and applying a layer of wax. The aluminium foil acts as a vapor barrier and reflects heat during the wax-dipping process. This preservation technique enables that the cores can be stored for a long time and remain suitable for subsequent testing. The experimental data of these shales are also discussed by Holt et al. (2018), Bakk et al. (2020b), Bakk et al. (2020a), and Duda et al. (2020). The key characteristics of the shales are summarized in Table 8.1. Representative samples, drilled next to the samples used in the mechanical testing, were used to estimate porosity from water loss upon heating and clay content from XRD analysis. All tests are conducted at room temperature. The field samples have not experienced any heating prior testing, apart from the in-situ temperature experienced prior coring and a slight temporary temperature rise during the waxing procedure for the "seal peel".

For each shale, three cylindrical samples (38 mm diameter, 50-60 mm long) were drilled at angles 0°, 45°, and 90° relative to the bedding plane (Figure 8.1). Following drilling, each sample was placed in a heat shrink sleeve for protection and

| Shale | Geological age | Depth | Porosity | Clay content | $\sigma_z$ | $\sigma_H$ | $p_f$ |
|---|---|---|---|---|---|---|---|
| | | [km] | [GPa] | [wt%] | [MPa] | [MPa] | [MPa] |
| M shale | Middle Miocene | 1.4 | 36 | 71 | 27.3 | 25.9 | 17.2 |
| D shale | Eocene | 2.5 | 29 | 73 | 50.3 | 49.2 | 37.9 |
| B shale | Early Miocene | 3.4 | 24 | 76 | 49.8 | 47.4 | 35.0 |

**Table 8.1:** Geological age, true vertical depth measured from sea-level, porosity, clay content (wt%: weight percent relative solid mass), in-situ vertical stress $\sigma_Z$, in-situ horizontal stress $\sigma_H$,, and in-situ pore pressure $p_f$ of the tested field shales

support during trimming and grinding of the end surfaces (Figure 8.2). All preparation was performed using Marcol82 as cooling and circulation fluid effectively providing an oil surface on the sample to preserve its natural moisture content without inducing any alterations. Between preparation and testing the sample was stored submerged in Marcol82, in separate closed-lid containers. During testing, a specially designed Viton rubber sleeve was used to seal off the sample from the confining fluid, allowing for the exertion of horizontal stress. Additionally, the sleeve allowed for insertion of steel pistons which exerted (vertical) force on the end faces of the samples and facilitated positioning of the horizontal ultrasonic sensors and the horizontal strain cantilevers that were in direct contact with the sample surface (Figure 8.3a). This stack was finally placed in a triaxial load frame where the vertical stress and the isotropic horizontal stress were adjusted independently. Note that "vertical" and "horizontal" in the experiments refers to the setup, where the axis of the cylindrical samples was aligned with the vertical direction. The vertical strain was determined as the average value of recordings from three linear variable differential transformers (LVDT's) distributed uniformly azimuthally (every 120°) around the sample. Similarly, the horizontal strains were determined as the average values of recordings from strain gauges attached to two orthogonal pairs of cantilevers located in the same horizontal plane (rotated 45° azimuthally relative to the P- and S-wave ultrasonic source-receiver planes). The deviation between the mean strain and the individual strains measured by the LVDTs, respectively, were one order of magnitude lower than the strain magnitude during the loading/unloading steps. This level of deviation falls within the range of uncertainty associated with the strain gauges. In the case of horizontal strains, this deviation is reduced to two orders of magnitude lower than the magnitude of the strain for the loading/unloading steps. The utilization of redundant strain

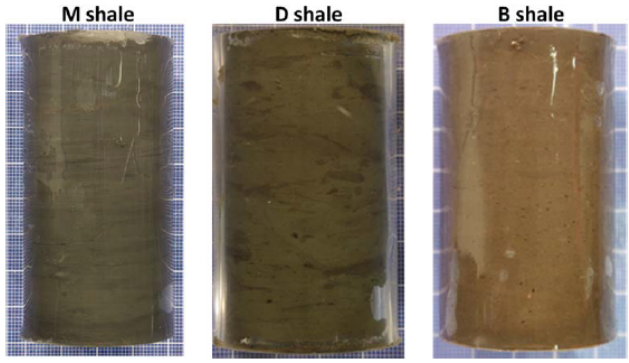


**Figure 8.2:** Images of the samples prior to the mechanical testing. These samples are drilled normal to the bedding (nominal 0°). To reduce the possibility of damage before testing, the samples were wrapped in a shrink sleeve at this stage

measurements is a well-established approach for enhancing strain estimation accuracy. Based on the individual strain measurements, there are no indications of significant non-uniformity or deviation of the considered samples from the assumption of TI symmetry. Pore pressure control was maintained with access through each piston, with a pore pressure sensor connected to each piston. Radial- and end-drainage were used during testing to reduce the drainage path and thereby reduce the time required for pore pressure equilibration.

P-wave ultrasonic velocities were estimated using pulse transmission in multiple ray-path directions at 0°, 22° (only used for B Shale), 37°, 47°, 68° and 90° relative to the cylinder axis of the sample (Figure 8.3b). All P-wave transducers were in the same vertical plane. S-wave velocities were estimated in the vertical and horizontal direction. The polarization directions of the S-waves are illustrated in Figure 8.4. The horizontal S-wave transducers are rotated by 90° azimuthally relative to the plane of the P-wave transducers. The velocities for the different angles and modes were sampled in a sequence, separated by a delay of a few seconds to avoid any noise (interference) from the preceding sampling. Small ultrasonic transducers (2 mm in diameter) for the oblique velocity measurements were utilized to obtain group velocities directly as verified by finite-difference wave-propagation simulations (Dellinger and Vernik 1994; Dewhurst and Siggins 2006; Hornby 1998; Larsen et al. 2011; Sarout and Guéguen 2008). The dominant excitation frequencies for the vertical and non-vertical P-waves were 500 kHz and 600 kHz, respectively, and 125 kHz for the S-waves.

In the beginning of the test, the sample was pre-stressed and exposed to the in-situ brine salinity based upon a pore fluid analysis of the field cores. After consolidation (i.e., maintaining constant initial stress and allowing drainage of the pore fluid), the sample was loaded in drained conditions to match the estimated in-situ stress and pore pressure values estimated by the field operator (Table 8.1).

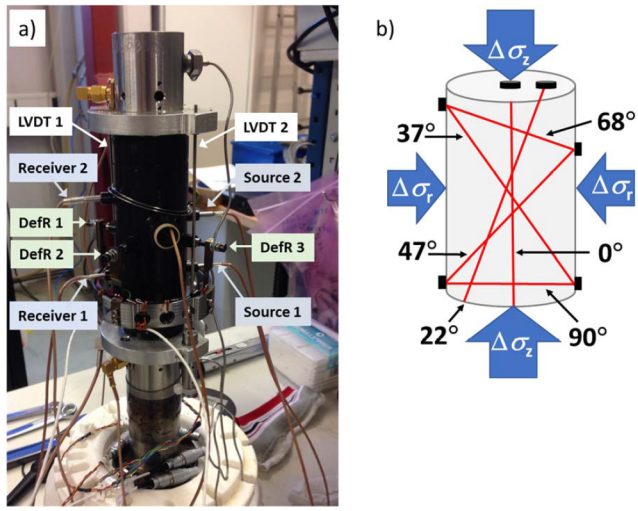


**Figure 8.3:** The setup (stack) for the testing prior to mounting in the load frame. The sample is embedded inside the black Viton rubber sleeve. Source/Receiver: two pairs of P-wave sources and receivers, respectively, for the oblique and the horizontal velocity measurements (37°, 47°, 68° and 90°) in the same azimuthal plane. The transducers for the vertical P- and S-waves (0°) and the 22° P-wave propagation are integrated in the front of the loading pistons above and beneath the sample. LVDT: linear variable differential transformers for vertical strain measurements (LVDT 3 is hidden). DefR: attachments for two pairs of cantilevers for horizontal strain measurements (DefR 4 is hidden). b) At the in-situ stress and pore pressure, the vertical and horizontal stress changes were independently exerted on the cylindrical samples according to the different stress paths (Table 8.2). Ultrasonic P-wave velocities were measured along the ray paths (red lines) in multiple directions (0°, 22°, 37°, 47°, 6° and 90° relative to the vertical direction), constrained by the positions of the transducers (black discs).

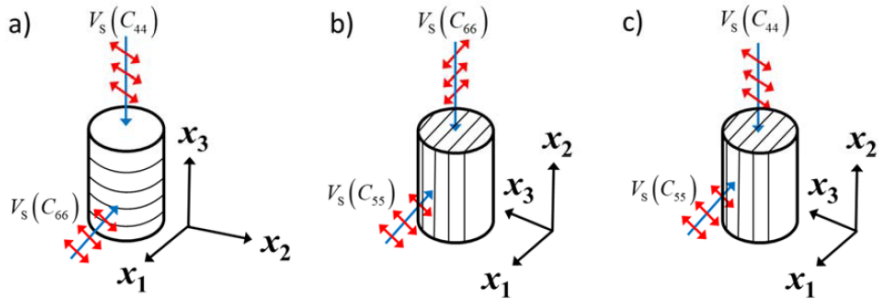


**Figure 8.4:** Polarization (red arrows) and propagation direction (blue arrows) of the S-waves in the a) 0° sample test (all samples), b) 90° sample test of M shale, and c) 90° sample test of D shale.

Drained condition means that the pore pressure is controlled externally by opening the valves to a pump ("reservoir") maintaining a constant (target) pore pressure. A drained loading to in-situ stress and pore pressure is expected to lead to full saturation (Dudley et al. 2016). The magnitude of stress changes applied in our tests (a few $MPa$) aligns with strain levels typically observed in the vicinity of a depleting reservoir. Therefore, our tests directly relate to field conditions. The changes in porosity and density associated with such stress changes are generally small in the surroundings of the reservoir (Holt et al. 2018). A clear sign of proper saturation was obtained by observing the undrained pore pressure response to the change of isotropic stress. The estimated Skempton B values (Skempton 1954) were 0.86 for M shale, 0.87 for D shale, and 0.83 for B shale. These values align with the range expected for saturated shales (Holt et al. 2018). For undersaturated samples, the Skempton B value would have been significantly lower. In the tests with the 45° and 90° samples, it was not possible to obtain the in-situ stress because the setup was constrained by isotropic horizontal stresses. For these samples the baseline stress was isotropic, equal to the horizontal in-situ stress. This bias from in-situ vertical stress is not expected to significantly influence the results because the horizontal and vertical in-situ stresses are very close for the tested samples. There was no indication of rock failure in any of the tests.

All measurements and analysis in this study assume intrinsic transverse isotropy of the samples with isotropic bedding in the $[x_1, x_2]$ plane, which is widely accepted for overburden shales (Asaka 2023; Dewhurst and Siggins 2006; Hornby 1998; Johnston 1987; Jones and Wang 1981; Piane et al. 2011; Sarout and Guéguen 2008; Thomsen 1986). A pair of P-wave transducers is employed to estimate the horizontal velocity (Figure 8.3a). The horizontal S-wave transducers can also be used to quantify possible anisotropy in the horizontal plane, as they are azimuthally aligned at 90° relative to the horizontal P-wave transducers. We exploit the fact that the horizontal S-wave source inevitably generates a small P-wave signal, which can be recorded as a first arrival by the S-wave receiver. This signal was used to estimate the horizontal P-wave velocity orthogonal to the P-wave velocity estimated from the horizontal P-wave transducer pair. Under constant in-situ stress conditions, the azimuthal variation of the P-wave velocity ranged from 10 $m/s$ to 40 $m/s$ for the three shales, which is one order of magnitude lower than the difference between vertical and horizontal P-wave velocities. This azimuthal variation in the horizontal P-wave velocities falls within the error of the P-wave velocity estimation (see Section 8.3.8). Thus, it is inconclusive whether this slight discrepancy arises from a small deviation from TI symmetry or measurement uncertainties. Furthermore, it should be noted that despite utilizing the best portion of the cores received from the field operator, determined through visual inspection and CT images, shales may still inevitably possess smaller natural inhomogeneities. Nevertheless, all this indicates that the assumption of VTI symmetry for our field shales is appropriate. To assess the consistency of the oblique P-wave velocities with the TI assumption, we monitored the fit over a 5-hour period under constant in-situ stress, recording 40–50 time-timesteps for each shale. With a maximum variation of 0.05 in Thomsen's $\delta$ parameter (Thomsen 1986), all oblique velocities

consistently matched at every time-step. This observation further reinforces the validity of the TI assumption.

### 8.3.2 In-situ stress paths

After consolidation at the in-situ stress and pore pressure, a sequence of undrained stress-cycles involving different stress paths was applied. Ultrasonic velocity data from these stress cycles were subsequently utilized to calibrate the TOE coefficients. The undrained state imposed during the stress-cycling is considered realistic for shales due to their low permeability, as discussed further in Section 8.3.5. The stress cycling around the in-situ stress state involved 1) isotropic stress changes, 2) uniaxial stress changes, 3) uniaxial strain changes (termed $K_0$), and 4) constant-mean-stress changes. Noteworthy, this leads to a variation in pore pressure due to the undrained conditions.

1. isotropic stress,
2. uniaxial stress,
3. uniaxial strain (horizontal stress adjust to ensure no radial strains),
4. constant-mean-stress,

The constant-mean-stress-path was included because close to constant mean-stress changes are predicted in a subsurface with equal stiffness of the reservoir and the surrounding rocks (Fjær et al. 2021; Geertsma 1973). One stress cycle consists of a loading step (vertical stress increase) followed by an unloading step (vertical stress decrease), both of equal magnitudes, accompanied with isotropic horizontal stress changes according to the stress path (Table 8.2). For instance, when applying a uniaxial stress change in the vertical direction, the horizontal stress was kept at the in-situ value specified in Table 8.1. The cycles around the in-situ stress state are schematically shown in Figure 8.5. After each step, the sample was kept at a constant stress level for 2–4 hours to consolidate. After this period, strains and velocity changes used in our analysis were measured. Prior each stress cycle, the connection between the sample and the pore pressure intensifier was opened to remove any pore pressure drift away from the in-situ conditions.

| Stress path | Sample alignment [°] | $\Delta\sigma_1$ [MPa] | $\Delta\sigma_2$ [MPa] | $\Delta\sigma_3$ [MPa] | $\Delta\sigma(45^\circ)$ [MPa] | M shale [steps] | D shale [steps] | B shale [steps] |
|---|---|---|---|---|---|---|---|---|
| Isotropic stress | 0 | 5.0 | 5.0 | 5.0 | 0 | 4 | 4 | 4 |
| Uniaxial strain | 0 | 3.3–3.8[a] | 3.3–3.8[a] | 5.0 | 0 | 4 | 2 | 4 |
| Uniaxial stress | 0 | 0 | 0 | 5.0 | 0 | 4 | 2 | 4 |
| Constant-mean-stress | 0 | -2.5 | -2.5 | 5.0 | 0 | 3 | 2 | 4 |
| Uniaxial stress | 45 | 0 | 0 | 0 | 5.0 | 4 | 2 | 4 |
| Isotropic stress | 90 | 5.0 | 5.0 | 5.0 | 0 | 3 | 4[b] | 4[b] |
| Uniaxial stress | 90 | 0 | 5.0 | 0 | 0 | 3 | 4 | 4[b] |

[a] 3.8 MPa for M shale and D shale; 3.3 MPa for B shale.

[b] Data not utilized.

**Table 8.2:** Sample alignment (Figure 8.1) and stress changes (for vertical loading steps) $\Delta\sigma_i$ for the different stress paths. For unloading steps, the signs of the stress changes are inverted. The 45° sample was loaded along the sample's cylinder axis ($\Delta\sigma(45°)$). Number of stress steps per stress path is provided

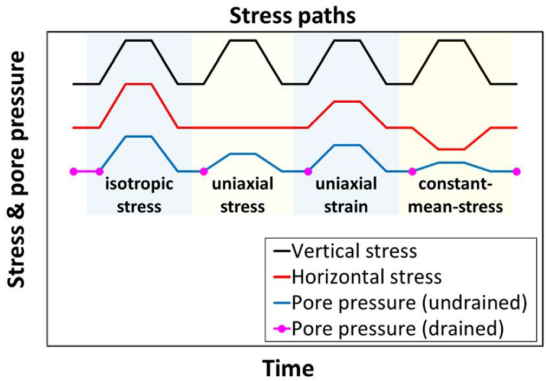


**Figure 8.5:** Schematic illustration of the test protocol with the different in-situ stress path cycles exerted by changing the isotropic stress, uniaxial stress, uniaxial strain, and constant-mean-stress (Table 8.2). The pore pressure was drained to the in-situ value prior each cycle to avoid drift in the test conditions (indicated by dots). During the stress cycles, the sample was kept undrained. The actual pore pressure response depends upon the specific material properties and the stress path.

### 8.3.3 Static stiffness from laboratory data

The TI static stiffnesses of the shales were used in the geomechanical modelling. Because of the small strains, we assume that the static stiffness is linear in strain. It can be mentioned that finite strains can be accounted for in a static TOE model as Wang and Schmitt (2021) suggested for isotropic materials. However, this will complicate the calculation of the static model, and consequently also the dynamic TOE model in our case, because a change of strain implies a change of moduli, which in consequence changes the strain.

Hooke's law for the stiffness $\boldsymbol{C}$ of a TI medium with the symmetry axis aligned with $x_3$ is (Fjær et al. 2021)

$$\begin{bmatrix} \sigma_1 \\ \sigma_2 \\ \sigma_3 \\ \sigma_4 \\ \sigma_5 \\ \sigma_6 \end{bmatrix} = \begin{bmatrix} C_{11} & C_{11}-2C_{66} & C_{13} & 0 & 0 & 0 \\ C_{11}-2C_{66} & C_{11} & C_{13} & 0 & 0 & 0 \\ C_{13} & C_{13} & C_{33} & 0 & 0 & 0 \\ 0 & 0 & 0 & C_{44} & 0 & 0 \\ 0 & 0 & 0 & 0 & C_{44} & 0 \\ 0 & 0 & 0 & 0 & 0 & C_{66} \end{bmatrix} \begin{bmatrix} e_1 \\ e_2 \\ e_3 \\ e_4 \\ e_5 \\ e_6 \end{bmatrix}. \tag{8.14}$$

Hooke's law for the compliance $\boldsymbol{S} \equiv \boldsymbol{C^{-1}}$ of a transversely isotropic material is

$$\boldsymbol{e} = \boldsymbol{S}\boldsymbol{\sigma}. \tag{8.15}$$

The static stiffness used in the geomechanical modelling is obtained from three samples drilled 0°, 45° and 90° relative to the symmetry axis (Figure 8.1). From the uniaxial strain ($e_i = 0$ for $i \neq 3$) along $x_3$ in the 0° sample, we obtain the vertical plane-strain modulus V H and the vertical $K_0$ modulus from Equation (8.14):

$$H_V = \frac{\Delta\sigma_3}{e_3} = C_{33}, \tag{8.16}$$

$$K_0 = \frac{\Delta\sigma_1}{\Delta\sigma_3} = \frac{C_{13}}{C_{33}}, \tag{8.17}$$

A uniaxial stress change along $x_3$ in the 0° sample test provide the vertical Young's modulus $E_V$, and a uniaxial stress change along $x_2$ in the 90° sample test provide the horizontal Young's modulus $E_H$. From Equation (8.15) we obtain:

$$E_V = \frac{\Delta\sigma_3}{e_3} = C_{33} - \frac{C_{13}^2}{C_{11}-C_{66}}, \sigma_i = 0 \text{ for } i \neq 3, \tag{8.18}$$

$$E_H = \frac{\Delta\sigma_2}{e_2} = \frac{4C_{66}\left[\left(C_{11} - C_{66}\right)C_{33} - C_{13}^2\right]}{C_{11}C_{33} - C_{13}^2}, \sigma_i = 0 \text{ for } i \neq 2, \tag{8.19}$$

For a uniaxial stress at a general angle relative to the symmetry axis (Nye 1985, p. 145) provide the Young's modulus expressed in compliances. The Young's modulus at 45°, $E_{(45)}$ , which relates a uniaxial stress change $\sigma_{(45)}$ a uniaxial strain $e_{(45)}$ at 45°, can be recast in terms of the stiffnesses to

$$\begin{aligned} E_{(45)} &= \frac{\Delta\sigma_{(45)}}{e_{(45)}} \\ &= \frac{16C_{44}C_{66}\left[C_{33}\left(C_{11} - C_{66}\right) - C_{13}^2\right]}{4\left[C_{11}C_{33} - C_{13}^2 + C_{44}\left(C_{11} - C_{13}\right) - C_{66}\left(C_{33} + C_{44}\right)\right]C_{66} + C_{44}\left(C_{11}C_{33} - C_{13}^2\right)}. \end{aligned} \tag{8.20}$$

Each of the five moduli estimated from the stress cycles, $H_V$, $K_0$, $E_V$, $E_H$ and $E_{(45)}$ is calculated as the average value of all steps for the relevant stress path. These moduli are combined with the compound parameter,

$$A = \frac{E_V K_0^2 H_V^2}{H_V - E_V}. \tag{8.21}$$

This allows for determination of the five independent TI static stiffness coefficients:

$$C_{11} = A\left(\frac{1}{E_{\mathrm{V}}} + \frac{E_{\mathrm{H}}}{4A - H_{\mathrm{V}}E_{\mathrm{H}}}\right), \tag{8.22}$$

$$C_{13} = H_{\mathrm{V}}K_0, \tag{8.23}$$

$$C_{33} = H_{\mathrm{V}}, \tag{8.24}$$

$$C_{44} = \left(\frac{4}{E_{(45)}} + \frac{H_{\mathrm{V}}K_0}{A} - \frac{1}{E_{\mathrm{V}}} - \frac{1}{E_{\mathrm{H}}}\right)^{-1}, \tag{8.25}$$

$$C_{66} = \frac{AE_{\mathrm{H}}}{4A - H_{\mathrm{V}}E_{\mathrm{H}}}. \tag{8.26}$$

Values of these stiffnesses can be verified by inserting them into Equation (8.16)–(8.20).

### 8.3.4 Dynamic stiffness from laboratory data

Wave propagation in the symmetry directions of the TI shales, i.e., in the $x_3$ direction or the $[x_1, x_2]$ plane, implies equal phase and group velocities and angles (Thomsen 1986). Thus, the $C_{11}$, $C_{33}$, $C_{44}$ and $C_{66}$ TI coefficients for both the baseline and monitor states are determined by

$$C_{ii} = \rho V_{ii}^2, i = 1, 3, 4, 6 \tag{8.27}$$

where $\rho$ is density (corrected for volumetric strain) and $V$ is the group velocity estimated from the laboratory test. To determine $C_{13}$ from the 0° sample test, the group velocities estimated at 22° (only for B shale), 37°, 47°, and 68° were utilized (Figure 8.3b). A complete set of velocities was estimated every 30 seconds. For each set (time-step) an optimization routine was run to estimate $C_{13}$. The ray angle $\phi$ corresponds to the angle of the straight line between the centre positions of the transducer pairs relative to the cylinder axis of the sample (Figure 8.3b). For the oblique P-wave velocities, the phase angle $\theta$ and the phase velocity $v$ were obtained from (Thomsen 1986)

$$\phi = \tan^{-1}\left\{\left(\tan\theta + \frac{1}{v}\frac{\partial v}{\partial \theta}\right)\left(1 - \frac{\tan\theta}{v}\frac{\partial v}{\partial \theta}\right)^{-1}\right\} \tag{8.28}$$

$$v = \left\{\frac{1}{2\rho}\left[C_{33} + C_{44} + (C_{11} - C_{33})\sin^2\theta + D\right]\right\}^{\frac{1}{2}} \tag{8.29}$$

with

$$\begin{aligned} D \equiv & \left\{(C_{33} - C_{44}) + 2\left[2\left(C_{13} - C_{44}\right)^2 - (C_{33} - C_{44})\left(C_{11} + C_{33} - 2C_{44}\right)\right]\sin^2\theta \right. \\ & \left. + \left[\left(C_{11} + C_{33} - 2C_{44}\right)^2 - 4\left(C_{13} - C_{44}\right)^2\right]\sin^4\theta\right\}^{\frac{1}{2}}. \end{aligned} \tag{8.30}$$

Following Berryman (1979), the scalar magnitude of the group velocity V was calculated according to

$$V = \left[v^2 + \left(\frac{\partial v}{\partial \theta}\right)^2\right]^{\frac{1}{2}}. \tag{8.31}$$

At each time-step, the $C_{13}$ was determined by minimizing the sum of square deviations between the predicted group velocities and the experimentally determined

group velocities (Duda et al. 2020). The theory involved in this routine is valid for arbitrary (not just weak) anisotropy. Commonly, for the determination of $C_{13}$ (or $\delta$) only the 45° direction of TI rocks is considered (Dewhurst and Siggins 2006; Hornby 1998; Sarout and Guéguen 2008). Obtaining and employing a surplus of oblique P-wave measurements improves the estimate of $C_{13}$ (Thomsen 1986), as done in this study. It is worth noting that there are also other methods for inverting stiffnesses in anisotropic media, e.g., Mah and Schmitt (2003) used an inversion technique based on plane wave decomposition.

### 8.3.5 Calibration of TOE coefficients to experimental data

The TOE coefficients are calibrated by optimizing the monitor stiffnesses predicted by Equation (8.12) with respect to the experimentally determined stiffnesses. In the 0° sample tests, the horizontal (H) strains are isotropic because isotropic horizontal stresses are exerted on a TI medium, i.e., $e_H \equiv e_1 = e_2$. There are no shear strains in the coordinate system of the sample, because the sample is vertically aligned with the laboratory setup where only normal stresses are exerted. The following baseline and monitor dynamic stiffnesses were estimated in the tests: $C_{11}$, $C_{13}$, $C_{33}$, $C_{44}$ and $C_{66}$. Thus, the corresponding monitor TI TOE stiffnesses in equation **(12)** simplifies to

$$\begin{aligned}
C_{11}^{\mathrm{m}} &= C_{11} + 2\left(C_{111} - 2C_{166}\right)e_{\mathrm{H}} + C_{113}e_3 \\
C_{13}^{\mathrm{m}} &= C_{13} + 2\left(C_{113} - C_{366}\right)e_{\mathrm{H}} + C_{133}e_3 \\
C_{33}^{\mathrm{m}} &= C_{33} + 2C_{133}e_{\mathrm{H}} + C_{333}e_3 \\
C_{44}^{\mathrm{m}} &= C_{44} + 2C_{144}^{*}e_{\mathrm{H}} + C_{344}e_3 \\
C_{66}^{\mathrm{m}} &= C_{66} + 2C_{166}e_{\mathrm{H}} + C_{366}e_3
\end{aligned} \tag{8.32}$$

with the compound coefficient

$$C_{144}^{*} = C_{144} + C_{456}. \tag{8.33}$$

To determine the TI TOE coefficients, P-wave velocities were measured along all ray-paths shown in Figure 8.3b in addition to horizontal and vertical S-wave velocities, for each of the stress-states shown in Figure 8.5. As a result, seven out of the nine TI TOE coefficients were determined from the test carried out on the 0° sample: $C_{111}$, $C_{113}$, $C_{133}$, $C_{144}$, $C_{166}$, $C_{344}$ and $C_{366}$, in addition to the compound coefficient $C_{144}^{*}$. A similar TOE model, constrained by isotropic horizontal strains, was discussed by Duda et al. (2020) and applied by Bakk et al. (2020a). In addition, we investigate the isotropic analogue of the anisotropic TOE model, as explained in the end of section Section 8.2, and compare it with the predictions of the anisotropic TOE. This is crucial because, until now, only isotropic TOE models have been employed in the modelling of sedimentary rocks (Asaka 2023; Donald and Prioul 2015; Fuck et al. 2009; Prioul et al. 2004; Prioul and Lebrat 2004; Rasolofosaon 1998; Sarkar et al. 2003; Shapiro 2017; Sinha and Kostek 1996; Winkler and Liu 1996). The calibration of the corresponding isotropic TOE coefficients, $C_{111}^{iso}$, $C_{113}^{iso}$ and $C_{144}^{iso}$, is performed uniquely with measurements obtained

from the 0° sample test. With the constraints in Equation (8.13) inserted into Equation (8.12), the relevant monitor stiffnesses used for the calibration of the isotropic TOE coefficients are

$$\begin{aligned}
C_{11}^{\mathrm{m,\,iso}} &= C_{11} + \left(C_{111}^{\mathrm{iso}} + C_{113}^{\mathrm{iso}}\right) e_{\mathrm{H}} + C_{113}^{\mathrm{iso}} e_3, \\
C_{13}^{\mathrm{m,iso}} &= C_{13} + 2\left(C_{113}^{\mathrm{iso}} - C_{144}^{\mathrm{iso}}\right) e_{\mathrm{H}} + C_{113}^{\mathrm{iso}} e_3, \\
C_{33}^{\mathrm{m,iso}} &= C_{33} + 2C_{113}^{\mathrm{iso}} e_{\mathrm{H}} + C_{111}^{\mathrm{iso}} e_3, \\
C_{44}^{\mathrm{m,\,iso}} &= C_{44} + \left[C_{144}^{\mathrm{iso}} + \frac{1}{4}\left(C_{111}^{\mathrm{iso}} - C_{113}^{\mathrm{iso}}\right)\right] e_{\mathrm{H}} + \frac{1}{4}\left(C_{111}^{\mathrm{iso}} - C_{113}^{\mathrm{iso}}\right) e_3, \\
C_{66}^{\mathrm{m,\,iso}} &= C_{66} + \frac{1}{4}\left(C_{111}^{\mathrm{iso}} - C_{113}^{\mathrm{iso}}\right) e_{\mathrm{H}} + C_{144}^{\mathrm{iso}} e_3.
\end{aligned} \tag{8.34}$$

Equation (8.34) is equivalent to the model proposed by Prioul et al. (2004), except they used a different set of independent TOE coefficients. Only the TOE coefficients are isotropic in Equation (8.34), whereas the SOE baseline coefficients are anisotropic and equal to the baseline SOE coefficients. This enables a direct comparison of the predictions with isotropic symmetry and TI symmetry within the TOE coefficients. The calibration of the coefficients in the TI TOE model in Equation (8.32) and of the isotropic TOE in Equation (8.34), is achieved by iteratively minimizing the residual $R$. The residual is defined as the sum of square deviations between the predicted (P) monitor stiffness $C_{ij}^{m,P}$ and the experimentally estimated (E) monitor stiffness $C_{ij}^{m,E}$ :

$$\begin{aligned}
R = \sum_i \frac{1}{N_i} \Bigg[ &\left(C_{11}^{\mathrm{m,P}} - C_{11}^{\mathrm{m,E}}\right)^2 + \left(C_{13}^{\mathrm{m,P}} - C_{13}^{\mathrm{m,E}}\right)^2 + \left(C_{33}^{\mathrm{m,P}} - C_{33}^{\mathrm{m,E}}\right)^2 \\
&+ \left(C_{44}^{\mathrm{m,P}} - C_{44}^{\mathrm{m,E}}\right)^2 + \left(C_{66}^{\mathrm{m,P}} - C_{66}^{\mathrm{m,E}}\right)^2 \Bigg].
\end{aligned} \tag{8.35}$$

Because the number of steps ($N_i$) per stress path ($i$) varied (Table 8.2), the residual is averaged per stress path giving equal weight to each of the stress paths in the inversion.

To obtain the last two TI TOE coefficients $C_{144}$ and $C_{456}$, we utilized the uniaxial stress path of the 90° sample tests to obtain a required strain anisotropy in the $[x_1, x_2]$ plane. By inserting $C_{144}^*$ from Equation (8.33) into $C_{44}^m$ and $C_{55}^m$ in Equation (8.12) we obtain

$$C_{44}^{\mathrm{m}} = C_{44} + C_{144} e_1 + \left(2C_{144}^* - C_{144}\right) e_2 + C_{344} e_3, \tag{8.36}$$

and

$$C_{55}^{\mathrm{m}} = C_{44} + \left(2C_{144}^* - C_{144}\right) e_1 + C_{144} e_2 + C_{344} e_3. \tag{8.37}$$

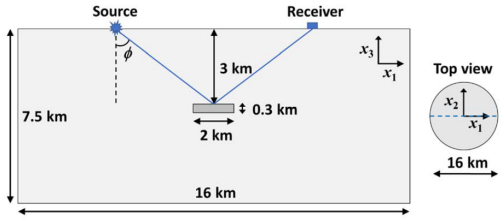


**Figure 8.6:** Vertical section of the axisymmetric geomechanical model. The top horizontal boundary of the disk-shaped reservoir is located at a depth of 3 km. The reservoir has a diameter of 2 km and a thickness of 0.3 km. Straight ray paths in the vertical section $[x_1, x_3]$ are used to quantify two-way traveltime shifts at different ray angles $\phi$ from the source to the receiver, via the mid-point reflector at the top of the reservoir. A miniature top view of the entire model in the $[x_1, x_2]$ plane is shown to the right, where the intersection of the vertical section is indicated by the broken line.

Since $C^*_{144}$ and $C_{344}$ are already calibrated from the 0° sample test, we could determine $C_{144}$ from the 90° sample test. The horizontally propagating S-waves in M shale ( $C^m_{55}$, Figure 8.4b), and both the vertically and horizontally propagating S-waves in D shale ($C^m_{44}$ and $C^m_{55}$, 8.4c) were utilized for the determination of $C_{144}$. Finally, the ninth TOE coefficient, $C_{456}$ , was estimated from Equation (8.33).

### 8.3.6 Geomechanical model

We conducted geomechanical simulations using a finite element software (DIANA FEM) to scale up laboratory results to field scale. An axisymmetric model was used to represent a simplified field case (Figure 8.6). Such model can highlight useful trends predicted by the TOE tensor related to angular dependence of time-shifts and time-strains in the overburden. Such insight is more difficult to attain with a complex geomechanical model. No horizontal displacements were permitted at the vertical (circumferential) boundary far away from the reservoir (right image in Figure 8.6), while no vertical displacements were permitted at the horizontal boundary at the bottom of the model. A free surface was assumed at the top of the model. We simulated the rock's response to a homogeneous pore pressure reduction (depletion) in a reservoir from 35 MPa (baseline state) to 0 MPa (monitor state). In both these equilibrium states, the pore pressure is uniform (constant) in the entire reservoir. The static isotropic moduli of the reservoir (Table 8.3) represent a weak sandstone (Fjær et al. 2021). In the non-reservoir formation, we assumed a homogeneous (undrained) TI static linear stiffness and a homogeneous dynamic TI baseline stiffness populated by the properties of the three shales corresponding to each simulation case (Table 8.3). For each of these cases, we assigned the calibrated values of TOE coefficients for both the TI TOE model and the isotropic TOE model from Table 8.4. This requires five different calculations, as the TI TOE tensor was not determined for B shale. The depth and size of the reservoir were kept unchanged in all cases.

| Rock | Modulus | $C_{11}$ [GPa] | $C_{33}$ [GPa] | $C_{13}$ [GPa] | $C_{44}$ [GPa] | $C_{66}$ [GPa] |
|---|---|---|---|---|---|---|
| M shale | Static | 7.6 (0.6) | 7.3 (0.3) | 5.6 (0.3) | 0.5 (0.1) | 1.3 (0.1) |
| D shale | Static | 9.7 (0.7) | 9.3 (0.4) | 7.0 (0.4) | 1.0 (0.1) | 1.9 (0.2) |
| B shale | Static | 13.7 (0.8) | 10.3 (0.4) | 6.7 (0.4) | 2.0 (0.1) | 4.5 (0.6) |
| M shale | Dynamic | 13.2 (0.6) | 9.9 (0.5) | 8.0 (0.9) | 1.6 (0.2) | 2.9 (0.3) |
| D shale | Dynamic | 15.7 (0.7) | 12.6 (0.6) | 9.2 (1.1) | 2.0 (0.3) | 2.8 (0.3) |
| B shale | Dynamic | 20.9 (0.8) | 15.3 (0.6) | 10.2 (1.0) | 3.1 (0.3) | 5.3 (0.4) |
| Reservoir | Static[a] | 2.4 | 2.4 | 1.3 | 0.6 | 0.6 |

[a] Drained stiffness.

**Table 8.3:** Static (undrained) and dynamic (ultrasonic) second-order elastic stiffness of the tested field shales within a 95 % confidence interval (in parenthesis). Static data are based on three differently oriented samples for each shale (Figure 8.1). Dynamic stiffness is obtained from the 0° sample tests, except for 66 C of M shale that was obtained from the isotropic stress path in the 90° sample test. A static isotropic drained elastic stiffness (frame modulus) of the reservoir rock was applied in the modelling case (Fjær et al. 2021, p. 665) with Biot's $\alpha$ parameter equal to 1.

| Shale | TOE | $C_{111}$ [GPa][a] | $C_{113}$ [GPa] | $C_{133}$ [GPa] | $C_{166}$ [GPa] | $C_{333}$ [GPa] | $C_{366}$ [GPa] | $C_{144}$ [GPa] | $C_{344}$ [GPa] | $C_{456}$ [GPa] |
|---|---|---|---|---|---|---|---|---|---|---|
| M shale | TI | 312 (179) | 107 (27) | 89 (27) | 68 (93) | 105 (24) | 21 (43) | 25 (10) | 33 (9) | 20 (20) |
| M shale | isotropic | 94 (17) | 57 (18) | 57 (18) | 9 (25) | 94 (17) | 11 (12) | 11 (12) | 9 (25) | -1 (14) |
| D shale | TI | 332 (67) | 145 (29) | 114 (35) | 61 (27) | 137 (31) | 32 (24) | 47 (14) | 34 (12) | 0 (23) |
| D shale | isotropic | 145 (27) | 104 (29) | 104 (29) | 10 (40) | 145 (27) | -2 (12) | -2 (12) | 10 (40) | 6 (16) |
| B shale | isotropic | 252 (14) | 194 (17) | 194 (17) | 14 (22) | 252 (14) | 13 (6) | 13 (6) | 14 (22) | 1 (8) |

[a] The corresponding unit of strain in equation (12) is 1.

**Table 8.4:** Calibrated TOE coefficients within a 95 % confidence interval (in parenthesis) for the TI TOE model and the isotropic TOE model.

### 8.3.7 Calculation of time-shifts and time-strains

In the geomechanical model, the baseline properties are homogenous, which implies straight ray paths in the baseline state within the overburden. After the depletion the strain field is heterogeneous. However, with the small strains involved in our study, straight ray paths are also assumed in the monitor state. The modelled strains in the irregular simulation grid were recalculated (interpolated) onto a regular grid (computational grid) consisting of cubes with edge length of 50 m. Each grid cell was assigned with a homogeneous (interpolated) strain. Consequently, the computational grid exhibits a cylindrical arrangement that reflects the physical situation of the axisymmetric model. The boundary of the vertical section depicted in Figure 8.6 is rectangular and aligns with the boundaries of both the computational and simulation grids. Although the use of a regular grid introduces a small numerical cubic anisotropic bias in the calculation of time-shifts, these errors are primarily of theoretical interest for this study, as our focus is on discussing overall trends. The selection of a 50-meter computational grid size represents a balance between ensuring sufficient quality of the interpolated strain data and achieving computational efficiency. We first consider a ray-path segment in one computational grid element of baseline length $L$ and ray angle $\phi$. The longitudinal strain of this segment is found by rotating the coordinate system of the strain tensor $\boldsymbol{\varepsilon}$ by an angle $\phi$ clockwise around $x_2$, such that the new (rotated) $x_3$-axis becomes aligned with the ray-path segment. This is obtained by the transformation (Fjær et al. 2021, p. 687):

$$\begin{bmatrix} \bar{\varepsilon}_{11} & \bar{\varepsilon}_{12} & \bar{\varepsilon}_{13} \\ \bar{\varepsilon}_{12} & \bar{\varepsilon}_{22} & \bar{\varepsilon}_{23} \\ \bar{\varepsilon}_{13} & \bar{\varepsilon}_{23} & \bar{\varepsilon}_{33} \end{bmatrix} = \begin{bmatrix} \cos\phi & 0 & \sin\phi \\ 0 & 1 & 0 \\ -\sin\phi & 0 & \cos\phi \end{bmatrix} \begin{bmatrix} \varepsilon_{11} & \varepsilon_{12} & \varepsilon_{13} \\ \varepsilon_{12} & \varepsilon_{22} & \varepsilon_{23} \\ \varepsilon_{13} & \varepsilon_{23} & \varepsilon_{33} \end{bmatrix} \begin{bmatrix} \cos\phi & 0 & -\sin\phi \\ 0 & 1 & 0 \\ \sin\phi & 0 & \cos\phi \end{bmatrix}. \tag{8.38}$$

Then, the longitudinal strain of the ray-path segment becomes in Voigt notation

$$\bar{e}_3 = e_1 \sin^2\phi + e_3 \cos^2\phi - e_5 \cos\phi \sin\phi. \tag{8.39}$$

We calculate time-shifts at a given offset, i.e., the source and receiver positions remain the same between the baseline and monitor states. This approach aligns with an offshore 4D seismic survey using towed streamers, where the source and receiver positions are not influenced by the subsurface strains. In this scenario, the contribution of geometric strain (seismic path length change) to the time-shifts are independent of the horizontal strain components, and only the vertical strain components are needed (e.g., Kudarova et al. 2016; Landrø and Stammeijer 2004). Additionally, the influence of fixed transducers versus transducers that move according to the strain at their respective positions difference is negligible, given the small overall contribution of geometric strain to the time-shift (section 8.4.2). The $e_1$ term thus vanishes in Equation (8.39). The shear strain $e_5$ is a sum of two displacement gradients of equal magnitudes related to strain along $e_1$ and $x_3$, respectively (Fjær et al. 2021, p.21), where only the $x_1$ component of $e_5$

is consequently kept. For a fixed offset (*), the longitudinal strain of the ray-path segment becomes

$$\bar{e}_3 = e_3 \cos^2\phi - \frac{1}{2} e_5 \cos\phi \sin\phi. \tag{8.40}$$

The time-shift $\Delta T$ for this segment is

$$\Delta T = T_{\mathrm{m}} - T_{\mathrm{b}} = L\left(\frac{1 - e_3\cos^2\phi + \frac{1}{2}e_5\cos\phi\sin\phi}{V_{\mathrm{m}}(\phi)} - \frac{1}{V_{\mathrm{b}}(\phi)}\right), \tag{8.41}$$

where $T$ is the traveltime and $V(\phi)$ is the group velocity in the baseline (b) and monitor (m) states. The two-way traveltime shift $\Delta TWT$ for ray angle $\phi$ is obtained by summing the local two-way traveltime changes in Equation (8.41) along the ray-path through the computational elements $i$:

$$\begin{aligned}\Delta TWT &= TWT_{\mathrm{m}} - TWT_{\mathrm{b}} \\ &= \sum_i L_i \left(\frac{1 - e_{3,i}\cos^2\phi + \frac{1}{2}e_{5,i}\cos\phi\sin\phi}{V_{\mathrm{m}}(\phi)} - \frac{1}{V_{\mathrm{b}}(\phi)}\right).\end{aligned} \tag{8.42}$$

From Equation (8.42) we can also estimate the geometric (G) contribution to the time-shift, i.e., the timeshift without velocity changes ($V_b(\phi)$=$V_m(\phi)$):

$$\Delta TWT_{\mathrm{G}} = -\sum_i \frac{L_i\left(e_{3,i}\cos^2\phi - \frac{1}{2}e_{5,i}\cos\phi\sin\phi\right)}{V_{\mathrm{b}}(\phi)}. \tag{8.43}$$

Time-strains, defined as fractional (local) time-shifts, are introduced to quantify the local dynamic alterations (Rickett et al. 2007). The time-strain is obtained from Equation (8.41)

$$\frac{\Delta T}{T_{\mathrm{b}}} = \frac{V_{\mathrm{b}}(\phi)}{V_{\mathrm{m}}(\phi)}\left(1 - e_3\cos^2\phi + \frac{1}{2}e_5\cos\phi\sin\phi\right) - 1. \tag{8.44}$$

To predict angular time-shifts and time-strains, the baseline velocities were first calculated. For a ray angle $\phi$, the corresponding phase angle and phase velocity were obtained by Equation (8.28) and (8.29). Subsequently, the group velocity was obtained by Equation (8.31). It is possible to have a higher symmetry of the monitor stiffness than of the TOE tensor, e.g., an isotropic strain with a hexagonal third-order stiffness tensor implies TI symmetry of the monitor stiffness (Fuck and Tsvankin 2009). However, in a field case the symmetry of the monitor stiffness will typically be lower than the lowest symmetry of the SOE tensor and the TOE tensor.

Hence, we need to deploy a more robust method to predict velocities for arbitrary symmetry of the monitor stiffness and arbitrary propagation directions. We utilized the open source Python module *christoffel* (Jaeken and Cottenier 2016), which is solving the Christoffel equation to obtain direction-dependent phase velocities, polarization vectors, group velocities, power flow angles, and enhancement factors based on a stiffness tensor of a solid (Fedorov 1968). The input to the *christoffel* module was the group angle, monitor stiffness calculated by Equation (8.12) populated with the strains from the modelling, and monitor density. The output was the group velocity that was used to predict angular time-shifts by Equation (8.42) and (8.43), and time strains by Equation (8.44).

The procedure for converting geomechanical data to velocity changes using the TI TOE coefficients can be summarized as followed:

1. Generate the complete six-component strain tensor from a fine-element simulation, expressed in Voigt notation.

2. Apply the strains and experimentally determined TOE coefficients to the monitor stiffness (Equation 8.12) to determine the monitor stiffness.

3. Calculate the monitor group velocity at a given ray angle using the Python module developed by Jaeken and Cottenier (2016).

### 8.3.8 Error analysis

A reference test on aluminium indicates a standard deviation of less than 2 % of the static Young's modulus. However, the moduli of shales will in general have less error than estimated for aluminium, since aluminium has a Young's modulus of 70 GPa while shales are much softer implying a larger strain for a given stress. Conservatively, we still assume a standard deviation of 2 % for the measured static compliances in Equation (8.16)–(8.20). The errors of the static moduli are determined through standard error propagation of the compliances into the static moduli in Equation (8.22)-(8.26). In the undrained state, there is a small fluid volume (dead volume) between the sample and the closing valves (about 2 ml) that is directly connected to the pore space of the sample. This may lead to a systematic error of the undrained moduli, which is not quantified.

The error associated with the velocities was estimated from uncertainties related to the picking of arrival times, sample length and radius, stresses, strains, and temperature fluctuations. Waveforms and picking of arrivals are discussed in detail by Bakk et al. (2020b). All measurements are done in a consolidated state and no significant drift in the measurements is observed. The standard deviation of the absolute value of the P-wave velocities was estimated to be 30 $m/s$. As this work focuses on velocity changes we analysed 50 consecutive waveforms from a field-shale test (25 minutes duration) recorded during cycling and determined that

standard deviations for the velocity changes were 2 $m/s$. To enhance the accuracy of the velocity change estimation, we took the average of 10 consecutive velocity estimates during the pauses between loading and unloading steps, after the sample consolidation at each new stress level was completed. For each of the shales, the in-situ stress cycles of the 0° tests lasted about three days and involved 20–28 steps (10-14 cycles). To assess any drift in the velocities, the velocities before the first in-situ cycle and after the last in-situ cycle step were compared at identical in-situ stress and pore pressure conditions. The average absolute velocity deviation across seven different modes was found to be around 2–3 $m/s$ for all three shales. Conservatively, the standard deviation of the relative velocity changes is estimated to be 2.8 $m/s$. Such a low discrepancy is indicative of a very high stability of the acoustic measurements, well-preserved core material, and near-perfect elastic behaviour (no plasticity) of the rock. Based on this error estimate, a Monte-Carlo simulation with $10^6$ inversions of the TOE coefficients was done. In each of these iterations, random errors from a Gaussian distribution were added to the experimentally determined dynamic stiffnesses. From the distribution of the individual TOE coefficients, the 95 % confidence interval was obtained (Table 8.4).

## 8.4 Results

### 8.4.1 Experimental data

The second-order static and dynamic stiffnesses for the different shales are provided in table 8.3. Overall, the stiffness increases with depth and decreases with porosity. For M shale, the quality of the horizontal S-wave signal in the 0° sample test was insufficient. Instead, we obtained $C_{66}$ from the isotropic stress path of the 90° sample test (Figure 8.1b). The second-order dynamic moduli are significantly larger than the static moduli.

The third-order TOE coefficients are provided in table 8.4. For B shale, the quality of the vertical S-wave velocity change was insufficient (affecting $C_{44}^M$), such that the TI TOE coefficients could not be determined. All inverted TI TOE coefficients exhibit a positive mean value. However, for three of the inverted isotropic TOE coefficients, slightly negative mean values are obtained. Additionally, for certain TOE coefficients, the confidence intervals exceed the corresponding mean values. This is plausible since there were no restrictions on the sign during the inversion. Negative signs for some of the third-order coefficients are also reported in other studies, such as Prioul et al. (2004) based on experiments, and Wang and Li (2009) based on ab initio simulations, along with references cited therein. The experimentally determined group velocity changes ($V_m - V_b$) due to 5 MPa vertical stress increase are provided for the different stress paths and ray angles, showing a significant dependence on stress path (Figure 8.7). These values are the mean of all steps for a given angle and stress path, with the velocity changes sign flipping

their sign for vertical unloading steps. The predictions by the TI TOE model and the isotropic TOE model are also shown in Figure 8.7. The experimental data exhibit relatively flat or slightly decreasing velocity changes with increasing angle for the isotropic stress path and the uniaxial-strain path. The velocity changes decrease significantly with angle for the uniaxial stress path and the constant-mean-stresspath, and become significantly negative at 68° and 90° for the constant-mean-stress path. The latter is caused by a significant compaction (negative strain) in the ray-path direction. These trends underline the strong coupling between the stress path and the angular strain dependence of velocities. The anisotropic TOE model demonstrates a good fit to the experimental data, considering the variety of stress paths and angles involved. The isotropic TOE model overestimates the velocity changes for the triaxial stress path and the constant-mean-stress path for all three shales, while for M shale and D shale the velocity changes for the isotropic stress path and the uniaxial-strain path are underestimated. The isotropic TOE model qualitatively predicts the angular trends of velocity changes well for all stress paths, despite its quantitative limitations.

### 8.4.2 Geomechanical modelling

The results based on the modelling data are only considered within the vertical section $[x_1, x_3]$ that intersects the symmetry axis of the reservoir (Figure 8.6). The strains in the reservoir surroundings are most significant in the proximity of the reservoir, with the horizontal in-plane strains ($e_1$) typically exhibit opposite sign as compared to the vertical strains (Figure 8.8). The horizontal tangential ("hoop") strains ($e_2$) around the reservoir are positive due to the reservoir depletion, which is accompanied by a shrinkage of the reservoir. Generally, the magnitudes of strains decrease with increasing static stiffness. With the axisymmetric model, the shear strains ($e_5$) are anti-symmetric about the vertical symmetry axis of the reservoir. Considering the vanishing strains outside the main strain cloud, the size of the geomechanical model is expected to be sufficient to avoid adverse boundary effects.

Two-way traveltime shifts were predicted as a function of angle with respect to the TI TOE model (not obtained for B shale) and the isotropic TOE model (Figure 8.9). For the TI TOE model, a pronounced peak of the traveltime shifts is predicted at ray angles around 45°. Contrarily, with the isotropic TOE model the time-shifts are decreasing with increasing angle for D shale and B shale, while for M shale times-shifts reach a slight peak at 20°. The contributions from the shear strains to time-shifts are particularly significant for the TI TOE model. The geometric contribution to the time-shifts (Equation 8.43) is relatively small for all shales, particularly for B shale. To better visualize the impact of the shear strains on the dynamic changes, time-strains are provided at 0° and 45° (Figure 8.10). The vertical time-shift is largest for B shale, which is a result of stress arching that increase with the stiffness of the non-reservoir formations (Mulders 2003; Yan et al. 2020).

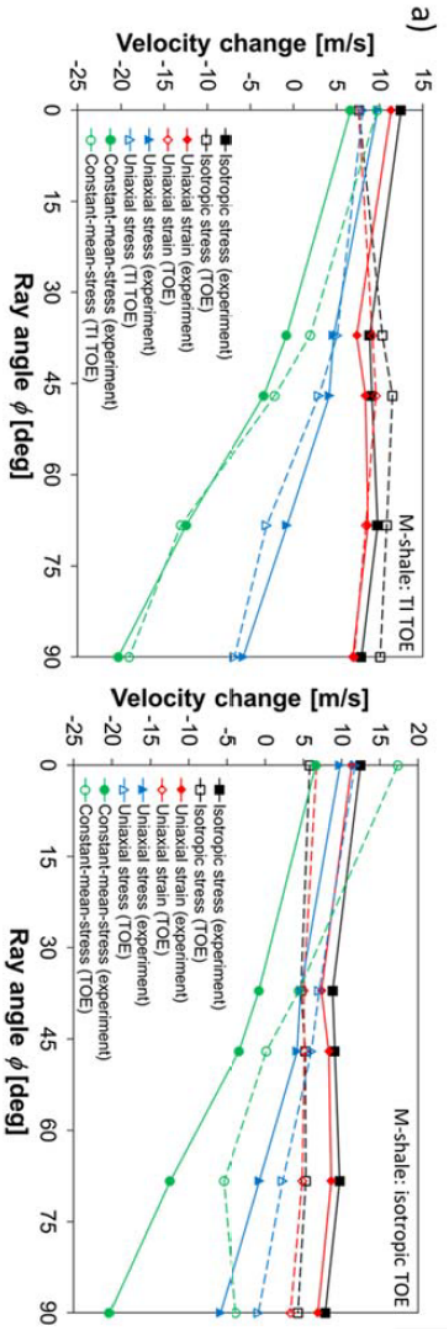
a)
Velocity change [m/s]
Ray angle ϕ [deg]
M-shale: TI TOE
Isotropic stress (experiment)
Isotropic stress (TOE)
Uniaxial strain (experiment)
Uniaxial strain (TOE)
Uniaxial stress (experiment)
Uniaxial stress (TI TOE)
Constant-mean-stress (experiment)
Constant-mean-stress (TI TOE)
Velocity change [m/s]
Ray angle ϕ [deg]
M-shale: isotropic TOE
Isotropic stress (experiment)
Isotropic stress (TOE)
Uniaxial strain (experiment)
Uniaxial strain (TOE)
Uniaxial stress (experiment)
Uniaxial stress (TOE)
Constant-mean-stress (experiment)
Constant-mean-stress (TOE)

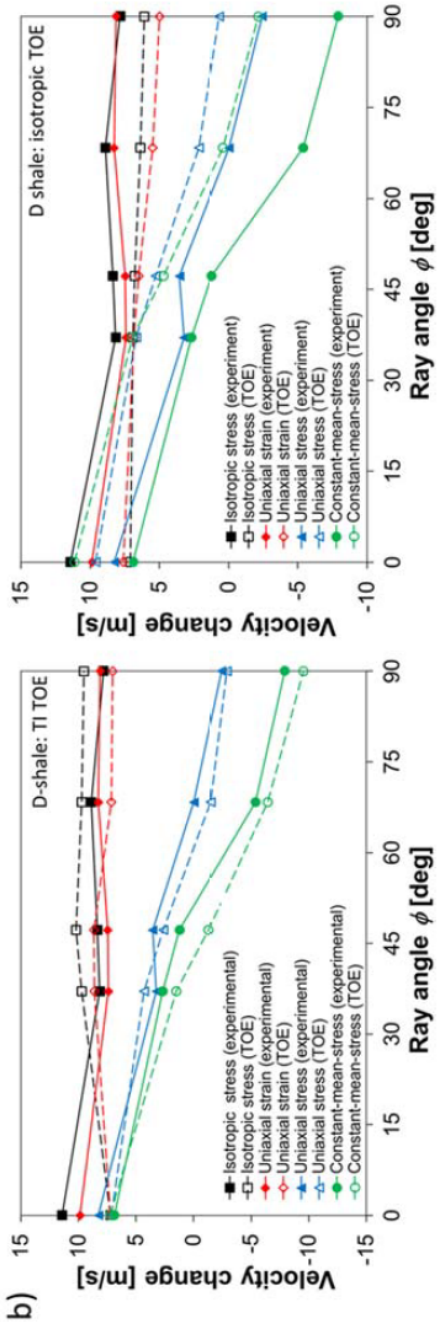
b)
D-shale: TI TOE
Velocity change [m/s]
Ray angle $\phi$ [deg]
Isotropic stress (experimental)
Isotropic stress (TOE)
Uniaxial strain (experimental)
Uniaxial strain (TOE)
Uniaxial stress (experimental)
Uniaxial stress (TOE)
Constant-mean-stress (experimental)
Constant-mean-stress (TOE)
D shale: isotropic TOE
Velocity change [m/s]
Ray angle $\phi$ [deg]
Isotropic stress (experiment)
Isotropic stress (TOE)
Uniaxial strain (experiment)
Uniaxial strain (TOE)
Uniaxial stress (experiment)
Uniaxial stress (TOE)
Constant-mean-stress (experiment)
Constant-mean-stress (TOE)

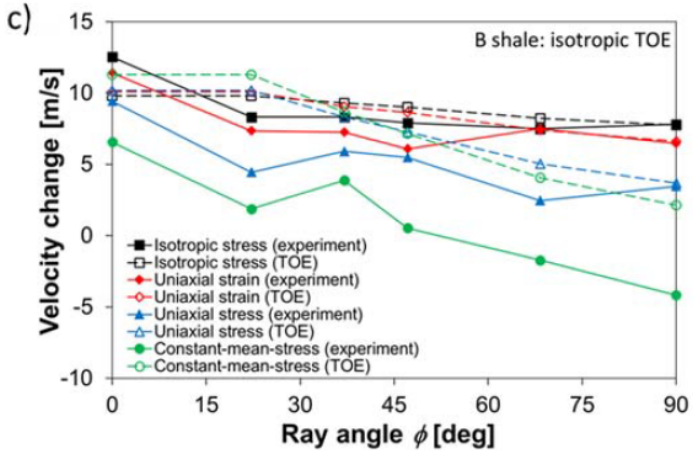


**Figure 8.7:** Group velocity changes versus ray angle for the different stress paths corresponding to 5 MPa vertical loading for a) M shale, b) D shale, and c) B shale. The experimental data (full lines) are shown together with the predicted data by the TI TOE model and the isotropic TOE model (broken lines). The 95 % confidence interval for the experimental group velocity changes is $\pm$ 5.6 $m/s$. B shale was not calibrated to the TI TOE model because the vertical S-wave velocity changes were not reliable.

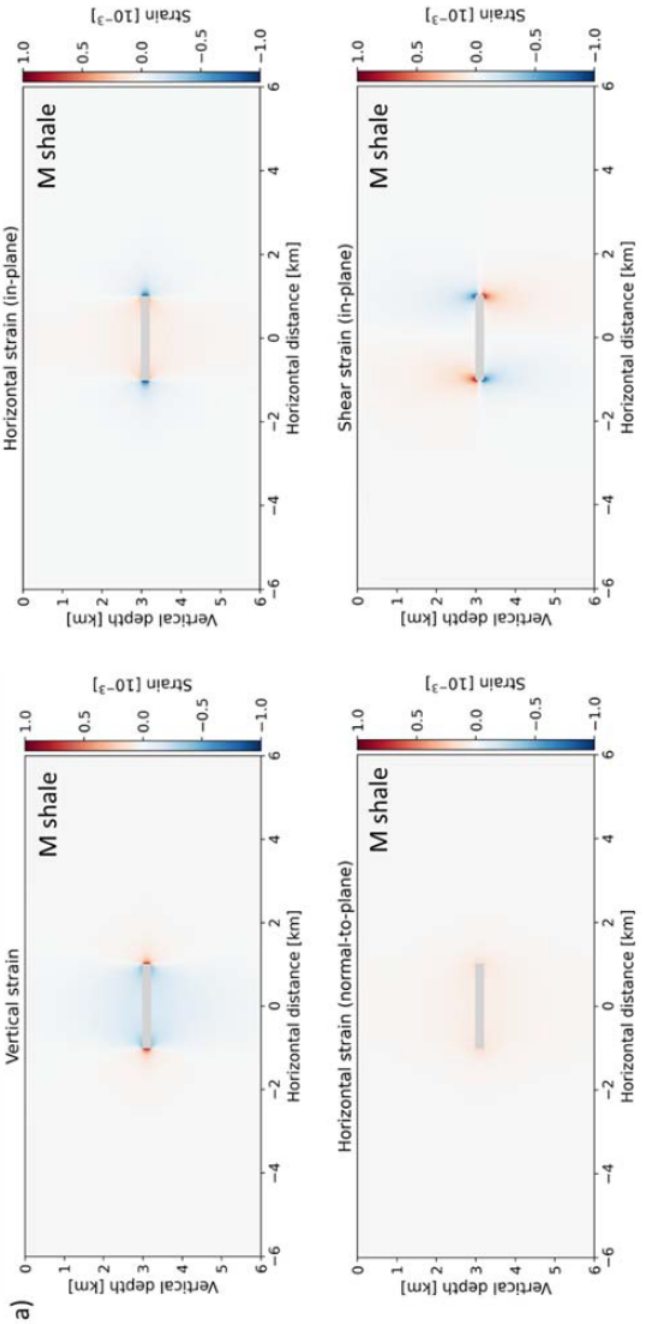
a)
Vertical strain
Horizontal strain (normal-to-plane)
Horizontal strain (in-plane)
Shear strain (in-plane)
M shale
Vertical depth [km]
Horizontal distance [km]
Strain [10⁻³]

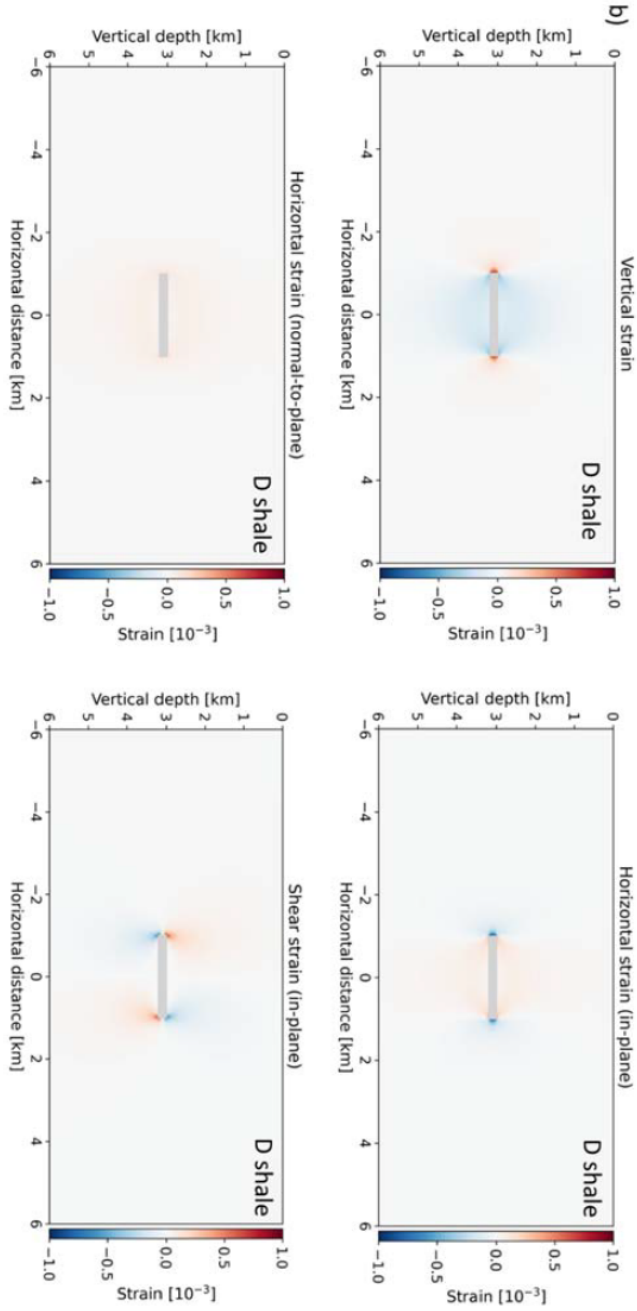
b)
Vertical strain
D shale
Horizontal strain (in-plane)
D shale
Horizontal strain (normal-to-plane)
D shale
Shear strain (in-plane)
D shale
Vertical depth [km]
Horizontal distance [km]
Strain [10⁻³]

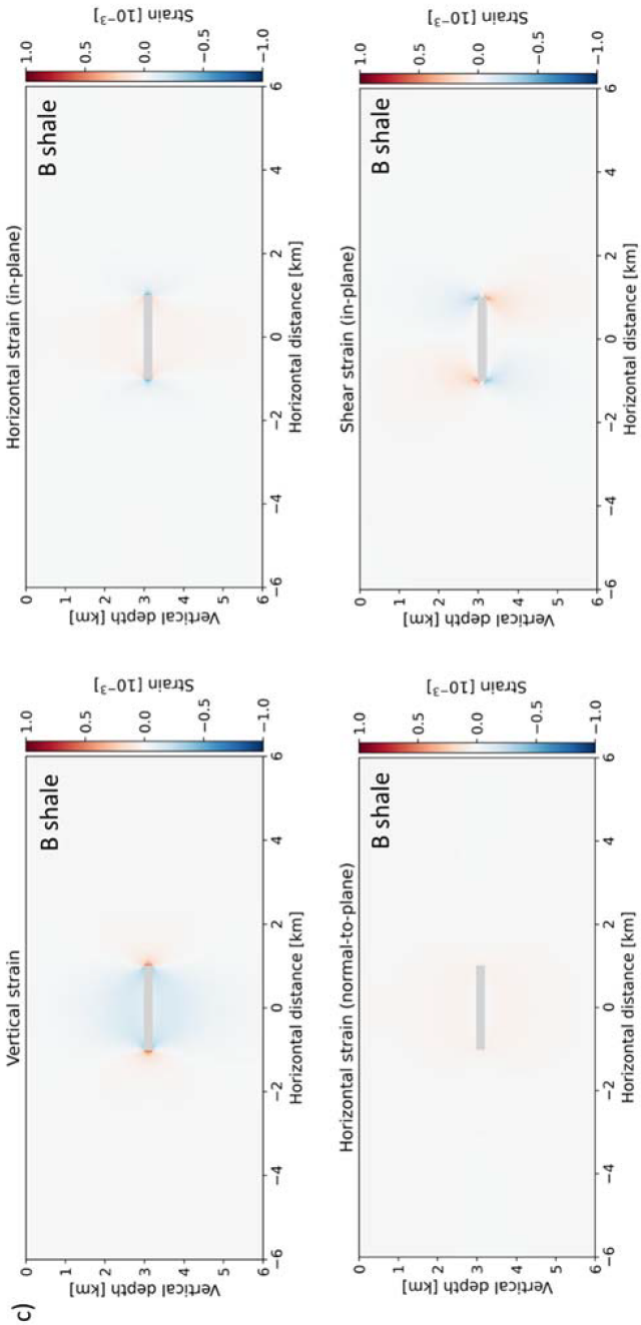


**Figure 8.8:** The strains in the vertical section $[x_1, x_3]$ for a) M shale, b) D shale, and c) B shale obtained from the modelling case resulting from 35 MPa uniform reservoir depletion. The grey rectangle in the centre of the figures marks the reservoir.

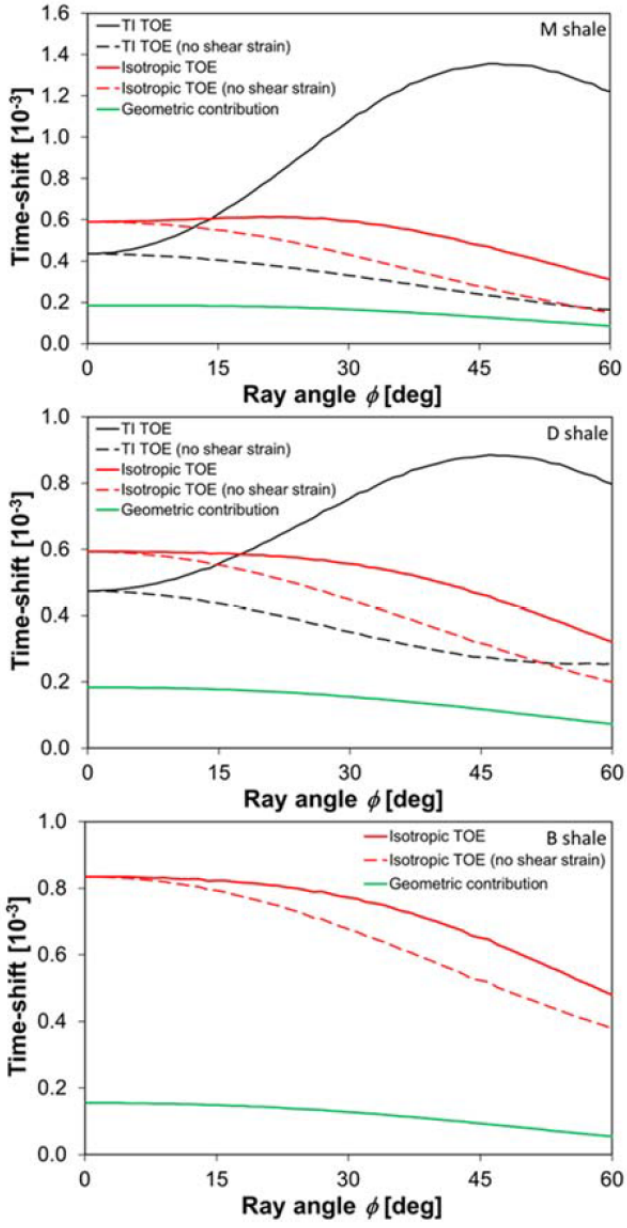


**Figure 8.9:** Two-way traveltime shifts for the modelling case predicted by the TI TOE tensor and the isotropic TOE tensor. For both tensors, prediction is also done without shear strains ($e_5$). The explicit contribution from the geometric strain (Equation (8.43)) to the time-shift is also provided.

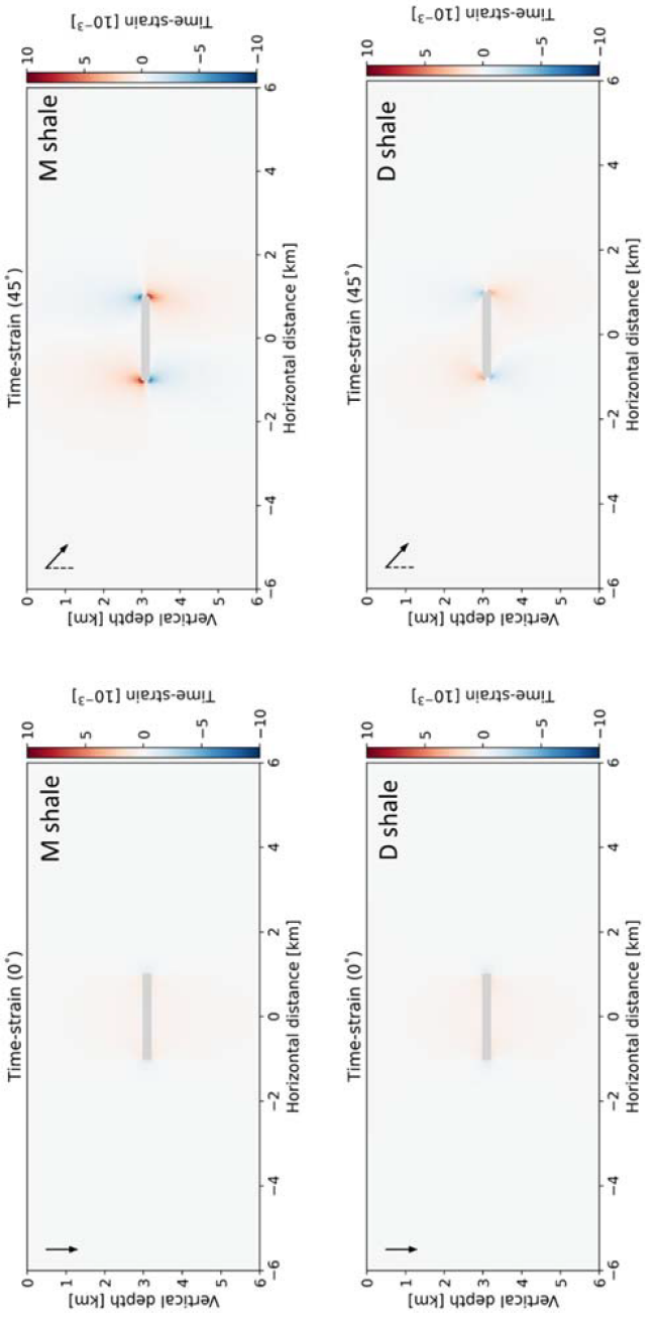


**Figure 8.10:** Time-strains for the modelling case predicted by the TI TOE model for ray angles at 0° and 45°. Directions are indicated with the inserted arrows.

## 8.5 Discussion

We have developed a TOE tensor with TI symmetry that satisfactorily predicts P-wave velocity changes measured in two overburden field shales, covering a wide range of propagation directions and stress variations. The anisotropy of the strain-sensitivity can be quantified by the TI TOE model by considering a small uniaxial strain in the direction of the P-wave propagation. The ratio of the horizontal velocity change (along $x_1$) to the vertical velocity change (along $x_3$) is 2.6 for M shale and 2.2 for D shale. This indicates a significant anisotropy of the strain sensitivity in shales. The corresponding ratio predicted by the isotropic TOE model is 0.9 for all three shales.

The calibration of the TOE coefficients seems to be robust. The calibrated TOE coefficients are close to the mean value of the TOE coefficients obtained from the error analysis where input data was varied randomly according to their limits of precision. This indicates a globally optimized parameter set. For the D shale, we bootstrapped the inversion of the TI TOE coefficients by using subsets of experimental data with two stress paths, as also discussed by Duda et al. (2020). Except for the inversion that includes only the isotropic stress path and the uniaxial-strain path, all bootstrapped TOE coefficients remained within the 95 % confidence interval obtained for the complete inversion. For M shale, only the isotropic stress path for $C_{66}$ was used in the inversion of the TI TOE, which implied relatively large errors of $C_{111}$ and $C_{166}$. The corresponding errors for D shale, obtained through the inversion utilizing four stress paths for $C_{66}$, are significantly smaller. To include a diversity of stress paths in the calibration of the TOE coefficients seems thus to improve the quality and the robustness of the predictions. Field-specific geomechanical modelling can be used to assess which stress paths are relevant from case to case (Mulders 2003; Yan et al. 2020).

Two tests were needed to obtain all nine TI TOE coefficients for each shale, because the setup was limited to isotropic horizontal stresses. In a true-triaxial setup, stresses and strains can be individually adjusted in three orthogonal directions. A complete inversion of all TI TOE coefficients and a larger variation in stress paths can thus be obtained from a single test in a true-triaxial setup.

In the light of previously reported and our results, we advocate the importance of undrained experiments on overburden shales, as the ones shown in this study. The strain sensitivity of shales will generally be different in drained conditions as compared to undrained conditions (Cheng 1997; Holt et al. 2018). Monitoring of a producing field typically spans from months to a few decades. Shales, which are abundant in these formations, are known for their low permeability. It is commonly assumed that shales exhibit undrained static stiffness (Bauer et al. 2008; Islam and Skalle 2013; MacBeth and Bachkheti 2021; Piane et al. 2011; Sarout and Guéguen 2008; Soldal et al. 2021; Thompson et al. 2021). In low-permeability formations, the immediate response in the vicinity of a depleting reservoir is a heterogeneous undrained pore pressure change within a substantial volume sur-

rounding the reservoir, encompassing the entire overburden (Duda et al. 2023; Yan et al. 2023). The permeability and characteristic diffusion lengths can be used to estimate the time required for pore pressure equilibration upon a strain in a low-permeable overburden, suggesting that undrained overburden response during reservoir's lifespan is realistic, as discussed by Duda et al. (2023). Overpressured zones and hydrocarbon containment over geological time further support the presence a low-permeable overburden that exhibits minimal drainage. However, in areas with more permeable formations outside the reservoir such as sandy layers, fractured zones, and gas clouds some drainage may occur. Drainage may also apply to formations proximate to wells and to the reservoir because of short diffusion lengths, though permeability is also a determining factor. Nevertheless, a significant proportion of the overburden can be reasonably assumed to exhibit undrained static behaviour, which our model accounts for. In zones more prone to drainage, an assessment of pore pressure equilibration is necessary to determine whether a drained TOE model is needed.

A drained TOE model is expected to be more complex than the TOE model described here because an explicit inclusion of the pore-pressure dependence is required in this TOE tensor. To calibrate a drained TI TOE model for overburden shales, laboratory tests conducted under drained conditions are necessary. The undrained tests we performed took 2-4 weeks per test, and it is anticipated that similar tests under drained conditions for the same material will require 4-8 weeks per tests due to its extremely low permeability. Notably, the isotropic TOE coefficients obtained by Prioul et al. (2004) and by Prioul and Lebrat (2004) were obtained from drained data (MacBeth and Bachkheti 2021). Prioul et al. (2004) and Bathija et al. (2009) showed that the strain sensitivity may be very different at low total stress as compared to high total stress. This underlines the importance of testing the rocks as close as possible to in-situ stress and pore pressure conditions.

Ultrasonic velocities in the laboratory are typically recorded in the 0.1–1 MHz range while seismic data effectively cover the 1–100 Hz range (Batzle et al. 2006; Delle Piane et al. 2014; Duranti et al. 2005; Lozovyi and Bauer 2019; Szewczyk et al. 2017). Laboratory measurements of Mancos (outcrop) shale indicate a higher stress sensitivity at seismic frequencies than at ultrasonic frequencies (Szewczyk et al. 2017). More tests are needed to investigate this. At present, ultrasonic tests have higher accuracy and is more flexible as compared to low-frequency tests.

The TOE models were used to predict overburden time-shifts based on the strains from the geomechanical modelling. The angular time-shifts trends are significantly impacted by the magnitude of shear strain (figure 8.9). The time-shifts predicted by the TI TOE model has a maximum at offset angles around 45°. This is consistent with vanishing shear strains along the 0° ray path, and significant shear-strains along the 45° ray path for which the shear strain peaks at a depth level 700–800 m above the reservoir (Figure 8.11). In our case $e_5$ is the only non-zero shear strain, which is a consequence of the axisymmetric model. Thus, the shear-strain contribution to the monitor stiffness is only associated with the TOE coefficients

$C_{144}$, $C_{344}$, and $C_{456}$ (Equation (8.12)). However, these coefficients are relatively small in the isotropic TOE model as compared to the TI TOE model (Table 8.4), which may explain the relatively low sensitivity to shear strains in the time-shifts predicted by the isotropic TOE model (Figure 8.9).

Various offset-trends of time-shifts are reported by MacBeth et al. (2018). However, these field cases are very different regarding location, processing, and analysis. For an idealized isotropic medium with no lateral variations in stiffness, strain, and velocity changes, the angular time-strain gradient for a stretching rock will be negative prior to moveout and positive after moveout (Landro and Janssen 2002; Landrø and Stammeijer 2004). This illustrates the importance of comparing 4D attributes within the same context, whether it is pre-stack or post-stack data. Even though post-stack analysis of 4D data in many cases gives substantial insight into production-induced events, pre-stack analysis may disclose details that would be difficult to observe in stacked data (Dvorak et al. 2018; Evensen and Landrø 2010; Røste et al. 2007; Shragge and Lumley 2013).

In addition to the synthetic cases addressed in this study, it is important to discuss the feasibility and applicability of our model and method for improving field data processing. Our work highlights the importance of integrating 4D seismic analysis, geomechanical modelling, and third-order elasticity models for velocity changes to better quantify strain and stress changes. A potential avenue for further investigation involves leveraging the significant dependence on stress-path observed in the offset trends (Figure 8.7) to quantify the magnitude and direction of strains and stress changes. This could be achieved by inverting 4D seismic time-shifts using the anisotropic TOE model, or a simplified version, in conjunction with geomechanical modelling data. To explicitly address the spatial and angular velocity dependencies associated with mechanical changes, the application of 4D tomography may be a suitable method for analysing pre-stack seismic data (e.g., Dvorak et al. 2018; Evensen and Landrø 2010). This approach can enable a more comprehensive understanding of the important interplay between mechanical alterations and spatial/angular velocity variations. Although the anisotropic TOE model predicts the experimental data well, the model has nine TOE coefficients that need to be determined. To make such models more applicable, correlations between the coefficients or a reduction of independent coefficients would be beneficial. More laboratory testing, better utilization of existing data, and a sensitivity analysis of the model will be important in this respect. Further progress may also benefit from comparison of TOE models to micromechanical models, to obtain a more intuitive understanding of the underlying physics (Sripanich et al. 2021). Since the TI TOE model seems to be sensitive to shear strains, such model could be used to detect shear-zones of importance for rock integrity, well stability, and infill drilling.

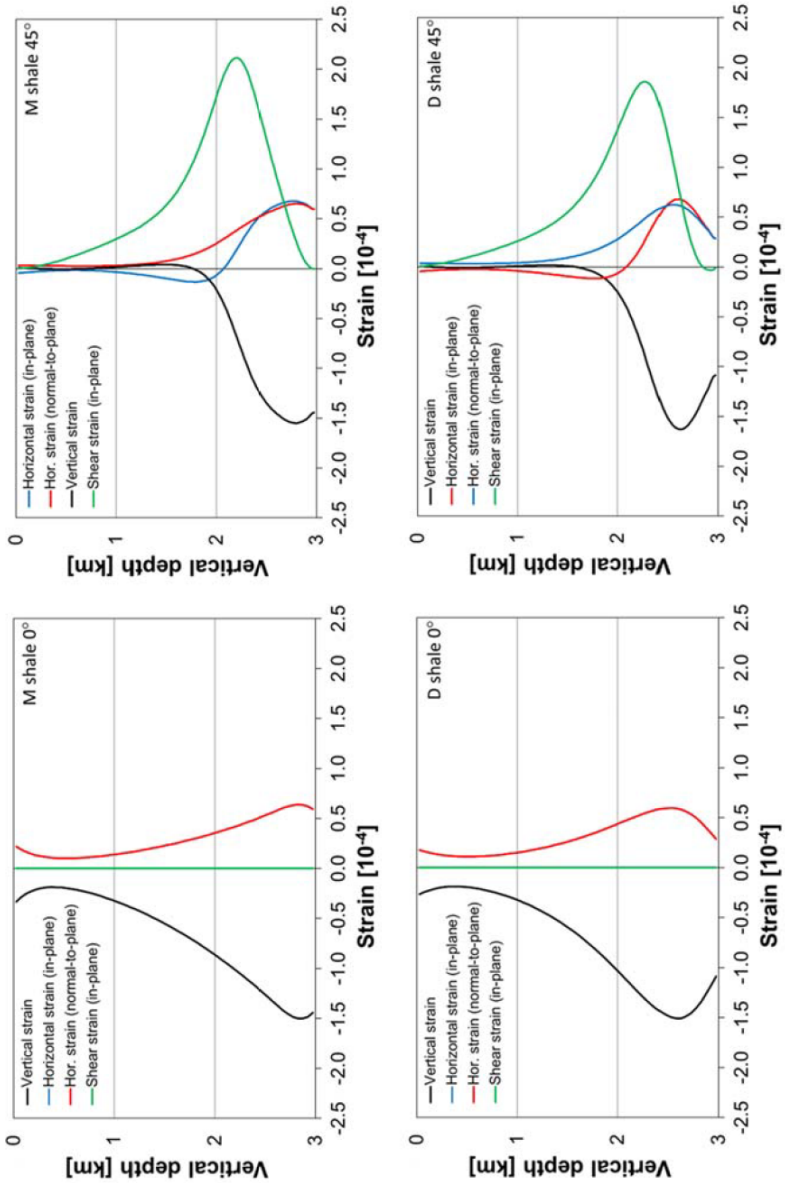


**Figure 8.11:** Vertical strain ($e_3$), horizontal in-plane strain ($e_1$), horizontal normal-to-plane strain ($e_2$), and shear strain ($e_5$) as function of depth obtained from the modelling with M shale and D shale. The data correspond to the straight ray-path from the left source to the reflection point at 0° and 45° ray angles, respectively (Figure 8.6). The two horizontal strains are equal at ° ray angle.

## 8.6 Summary

A strain-dependent TOE tensor with TI symmetry is developed. This model, along with the isotropic analogue of the TOE tensor, is calibrated using experimental velocity data from field shales. The TI TOE model is predicting well the P-wave velocity data across a large span of stress paths and propagation angles. The isotropic TOE model captures the angular trends of velocity changes satisfactorily but exhibits some quantitative misfit depending on the stress path. To study a modelling case of a depleting reservoir surrounded by shales, the strains obtained from the modelling were used to predict angular time-shifts using both TOE models. The results demonstrate that the isotropic TOE model significantly underestimates the time-shifts at higher angles, as compared to the TI TOE model, mainly attributed to low sensitivity to shear strains. This study highlights the potential of pre-stack time-lapse data analysis for improved in detecting altered stresses and strains, which may not be evident in post-stack data. It also emphasizes the importance of interaction between the geophysics, geomechanics, and rock physics disciplines in gaining a better understanding of subsurface alterations.

## 8.7 Acknowledgements

This work was supported by the Research Council of Norway (grant 294369; PETROMAKS 2) in collaboration with AkerBP, Equinor, Shell, and Vår Energi; and by the Research Council of Norway (grant 234074; PETROMAKS 2) in collaboration with AkerBP, ENGIE, INEOS, and Total. We are grateful to Eyvind F. Sønstebø for performing several multistage shale tests at SINTEF Formation Physics Laboratory, and to Andreas Bauer and Idar Larsen for their valuable discussions and analysis of the laboratory data.

# References

Angus, D. A., M. Dutko, T. G. Kristiansen, Q. J. Fisher, J. M. Kendall, A. F. Baird, J. P. Verdon, O. I. Barkved, J. Yu and S. Zhao (2015). 'Integrated hydro-mechanical and seismic modelling of the Valhall reservoir: A case study of predicting subsidence, AVOA and microseismicity'. In: *Geomechanics for Energy and the Environment* 2, pp. 32–44. ISSN: 2352-3808. DOI: https://doi.org/10.1016/j.gete.2015.05.002. URL: https://www.sciencedirect.com/science/article/pii/S2352380815000283.

Asaka, M. (2023). 'Anisotropic 4D seismic response inferred from ultrasonic laboratory measurements: A direct comparison with the isotropic response'. In: *Geophysical Prospecting* 71.1, pp. 17–28. ISSN: 0016-8025. DOI: https://doi.org/10.1111/1365-2478.13273. URL: https://onlinelibrary.wiley.com/doi/abs/10.1111/1365-2478.13273.

Bakk, A., R. Holt, M. Duda and C. MacBeth (2020a). 'The Fate of R in Light of Field Shale Laboratory Tests'. In: 2020.1, pp. 1–5. ISSN: 2214-4609. DOI: https://doi.org/10.3997/2214-4609.202011500. URL: https://www.earthdoc.org/content/papers/10.3997/2214-4609.202011500.

Bakk, A., R. M. Holt, A. Bauer, B. Dupuy and A. Romdhane (2020b). 'Offset dependence of overburden time-shifts from ultrasonic data'. In: *Geophysical Prospecting* 68.6, pp. 1847–1863. ISSN: 0016-8025. DOI: https://doi.org/10.1111/1365-2478.12963. URL: https://onlinelibrary.wiley.com/doi/abs/10.1111/1365-2478.12963.

Barker, L., J. Nunziato, K. Schuler, R. Thurston, C. Truesdell and E. Walsh (1974). *Mechanics of Solids: Volume IV Waves in elastic and viscoelastic solids (theory and experiment)*. Springer-Verlag. URL: https://books.google.no/books?id=9gojywEACAAJ.

Barkved, O. I., T. Kristiansen and E. Fjær (2005). 'The 4D seismic response of a compacting reservoir—examples from the Valhall Field, Norway'. In: *SEG Technical Program Expanded Abstracts 2005*, pp. 2508–2511. DOI: 10.1190/1.2148232. URL: https://library.seg.org/doi/abs/10.1190/1.2148232.

Bathija, A. P., M. L. Batzle and M. Prasad (2009). 'An experimental study of the dilation factor'. In: *GEOPHYSICS* 74.4, E181–E191. DOI: 10.1190/1.3137060. URL: https://library.seg.org/doi/abs/10.1190/1.3137060.

Batzle, M. L., D.-H. Han and R. Hofmann (2006). 'Fluid mobility and frequency-dependent seismic velocity — Direct measurements'. In: *GEOPHYSICS* 71.1, N1–N9. DOI: 10.1190/1.2159053. URL: https://library.seg.org/doi/abs/10.1190/1.2159053.

Bauer, A., C. Lehr, F. Korndorffer, A. v. d. Linden, J. Dudley, T. Addis, K. Love and M. Myers (2008). 'Stress and pore-pressure dependence of sound velocities in shales: Poroelastic effects in time-lapse seismic'. In: *SEG Technical Program Expanded Abstracts 2008*, pp. 1630–1634. DOI: 10.1190/1.3059221. URL: https://library.seg.org/doi/abs/10.1190/1.3059221.

Berryman, J. G. (1979). 'Long-wave elastic anisotropy in transversely isotropic media'. In: *GEOPHYSICS* 44.5, pp. 896–917. DOI: 10.1190/1.1440984. URL: https://library.seg.org/doi/abs/10.1190/1.1440984.

Birch, F. (1947). 'Finite Elastic Strain of Cubic Crystals'. In: *Physical Review* 71.11. PR, pp. 809–824. DOI: 10.1103/PhysRev.71.809. URL: https://link.aps.org/doi/10.1103/PhysRev.71.809.

Brugger, K. (1964). 'Thermodynamic Definition of Higher Order Elastic Coefficients'. In: *Physical Review* 133.6A. PR, A1611–A1612. DOI: 10.1103/PhysRev.133.A1611. URL: https://link.aps.org/doi/10.1103/PhysRev.133.A1611.

Brugger, K. (1965). 'Pure Modes for Elastic Waves in Crystals'. In: *Journal of Applied Physics* 36.3, pp. 759–768. DOI: 10.1063/1.1714215. URL: https://aip.scitation.org/doi/abs/10.1063/1.1714215.

Cheng, A. H. D. (1997). 'Material coefficients of anisotropic poroelasticity'. In: *International Journal of Rock Mechanics and Mining Sciences* 34.2, pp. 199–205. ISSN: 1365-1609. DOI: https://doi.org/10.1016/S0148-9062(96)00055-1. URL: http://www.sciencedirect.com/science/article/pii/S0148906296000551.

Crampin, S., E. M. Chesnokov and R. G. Hipkin (Jan. 1984). 'Seismic anisotropy — the state of the art: II'. In: *Geophysical Journal International* 76.1, pp. 1–16. DOI: 10.1111/j.1365-246X.1984.tb05017.x. eprint: https://academic.oup.com/gji/article-pdf/76/1/1/1782363/76-1-1.pdf. URL: https://doi.org/10.1111/j.1365-246X.1984.tb05017.x.

Delle Piane, C., J. Sarout, C. Madonna, E. H. Saenger, D. N. Dewhurst and M. Raven (2014). 'Frequency-dependent seismic attenuation in shales: experimental results and theoretical analysis'. In: *Geophysical Journal International* 198.1, pp. 504–515. ISSN: 0956-540X. DOI: 10.1093/gji/ggu148. URL: https://doi.org/10.1093/gji/ggu148.

Dellinger, J. and L. Vernik (1994). 'Do traveltimes in pulse-transmission experiments yield anisotropic group or phase velocities?' In: *GEOPHYSICS* 59.11, pp. 1774–1779. DOI: 10.1190/1.1443564. URL: https://library.seg.org/doi/abs/10.1190/1.1443564.

Dewhurst, D. N. and A. F. Siggins (2006). 'Impact of fabric, microcracks and stress field on shale anisotropy'. In: *Geophysical Journal International* 165.1, pp. 135–148. ISSN: 0956-540X. DOI: 10.1111/j.1365-246X.2006.02834.x. URL: https://doi.org/10.1111/j.1365-246X.2006.02834.x.

Ditlevsen, F., F. Bourgeois and M. Calvert (2018). *Handling Wellbore Instability in Overburden Tertiary Shales*. Conference Paper. DOI: https://doi.org/10.3997/2214-4609.201800721. URL: https://www.earthdoc.org/content/papers/10.3997/2214-4609.201800721.

Donald, J. A. and R. Prioul (2015). 'In situ calibrated velocity-to-stress transforms using shear sonic radial profiles for time-lapse production analysis'. In: *The Leading Edge* 34.3, pp. 286–294. DOI: 10.1190/tle34030286.1.

Duda, M., A. Bakk, R. Holt and J. F. Stenebråten (2023). 'Anisotropic Poroelastic Modelling of Depletion-Induced Pore Pressure Changes in Valhall Overburden'.

In: *Rock Mechanics and Rock Engineering*. ISSN: 1434-453X. DOI: 10.1007/s00603-022-03192-0. URL: https://doi.org/10.1007/s00603-022-03192-0.

Duda, M., R. Holt and A. Bakk (2020). *Third-order elastic tensor of shales determined through ultrasonic velocity measurements*. Conference Paper.

Dudley, J., M. Brignoli, B. Crawford, R. Ewy, D. Love, J. McLennan, G. Ramos, J. Shafer, M. Sharf-Aldin, E. Siebrits, J. Boyer and M. Chertov (2016). 'ISRM Suggested Method for Uniaxial-Strain Compressibility Testing for Reservoir Geomechanics'. In: *Rock Mechanics and Rock Engineering* 49, pp. 4153–4178. DOI: 10.1007/s00603-016-1055-4.

Duranti, L., R. Ewy and R. Hofmann (2005). 'Dispersive and attenuative nature of shales: multiscale and multifrequency observations'. In: *SEG Technical Program Expanded Abstracts 2005*, pp. 1577–1580. DOI: 10.1190/1.2147994. URL: https://library.seg.org/doi/abs/10.1190/1.2147994.

Dvorak, I., C. MacBeth and H. Amini (2018). *Evaluating 4D Overburden Velocity Perturbation for the Shearwater Field via Pre-Stack Time-Shift Inversion*. Conference Paper. DOI: https://doi.org/10.3997/2214-4609.201800699. URL: https://www.earthdoc.org/content/papers/10.3997/2214-4609.201800699.

Evensen, A. K. and M. Landrø (2010). 'Time-lapse tomographic inversion using a Gaussian parameterization of the velocity changes'. In: *GEOPHYSICS* 75.4, U29–U38. DOI: 10.1190/1.3442573. URL: https://library.seg.org/doi/abs/10.1190/1.3442573.

Ewy, R. T. (2021). 'Well Shear Associated with Conventional and Unconventional Operations: Diagnosis and Mechanisms'. In: *SPE Drilling & Completion* 36.02, pp. 427–444. ISSN: 1064-6671. DOI: 10.2118/205007-pa. URL: https://doi.org/10.2118/205007-PA.

Fedorov, F. I. (1968). *Theory of Elastic Waves in Crystals*. ISBN: 978-1-4757-1275-9.

Fjær, E., R. Holt, P. Horsrud and A. M. Raaen (2021). *Petroleum Related Rock Mechanics. 3rd edition*. ISBN: 9780128221952.

Fuck, R. F. and I. Tsvankin (2009). 'Analysis of the symmetry of a stressed medium using nonlinear elasticity'. In: *GEOPHYSICS* 74. DOI: 10.1190/1.3157251.

Fuck, R. F., A. Bakulin and I. Tsvankin (2009). 'Theory of traveltime shifts around compacting reservoirs: 3D solutions for heterogeneous anisotropic media'. In: *GEOPHYSICS* 74.1, pp. D25–D36. DOI: 10.1190/1.3033215. URL: https://library.seg.org/doi/abs/10.1190/1.3033215.

Fumi, F. G. (1951). 'Third-Order Elastic Coefficients of Crystals'. In: *Physical Review* 83.6. PR, pp. 1274–1275. DOI: 10.1103/PhysRev.83.1274. URL: https://link.aps.org/doi/10.1103/PhysRev.83.1274.

Fumi, F. G. (1952). 'Third-Order Elastic Coefficients in Trigonal and Hexagonal Crystals'. In: *Physical Review* 86.4. PR, pp. 561–561. DOI: 10.1103/PhysRev.86.561. URL: https://link.aps.org/doi/10.1103/PhysRev.86.561.

Geertsma, J. (1973). 'A Basic Theory Of Subsidence Due To Reservoir Compaction; The Homogeneous Case'. In: *Verhandelingen Kon. Ned. Geol. Mijnbouwk. Gen* 28, pp. 43–62.

Gennaro, S. de, A. Onaisi, A. Grandi, L. ben brahim and V. Neillo (2008). '4D reservoir geomechanics: A case study from the HP/HT reservoirs of the Elgin and Franklin fields'. In: *First Break* 26. DOI: 10.3997/1365-2397.2008019.

Guilbot, J. and B. Smith (2002). '4-D constrained depth conversion for reservoir compaction estimation: Application to Ekofisk Field'. In: *The Leading Edge* 21.3, pp. 302–308. DOI: 10.1190/1.1463782. URL: https://library.seg.org/doi/abs/10.1190/1.1463782.

Hall, S. A., C. MacBeth, O. I. Barkved and P. Wild (2002). 'Time-lapse seismic monitoring of compaction and subsidence at Valhall through cross-matching and interpreted warping of 3D streamer and OBC data'. In: *SEG Technical Program Expanded Abstracts 2002*, pp. 1696–1699. DOI: 10.1190/1.1817004. URL: https://library.seg.org/doi/abs/10.1190/1.1817004.

Hatchell, P. and S. Bourne (2005). 'Rocks under strain: Strain-induced time-lapse time shifts are observed for depleting reservoirs'. In: *The Leading Edge* 24.12, pp. 1222–1225. DOI: 10.1190/1.2149624. URL: https://library.seg.org/doi/abs/10.1190/1.2149624.

Hawkins, K. (2008). 'Defining the extent of the compacting Elgin reservoir by measuring stress-induced anisotropy'. In: *First Break* 26.10. ISSN: 1365-2397. DOI: https://doi.org/10.3997/1365-2397.26.10.28559. URL: https://www.earthdoc.org/content/journals/0.3997/1365-2397.26.10.28559.

Hearmon, R. (1953). ''Third-order' elastic coefficients'. In: *Acta Crystallographica* 6.4, pp. 331–340. ISSN: 0365-110X. DOI: doi:10.1107/S0365110X53000909. URL: https://doi.org/10.1107/S0365110X53000909.

Helbig, K. and L. Thomsen (2005). '75-plus years of anisotropy in exploration and reservoir seismics: A historical review of concepts and methods'. In: *GEOPHYSICS* 70.6, 9ND–23ND. DOI: 10.1190/1.2122407.

Herwanger, J. and N. Koutsabeloulis (2011). *Seismic Geomechanics: How to Build and Calibrate Geomechanical Models using 3D and 4D Seismic Data*. ISBN: 978-90-73834-10-1.

Herwanger, J. V. and S. A. Horne (2009). 'Linking reservoir geomechanics and time-lapse seismics: Predicting anisotropic velocity changes and seismic attributes'. In: *GEOPHYSICS* 74.4, W13–W33. DOI: 10.1190/1.3122407. URL: https://library.seg.org/doi/abs/10.1190/1.3122407.

Hodgson, N. A. (2009). 'Inversion for reservoir pressure change using overburden strain measurements determined from 4D seismic'. Thesis.

Holt, R. M., A. Bauer and A. Bakk (2018). 'Stress-path-dependent velocities in shales: Impact on 4D seismic interpretation'. In: *GEOPHYSICS* 83.6, MR353–MR367. DOI: 10.1190/geo2017-0652.1. URL: https://library.seg.org/doi/abs/10.1190/geo2017-0652.1.

Hornby, B. E. (1998). 'Experimental laboratory determination of the dynamic elastic properties of wet, drained shales'. In: *Journal of Geophysical Research: Solid Earth* 103.B12, pp. 29945–29964. ISSN: 0148-0227. DOI: https://doi.org/10.1029/97JB02380. URL: https://agupubs.onlinelibrary.wiley.com/doi/abs/10.1029/97JB02380.

Hudson, J. A. (1981). 'Wave speeds and attenuation of elastic waves in material containing cracks'. In: *Geophysical Journal International* 64.1, pp. 133–150.

ISSN: 0956-540X. DOI: 10.1111/j.1365-246X.1981.tb02662.x. URL: https://doi.org/10.1111/j.1365-246X.1981.tb02662.x.

Hughes, D. S. and J. L. Kelly (1953). 'Second-Order Elastic Deformation of Solids'. In: *Physical Review* 92.5. PR, pp. 1145–1149. DOI: 10.1103/PhysRev.92.1145. URL: https://link.aps.org/doi/10.1103/PhysRev.92.1145.

Islam, M. and P. Skalle (Nov. 2013). 'An Experimental Investigation of Shale Mechanical Properties Through Drained and Undrained Test Mechanisms'. In: *Rock Mechanics and Rock Engineering* 46. DOI: 10.1007/s00603-013-0377-8.

Jaeken, J. W. and S. Cottenier (2016). 'Solving the Christoffel equation: Phase and group velocities'. In: *Computer Physics Communications* 207, pp. 445–451. ISSN: 0010-4655. DOI: https://doi.org/10.1016/j.cpc.2016.06.014. URL: https://www.sciencedirect.com/science/article/pii/S0010465516301795.

Johnston, D. H. (1987). 'Physical properties of shale at temperature and pressure'. In: *GEOPHYSICS* 52.10, pp. 1391–1401. DOI: 10.1190/1.1442251. URL: https://library.seg.org/doi/abs/10.1190/1.1442251.

Jones, L. E. A. and H. F. Wang (1981). 'Ultrasonic velocities in Cretaceous shales from the Williston basin'. In: *GEOPHYSICS* 46.3, pp. 288–297. DOI: 10.1190/1.1441199. URL: https://library.seg.org/doi/abs/10.1190/1.1441199.

Jr., T. E. S. (2007). 'The effects of stress paths on acoustic velocities and 4D seismic imaging'. In: *The Leading Edge* 26.5, pp. 602–608. DOI: 10.1190/1.2737101. URL: https://library.seg.org/doi/abs/10.1190/1.2737101.

Kenter, C. J., A. v. d. Beukel, A. C. Hatchell, P. Maron, K. Molenaar, M. M. Molenaar and J. Stammeijer (2004). 'Geomechanics And 4D: Evaluation Of Reservoir Characteristics From Timeshifts In The Overburden'. In: *6th North America Rock Mechanics Symposium*.

Kristiansen, T., O. Barkved, K. Buer and R. Bakke (2005). 'Production-Induced Deformations Outside the Reservoir and Their Impact on 4D Seisimic'. In: *2005 International Petroleum Technology Conference inproceedings*. DOI: 10.2523/10818-MS.

Kudarova, A., P. Hatchell, J. Brain and C. Macbeth (2016). 'Offset-dependence of production-related 4D time shifts: Real data examples and modeling'. In: *SEG Technical Program Expanded Abstracts 2016*, pp. 5395–5399. DOI: 10.1190/segam2016-13611549.1. URL: https://library.seg.org/doi/abs/10.1190/segam2016-13611549.1.

Landro, M. and R. Janssen (2002). *Estimating Compaction and Velocity Changes from Time-Lapse near and far Offset Stacks*. Conference Paper. DOI: https://doi.org/10.3997/2214-4609-pdb.5.P036. URL: https://www.earthdoc.org/content/papers/10.3997/2214-4609-pdb.5.P036.

Landrø, M. and J. Stammeijer (2004). 'Quantitative estimation of compaction and velocity changes using 4D impedance and traveltime changes'. In: *GEOPHYSICS* 69.4, pp. 949–957. DOI: 10.1190/1.1778238. URL: https://library.seg.org/doi/abs/10.1190/1.1778238.

Larsen, I., J. Stenebråten and A. Bakk (2011). *Stress dependent dynamic anisotropy in shales*. Conference Paper.

Lozovyi, S. and A. Bauer (2019). 'Velocity dispersion in rocks: A laboratory technique for direct measurement of P-wave modulus at seismic frequencies'. In: *Review of Scientific Instruments* 90.2, p. 024501. DOI: 10.1063/1.5026969. URL: https://aip.scitation.org/doi/abs/10.1063/1.5026969.

Lubarda, V. A. (1997). 'New estimates of the third-order elastic constants for isotropic aggregates of cubic crystals'. In: *Journal of the Mechanics and Physics of Solids* 45.4, pp. 471–490. ISSN: 0022-5096. DOI: https://doi.org/10.1016/S0022-5096(96)00113-5. URL: https://www.sciencedirect.com/science/article/pii/S0022509696001135.

MacBeth, C. and S. Bachkheti (2021). 'A geomechanical correction for time-lapse amplitude variation with offset'. In: *GEOPHYSICS* 86.2, pp. M29–M40. DOI: 10.1190/geo2020-0398.1. URL: https://library.seg.org/doi/abs/10.1190/geo2020-0398.1.

MacBeth, C., A. Kudarova and P. Hatchell (2018). 'Review Paper: A semi-empirical model of strain sensitivity for 4D seismic interpretation'. In: *Geophysical Prospecting* 66.7, pp. 1327–1348. DOI: https://doi.org/10.1111/1365-2478.12648. eprint: https://onlinelibrary.wiley.com/doi/pdf/10.1111/1365-2478.12648. URL: https://onlinelibrary.wiley.com/doi/abs/10.1111/1365-2478.12648.

Mah, M. and D. R. Schmitt (2003). 'Determination of the complete elastic stiffnesses from ultrasonic phase velocity measurements'. In: *Journal of Geophysical Research: Solid Earth* 108.B1, ECV 6-1-ECV 6–11. ISSN: 0148-0227. DOI: https://doi.org/10.1029/2001JB001586. URL: https://agupubs.onlinelibrary.wiley.com/doi/abs/10.1029/2001JB001586.

Mavko, G., T. Mukerji and N. Godfrey (1995). 'Predicting stress-induced velocity anisotropy in rocks'. In: *GEOPHYSICS* 60.4, pp. 1081–1087. DOI: 10.1190/1.1443836. URL: https://library.seg.org/doi/abs/10.1190/1.1443836.

Mulders, F. (2003). 'Modelling of Stress Development and Fault Slip in and Around a Producing Gas Reservoir'. Thesis.

Nye, J. (1985). *Physical Properties of Crystals: Their Representation by Tensors and Matrices*. Clarendon Press. ISBN: 9780198511656.

Pervukhina, M., D. Dewhurst, B. Gurevich, U. Kuila, T. Siggins, M. Raven and H. M. N. Bolås (2008). 'Stress-dependent elastic properties of shales: Measurement and modeling'. In: *The Leading Edge* 27.6, pp. 772–779. DOI: 10.1190/1.2944162. URL: https://library.seg.org/doi/abs/10.1190/1.2944162.

Piane, C. D., D. N. Dewhurst, A. F. Siggins and M. D. Raven (Feb. 2011). 'Stress-induced anisotropy in brine saturated shale'. In: *Geophysical Journal International* 184.2, pp. 897–906. ISSN: 0956-540X. DOI: 10.1111/j.1365-246X.2010.04885.x. eprint: https://academic.oup.com/gji/article-pdf/184/2/897/1609842/184-2-897.pdf. URL: https://doi.org/10.1111/j.1365-246X.2010.04885.x.

Prioul, R., A. Bakulin and V. Bakulin (2004). 'Nonlinear rock physics model for estimation of 3D subsurface stress in anisotropic formations: Theory and laboratory verification'. In: *Geophysics* 69, pp. 415–425. DOI: 10.1190/1.1707061.

Prioul, R. and T. Lebrat (2004). 'Calibration of velocity-stress relationships under hydrostatic stress for their use under non-hydrostatic stress conditions'. In: *SEG Technical Program Expanded Abstracts 2004*, pp. 1698–1701. DOI: 10.1190/1.1851153. URL: https://library.seg.org/doi/abs/10.1190/1.1851153.

Rasolofosaon, P. (1998). 'Stress-Induced Seismic Anisotropy Revisited'. In: *Revue de l'Institut Français du Pétrole* 53, pp. 679–692. DOI: 10.2516/ogst:1998061.

Rickett, J., L. Duranti, T. Hudson, B. Regel and N. Hodgson (2007). '4D time strain and the seismic signature of geomechanical compaction at Genesis'. In: *The Leading Edge* 26.5, pp. 644–647. DOI: 10.1190/1.2737103. URL: https://library.seg.org/doi/abs/10.1190/1.2737103.

Roste, T. and G. Ke (2017). 'Overburden 4D time shifts — Indicating undrained areas and fault transmissibility in the reservoir'. In: *The Leading Edge* 36.5, pp. 423–430. DOI: 10.1190/tle36050423.1. URL: https://library.seg.org/doi/abs/10.1190/tle36050423.1.

Røste, T., M. Landro and P. Hatchell (2007). 'Monitoring overburden layer changes and fault movements from time-lapse seismic data on the Valhall Field'. In: *Geophysical Journal International - GEOPHYS J INT* 170, pp. 1100–1118. DOI: 10.1111/j.1365-246X.2007.03369.x.

Røste, T., A. Stovas and M. Landrø (2006). 'Estimation of layer thickness and velocity changes using 4D prestack seismic data'. In: *GEOPHYSICS* 71.6, S219–S234. DOI: 10.1190/1.2335657. URL: https://library.seg.org/doi/abs/10.1190/1.2335657.

Sarkar, D., A. Bakulin and R. L. Kranz (2003). 'Anisotropic inversion of seismic data for stressed media: Theory and a physical modeling study on Berea Sandstone'. In: *GEOPHYSICS* 68.2, pp. 690–704. DOI: 10.1190/1.1567240.

Sarout, J. and Y. Guéguen (2008). 'Anisotropy of elastic wave velocities in deformed shales: Part 1 — Experimental results'. In: *GEOPHYSICS* 73.5, pp. D75–D89. DOI: 10.1190/1.2952744. URL: https://library.seg.org/doi/abs/10.1190/1.2952744.

Sayers, C. M. and M. Kachanov (1995). 'Microcrack-induced elastic wave anisotropy of brittle rocks'. In: *Journal of Geophysical Research: Solid Earth* 100.B3, pp. 4149–4156. ISSN: 0148-0227. DOI: https://doi.org/10.1029/94JB03134. URL: https://agupubs.onlinelibrary.wiley.com/doi/abs/10.1029/94JB03134.

Shapiro, S. A. (2017). 'Stress impact on elastic anisotropy of triclinic porous and fractured rocks'. In: *Journal of Geophysical Research: Solid Earth* 122.3, pp. 2034–2053. ISSN: 2169-9313. DOI: https://doi.org/10.1002/2016JB013378. URL: https://agupubs.onlinelibrary.wiley.com/doi/abs/10.1002/2016JB013378.

Shragge, J. and D. Lumley (2013). 'Time-lapse wave-equation migration velocity analysis'. In: *GEOPHYSICS* 78.2, S69–S79. DOI: 10.1190/geo2012-0182.1. URL: https://library.seg.org/doi/abs/10.1190/geo2012-0182.1.

Sinha, B. K. (1982). 'Elastic waves in crystals under a bias'. In: *Ferroelectrics* 41.1. doi: 10.1080/00150198208210610, pp. 61–73. ISSN: 0015-0193. DOI: 10.1080/00150198208210610. URL: https://doi.org/10.1080/00150198208210610.

Sinha, B. K. and S. Kostek (1996). 'Stress-induced azimuthal anisotropy in borehole flexural waves'. In: *GEOPHYSICS* 61.6, pp. 1899–1907. DOI: 10.1190/1.1444105. URL: https://library.seg.org/doi/abs/10.1190/1.1444105.

Skempton, A. W. (1954). 'The Pore-Pressure Coefficients A and B'. In: *Géotechnique* 4.4, pp. 143–147. DOI: 10.1680/geot.1954.4.4.143. URL: https://www.icevirtuallibrary.com/doi/abs/10.1680/geot.1954.4.4.143.

Soldal, M., E. Skurtveit and J. C. Choi (2021). 'Laboratory Evaluation of Mechanical Properties of Draupne Shale Relevant for CO2 Seal Integrity'. In: *Geosciences* 11.6, p. 244. ISSN: 2076-3263. URL: https://www.mdpi.com/2076-3263/11/6/244.

Sripanich, Y., I. Vasconcelos, J. Tromp and J. Trampert (2021). 'Stress-dependent elasticity and wave propagation — New insights and connections'. In: *GEOPHYSICS* 86.4, W47–W64. DOI: 10.1190/geo2020-0252.1. URL: https://library.seg.org/doi/abs/10.1190/geo2020-0252.1.

Szewczyk, D., A. Bauer and R. M. Holt (2017). 'Stress-dependent elastic properties of shales—laboratory experiments at seismic and ultrasonic frequencies'. In: *Geophysical Journal International* 212.1, pp. 189–210. ISSN: 0956-540X. DOI: 10.1093/gji/ggx392. URL: https://doi.org/10.1093/gji/ggx392.

Thompson, N., J. S. Andrews and T. I. Bjørnarå (2021). 'Assessing Potential Thermo-Mechanical Impacts on Caprock Due to CO2 Injection—A Case Study from Northern Lights CCS'. In: *Energies* 14.16. ISSN: 1996-1073. DOI: 10.3390/en14165054. URL: https://www.mdpi.com/1996-1073/14/16/5054.

Thomsen, L. (1986). 'Weak elastic anisotropy'. In: *GEOPHYSICS* 51.10, pp. 1954–1966. DOI: 10.1190/1.1442051. URL: https://library.seg.org/doi/abs/10.1190/1.1442051.

Thurston, R. N. and K. Brugger (1964). 'Third-Order Elastic Constants and the Velocity of Small Amplitude Elastic Waves in Homogeneously Stressed Media'. In: *Physical Review* 133.6A. PR, A1604–A1610. DOI: 10.1103/PhysRev.133.A1604. URL: https://link.aps.org/doi/10.1103/PhysRev.133.A1604.

Tsvankin, I. (1997). 'Moveout analysis for tranversely isotropic media with a tilted symmetry axis'. In: *Geophysical Prospecting* 45.3, pp. 479–512. DOI: https://doi.org/10.1046/j.1365-2478.1997.380278.x.

Wang, H. and M. Li (June 2009). 'Ab initio calculations of second-, third-, and fourth-order elastic constants for single crystals'. In: *Phys. Rev. B* 79 (22), p. 224102. DOI: 10.1103/PhysRevB.79.224102. URL: https://link.aps.org/doi/10.1103/PhysRevB.79.224102.

Wang, W. and D. Schmitt (2021). 'Static Measurements of the Third-Order Elastic Constants of Rocks'. In: *55th U.S. Rock Mechanics/Geomechanics Symposium*. Vol. All Days. ARMA-2021-1189.

Winkler, K. W. and X. Liu (1996). 'Measurements of third-order elastic constants in rocks'. In: *The Journal of the Acoustical Society of America* 100.3, pp. 1392–1398. DOI: 10.1121/1.415986. URL: https://asa.scitation.org/doi/abs/10.1121/1.415986.

Yan, H., A. Bakk, R. M. Holt and S. Lozovyi (2023). 'Overburden 4D seismic: Influence of stress and pore pressure changes accounting for elastic contrast

between a reservoir and its anisotropic surrounding rocks'. In: *GEOPHYSICS* In Press.

Yan, H., A. Bakk, R. M. Holt and S. Lozovyi (2020). 'Stress paths and predicted time-shifts around a depleting reservoir'. In: *SEG Technical Program Expanded Abstracts 2020*, pp. 2464–2468. DOI: 10.1190/segam2020-3420041.1. URL: https://library.seg.org/doi/abs/10.1190/segam2020-3420041.1.

Zoback, M. D. and J. C. Zinke (2002). 'Production-induced Normal Faulting in the Valhall and Ekofisk Oil Fields'. In: *pure and applied geophysics* 159.1, pp. 403–420. ISSN: 1420-9136. DOI: 10.1007/PL00001258. URL: https://doi.org/10.1007/PL00001258.

# Appendices

This section presents a collection of minor studies, or studies in which the author of this thesis had limited involvement, in the form of short or extended abstracts.

The abstracts are arranged chronologically.

The symbols used in the abstracts were not standardized to match those used in previous chapters. This was a deliberate decision to provide an overview of the evolution of the research process. However, it resulted in some inconsistencies.

# POSTER H: The impact of Skempton's $A$ on overburden pore pressure response above a depleting reservoir

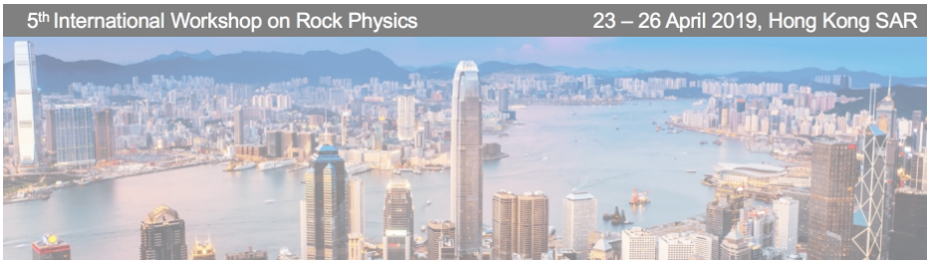


Marcin Ireneusz Duda[1], Rune Martin Holt[1], Jørn Fredrik Stenebråten[2]

[1] Norwegian University of Science and Technology, 7031 Trondheim, Norway
[2] Sintef Petroleum, 7031 Trondheim, Norway

Presented at 5th International Workshop on Rock Physics, 23-26 April 2019, Hong Kong, SAR

## Introduction

Depletion or inflation of a reservoir introduce stress changes in the reservoir itself as well as in its surroundings. As the cap rock is assumed to have very low permeability, negligible fluid movement, and hence no pore pressure equilibration is expected between the reservoir and the overburden within a typical reservoir lifetime. However, alteration of the stress state of a porous impermeable cap rock, caused by pore pressure changes in the reservoir, can lead to undrained pore pressure changes around it. According to Skempton (1954), pore pressure changes in the undrained conditions are governed by two parameters, as shown in equation (1):

$$\Delta p_f = B\left[\Delta\sigma_3 + A\left(\Delta\sigma_1 - \Delta\sigma_3\right)\right] \tag{9.1}$$

where: $p_f$- pore pressure, $\sigma_1$- maximum principle stress, $\sigma_3$- minimum principle stress. Skempton's parameter $B_S$ depends on rock and fluid compressibility, and Skempton's $A$is sensitive to elastic anisotropy and non-elastic characteristics of the rock, as reported by Holt et al. (2018a).

The parameter $B_S$, capturing the influence of the mean stress, is frequently measured and used

in geomechanical modelling. The parameter $A$, describing pore pressure response to shear stress, is usually assumed to be 1/3, which is the expected value for a linearly poroelastic isotropic medium. Experimental results obtained with typical overburden shales (Holt et al. 2018a) show that both elastic anisotropy and nonelastic behavior strongly affect the values of the Skempton parameters. Further, both parameters may have a significant impact on pore pressure changes in the field. In extreme cases of a near-critical state of the overburden, undrained pore pressure changes could lead to cap rock failure. figure 9.1 shows a fictitious case, where Geertsma's nucleus of strain approach (Geertsma 1973) has been used to calculate overburden stresses above the centre and near the edge of the reservoir. While Geertsma's model predicts constant mean stress and hence no pore pressure change in the overburden, the consequence of making $A \neq 1/3$ are significant changes, in particular near the edge of the reservoir, where depletion leads to pore pressure increase if $A > 1/3$. Above the reservoir centre the situation is opposite, and pore pressure may increase by depletion if $A < 1/3$.

The undrained pore pressure response may also modify the effective stress field in the overburden sufficiently to be detected with the use of time-shifts extracted from 4D seismic datasets. This has motivated an experimental study combining measurements of the Skempton parameters and ultrasonic wave velocities under stress paths representative for overburden shales.

## Experimental methodology

Laboratory tests are carried out within a triaxial cell, using a core material from an overburden shale. The samples are cut normally to bedding, confined with a fluid of composition and properties matching those of the pore fluid (determined by pore fluid extraction and physico-chemical analysis), loaded to in-situ stresses and further tested in undrained conditions. Testing procedure consists of multiple loading cycles of varying amplitude and stress paths (see Holt et al. 2018a, for examples). Stresses, strains and pore pressure are recorded, and stress path dependent ultrasonic velocities are measured with pulse transmission. Both Skempton parameters are determined from the pore pressure response during different stress paths.

## Data analysis

The collected data will be used to assess overburden pore pressure response in fictitious field cases like that illustrated in figure 9.1. The data will also be used with geomechanically modelled stress changes above a depleting reservoir, comparing the traditional approach of not including Skempton's $A$ (i.e., $A = 1/3$) with an approach using the measured$A$ from the laboratory tests. Further, based on this, we will discuss to what extent overburden pore pressure change can be detected with 4D seismic.

## Acknowledgements

The authors acknowledge the support from Norwegian CCS Research Centre and AkerBP.

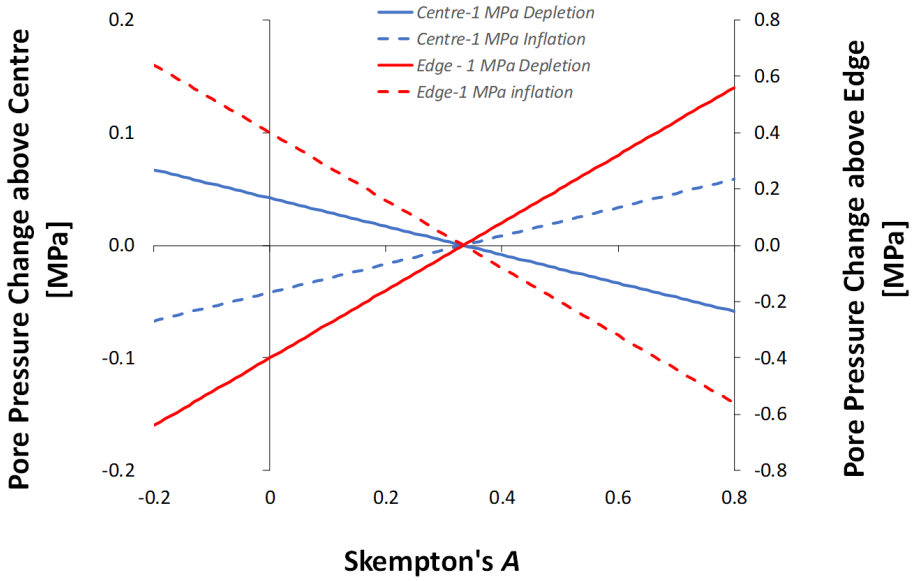


**Figure 9.1:** Undrained pore pressure change in the overburden above a disk-shaped reservoir with aspect ratio 0.1, assuming Geertsma's solution for the total stresses. Note that Geertsma's model is isotropic and linear elastic, so by default $A = 1/3$, and the pore pressure change would then be zero. The graph shows the consequences if $A$ has a different value, without imposing anisotropy nor non-elasticity in the stress calculation itself. Poisson's ratio $\nu = 0.25$, Biot's $\alpha = 1$.

# PRESENTATION I: Top seal undrained pore pressure response - sensitivity to Skempton's $A_S$


Marcin Ireneusz Duda[1], Rune Martin Holt[1], Jørn Fredrik Stenebråten[2]

[1] Norwegian University of Science and Technology, 7031 Trondheim, Norway
[2] Sintef Petroleum, 7031 Trondheim, Norway

Presented at 5th International Conference on Fault and Top Seals, 8-12 September 2019, Palermo, Italy

## Introduction

Under the assumption of low permeability of the seal rock, no significant fluid movement is expected between the cap and the reservoir rocks, which results in lack of diffusive pressure equilibration between the two formations within a typical reservoir life cycle timescale. However, change of pore pressure in the reservoir, due to injection or depletion, causes stress state modification in the reservoir itself and its surroundings. Change of the stresses may further cause an undrained pore pressure response in seal impermeable rocks, hence modify effective stresses, and therefore affect seal's 4D seismic parameters and, in an extreme case of near-failure rocks, trigger faulting. The purpose of this study is to explore the importance of Skempton's parameter $A_S$ for undrained pore pressure response in the reservoir's overburden.

## Theory

Skempton (1954) described the undrained pore pressure response using two parameters, as shown in equation (1):

$$\Delta p_f = B_S \left[\Delta\sigma_3 + A_S \left(\Delta\sigma_1 - \Delta\sigma_3\right)\right] \tag{10.1}$$

where: $p_f$- pore pressure, $\sigma_1$- maximum principle stress, $\sigma_3$- minimum principle stress, $A_S$ and $B_S$ - Skempton's parameters.

Parameter $B_S$, reflecting the impact of mean stress on the undrained pore pressure response, depends mostly on rock and fluid compressibility. It is often measured during laboratory tests and used for modelling purposes. On the other hand, Skempton's parameter $A_S$, giving information on the impact of shear stress on pore pressure evolution (Holt et al. 2018b), is often assumed to be 1/3, as predicted by linearly isotropic poroelasticity. Laboratory tests carried out on typical overburden shales (Holt et al. 2018b) indicate that $A_S$ values are usually significantly different from the theoretical value, and are sensitive to the rock's elastic anisotropy and its non-elastic behaviour.

In an anisotropic (TI) medium, Skempton's parameters form a part of an invariant second-rank tensor consisting of components $B_V$ and $B_H$, where the subscripts refer to directions parallel and normal to the symmetry axis of the TI medium, respectively (Cheng 1997), and can be expressed as

$$B_S = \frac{B_V + 2B_H}{3} \tag{10.2}$$

and

$$A_S = \frac{B_V \cos^2\theta + B_H \sin^2\theta}{3B_S} \tag{10.3}$$

Anisotropic Skempton's parameter $A_S$ depends on the angle $\theta$ between the symmetry axis of the medium and the maximum principal stress direction. Skempton's parameters may be also directly related to the strain sensitivity factor R introduced by Hatchell and Bourne (2005) and Røste et al. (2006). The R - factor depends on intrinsic properties of the rock (including Skempton's $A_S$ and $B_S$) and stress path, and may be used as a tool for seismic monitoring of reservoir overburden.

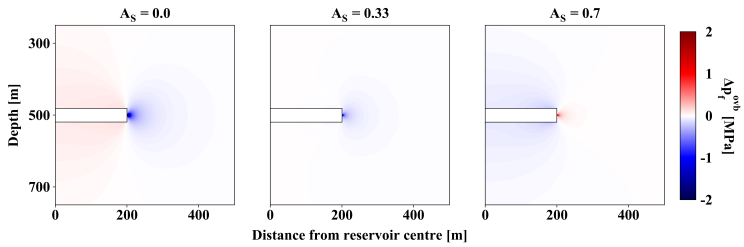


**Figure 10.1:** Undrained response to pore pressure change of – 5 MPa in a disc-shaped reservoir (white box in the mid-left of each plot) of aspect ratio a = 0.1 obtained using Geertsma (1973) formulations, Biot's coefficient $\alpha = 0.9$ and Poisson's ratio $\nu = 0.39$ for stress computations and constant value of Skempton's $B_S = 0.86$ for pore pressure.

Skempton's equation 10.1 clearly indicates the importance of both parameters for the undrained

pore pressure response. The impact of changing Skempton's $A_S$ is demonstrated in figure 10.1, showing pore pressure evolution modelling results obtained with the use of the Geertsma (1973) model (i.e. isotropic, linearly-elastic, disc-like reservoir, no elastic properties contrast between the reservoir and its surroundings) to compute stress changes, and Skempton's parameters to estimate pore pressure response around the reservoir. Even for this simplified example, Skempton's $A_S$ deviation from 1/3 not only modifies the magnitude of pore pressure change, but also affects its direction above the reservoir centre and on the reservoir edges. In the light of evidence for varying $A_S$ value, it is clear that both Skempton's parameters should be estimated in the laboratory conditions and used for large scale geomechanical modelling.

## Laboratory measurements

In order to estimate elastic properties, Skempton's parameters and stress sensitivity parameters of an overburden shale, a laboratory test consisting of several undrained stress cycles along different stress paths was carried out. The core was carefully stored in Marcol oil to maintain its initial humidity, and during the test it was exposed only to expected in-situ brine salinity to avoid unwanted chemico-mechanical and –osmotic effects (Ewy 2015). Before the experiment, the sample was brought to near in-situ stresses and pore pressure.

The experimental setup allowed to measure stresses, strains, pore pressure and ultrasonic seismic velocities, as shown in figure 10.2.

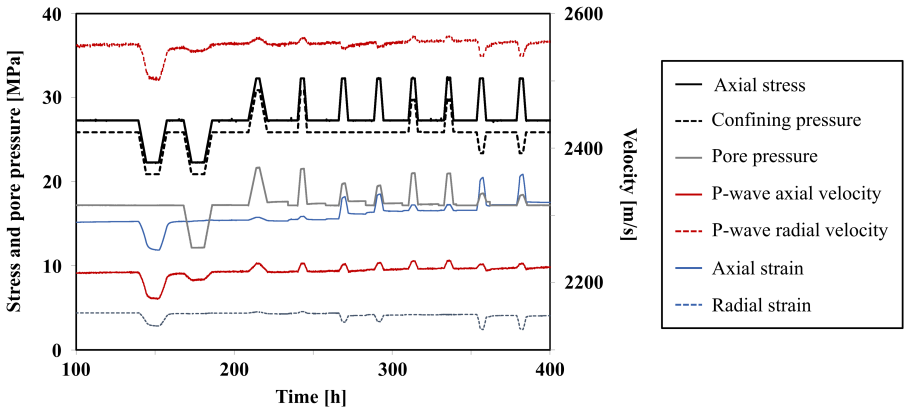


**Figure 10.2:** Drained isotropic and constant net stress cycles, followed with undrained hydrostatic, uniaxial stress, uniaxial strain and constant mean stress loading cycles (modified after Holt et al. 2018b)

Stress and pore pressure measurements were used to approximate $B_V$ and $B_H$, while ultrasonic seismic velocities combined with stress measurements for three different stress paths allowed to estimate stress sensitivity coefficients. The above parameters were further used in geomechanical modelling of the undrained pore pressure response developing in an overburden shale for over 30 years.

## Pore pressure response modelling

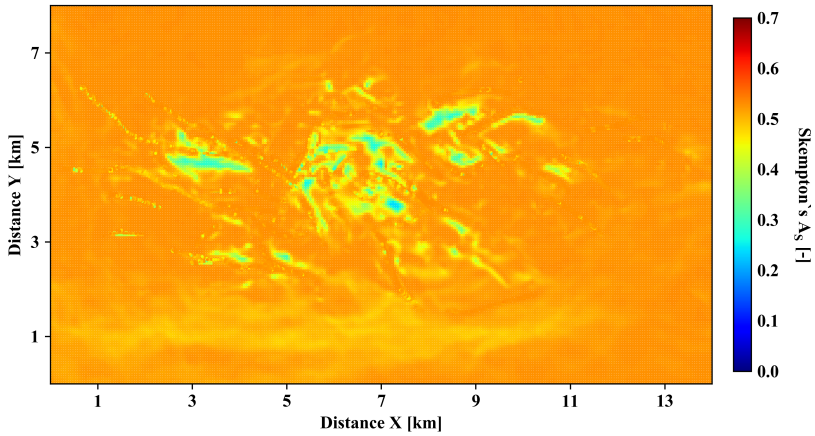


**Figure 10.3:** Skempton's $A_S$ distribution in reservoir's top seal

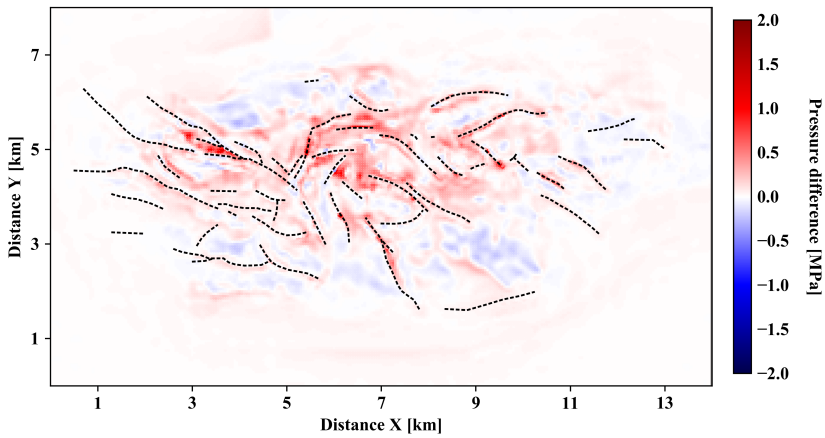


**Figure 10.4:** Difference between undrained pore pressure responses: $\Delta p_f\left(A_S\left[\theta\right]\right) - \Delta p_f\left(A_S = 1/3\right)$. Dashed lines mark location of faults.

For the purpose of this sensitivity study, the experimental parameters were used to model behaviour of an existing oil reservoir top seal formation consisting of a different shale than the tested one (corresponding shale is to be tested in our laboratory in the near future). In order to model the undrained pore pressure response in the top seal, the sealing formation surface normal vector, and the direction and the magnitude of the maximum principal stress in every model grid point must be determined. The approximated angle $\theta$ between the two vectors, combined with experimentally estimated $B_V$ and $B_H$ (equation 10.3), gives $A_S$ distribution in the seal, as shown in Figure 10.3. It is worth noting that the resultant Skempton's $A_S$ values are significantly different from the usually assumed $A_S = 1/3$ in a vast majority of modelled points and approach this value only in zones characterized by large deviation of the maximum principal stress from the surface normal vector.

Combining constant Skempton's $B_S$, approximated $A_S$ distribution and pre-modelled total principal stress change values, the undrained pore pressure response of the top seal can be modelled (equation 10.1). Pore pressure changes were modelled for an isotropic linearly elastic case of constant $A_S = 1/3$ and for transverse isotropy, i.e. angle-dependent $A_S(\theta)$. Figure 4 shows the difference between the two pore pressure responses, ranging from around - 0.5 to 1.7 MPa. Zones characterized by the most significant deviation of pore pressure response from the isotropic case are located directly above the reservoir. In many instances, the maxima and the minima of the difference between the model realisations are located in direct proximity of pre-existing faults. In some cases, the two zones are separated by faults, effectively increasing the effective stress contrast modelled on the opposite sites of the fault zones. The location of the aforementioned zones increases potential impact of Skempton's $A_S$ on top seal stability analysis.

## Conclusions

Typical Skempton's $A_S$ values estimated from laboratory experiments differ significantly from the often assumed $A_S = 1/3$, and this discrepancy has observable consequences for computation of angle-dependent $A_S$ distribution in an existing reservoir stress state and geometry. According to this sensitivity study, the anisotropic parameter $A_S$ has a non-negligible impact on overburden undrained pore pressure response, and hence effective stress distribution in the top seal. Taking into account the location of the zones with the largest differences in predicted pore pressure responses between the isotropic linearly elastic and the anisotropic cases, it may be concluded that introducing experimental values of Skempton's $A_S$ in geomodelling may help greatly in predicting failure risk in the near-failure overburden rocks. The impact of Skempton's parameters on time-lapse seismic modelling, being the next planned step of this study, should be also addressed, as it could increase significantly reliability of top seal and reservoir seismic monitoring.

## Acknowledgments

This publication has been produced with support from SINTEF Industry (Petroleum department), in particular through their past Shale Rock Physics programme, Aker BP and the NCCS Centre, performed under the Norwegian research program Centres for Environment-friendly Energy Research (FME). The authors acknowledge the following partners for their contributions Aker Solutions, ANSALDO Energia, CoorsTek Membrane Sciences, Gassco, KROHNE, Larvik Shipping, Norcem, Norwegian Oil and Gas, Quad Geometrics, Shell, Statoil, TOTAL, and the Research Council of Norway (257579/E20).

# PRESENTATION J: The fate of R in light of field shale laboratory tests


Audun Bakk[1], Rune Martin Holt[2], Marcin Ireneusz Duda[2], , Colin MacBeth[3]

[1] Sintef Petroleum, 7031 Trondheim, Norway
[2] Norwegian University of Science and Technology, 7031 Trondheim, Norway
[3] Heriot-Watt University, Institute of GeoEnergy Engineering, Edinburgh, EH14 4AS, United Kingdom

Presented at 82nd EAGE Annual Conference and Exhibition, 8 - 11 December 2020, ONLINE

## Introduction

Successful utilization of petroleum resources requires a comprehensive monitoring of the subsurface, where time-lapse (4D) seismic is among the most important sources of knowledge. However, this requires that the 4D seismic attributes such as time- and impedance-shifts are adequately interpreted, for a proper quantification of the geomechanical changes caused by the depletion. In the early stages of the millennium 4D seismic was proven not only to be influenced by the reservoir itself via the depletion process, but also by the geomechanical changes in the non-reservoir rocks. The overburden in particular is significantly influenced, which is associated with subsidence, stress changes and potential fault reactivation manifesting as detectable time-shifts (e.g., Hall et al. 2002; Kenter et al. 2004; Zoback and Zinke 2002). The main goal with the processing of the 4D seismic data is a proper separation of the velocity changes and the strains, where the offset dependence of time-shifts turns out to be essential (Landro and Janssen 2002). This requires a physical rock model that links geomechanical changes to time-shifts. In this respect the R-factor model has been widely used (Hatchell and Bourne 2005; Røste et al. 2006). This model assumes that the normalized vertical velocity change ($\Delta V_z$) is linearly related to the vertical strain ($\varepsilon_z$; defined positive for compaction):

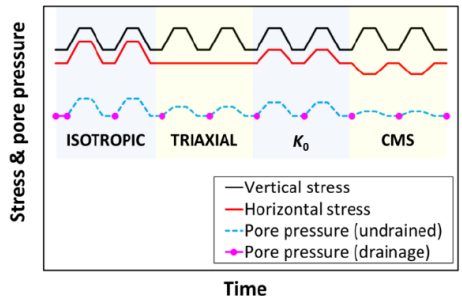


**Figure 11.1:** In-situ stress path variations (schematic). Prior to each undrained stress cycle the samples were drained back to the in-situ pore pressure (the reference state). The vertical stress was changed by 5 MPa in all cycles.

$$R_z = \frac{\Delta V_z}{V_z \varepsilon_z} \tag{11.1}$$

Most commonly the $R_z$ is used to interpret post-stack data, even though this model has also been used on pre-stack data (MacBeth et al. 2018). Although the $R$-factor has been regarded as an "earth constant" in some studies, most publications now regard the $R$ as a spatially varying quantity for which specific values are linked to specific layers or formations (e.g., Gennaro et al. 2008). The increased focus on the offset-dependence of time-shifts has also challenged the original R-factor model as it lacks a tie to non-vertical strains.

A rock physics model to be used to invert 4D seismic data, should have a physical validation that enables reliable generalization and predictability of results. In this work we discuss the $R$-factor and some generalizations of this model by considering experimental data obtained in laboratory experiments on overburden field shales. We also demonstrate how a higher order (non-linear) optimized elastic dynamic stiffness tensor may adequately describe the strain dependence of velocities, which provide a good fit to the offset-dependence of time-shifts from a North-Sea shale.

## Experimental method

All measurements and further analysis assume TI symmetry where the symmetry axis is normal to the horizontal (bedding) plane. The ultrasonic data were acquired on single plugs, where the P-wave velocities were measured along multiple ray (group) angles with different stress variations (stress paths) around the in-situ stress state: constant mean stress change (CMS), vertical stress change (triaxial); zero radial strain ($K_0$) and isotropic stress change (cf. Figure 11.1). The offset angle refers to the vertical axis, i.e. 0° is vertically and 90° is in the horizontal plane. During the stress cycles the pore pressure was undrained, which is assumed to be most representative of low permeability overburden rocks (cap). The field shale cores were stored as "seal-peels" at ambient conditions prior to testing (Bakk et al. 2020).

The assumption of a constant $R$-factor model is appealing since it explicitly relates the velocity change and the strain. This implies that only the vertical strain is a variable when the time-shifts are considered. However, it turns out that the $R$ is not constant throughout the subsurface. Hatchell and Bourne (2005) attributed different $R$-factors to the depleting reservoir and to the surroundings under extension. It should be noted that the depleting reservoir undergoes

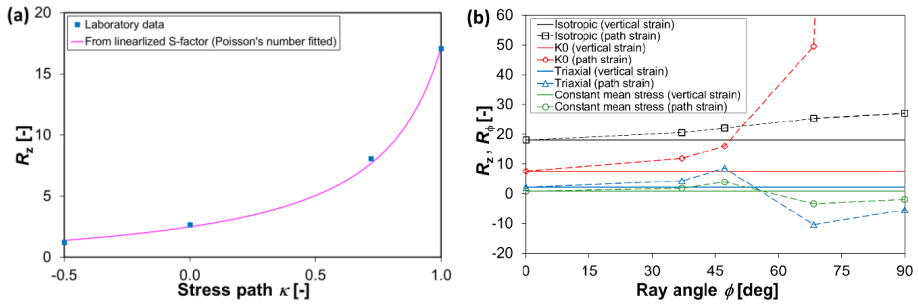


**Figure 11.2:** Laboratory data from overburden field shales. (a): The average values of $R_z$ from three different shales, calculated according to equation 11.1 (based on the vertical strain), as function of stress path $\kappa$ (ratio between the horizontal and vertical stress changes). The fit is obtained by converting the linearized stress sensitivities to $R$-factors by optimizing the Poisson's number (full line). (b): $R_z$ for different stress paths as function of ray angle (full lines) for a North-Sea shale. The $R_\phi$ (open symbols and broken connection lines) are based on the path strain (replacing $\varepsilon_z$ in equation 11.1).

significant and potentially inelastic compaction in addition to fluid substitution, which makes the comparison to its surroundings difficult. Gennaro et al. (2008) show that even within the overburden R is significantly varying in the Elgin and Franklin Fields. The overburden in these fields exhibit large mechanical contrasts between the layers, and between the overburden and the reservoir. Such heterogeneities in the static stiffness throughout the subsurface may also lead to complex stress variations due to the reservoir depletion, i.e. the change in magnitudes (Mulders 2003) and directions (Herwanger et al. 2007) of the principal stresses. Laboratory experiments on field cores may be used to systematically study the impact of different stress paths in the overburden. In figure 11.2a we show the significance of stress path dependence on the $R$-factor. The data in this case are fitted by using Hooke's law to relate the stress and strain sensitivities of velocities (Holt et al. 2018b). In a field case one will experience a range of different stress paths depending on the subsurface location of interest and the specific field (layer properties and production history). Stress and strain data may be obtained from geomechanical simulations coupled to seismic analysis. One should note that often only isotropic stress variations are investigated in laboratory tests, for which the $R$-factors may lead to misinterpretation of the 4D seismic data. An isotropic stress path implies very different $R$-factors as compared to, for example, uniaxial stress ($\kappa = 1$ versus $\kappa = 0$ in figure 11.2a).

The huge potential of pre-stack offset data has in practice challenged the R-factor as it is not obvious why the vertical strain is unique. Kudarova et al. (2016) discussed how to generalize the $R$-factor to account for the path strain ($R_\phi$), defined as the normal strain at ray angle $\theta$, as an alternative to the traditional vertical strain dependence ($R_z$). They analysed the offset-dependence of time-shift data obtained from the Mars and the Shearwater Fields. In figure 11.2b we compare these two approaches on ultrasonic laboratory data of a North-Sea overburden shale. The $R_\phi$ has a strongly fluctuating trend as function of offset. For the $K_0$ stress path, $R_\phi$ is rapidly increasing versus offset as the path strain becomes zero for 90°. On the other hand, the $R_z$ is independent of ray angle for a given stress path according to equation 11.1. If we consider a single homogeneous isotropic layer and straight ray paths, the relative time-shift (equal to time-strain here) is obtained by a differentiation of the (pre-stack) two-way travel-time:

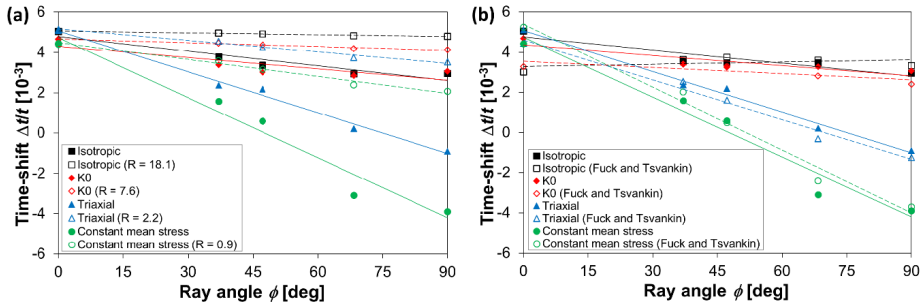


**Figure 11.3:** Relative time-shifts for vertical unloading versus ray angle for different stress paths (cf. figure 11.1) with linear trendlines. The reference data are calculated from ultrasonic measurements on a North-Sea overburden shale cf. equation 11.2 (filled symbols; full trendlines). (a) Time-shifts with the experimental value of $R_z$ for each stress path cf. equation 11.3 (open symbols; broken trendlines). (b) Time-shifts based upon an optimized fit to the TOE model of Fuck and Tsvankin (2009) (open symbols; broken trendlines)

$$\frac{\Delta t}{t} = -\varepsilon_z \cos^2\phi - \frac{\Delta V(\phi)}{V(\phi)} \tag{11.2}$$

which is valid for anisotropic velocities ($V(\phi)$). By inserting the $R_z$ from equation 11.1 into equation 11.2 this simplifies to:

$$\frac{\Delta t}{t} = -\varepsilon_z \left(\cos^2\phi + R_z\right) \tag{11.3}$$

where the $R_z$ implies an isotropic strain sensitivity. By using the same dataset as in figure 11.2b, we calculate the experimental relative time-shifts according to equation 11.2 (cf. figure 11.3a). The experimental data exhibit qualitatively different trends for the respective stress paths, where the CMS stress path exhibits the largest offset gradient. In the same plot we fix the $R_z$ for each stress path to calculate the time-shifts cf. equation 11.3. Consequently, the time shifts for zero offset are perfectly matched, but the offset trends do not match the experimental data neither qualitatively nor quantitatively, as expected (figure 11.3a). Thus, a model capturing strain dependence must also include offset dependence of strain sensitivity, in addition to the stress-path dependence. One should note that by using anisotropic offset velocity changes in the $R_z$, i.e. replacing $V_z$ with the angular velocity in equation 11.1 similar to Hawkins (2008), the time-shift trends are equally variable and do not adequately match the experimental data.

To better match the time-shift data, third order elasticity (TOE) models can be used. The model of Prioul et al. (2004) is appealing with only three additional elastic constants. This model does not match the time-shifts obtained from laboratory shale tests, as its underlying assumption of isotropic strain sensitivity is an oversimplification. However, the TOE of Fuck and Tsvankin (2009) with VTI symmetry of the strain dependence gives a good fit to the experimental time-shift data as shown in figure 11.3b. The latter model involves effectively eight independent TOE parameters (seven for the P-waves) to describe VTI anisotropic strain sensitivity of the velocities.

By including more experimental data one may find correlations between the parameters to make such model better suited for 4D seismic inversion.

## Conclusion

Quantification of the strain sensitivities of velocities is required to adequately invert pre-stack 4D seismic data for static strains in and around a depleting reservoir. Laboratory tests on field shale cores are conducted where different stress paths are systematically varied. The widely used $R$-factor model, assumed to represent the strain sensitivity of P-wave velocities, is shown to be significantly influenced by the stress path. Shales are inherently anisotropic in terms of both static and dynamic stiffnesses, and we also find evidence that shales exhibit anisotropic strain sensitivities. We demonstrate a satisfying fit to offset velocity data from laboratory shale tests when we include VTI symmetry in a third order elastic dynamic stiffness model, contrary to the $R$-factor model. Further data from such experiments together with an adequate constitutive description of the strain sensitivity, may give a good basis to better understand these systems and how this may be used to improve 4D seismic field data analysis.

## Acknowledgements

The authors thank the Research Council of Norway (PETROMAKS 2) for funding; Grant 294369 with AkerBP, Equinor, and Shell; Grant 234074 with AkerBP, Engie, INEOS, and Total.

# PRESENTATION K: Modelling of the undrained pore pressure changes around (an inflating) reservoir

The 14th Euroconference on Rock Physics and Rock Mechanics

## Modelling of the undrained pore pressure changes around (an inflating) reservoir

Marcin Ireneusz Duda[1], Hong Yan[1], Rune Martin Holt[1], Audun Bakk[2]

[1] Sintef Petroleum, 7031 Trondheim, Norway
[2] Norwegian University of Science and Technology, 7031 Trondheim, Norway

Presented at 14th Euroconference on Rock Physics and Rock Mechanics, 30 August - 3 September 2021, ONLINE

The sealing efficiency and fault stability of the reservoir's overburden are essential in both CO2 storage and hydrocarbon production. This elevates the importance of induced stress and pore pressure change prediction in the proximity of the production or injection zones. The low-permeability nature of the overburden makes it necessary to quantify the undrained pore pressure response to stress changes.

The primary objective of our work is to model and comprehensively visualize the undrained pore pressure response of low permeability surroundings (typically shales) of various geological bodies in multiple scenarios of inflation or depletion. We carry out this task for each considered scenario in two steps: First, we perform finite element simulations of stress and strain evolution. Then, we post-process the modelling results to compute the undrained pore pressure change. In order to permit parametric sensitivity studies and provide an understanding of mechanisms that may act in the field, we model isolated geo-features, e.g., disk- and dome-shaped reservoir surroundings, tilted layers, and fault zones. This may serve as a basis for subsequent studies of real-life reservoirs with their excessive complexity and ambiguity of result interpretation.

Moreover, we aim to demonstrate the consequences of using different geomechanical finite-element modelling approaches on the predicted pore pressure distribution trends and values. Our study investigates the impact of factors such as boundary conditions of the model, properties assigned to the modelled deposits, relations between all three principal stresses, and the choice of pore

pressure prediction model. The impact of anisotropy assigned to reservoir surroundings during geomechanical modelling on the estimated pore pressure response is shown in figure 12.1. We compare the approaches in terms of the complexity of their application and the results their produce. Finally, we identify the most important factors, which should be taken into consideration during a full-scale reservoir modelling.

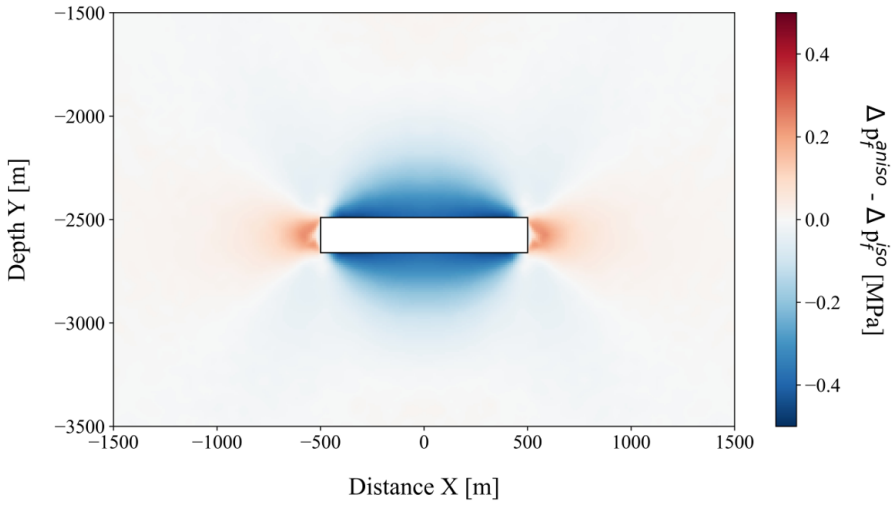


**Figure 12.1:** Difference between the undrained pore pressure responses of anisotropic (transversely isotropic) and isotropic reservoir surroundings. The two media were roughly matching in terms of their effective bulk properties. Stress state changed due to homogenous inflation of 30 MPa in a disk-shaped reservoir (indicated by the white box in the middle of the plot).

# PAPER L: Effects of anisotropic poroelasticity on stress and pore pressure changes around subsurface reservoirs and storage sites


Rune Martin Holt[1], Audun Bakk[2], Marcin Ireneusz Duda[1], Hong Yan[1]

[1] Norwegian University of Science and Technology, 7031 Trondheim, Norway
[2] Sintef Petroleum, 7031 Trondheim, Norway

Presented at 56th U.S. Rock Mechanics/Geomechanics Symposium, 26 - 29 June 2022, Santa Fe, USA

Stresses and pore pressures change around depleting hydrocarbon reservoirs or fluid injection sites as result of reservoir pore pressure change. Such changes influence the stability of new wells drilled and may lead to fault activation, resulting in induced seismicity and possibly to casing damage in existing wells. Forecasting requires reliable geomechanical modeling of the reservoir and its surroundings. Classical analytical solutions are too simple, so numerical models are required. The rocks surrounding reservoirs are often anisotropic (like overburden shale), but their anisotropic elasticity is normally neglected, either because of model limitations, or in lack of input data. Here, however, the impact of anisotropy along with the elastic contrast between undrained surroundings and drained (isotropic) reservoir rock is addressed through a series of numerical scenarios. It is shown that isotropic models are unable to reproduce the stress changes predicted by the anisotropic models. Pore pressure changes may be underestimated by neglecting the anisotropic nature of the poroelastic Skempton parameters.

# PAPER M: Effect of field caprock shale exposure to $CO_2$ on its mechanical properties — A comparison of experimental techniques


Pierre Cerasi[1], Marcin Ireneusz Duda[1,2], Laura Edvardsen[1], Nicolaine Agofack[1], Mohammad Hossain Bhuiyan[1]

[1] Sintef Petroleum, 7031 Trondheim, Norway
[2] Norwegian University of Science and Technology, 7031 Trondheim, Norway

Presented at the 19th International Conference on Experimental Mechanics, 17–21 July 2022, Kraków, Poland

Laboratory tests were performed on the Draupne shale formation, which may serve as a seal over $CO_2$ storage sites. Different techniques were used to assess the integrity and mechanical properties of the shale, with the main objective of investigating whether exposure to $CO_2$ would in any manner alter these properties. The laboratory methods used encompass traditional triaxial tests; however, with fluid substitution prior to increasing axial stress to failure. These tests were conducted on smaller cylindrical plugs than standard, taking advantage of the finer grained nature of the shale. Another set of experiments used the low-frequency technique, whereby small amplitude, cyclic axial strains are applied on the specimen, allowing a direct measurement of stiffness. Long exposure, with change of fluid from brine to $CO_2$, allowed for quantifying small changes in stiffness, thanks to the many repeated cycles of non-destructive testing. In a final experimental technique, the punch test, shear strength of the same material was obtained by cutting a central disk from a larger intact shale disk, while measuring the shear force needed to perform the cut.

# PAPER N: Overburden 4D seismic: Influence of stress and pore pressure changes accounting for elastic contrast between a reservoir and its anisotropic surrounding rocks

Hong Yan[1], Audun Bakk[2], Marcin Ireneusz Duda[1,2], Rune Martin Holt[1,2], Serhii Lozovyi[2]

[1] Norwegian University of Science and Technology, 7031 Trondheim, Norway
[2] Sintef Petroleum, 7031 Trondheim, Norway

Published in *GEOPHYSICS* on 28 March 2023

Time-lapse (4D) seismic is one of the most widely used techniques to monitor producing hydrocarbon or CO2 storage reservoirs and their surroundings. The influence of potentially significant undrained pore pressure changes around depleting (or injected) reservoirs appears to be neglected in most previous studies. The 4D seismic response in the overburden depends on the stress changes and strains induced by the reservoir. These alterations may challenge stable infill drilling and well integrity. We utilize anisotropic static elastic moduli from laboratory measurements for two different field shales to predict stress changes and strains in the surroundings of a depleting reservoir through geomechanical modelling. These mechanical changes are used to quantify undrained pore pressure changes using anisotropic poroelastic theory constrained with Skempton parameters. Finally, an empirical rock physical model quantifies the impact of these poroelastic changes on vertical velocity changes and time-strains. This model explicitly quantifies the individual contributions to vertical velocity changes from undrained pore pressure, mean stress, and shear stress above (and below) the depleting reservoir. We show that a stiffer surrounding rock exhibits significantly larger vertical time-strains and time-shifts in the overburden as compared to softer surrounding rocks because of promoted arching. Undrained overburden pore pressure changes significantly contribute to overburden velocity changes and time-shifts. Ignoring anisotropy in the Skempton parameters can lead to overestimating overburden undrained pore pressure and time-shifts after reservoir depletion. The anisotropy in static stiffnesses significantly impacts the dynamic changes in the vertical direction, and the dynamic changes are particularly pronounced in the vicinity of the reservoir. We show how a tailored rock physics model can link 4D seismic and geomechanics to separate stress, strain, and pore pressure changes — all essential for optimizing drilling and production.

## References

Bakk, A., R. M. Holt, A. Bauer, B. Dupuy and A. Romdhane (2020). 'Offset dependence of overburden time-shifts from ultrasonic data'. In: *Geophysical Prospecting* 68.6, pp. 1847–1863. ISSN: 0016-8025. DOI: https://doi.org/10.1111/1365-2478.12963. URL: https://onlinelibrary.wiley.com/doi/abs/10.1111/1365-2478.12963.

Cheng, A. H. D. (1997). 'Material coefficients of anisotropic poroelasticity'. In: *International Journal of Rock Mechanics and Mining Sciences* 34.2, pp. 199–205. ISSN: 1365-1609. DOI: https://doi.org/10.1016/S0148-9062(96)00055-1. URL: http://www.sciencedirect.com/science/article/pii/S0148906296000551.

Ewy, R. (2015). 'Shale/claystone response to air and liquid exposure, and implications for handling, sampling and testing'. In: *International Journal of Rock Mechanics and Mining Sciences* 80, pp. 388–401. DOI: 10.1016/j.ijrmms.2015.10.009.

Fuck, R. F. and I. Tsvankin (2009). 'Analysis of the symmetry of a stressed medium using nonlinear elasticity'. In: *GEOPHYSICS* 74. DOI: 10.1190/1.3157251.

Geertsma, J. (1973). 'A Basic Theory Of Subsidence Due To Reservoir Compaction; The Homogeneous Case'. In: *Verhandelingen Kon. Ned. Geol. Mijnbouwk. Gen* 28, pp. 43–62.

Gennaro, S. de, A. Onaisi, A. Grandi, L. ben brahim and V. Neillo (2008). '4D reservoir geomechanics: A case study from the HP/HT reservoirs of the Elgin and Franklin fields'. In: *First Break* 26. DOI: 10.3997/1365-2397.2008019.

Hall, S. A., C. MacBeth, O. I. Barkved and P. Wild (2002). 'Time-lapse seismic monitoring of compaction and subsidence at Valhall through cross-matching and interpreted warping of 3D streamer and OBC data'. In: *SEG Technical Program Expanded Abstracts 2002*, pp. 1696–1699. DOI: 10.1190/1.1817004. URL: https://library.seg.org/doi/abs/10.1190/1.1817004.

Hatchell, P. and S. Bourne (2005). 'Rocks under strain: Strain-induced time-lapse time shifts are observed for depleting reservoirs'. In: *The Leading Edge* 24.12, pp. 1222–1225. DOI: 10.1190/1.2149624. URL: https://library.seg.org/doi/abs/10.1190/1.2149624.

Hawkins, K. (2008). 'Defining the extent of the compacting Elgin reservoir by measuring stress-induced anisotropy'. In: *First Break* 26.10. ISSN: 1365-2397. DOI: https://doi.org/10.3997/1365-2397.26.10.28559. URL: https://www.earthdoc.org/content/journals/0.3997/1365-2397.26.10.28559.

Herwanger, J., E. Palmer and C. R. Schiøtt (2007). 'Anisotropic velocity changes in seismic time-lapse data'. In: *SEG Technical Program Expanded Abstracts 2007*, pp. 2883–2887. DOI: 10.1190/1.2793065.

Holt, R., A. Bakk, J. F. Stenebråten, A. Bauer and E. Fjær (2018a). *Skempton's A — A Key to Man-Induced Subsurface Pore Pressure Changes*. Conference Paper.

Holt, R. M., A. Bauer and A. Bakk (2018b). 'Stress-path-dependent velocities in shales: Impact on 4D seismic interpretation'. In: *GEOPHYSICS* 83.6, MR353–

MR367. DOI: 10.1190/geo2017-0652.1. URL: https://library.seg.org/doi/abs/10.1190/geo2017-0652.1.

Kenter, C. J., A. v. d. Beukel, A. C. Hatchell, P. Maron, K. Molenaar, M. M. Molenaar and J. Stammeijer (2004). 'Geomechanics And 4D: Evaluation Of Reservoir Characteristics From Timeshifts In The Overburden'. In: *6th North America Rock Mechanics Symposium*.

Kudarova, A., P. Hatchell, J. Brain and C. Macbeth (2016). 'Offset-dependence of production-related 4D time shifts: Real data examples and modeling'. In: *SEG Technical Program Expanded Abstracts 2016*, pp. 5395–5399. DOI: 10.1190/segam2016-13611549.1. URL: https://library.seg.org/doi/abs/10.1190/segam2016-13611549.1.

Landro, M. and R. Janssen (2002). *Estimating Compaction and Velocity Changes from Time-Lapse near and far Offset Stacks*. Conference Paper. DOI: https://doi.org/10.3997/2214-4609-pdb.5.P036. URL: https://www.earthdoc.org/content/papers/10.3997/2214-4609-pdb.5.P036.

MacBeth, C., A. Kudarova and P. Hatchell (2018). 'Review Paper: A semi-empirical model of strain sensitivity for 4D seismic interpretation'. In: *Geophysical Prospecting* 66.7, pp. 1327–1348. DOI: https://doi.org/10.1111/1365-2478.12648. eprint: https://onlinelibrary.wiley.com/doi/pdf/10.1111/1365-2478.12648. URL: https://onlinelibrary.wiley.com/doi/abs/10.1111/1365-2478.12648.

Mulders, F. (2003). 'Modelling of Stress Development and Fault Slip in and Around a Producing Gas Reservoir'. Thesis.

Prioul, R., A. Bakulin and V. Bakulin (2004). 'Nonlinear rock physics model for estimation of 3D subsurface stress in anisotropic formations: Theory and laboratory verification'. In: *Geophysics* 69, pp. 415–425. DOI: 10.1190/1.1707061.

Røste, T., A. Stovas and M. Landrø (2006). 'Estimation of layer thickness and velocity changes using 4D prestack seismic data'. In: *GEOPHYSICS* 71.6, S219–S234. DOI: 10.1190/1.2335657. URL: https://library.seg.org/doi/abs/10.1190/1.2335657.

Skempton, A. W. (1954). 'The Pore-Pressure Coefficients A and B'. In: *Géotechnique* 4.4, pp. 143–147. DOI: 10.1680/geot.1954.4.4.143. URL: https://www.icevirtuallibrary.com/doi/abs/10.1680/geot.1954.4.4.143.

Zoback, M. D. and J. C. Zinke (2002). 'Production-induced Normal Faulting in the Valhall and Ekofisk Oil Fields'. In: *pure and applied geophysics* 159.1, pp. 403–420. ISSN: 1420-9136. DOI: 10.1007/PL00001258. URL: https://doi.org/10.1007/PL00001258.

# Post scriptum

Working on this thesis was an enjoyable experience.

At least, it was enjoyable until my project concluded and I transitioned to a full-time job. Consequently, I found myself finalizing the thesis during evenings and weekends. From that point on, the experience was not always as enjoyable.

However, during this time, I discovered that in certain circumstances, what is necessary takes precedence over what seems interesting, that enough is really enough, and that every story needs an ending.

In short, I suppose I "fooled around and found out". Which I believe aptly captures the essence of a PhD project...

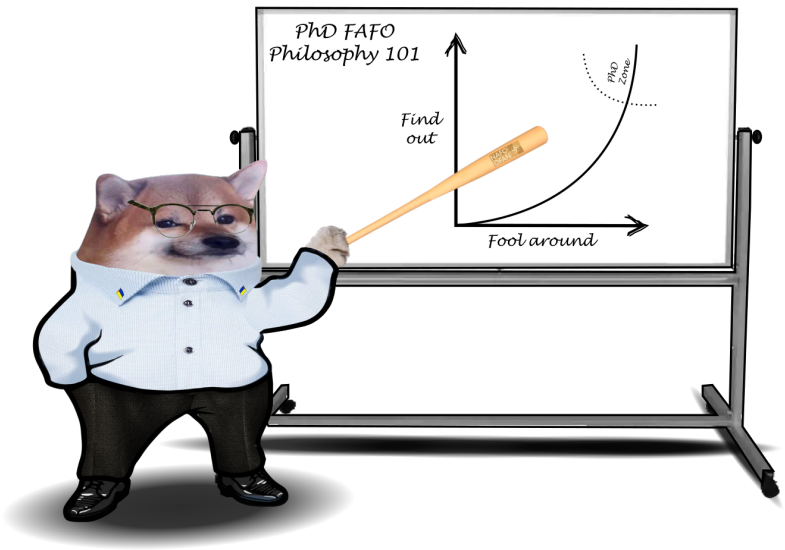

... and then, on February 24th, 2022,
the importance of all this became questionable.

ISBN 978-82-326-7352-0 (printed ver.)
ISBN 978-82-326-7351-3 (electronic ver.)
ISSN 1503-8181 (printed ver.)
ISSN 2703-8084 (online ver.)





NTNU

Norwegian University of
Science and Technology